COUPLED DYNAMICS OF ABOVE- AND BELOW-GROUND INTERACTIONS IN THE CRITICAL ZONE

BY

JUAN CAMILO QUIJANO

DISSERTATION

Submitted in partial fulfillment of the requirements
for the degree of Doctor of Philosophy in Civil Engineering
in the Graduate College of the
University of Illinois at Urbana-Champaign, 2013

Urbana, Illinois

Doctoral Committee:

Professor Praveen Kumar
Professor Murugesu Sivapalan
Professor Amilcare Porporato
Professor Carl Bernacchi
Assistant Professor Andrew Leakey

Abstract

A detailed understanding of the processes and interactions that occur in the Critical Zone (CZ) is extremely important. It will help us to sustainably manage natural resources while maintaining a balance between the natural dynamics and anthropogenic modifications. In this study I have developed a predictive understanding of the above- and below-ground interactions that occur in the CZ in the light of different dynamics involving water, carbon, nitrogen, energy, and thermodynamic entropy fluxes. In addition, these processes are analyzed within a multi-species framework where different plant species coexist and share resources. Coexistence of species originates competitive and mutualistic interactions that impact the fluxes described above. This study represents the first numerical attempt that simulates all these dynamics using a common framework and numerical formulation.

The above- and below-ground dynamics were analyzed using data from three Ameriflux Sites: (i) Blodgett Ameriflux Site, California, US, (ii) Tapajos Km 67, Para, Brazil, and (iii) Harvard Forest, Massachusetts, US. The ecosystems in these sites have different species composition, and experience different climatic conditions. In addition, these sites have more than three years of records, and detailed experimental research has been performed by others which facilitates the validation of the simulations performed in this study.

I analyzed the role of vegetation structure and composition on the fluxes of water, energy, and entropy. Our simulations recognized mutualistic and competitive interactions for water resources that impacted the ecosystem productivity, and the energy and water balance in the land surface. These results suggest plant species composition is an important factor that regulates the fluxes of water in the soil and should be included in ecohydrological models. Long term simulations demonstrate that plants impact the below-ground biogeochemical cycling of nitrogen and carbon, not only by litter drop, as had been recognized in previous ecological experimental studies, but also from their impact on the water and energy balance of the surface. Alteration of energy and water balance under different vegetation structure also represents significant differences in the budget of entropy, which increases with leaf area index (LAI) and is constrained by the below-ground capacity (e.g. deep roots) to sustain

high rates of latent heat (LE) fluxes.

Lastly, I explored the production of entropy as a general organizing principle that explains the structure, composition, and functioning of ecosystems resembling different levels of organization in the CZ. I found there is no significant difference in the total entropy production between the different levels of organization. However, the diurnal patterns of entropy production and the forms of the outgoing entropy flux varies considerably. There is an important trade off between the dissipation of energy in the forms of LE and longwave (LW). LE enhances entropy production by reducing the surface effective temperature while LW enhances the production of entropy because it has higher levels of entropy than the LE fluxes. I found this trade off changes according to the level of organization that is present in the CZ.

I dedicate this thesis to my wife Vivi for her love, and support. She makes me happy every single day, and her company illuminates my life. Her presence allowed me to enjoy my research even more.

Also, I dedicate this thesis to my parents, as they supported me all the way, and taught me the most important values of life. They taught me hard work, perseverance, humility, honesty and integrity. They are the best human beings I have known and their life is my favorite book because from that I learn every day.

Acknowledgments

I would like to thank my advisor Professor Praveen Kumar for all his support and teaching. He supported my ideas and motivated me with new paradigms. He always challenged my thinking during my learning process and taught me hard work and integrity. I feel extremely lucky I had the opportunity to be his student. He is an amazing researcher, and a charismatic advisor. I really appreciate all the time he spent to think and work with me. Beyond the articles, or even beyond this document the most important product of my PhD is my new conceptualization of the world, the new ideas I have, and my motivation to continue working with these ideas. This conceptualization was structured during hours of discussion with Professor Kumar, hours of thinking, and for me, this is my PhD. My special thanks to Darren Drewry for all his help, teaching, and support during my PhD. Today he is a very good friend who is always supporting me.

I am grateful to my parents for all their support, and teaching. They always encouraged me with positive comments, and taught the most important values of life. They worked very hard for my education and adviced me to follow my dreams and always do the best I can. I would not have been able to reach this stage without their unconditional love and guidance. I would like to thank Vivi, for all her support during this time, as she is my strength and happiness. She has been always very supportive and without her I would not have been able to perform the same research. She makes my life happy and she helped to enjoy my research even more. I wish to express my gratitude to my brothers, Bernardo, Pillo, and Pipe. We grew up together and they taught me how to be a good person and influenced the way I think. Because of them I have never felt alone, and because of them I will never feel alone because I know I always have them. I would like to thank my sisters in law Caro, Clari, and Zulmis, as they have always been very supportive of me. In particular, I would like to thank my nephews Nico, Pipe, and Samu, and nieces Maria Jose, and Maria Carito. Their enthusiasm make my world shine and their innocence always reminds me on how to be a good researcher. I would like to thank my cousins Chato, Chela, and Tuqui for all their support during all these years. They always looked after me and helped with their

positiveness. In particular Chato who visited me twice.

My thanks and appreciations to all the students in Professor Kumar′s group with whom I shared many special moments during these years. Ciaran, Venkat, Satish, Namrata, Phong, Sayo, Allison, and Deb. In particular, I would like to thank Venkat, we took many courses together and work simultaneously all these years in our PhD. I learned a lot from him. Also I would like to thank all my friends and professors from the Hydro Lab. In particular I would like to thank Professor Murugesu Sivapalan for his advice during my PhD.

I would like to thank my best friends in Urbana Champaign, Osquitar, Taty, El compadrito, Perri, Oki, Nestor, Olga, Migue, Pao, Sara, El Boli, la Vaca, Emerson, Patrick, Gris, Los Cachorros, Kia, Mat, and all the members of the Colombian Association, as you all helped me to enjoy all these years in Urbana-Champaign.

I am truly thankful to professors Andrew Leakey, Carl Bernacchi, and Amilcare Porporato for being part of my committee, for all their feedbacks, and for their time and support during my PhD.

Above all, I would like to thank God for giving me the opportunity to be a student in this prestigious University. I know God would guide my future to use the knowledge I obtained during my PhD to help other people.

Finally, yet importantly, I would like to acknowledge the support of the National Scientific Foundation, Grants ATM 06-28687 and EAR 09-11205, and I would like to thank the Graduate College of the University of Illinois for granting me the Dissertation Completion Fellowship that allowed me to finish my thesis in a timely manner.

Table of Contents

List of Tables ix

List of Figures x

List of Abbreviations xiii

CHAPTER 1 Introduction 1
1.1 Above- and Below-Ground Interactions: Open Issues 3
1.2 Research Questions 8
1.3 Research Contribution 9

CHAPTER 2 Competitive and Mutualistic Dependencies in Multi-Species Vegetation Dynamics Enabled by Hydraulic Redistribution 15
2.1 Introduction 15
2.2 Methods 18
2.3 Results and Analysis 25
2.4 Summary and Discussion 38

CHAPTER 3 Role of Climate and Species Composition on Hydraulic Redistribution 52
3.1 Introduction 52
3.2 Methods 54
3.3 Results and Analysis 57
3.4 Summary and Discussion 71

CHAPTER 4 Passive Regulation of Soil Biogeochemical Cycling by Root Water Transport 74
4.1 Introduction 74
4.2 Methods 76
4.3 Results and Analysis 84
4.4 Summary and Discussion 102

CHAPTER 5 Entropy Production in Ecohydrologic Systems 108
5.1 Introduction 108
5.2 Methods 111
5.3 Results and Analysis 119
5.4 Summary and Discussion 132

CHAPTER 6 Conclusions 136
6.1 Research Summary 136
6.2 Integrated Examination Across Different Processes 141
6.3 Future Research 143

APPENDIX A Multi-Species Mlcan Model Description 150
A.1 Previous Models 150
A.2 Model Introduction 156
A.3 Above-Ground Interactions 158
A.4 Below-Ground Interactions 160

APPENDIX B Litter Model 182

APPENDIX C Solution of Snow-Litter Dynamics 185
C.1 Change of Phase in the Soil 185
C.2 Solution of the Snow-Litter Pack 188
C.3 Mass Balance in the Snow-Litter Pack 196

APPENDIX D Estimation Root Conductivities 202
D.1 Root Conductivities Computation 202

APPENDIX E Soil Carbon and Nitrogen Model 213
E.1 Fine Root Response to Drought 213
E.2 C-N Model Equations 214
E.3 LAI Dynamics and Litter Production 219
E.4 Organic Carbon Concentrations and Calibration of k_s and k_b 221
E.5 Soil Moisture and Temperature Dependence 222

APPENDIX F Entropy Budget in Open Systems 228
F.1 Approximation for the Calculation of Entropy of Thermal Radiation 230
F.2 Aoki Approximation to Compute Radiation Entropy Budgets in Earth Systems 237
F.3 Entropy and Energy Balance 242

REFERENCES 243

List of Tables

2.1 List of symbols for Multi-Species MLCan implementation in Blodgett. 45
2.2 List of parameters used in the simulations for the Blodgett Ameriflux Site. . 48
2.3 List of parameters for the soil and litter model. 51

4.1 Carbon and nitrogen model parameters. 105
4.2 Total annual nitrogen fluxes in Blodgett. 107

C.1 List of symbols used in the snow model. 199

D.1 Ecosystems information used to compute the root hydraulic conductivities. . 210
D.2 Ecophysiological parameters in Blodgett, Tapajos, and Harvard Forest Ameriflux Sites. 212

E.1 List of symbols in the carbon and nitrogen model. 224
E.2 Description of the different horizons included in the simulation. 226

List of Figures

1.1 Above- and below-ground interactions in the Critical Zone 2
1.2 Dynamics and scientific fields that are related with the above- and below-ground interactions. 10

2.1 Physiological and climatological data from Blodgett used in the model simulations. 21
2.2 Schematic representation of the multi-species MLCan model 22
2.3 Sensitivity of ground heat flux (G) to litter layer thickness (Δz) and thermal conductivity 26
2.4 Illustration of the annual variation of latent heat flux in Blodgett. Single species. 28
2.5 Illustration of the annual variation of latent heat flux in Blodgett. Multi Species. 31
2.6 Water uptake patterns in 2001 and 2002. 32
2.7 Diurnal pattern of water uptake by PP and Shrubs in summer. 34
2.8 Soil moisture dynamics at the Blodgett site during the year 2002 at depths of 10 cm, 30 cm, and 50 cm. 36
2.9 Illustration of the trade-off between soil evaporation and shrubs transpiration 40
2.10 Illustration of the annual variation of carbon assimilation in Blodgett in the presence and absence of HR in 2002. 43

3.1 Normalized root and leaf area distributions for each plant functional type . . 56
3.2 Fluxes of latent heat recorded and simulated in Blodett, Tapajos, and Harvard Forest 58
3.3 Monthly fluxes of water uptake in Blodgett, Tapajos, and Harvard Forest . . 61
3.4 Effect of overstory plant species on understory dynamics. 66
3.5 Effect of specific root axial hydraulic conductivity on the fluxes of transpiration and hydraulic redistribution. 68
3.6 Effect of specific root radial hydraulic conductivity on the fluxes of transpiration and hydraulic redistribution 70
3.7 Effect of mean annual precipitation on the fluxes of transpiration and hydraulic redistribution 73

4.1 Schematic representation of the coupling between the multi-species MLCan model and the C:N model. 78
4.2 Annual time series of atmospheric variables used to force MLCan eco-hydrological mode. 81
4.3 Annual time series of biogeochemical variables observed in Blodgett Forest. . 82
4.4 Initial conditions in the vertical distribution of soil carbon in the organic matter and soil carbon in the microbial biomass 84
4.5 Fine root conductivity loss functions at the top 3 cm of horizon A1. 86
4.6 Energy balance at the surface and implications on water fluxes 88
4.7 Long term dynamics of carbon in the soil organic matter. 91
4.8 Sensitivity analysis on fine root functioning at the top surface. 93
4.9 Soil temperature and soil respiration 95
4.10 Dynamics of water and nitrate (NO_3^-) uptake in Blodgett 98
4.11 Long term simulation results of mineral nitrogen in the soil. 100
4.12 Trade off between nitrification rate, root diffusion nitrogen uptake factor and total leaching of mineral nitrogen from the root zone 104

5.1 Forcing for Blodgett, Tapajos and Harvard Forest 112
5.2 Scheme for entropy calculation. 114
5.3 Validation fluxes of latent and sensible heat in Blodgett, Tapajos, and Havard Forest 120
5.4 Net fluxes of energy and entropy in Blodgett, Tapajos, and Harvard Forest. . 122
5.5 Seasonal entropy fluxes in Blodgett, Tapajos, and Harvard Forest 125
5.6 Radiation factors for shortwave and longwave. 127
5.7 Effective temperatures for the different scenarios in Blodgett, Tapajos, and Harvard Forest 129
5.8 Influence of soil moisture on albedo and entropy fluxes. 134
5.9 Sensitivity analysis of LAI on the entropy production 134

6.1 Illustrative figure of all the above- and below-ground feedbacks in the Critical Zone. 145

A.1 Schematic representation of the multi-species MLCan model. 157
A.2 Schematic representation of above-ground dynamics considered in Multi-Species MLCan. 161
A.3 Flowchart illustrating the numerical solution of the above-ground dynamics in multi-MLcan. 162
A.4 Flowchart illustrating the numerical solution for the below-ground soil moisture dynamics in multi-MLcan. 165
A.5 Representation of Soil Mass Balance. 166
A.6 Schematic representation of root discretization. 170
A.7 Schematic representation of root discretization at the top. 171
A.8 Schematic representation of root discretization at the bottom. 172

A.9 Schematic representation of soil discretization. 174
A.10 Schematic representation of soil discretization at the top. 176
A.11 Schematic representation of soil discretization at the bottom. 177

B.1 Schematic illustrating the litter model. 183

C.1 General description of snow and litter solution. 186
C.2 Representation of the energy solution of the snow-litter pack. 191
C.3 Flow chart of the different processes involves to solve the energy balance inside the snow-litte pack layer. 194

E.1 Schematic representation of the vertical structure and carbon fluxes below the ground. 227

List of Abbreviations

CZ: Critical Zone
HR: Hydraulic Redistribution
HL: Hydraulic Lift
HD: Hydraulic Descent
MEPP: Maximum Entropy Production Principle
LE: Latent Heat Flux
H: Sensible Heat Flux
SW: Shortwave Radiation Flux
LW: Longwave Radiation Flux
G: Ground Heat Flux

CHAPTER 1

Introduction

The Critical Zone (CZ) is defined as the *heterogeneous, near surface environment in which complex interactions involving rock, soil, water, air, and living organisms regulate the natural habitat and determine the availability of life-sustaining resources* [NRC, 2001]. The word *critical* in this concept refers to the presence of living systems and the processes they influence. The CZ hosts the highest biodiversity pool in our planet and therefore the interactions between living systems and the environment is particularly important.

The CZ provides a unifying network for integrating terrestrial surface and near-surface environments, and reflects the intricate web of transformations, cycling and transport associated with hydrologic, geochemical, carbon, and nutrient processes, as well as gas exchange, erosion and deposition, weathering, lithification, soil formation, life processes, and human impacts. Although the CZ concept enables us to study these processes in an integrated framework, there are several complex non-linear interactions between all these processes that are difficult to understand. In order to study the CZ it is important to perform a multidisciplinary research and analyze these coupled interactions involving the different processes.

In particular the above- and below-ground interactions that occurs continuously in the CZ influence the flows of mass, energy, and entropy, which in turn over different time scales structure the shape and functioning of the CZ. Figure 1.1 shows a schematic representation of the most relevant processes that occurs above and below the ground in the CZ.

The most prominent fluxes of energy and water that drive the dynamics in the CZ comes from above the CZ. The above-ground part of the CZ dissipates the incoming energy. Therefore, the capacity of the CZ to extract free energy from the incoming energy flux is regulated by the above-ground structure. In addition, the above-ground structure influences the storage of free energy in biochemical compounds and the uptake of CO_2 during photosynthesis. However, the performance of the above-ground structure is constrained by the availability of water and nutrients, and the capacity of the below-ground roots to support the uptake of these resources.

Plants continuously release biochemical energy in the soil by different mechanisms such

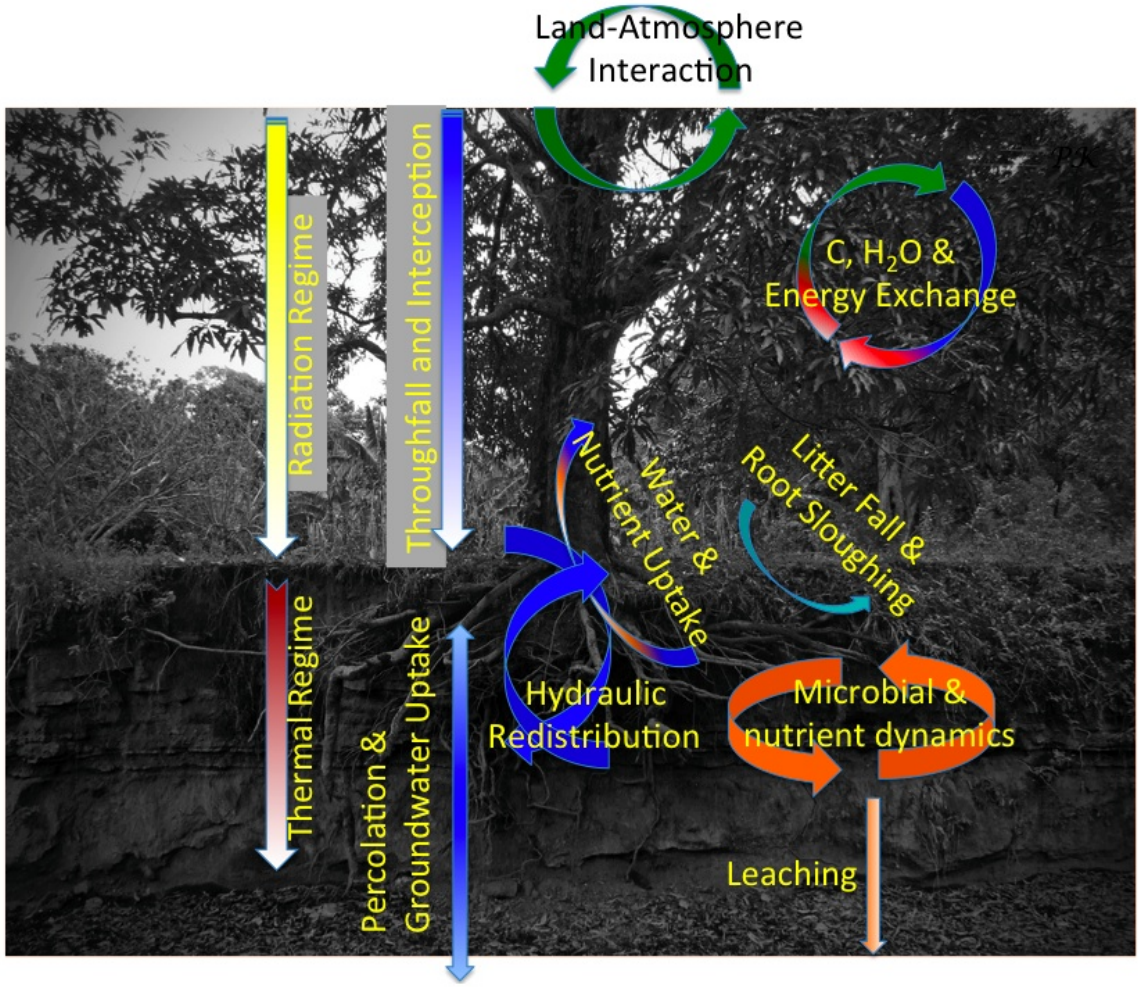

Figure 1.1: Above- and below-ground interactions in the Critical Zone. From Kumar [2010]

as litter fall, root sloughing, or whole plant death. This biochemical energy sustains a vast amount of micro flora and fauna communities below the ground. These communities, in turn decompose the organic material and release mineral nutrients that are again readily taken up by the plants, completing a cycle of energy and biogeochemical nutrients. This cycling is constantly producing entropy and is fueled by the high free energy content in the incoming shortwave radiation (SW).

Apart from being the most prominent source of biochemical energy, plants also regulate the distribution of moisture in the subsurface by processes such as water uptake and water release through hydraulic redistribution (HR) in different horizons of the soil. Soil moisture is a principal regulator of biochemical reactions, therefore, the distribution of moisture by plants also influences the micro flora and fauna dynamics below the ground. However, the uptake of moisture by plant roots is driven by the above-ground demands of water.

In summary, the above- and below-ground processes are in a continuous interaction and are mutually regulated. There are different hydrological, biogeochemical, and energetic processes that are controlled by these coupled interactions. A detailed examination of the above- and below-ground interactions, a target of this study, will be very useful in improving our understanding of the evolution and functioning of the CZ.

1.1 Above- and Below-Ground Interactions: Open Issues

Studies performed in the recent years have improved our understanding about the interactions between above- and below-ground processes in the CZ [Bardgett and Wardle, 2010]. Although the investigation from previous studies have uncovered some fundamental principles and identified critical process, still there are important issues that deserve deeper understanding. In this section we describe some of these issues.

Different experimental studies from the last twenty years have underlined the importance of the above- and below-ground interactions as a regulator of ecosystem dynamics [Berg and McClaugherty, 2008, Deluca et al., 2002, Hansen, 1999, Vitousek and Walker, 1989, Wardle et al., 2004]. However, most of the research oriented to analyze these interactions has been approached from experimental studies. Although experimental studies represents the most reliable and fundamental approach, there are several questions that are challenging to explore from a purely empirical approach.

On other other hand, the development of ecohydrology as a field has enhanced the development of more detailed analytical and numerical models. These models have analyzed

the coupled interactions between hydrological, ecological, and biogeochemical dynamics [Eagleson, 1978a, Ivanov et al., 2004, Laio et al., 2001b, Oleson et al., 2010, Porporato et al., 2001, Rodriguez-Iturbe et al., 2001]. However, the role of plant biodiversity is a missing part of most ecohydrological models. According to the experimental evidence from the last two decades, plant biodiversity is an important component that regulates the above- and below-ground dynamics [Bardgett and Wardle, 2010] and should be incorporated in such analyses. Moreover, the main goal of modeling has been to capture and explain different ecohydrological patterns in soil moisture, transpiration, or ecosystem productivity rather than analyze the connection between the above- and below-ground structure and their interplay with the fluxes of water, carbon, nutrients, energy, and entropy.

It is important to complement the experimental research with modeling to improve our understanding of the the above- and below-ground interactions that occur in the CZ. The implementation of models should be oriented to analyze patterns that are difficult to examine from an experimental perspective.

The above-and below-ground interactions in ecology have been studied since the 1970s when soil ecologists realized the role of trophic interactions in the cycling of nutrients in the soil that was a main controller of plant uptake and productivity [Bardgett and Wardle, 2010]. However the ecological approach has considered the interactions in terms of biochemical energy and biogeochemical nutrients only. The positive and negative feedbacks from the soil biota to the plants, and, from the plants to the soil biota, are represented mostly in terms of (i) provisioning of biochemical energy (photosynthates), and (ii) provision of nutrients. Similarly the main objective of these interactions is conceptualized as a ultimate ecological goal which is biodiversity and ecosystem composition. Although the ecological component is very important, there are other relevant above- and below-ground interactions that regulate the dynamics in the CZ and should be considered.

The role of water in the above- and below-ground interactions is significantly important. Water is an important molecule that is present in all living organisms and is relevant in many biochemical reactions [Chaplin, 2006]. Therefore, it is not surprising that in different ecosystems water is a main factor that limits productivity [Fay, 2009]. According to Abrahams and Parsons [1994] water limited ecosystems account for up to 50% of the total global area. The relationship between plants and water is particularly interesting. Roots uptake water from the soil and leaves above-ground release it in the atmosphere. The movement of water by vegetation through this process is enormous, accounting for about 75% of the total flux of water from the soil to the atmosphere in continental areas, becoming the most prominent

and relevant flux from the soil to the atmosphere in the continental hydrological cycle. In addition, there is increasing experimental evidence that plant roots redistribute moisture in the soil through HR [Neumann and Cardon, 2012, Prieto et al., 2012]. This process may influence the distribution of soil moisture below the ground significantly and impact several functions in the CZ.

Water demand from the above-ground structure needs to be supplied from the below-ground root structure. If the root structure is not able to supply the demand or if the soil water is being reduced significantly, the above-ground demand would not be satisfied which in turn will limit the productivity of vegetation. Therefore, the above- and below-ground fluxes of water are mutually regulated by coupled feedbacks and they impact other relevant components such as ecosystem productivity which is the most prominent mechanism for the uptake of biogeochemical energy and sustenance most of living systems in the CZ.

CZs, as most thermodynamic systems on the earth, are open and are not in thermal equilibrium. They experience a continuous exchange of mass and energy fluxes with their environment. The interaction between above- and below-ground processes impacts the dissipation of energy, and therefore all the components of the energy balance, such as latent heat (LE), sensible heat, ground heat flux, and longwave radiation (LW). For instance the dissipation of latent heat is controlled by water availability, and the capacity of the below-ground structure to uptake and transport water. The ultimate energy balance and the dissipation of energy into different forms regulate the fate of relevant variables in the CZ such as temperature.

It is important to examine the above- and below-ground interactions in the light of the coupling between water and energy dynamics and how this coupling impacts ecosystem productivity. Previous modeling studies have looked into the interaction between below-ground roots and above-ground fluxes such as transpiration and carbon uptake [Anderson et al., 2000, Foley et al., 1996, Nikolov and Zeller, 2003]. Some of them have examined the role of HR to enhance transpiration and modify soil moisture states [Amenu and Kumar, 2008, Ryel et al., 2002, Wang, 2011]. Other studies have analyzed the energy balance in the surface under vegetated areas [Dolman, 1993], and also the water and energy dynamics under climate change [Drewry et al., 2010a,b, Le et al., 2011].

However, the above- and below-ground interactions of water and energy have not been analyzed in the light of several plant species that coexist. In particular the competitive and mutualistic interactions between plants that arises when they coexist and share resources may be an important factor influencing the energy and mass balance. Therefore, two options

should be contemplated in future research to improve our understanding of above- and below-ground interactions in the CZ: (i) consideration of biodiversity in hydrology as an important factor that impacts water and energy fluxes, and, (ii) consideration of water and energy fluxes in ecology as relevant variables that drives biodiversity.

Biogeochemical cycling of nutrients is driven by microbial communities that are able to decompose and mineralize the residues of organic matter released by plants. In addition to biogeochemical energy, the fate of microorganisms and soil communities is strongly influenced by the availability of moisture and the temperature of the soil [Herron et al., 2009, Iovieno and Båå th, 2008, Qi and Xu, 2001, Sylvia et al., 2005].

Hydrological and energetics interactions between the above- and below-ground components of the CZ regulate the states of soil moisture and soil temperature. Therefore, the biogeochemical cycling of nutrients is affected by these processes. Ecological studies have analyzed the role of biogeochemical cycling in the above- and below-ground interactions. They have examined the interactions between plants and microorganisms and how these interactions regulate the transfer of photosynthates and mineral nutrients. However, they have not explicitly analyzed how the above- and below-ground structure of the CZ impacts the water and energy balance at the surface, that further impacts the biogeochemical cycling of nutrients.

On the other hand, some ecohydrological studies have analyzed the role of water on the biogeochemical cycling of nutrients for different ecosystems and under different spatial and temporal scales [Schimel et al., 1997]. However, the influence of above- and below-ground structure on the biogeochemical cycling of elements by a top-down regulation of the surface energy balance has not been studied. In addition previous numerical studies have not analyzed the role of different species composition, consisting of different ecophysiological and structural properties, on the water and energy balance and its implications on the biogeochemical cycling of nutrients in the soil.

Experimental studies have emphasized the role of plant biodiversity. Specially, the difference between plant species in the composition of litter quality in terms of nitrogen, phosphorus, lignin, and other components have been recognized as important factors that control organic matter decomposition and microbial diversity in the soil [Ayres et al., 2009, Berg and McClaugherty, 2008, Hansen, 1999, Negrete-Yankelevich et al., 2008].

It is important for numerical studies to analyze the role of plant biodiversity on the biogeochemical cycling of nutrients below the ground. These studies should complement the understanding and examine conditions that are difficult to achieve trough experimental

approaches. In particular, the role of the above- and below-ground structure to regulate the water and energy balance is an important mechanism that regulates the biogeochemical cycling below the ground and should be considered.

The CZ can be conceptualized as an open thermodynamic system that is continuously exchanging mass and energy with the environment. At the top, the CZ receives a permanent flux of energy in the form of direct and diffuse SW radiation, and LW radiation. The SW is particularly important because it contains high levels of free energy (low entropy) available to perform work. The CZ dissipates the incoming energy in different forms such as physical and chemical denudation, sediment transport, emission of latent and sensible heat fluxes, and emission of LW radiation [Chorover et al., 2007, Rasmussen et al., 2011]. The energy dissipated contains lower levels of free energy, and higher levels of entropy, than the incoming energy. Therefore, the dissipation process is associated with a change in free energy or ΔG_{cz}. ΔG_{cz} is therefore the fraction of energy useful to perform work and is associated with the structure and self organization of the CZ such as the composition of above- and below-ground species, the physicochemical properties of all living and non-living subsystems, and the connectivity between all these different components.

In addition, some fraction of the incoming SW is absorbed and stored in chemical compounds to support life through photosynthesis which allows living systems to store high levels of free energy and use it later to do work when desired. The amount of free energy captured and used by living systems (ΔG_{life}) is also associated with the self organization of the living components of the CZ. Although the amount of free energy associated with living systems is much smaller than the total free energy dissipated from the CZ ($\Delta G_{cz} \gg \Delta G_{life}$), living systems play an important role in the structure and self organization of the CZ due to their ability to store free energy and use when desired.

Entropy and free energy budgets are thermodynamic concepts that are explicitly related to work and very likely more fundamental than purely energy balances. Therefore, the role of above- and below-ground interactions on entropy production or dissipation of free energy are relevant concepts that can help to decipher fundamental principles regarding the organization of the CZ. The most accepted thermodynamic hypothesis to examine open systems are expressed in terms of entropy budgets rather than free energy [Prigogine and Wiame, 1946]. In fact, the maximum entropy production principle (MEPP), is currently a widely accepted hypothesis to study the fate of open systems [Martyushev and Seleznev, 2006, Ozawa et al., 2003]. This principle implies that open thermodynamic systems evolve towards a state at which they maximize the entropy production under a given set of constraints imposed by

the environment [Martyushev and Seleznev, 2006].

Some previous studies have calculated the budget of entropy in the canopy [Aoki, 1987b, 1989] and at the entire ecosystem scale [Holdaway et al., 2010]. However, these budgets of entropy were calculated with annual average values of energy fluxes or using eddy covariance measurements assuming a fixed temperature for the ecosystem. The approach implemented in these studies relies on measurements of energy recorded for a given set of conditions and no effort was made to model the dynamics of entropy production to examine the above- and below-ground structural or physiological properties or fluxes that impact the entropy fluxes

Previous studies in ecohydrology have used the MEPP to analyze ecosystems patterns. Schymanski et al. [2010] analyzed subgrid heterogeneity by maximizing the entropy production from a simplified two box model to obtain the vegetation fraction. They found the MEPP formulation was able to obtain a good match with biomass patterns. Porada et al. [2011] calculated the entropy budget at the surface by focusing on the water fluxes. They applied the MEPP to parameterized a global hydrological model and applied it to compute different fluxes at the global scale. Wang and Bras [2011] used the MEPP to obtain an analytical formulation of LE fluxes from bare soil and vegetated surfaces. The implementation of free energy budgets has also been useful in ecohydrological approaches. For instance, Rasmussen et al. [2011] connected the rate of change of exergy to structural and functional properties in critical zones. They were able to link several critical zone patterns with exergy storage.

However, the budget of entropy in some of these approaches has been simplified and in some cases [Porada et al., 2011, Rasmussen et al., 2011, Schymanski et al., 2010] they have neglected radiative energy fluxes, which are the largest fluxes of energy, and entropy between the critical zone and the environment. In addition, surface temperature is a relevant variable that regulates the entropy fluxes and it has been specified with single point measurements instead of solving the energy balance. Although previous approaches have calculate budgets of entropy (or exergy storage) to understand ecohydrological patterns, still a detailed analysis of the entropy budget in the surface that consider all the water and energy fluxes is missing.

1.2 Research Questions

In particular, in this study we address the next open questions:

Question 1 What is the role of multiple species composition in the above- and below-ground interactions, and how they impact the energy and water balance in the surface?

Question 2 How do below-ground processes impact above-ground functions?

Question 3 What is the role of root water transport in the above- and below-ground interactions. In particular what is the role of hydraulic redistribution in facilitating above- and below-ground interactions?

Question 4 Are there general organizing principles that can explain the existing structure, composition and functioning of ecological systems that arise from an understanding of these interactions?

1.3 Research Contribution

The traditional ecological approach to study the above- and below-ground interactions in the critical zone has focused mostly in the interactions between plant and soil microbial species. This approach has been implemented by experimental studies mostly and it has not examined the feedbacks of water and energy in these interactions. On the other hand, ecohydrological approaches have modeled the above- and below-ground interactions considering dynamics related to water and energy but they have neglected the influence of biodiversity and the coupled dynamics between water, energy, and thermodynamic entropy.

The above- and below-ground interactions influence different processes in the CZ (See Figure 1.2) and they should be considered. In this study we make an attempt to explore the above- and below-ground interactions in the light of some of these processes. The most important contributions of this study are:

1. The modeling study is performed in the light of different configuration of plant species that coexists in the same location and share resources. This analysis allows us to examine the connection between plant biodiversity (expressed as different species that coexist) and their connection with the fluxes of water, nitrogen, carbon, energy, and entropy. In order to perform this analysis we developed a multi-species model (Multi-Species MLCan) by extending the work of Drewry et al. [2010a,b] where the multi-layer canopy MLCan model was developed. This model allows us to simulate ecohydrological dynamics in the presence of different plants species.

2. The above- and below-ground interactions are examined in the light of (i) water, (ii) ecosystem productivity, (iii) energy, (iv) soil carbon, (v) nitrogen, and (iv) thermodynamic entropy. This is the first time that all these dynamics are examined together

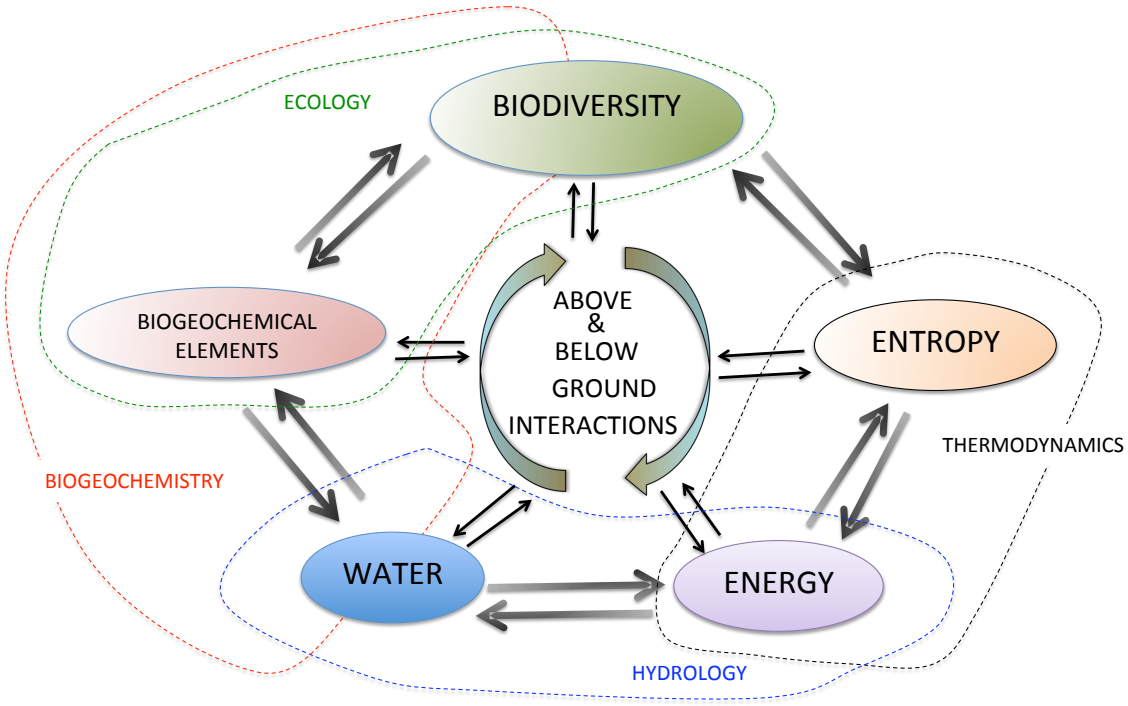

Figure 1.2: Dynamics that are influenced by the above- and below-ground interactions. Dash lines refers to disciplines that are associated to the above- and below-ground interactions and encircle the main dynamics they investigate.

using an integrated modeling approach. This exercise allowed us to have a better understanding of the connection between above and below-ground processes from different perspectives.

Research experience from current Critical Zone Observatories has pointed the capacity of both, bottom up and top down approaches to elucidate patterns in the CZ. The bottom up approach allows to merge different disciplinary principles through the coupling of mechanistic approaches (or models) involving different interdisciplinary knowledge [Hoosbeek and Bryant, 1992]. Although this approach allows us to study the interactions between different principles, at some point it may be difficult to deal with all the non-linear processes that are present. On the other hand the top-down approach has been useful to analyze the evolution of the structure and function of the CZ by examining it as a unit. However, this approach is not able to quantify the role of some specific subunits of the CZ and their own interactions. Instead it looks at the whole CZ [Rasmussen et al., 2011].

In this study we follow a bottom up approach with the following considerations.

- All the simulations are performed at Ameriflux sites with available records of atmospheric fluxes and data for validation.
- A mechanistic model is implemented to simulate different processes in the CZ with both single and multi-species composition. This mechanistic approach allows us to couple knowledge from different disciplines such as thermodynamics, hydrology, biogeochemistry, and plant biology.
- From the numerical simulations performed with the mechanistic approach we compute functions at the aggregate scale following a bottom up approach.
- The functions calculated at the entire CZ are analyzed to infer how different properties and processes impact the general functioning of the CZ.

The present study is divided in five independent chapters. In each of these chapters we examined the above- and below-ground interactions from different perspectives. All the simulations in each chapter are performed with Multi Species MLCan model. However, some additional code development was made in some chapters. The main objectives and open questions addressed in each chapter are described below:

Competitive and Mutualistic Dependencies in Multi-Species Vegetation Dynamics Enabled by Hydraulic Redistibution

In second chapter we explore the first and second research question. In this study we analyze the ecohydrological dynamics in the presence of ponderosa pine and shrubs, which are two dominant species that coexist in the Sierra Nevada mountains of California, US. The model is run with data from the Blodgett Ameriflux site. In particular we explore how the presence or absence of shrubs impact the water and energy fluxes above and below the ground. Special attention is paid to include interactions that arise below the ground when both species coexist. Under the presence of both species, water is taken up simultaneously from the soil inducing a competitive interaction. However, when hydraulic redistribution is active there is a facilitation of resources that compensate the competition between these two species. The main objectives of this chapter are:

- Examine the contribution from each species in the fluxes of water, and energy from the surface.
- Examine the competition for moisture between shallow and deep rooted vegetation during the dry summer that is experienced in this site.
- Examine the role of litter layer in its influence on energy balance, and ecohydrological dynamics at the near surface zone.
- Analyze whether facilitation of water resources in the presence of hydraulic redistribution impact the productivity of the shallow rooted vegetation species.

In order to achieve these objectives a detail solution of the energy balance at the soil surface is required. This solution includes the presence of a litter layer above the soil.

Role of Climate and Species Composition on Hydraulic Redistribution

In third chapter we explore the second and third research questions and analyze them in the light of several sites experiencing different climate. In particular, We investigate the role of climate, biodiversity, and root hydraulic conductivities as they affect multi-vegetation interaction and associated fluxes. The simulations are performed in three Ameriglux sites that have different climatic conditions: (i) Blodgett site in CA, US, (ii). Tapajos Km 67, Brazil, and (iii). Harvard Forest in MA, US. The main objectives of this chapter are:

- Examine the role of precipitation, and incoming shortwave radiation on the fluxes of transpiration and HR.

- Analyze whether the consideration of different plant functional types, as a surrogate of biodiversity affect the fluxes of water.

- Examine the sensitivity of transpiration and hydraulic redistribution to root hydraulic conductivities. Analyze whether the axial or the radial conductivity is the limiting factor that controls transpiration and hydraulic redistribution.

- Compare the patterns of transpiration and hydraulic redistribution, and analyze the differences and similarities between these two fluxes. Examine whether measurements of transpiration fluxes are a good approach for the validation of hydraulic redistribution fluxes simulated by models.

Passive Regulation of Soil Biogeochemical Cycling by Root Water Transport

In fourth chapter we explore the second and third research question. We examine the role of water transport in the biogeochemical dynamics involved in the above- and below-ground interactions and how these dynamics are affected by HR. In particular, we analyze how the impact of moisture and temperature states in the soil by plants influence the biogeochemical cycling of nitrogen and carbon. We analyze these interactions under the presence of different species composition and explore the role of hydraulic redistribution on these processes. The main objectives are:

- Examine the biogeochemical cycling of carbon and nitrogen under the presence of different species that differ in the quantity and quality of nitrogen content in the litter drop.

- Examine the role of hydraulic redistribution in the decomposition and mineralization of organic matter in the soil.

- Examine the effect of species composition and hydraulic redistribution in the dynamics of ammonium and nitrate in the soil.

- Analyze the long term accumulation and distribution of carbon and nitrogen in the soil column.

In order to achieve these objectives we coupled Multi-Species MLCan with a biogeochemical model derived from the work of Porporato et al. [2003] that includes the dynamics of carbon and nitrogen in the soil.

Entropy Production in Eco-Hydrologic Systems

In fifth chapter we analyze the fourth research question. We explore the second law of thermodynamics as an organizing principle that can explain the structure and functioning of the CZ. In particular, we link the production of entropy with different levels of organization of ecosystems. We examine how the organization of ecosystems impact the fluxes of energy and entropy. We develop a detailed quantification of entropy budgets in ecosystems. This quantification includes radiation fluxes and the solution of energy balance is obtained at different positions in the ecosystem. This approach provides more accurate estimates of surface temperature which is relevant for the calculation of entropy fluxes. We perform this analysis in the same three Ameriflux sites that are mentioned before. The main objectives of this chapter are:

- Examine how the entropy production in the surface is affected by functional and structural properties resembling different levels of organization in ecosystems.
- Understand the mechanisms and components that impact the entropy production under different functional and structural properties.
- Analyze how the interaction between the ecosystem properties and the production of entropy varies under different climates?

In order to achieve these objectives numerical implementation was required to compute the production of entropy. This module calculates the production of thermodynamic entropy in all the species that are considered separately. In addition the computation is performed for sunlit and shaded fractions independently at all the canopy layers including the soil.

The Appendixes present details of mathematical formulation and numerical algorithms used used in this study. Appendix A describes multi species-MLCan, Appendix B describes the numerical solution of energy balance in the soil surface when a litter layer is included, Appendix C describes the numerical solution of energy, and mass balance in the presence of snow, Appendix D describes an approximation to compute the root hydraulic conductivities of the root system, Appendix E describes the biogeochemical model implemented and coupled with Multi Species MLCan, Appendix F describes the equations used for the computation of entropy fluxes.

CHAPTER 2

Competitive and Mutualistic Dependencies in Multi-Species Vegetation Dynamics Enabled by Hydraulic Redistribution

2.1 Introduction

[1]. The dynamics of water flow between plant roots and the surrounding soil play an important role in controlling the link between above-ground ecophysiological processes governing carbon, water and energy exchange, and the atmosphere [Bardgett and Wardle, 2010]. At longer timescales, these processes contribute to the formation of soil structure and the distribution of carbon and nutrients through the soil column [Allton et al., 2007, Angers and Caron, 1998, Huxman et al., 2004]. The flow of water from the roots to soil was first established experimentally by Kramer [1933], and has since been identified in a wide variety of plant species including shrubs [Prieto et al., 2010, Richrads and Caldwell, 1987, Ryel et al., 2002], grasses [Schulze et al., 1998] and trees [Brooks et al., 2006, Burgess et al., 1998, 2000, Smith et al., 1999] across a range of dry to wet climates. The conductivities of transport through the root system are significantly larger than that of the surrounding soil [Blizzard, 1980], resulting in movement of moisture at rates that are substantially larger than those through the soil matrix [Amenu and Kumar, 2008]. As a result, the roots serve as preferential pathways for the movement of moisture from wet to dry soil layers. This passive transport is determined by the soil-water potential gradients and can result in the transport of moisture deeper in the soil column during the wet season (hydraulic descent, HD) [Burgess et al., 1998, Hultine et al., 2003, Schulze et al., 1998, Smith et al., 1999], and transport of moisture from deep to shallow layers during the dry seasons (hydraulic lift, HL) [Dawson, 1993, Espeleta et al., 2004, Ishikawa and Bledsoe, 2000, Ludwig et al., 2003]. There is also evidence that roots can transport moisture laterally when a strong gradient in soil water potential is imposed across the breadth of a plant root system [Brooks et al., 2002, 2006, Nadezhdina

[1]This chapter has been published as: Quijano, J.C., P. Kumar, D. Drewry, A. Goldstein, and L. Misson. 2012. Competitive and mutualistic Dependencies in Multi-Species Vegetation Dynamics Enabled by Hydraulic Redistribution. *Water Resources Research*, 48(5)

et al., 2010]. This general phenomena of moisture transport through the soil system by way of the root system has been referred to as hydraulic redistribution (HR) [Burgess et al., 1998, 2001, 2000, Hultine et al., 2003, 2004].

A number of studies have attempted to characterize the hydrologic and ecological significance of HR. The roles of HR include buffering against daily soil water depletion and seasonal drought [Bleby et al., 2010, Emerman and Dawson, 1996], facilitation of savanna tree-shrub clusters [Zou et al., 2005], root litter decomposition and nutrient acquisition [McCulley et al., 2004], extension of the growing season [Ryel et al., 2002, Scott et al., 2008], impact on competition between different plant functional types at continental scales [Wang et al., 2010] and even alteration of seasonal climate [Lee et al., 2005]. Although a number of species across a range of climate gradients from the tropical Amazon to the semi-arid southwestern United States have been studied in this context, a predictive modeling based characterization that develops a comprehensive understanding of the impact of HR on the biophysical processes occurring in ecosystems with different species that coexist and share resources remains an open challenge.

The objective of this study is to understand the role of HR in the interaction of above- and below-ground ecohydrologic dynamics using a modeling approach. Specifically we explore the role of HR in regulating the partitioning, and trade-off of hydrologic fluxes between tall and understory vegetation and soil evaporation. This is accomplished using a "shared resource model" where the soil serves as a common reservoir whose state is altered by the addition and withdrawal of moisture by vegetation roots, in conjunction with the moisture transport dynamics and the non-linear dependence of vegetation uptake and release on the existing soil-moisture state. The model extends the work of Amenu and Kumar [2008] for root and soil interactions through HR for a single species to incorporate moisture uptake and release dynamics involving roots of multiple plant species. It also extends the model of Drewry et al. [2010a,b] developed for coupling the below-ground moisture transport through soils and root system, and above-ground water, energy, and carbon fluxes for both C3 and C4 vegetation to allow for multi-species composition of above-ground vegetation. Further, the existing functional representation of HR is enhanced to represent ecosystem scale dependencies such as soil evaporation and its dependency on the litter layer.

Both hydraulic descent and lift affect soil evaporation. Ryel et al. [2002] suggested that by transporting water down to deeper layers, hydraulic descent reduces the moisture that would otherwise be available for soil evaporation. On the other hand hydraulic lift may allocate water to shallow layers that is likely to support evaporation [Dawson, 1993, 1996]

which could be detrimental for the plants in water-limited environments. In some cases water potential in the soil can reach very low levels thereby creating a soil-root potential gradient for the movement of significant volume of moisture from the roots into the soil. It has been suggested that in such conditions it is likely that physiological controls may act to reduce the efflux of water [Caldwell et al., 1998, Espeleta et al., 2004, Jackson et al., 2000], for example through the death [Espeleta et al., 2004] or shrinkage [Jackson et al., 2000] of fine roots near the ground surface. We explore this situation by implementing a hydraulic fuse mechanism [Espeleta et al., 2004], which is a hydraulic disconnection between roots and the surrounding soil when the daily average water-potential in the soil falls below the wilting point thereby preventing both uptake and release of water by the roots. On the other hand the presence of a litter layer lying over the soil has been observed to influence the energy balance at the surface. Experimental and numerical studies have recognized that the presence of a litter layer above the soil reduces evaporative fluxes [Bristow et al., 1986, Bussiere and Cellier, 1994, Chung and Horton, 1987, Park et al., 1998] and reduces soil temperature [Bussiere and Cellier, 1994, Chung and Horton, 1987]. Therefore, the presence of litter introduces a new level of complexity that impacts the dynamics occurring below-ground. Here we also analyze how the presence of litter influences the subsurface transport of moisture by HR through the regulation of soil evaporation.

The role of water uptake and its redistribution is of significant interest at the ecosystem scale [Scott et al., 2008]. Although important advances have been made in detecting the presence of HR and the quantification of the moisture fluxes it produces [Burgess et al., 1998, Caldwell et al., 1998, Domec et al., 2010, Wang, 2011, Yoder and Nowak, 1999], most studies have been conducted to understand its significance on the transpiration and gross productivity of a single plant species [Brooks et al., 2002, Caldwell and Richards, 1989, Ryel et al., 2002], or have considered a lumped system that encapsulates the net impact of species composition [Amenu and Kumar, 2008] rather than resolving the competitive or mutualistic dependencies between different species. Although the presence of more than one species sharing the soil and resources, such as water and nutrients, in the same ecosystem imply competition for resources, there is experimental evidence that also suggests that facilitation of shared resources between different species may occur [Ludwig et al., 2003, Scott et al., 2008]. It has also been suggested that HR may influence the dynamics of microbial populations and consequently the biogeochemical cycling [Caldwell et al., 1998, Caldwell and Richards, 1989, McCulley et al., 2004, Querejeta et al., 2007] resulting in a mutual feedback effect between vegetation and microbial populations in the soil. These studies have established

HR as a significant ecohydrological process with implications for ecosystem dynamics and the interactions between vegetation and the atmosphere. Model and simulation studies present an opportunity to further unravel the complexity of these ecohydrological processes and their role in ecosystem functioning [Kumar, 2011]. Here we use a novel process-based model, capable of incorporating HR in a multi-species framework, to gain deeper insight into ecosystem scale hydrological dynamics and interactions. In particular, we explore how the presence of multiple species utilizing the same soil domain induces both competitive trade-off in water utilization and mutualistic benefits in ecosystem productivity, and the role of HR in mediating these interactions. The impact of these processes on sub-surface nutrient dynamics is presently being studied.

In section 2.2.1 we describe the Blodgett Forest study site. The shared resource model developed for this study is described in section 2.2.2. Results and analyses for above- and below-ground hydrologic fluxes and states is presented in section 2.3. Section 2.4 provides a summary and discussion of the key points. A list of symbols is included in Table 2.1.

2.2 Methods

2.2.1 Study Site

The Ameriflux study site in the Blodgett Forest was established in 1997 in the Sierra Nevada Mountains in California, United States (38.8952°N, 120.6328°W, 1315 m above MSL) [Goldstein et al., 2000]. In 1997 the ground cover consisted of 25% shrubs, 30% conifer trees, 2% deciduous trees, 7% forbs, 3% grasses and 3% stumps [Fisher et al., 2005]. The dominant overstory species is *Pinus Ponderosa* (hereafter PP) and the the most ubiquitous understory shrubs are *Arctostaphylos manzanita* and *Ceanothus Cordulatus* (hereafter shrubs) [Misson et al., 2006, Xu and Qi, 2001]. The region is characterized by a Mediterranean climate with wet winters and long dry summers in which most of the precipitation falls between September and May with little rainfall between June and October. PP is a native forest species in the western regions of North America which has adapted to the long dry summers in California and the Pacific Northwestern United States [Panek, 2004]. PP trees are able to sustain high transpiration rates during the dry period [Panek, 2004]. Observational studies have demonstrated the presence of HR in PP [Brooks et al., 2002, Domec et al., 2004, Warren et al., 2007], indicating that hydraulically lifted water provides a substantial portion of dry-season

transpiration in these deep-rooted trees.

Ponderosa pine was initially planted at the Blodgett Forest site in 1990 [Tang et al., 2005]. At the end of the 1998 growing season the leaf area index (LAI) of overstory (total needle surface area) and understory (total surface area) vegetation was about 4.5 and 1.6, respectively [Xu and Qi, 2001]. In June of 1999 most of the shrubs were removed and in the spring of 2000 the PP plantation was thinned in order to analyze variations in carbon flux due to management practices [Misson et al., 2005]. The LAI reduction after the thinning was around 30% [Xu and Qi, 2001]. PP was the predominant species in 2001 but in 2002 the shrubs returned. The LAI trends for the shrubs and the pines are shown in Figure 2.1 (note zero LAI for the shrubs in 2001) along with ecophysiological parameters V_{cmax} and J_{max} [Farquhar et al., 1980]. Figure 2.1 also shows the seasonal rainfall and incoming shortwave radiation patterns, where the signature of the Mediterranean climate is clearly evident.

These site and climate characteristics provide for an ideal environment to study the role of HR and multi-species interactions. Simulations for 2001 involving only PP and for 2002 involving PP and shrubs allow us to compare and contrast the single and multi-species response. Shrubs started to grow back in 2002 but the maximum LAI of 1 reached during 2002 is low compared with the maximum value of 2 reached in 1998 [Goldstein et al., 2000] before they were cut. This suggest that the shrubs had not fully established in 2002. The parameters for the model described in the next section are obtained from published literature and listed in Tables 2.2 and 2.3. In most cases they were measured directly at the Blodgett Forest site. The data for year 2000 are used for model spin-up by running the model several times consecutively with this one year of data until the annual cycle of soil moisture reaches steady-state. Each scenario (see section 2.3) is spun-up independently using year 2000 forcing data, resulting in different initial conditions for the start of each simulation experiment, which spanned the study period 2001-2002.

2.2.2 Shared Resource Model for Multiple Species Interactions

The model development is based upon the multi-layer canopy-soil-root (MLCan) biophysical model of Drewry et al. [2010a,b]. MLCan incorporates explicit coupling between leaf-level ecophysiological processes (photosynthesis and stomatal conductance), physical processes (energy balance and boundary layer conductance), and below-ground water status which incorporates the HR model of Amenu and Kumar [2008]. It resolves the radiation regimes, both direct and diffuse shortwave as well as longwave, throughout the vertical domain of

the canopy. Radiation attenuation is determined by the leaf area density (LAD) profile [Drewry et al., 2010a]. It predicts the latent and sensible heat fluxes for each canopy layer through an iterative solution of the leaf energy balance, considering sunlit, shaded, and wet leaf fractions (due to dew or rainfall interception) separately. CO_2 fluxes (assimilation and respiration) are also calculated for each canopy layer, being directly coupled to the energy balance through stomatal dynamics. The details of the MLCan formulation can be found in the online supplement of Drewry et al. [2010a].

For this study, the MLCan model is extended to include formulations for several plant species coexisting in the same environment. As the MLCan model is designed to include both C3 and C4 photosynthetic pathways, it allows us to study the interaction between different tall and understory vegetation combinations: C3-C3, C3-C4 (or in rare cases C4-C4). This enables us to simulate the water, energy, and carbon dynamics when several species with different structural and ecophysiological characteristics interact and share resources. The role of HR in these interactions is of particular interest in this study.

The schematic of the model is presented in Figure A.1. As illustrated, we assume that several species can coexist in the same environment and they are homogeneously distributed in the spatial domain. Above-ground, their coexistence affects the radiation regime. For example, tall vegetation can shade the understory vegetation, thus reducing the radiation available for understory plants. Radiative effects such as this will directly impact the partitioning of energy between ecosystem components, the energy balance of each vegetation type and the soil, and consequently the net photosynthetic productivity of the system. The different rooting depths and root distributions of tall and understory vegetation impact below-ground resource acquisition, as different species draw from the same resource pool, but potentially with different strengths and from different locations in the soil profile.

We assume that all the individuals of a given species have the same structural and ecophysiological characteristics, but each plant species is different from the other. To resolve the light regime we use a composite LAD obtained as a linear sum of the LAD of the individual species. This composite LAD is then used to attenuate the transmission of downward radiation. Once the light attenuation is solved, the energy absorbed by the canopy at different layers is obtained using a weighted average calculation based on the fraction of LAD from each species in the composite LAD at each layer (see equation A.11). This approach allows us to separately consider the ecophysiological and structural differences of each species. As a result, the latent heat, sensible heat, and CO_2 flux profiles for each species are different.

The HR dynamics are formulated by extending the single species model of Amenu and

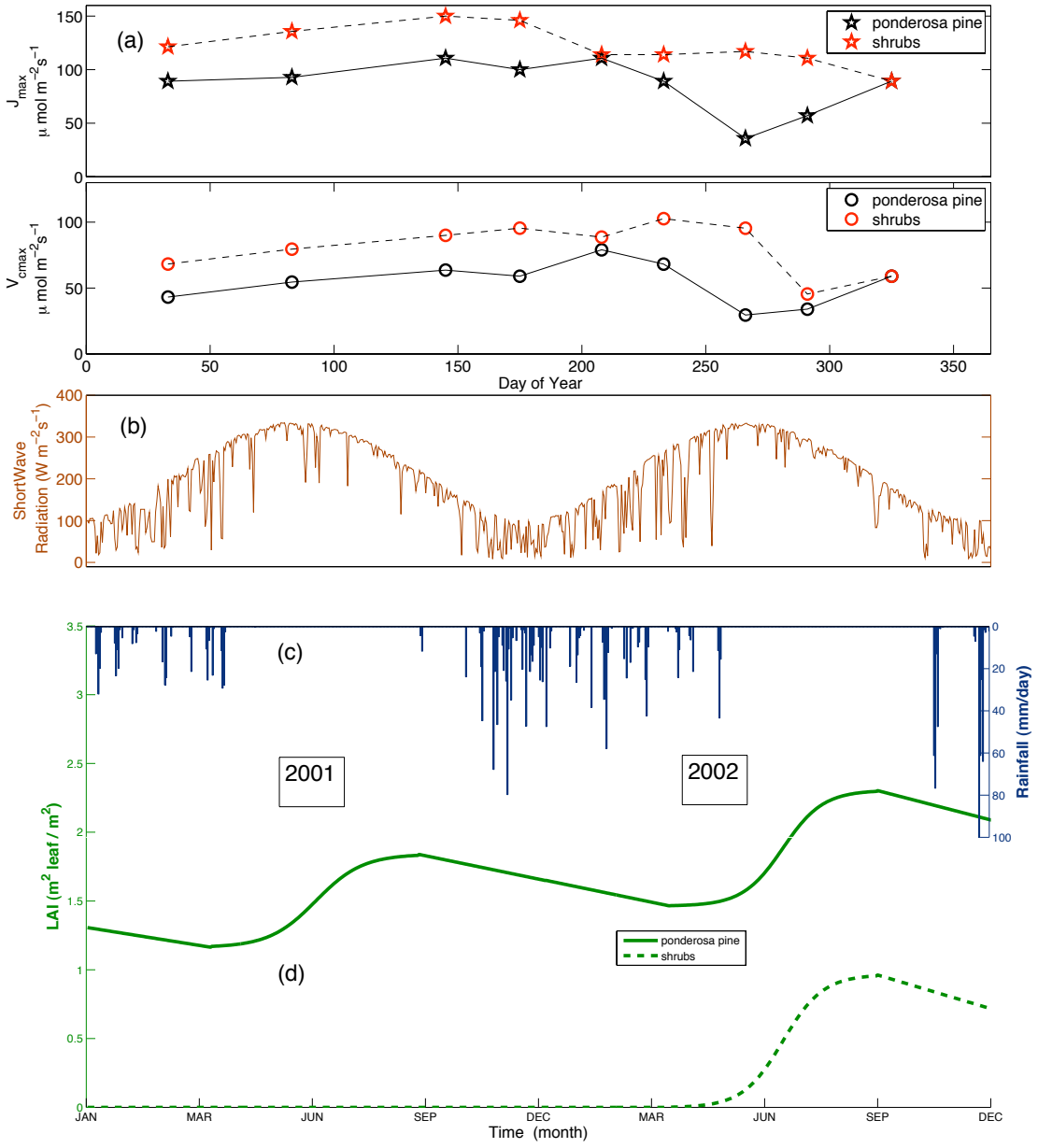

Figure 2.1: Physiological and climatological data from Blodgett used in the model simulations. **(a)** Variation of maximum rate of electron transport (J_{max}) and **(b)** maximum carboxylation velocity (V_{cmax}) throughout the year (data obtained from Misson et al. [2006]). **(c)** Daily averaged downward shortwave radiation, and **(d)** leaf area index (LAI), and rainfall for 2001 and 2002. All-sided ponderosa pine LAI is 2.3 times LAI shown (projected). (LAI Data obtained from Misson et al. [2005]).

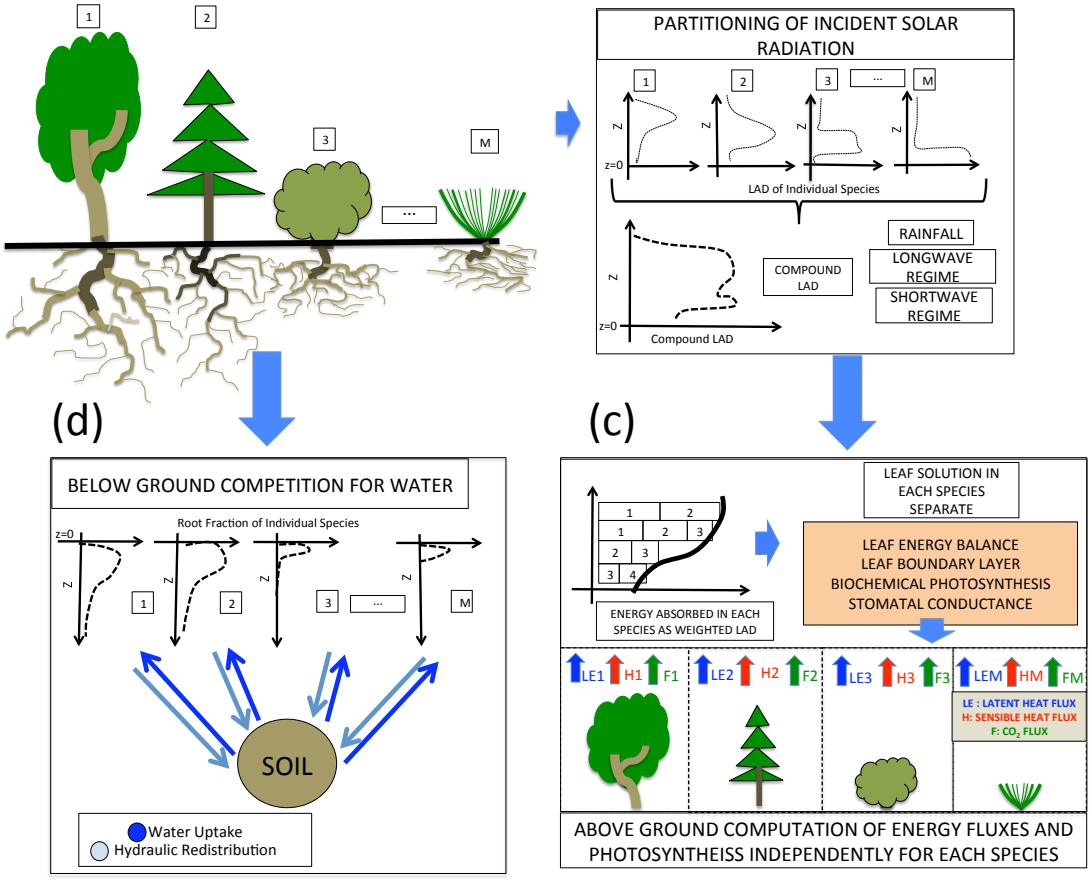

Figure 2.2: Schematic representation of the multi-species MLCan model. **(a)** The structure and composition of the above ground canopy involving several vegetation species determines the partitioning of the incident solar radiation and water uptake patterns. **(b)** The combination of the leaf area density (LAD) of each individual species is used to develop a compound LAD. This compound LAD in turn determines the radiation regime through the vertical profile and the radiation reaching the soil. **(c)** The energy absorbed or emitted by each species at different levels is a function of the fraction of the LAD of that species in the compound LAD. **(d)** Below the ground the uptake of water and nutrients by each species is coupled with a common soil pool. The model framework allows the incorporation of different ecophysiological and structural parameters for the vegetation species considered.

Kumar [2008] and Mendel et al. [2002], which are based on coupling two equations for the transport of moisture through the soil and the root system. The presence of M different plant species necessitates the use of M independent equations for the transport of moisture through the root systems. This allows for their differences in structural and functional properties to be incorporated. These root system equations are coupled with a single Richards equation for soil-moisture transport through the soil profile. The system of equations is:

$$\begin{aligned}
&\tfrac{\partial\theta}{\partial t} - \tfrac{\partial}{\partial z}\left[K_s\left(\tfrac{\partial \psi s}{\partial z} - 1\right)\right] = -\textstyle\sum_{i=1}^{M} K_{r_i}^R\left(\psi_s - \psi_{r_i}\right) \\
&-\tfrac{\partial}{\partial z}\left[K_{r_1}^A\left(\tfrac{\partial \psi_{r_1}}{\partial z} - 1\right)\right] = K_{r_1}^R\left(\psi_s - \psi_{r_1}\right) \\
&-\tfrac{\partial}{\partial z}\left[K_{r_2}^A\left(\tfrac{\partial \psi_{r_2}}{\partial z} - 1\right)\right] = K_{r_2}^R\left(\psi_s - \psi_{r_2}\right) \\
&\ldots \\
&-\tfrac{\partial}{\partial z}\left[K_{r_M}^A\left(\tfrac{\partial \psi_{r_M}}{\partial z} - 1\right)\right] = K_{r_M}^R\left(\psi_s - \psi_{r_M}\right)
\end{aligned} \tag{2.1}$$

where the first equation is the Richards equation and the other M equations represent transport through M different plant species. The terms ψ_s and ψ_{r_i} are the water potential in the soil and the root of the i^{th} plant species, respectively, and θ is the soil-moisture. The vertical coordinate and time are represented as z and t, respectively. Note that there is a unique water potential value for the roots of each plant species in each layer. The term K_s is the soil hydraulic conductivity, and $K_{r_i}^R$ and $K_{r_i}^A$ are the radial and axial root conductivities of the i^{th} plant species, respectively [Amenu and Kumar, 2008]. These equations are solved simultaneously for 12 layers where central nodes are located at 0.7, 2.8, 6.2, 11.9, 21.2, 36.6, 62.0, 103.8, 172.7, 286.5, 474.0, 783.0 cms below the surface.

The individual root systems of each species do not directly interact. They do share the common soil system, such that θ and ψ_s in each soil layer are the same for all species (see Figure A.1). This conceptualization of shared resource dynamics allows us to capture inter-species interactions, both competition and mutualism, as the water uptake or release by one species affects the shared soil moisture state, resulting in an indirect effect of each vegetation species on the dynamics of the others. When plants uptake water from the same layer they compete for available water. The release of water through hydraulic redistribution may, however, benefit the other species that share that layer by increasing available moisture. The model can simulate HR in all plant species and is structured so that the ability to hydraulically redistribute water can be switched off on a selective basis by setting the root radial conductivity of a species to zero, i.e. $K_{r_i} = 0$, when the water potential in the roots

is higher than the water potential in the soil, i.e. $\psi_{r_i} > \psi_s$. This approach to simulate the impacts of HR has been used previously by Mendel et al. [2002].

The maximum root distribution for shrubs during 2002 is unknown. *Ceanothus Cordulatus*, which accounts for 22 % of the understory shrubs [Fisher et al., 2007], are able to resprout from remnants of roots below-ground [Oakley et al., 2003]. *Arctostaphylos manzanita* comprise the remaining 78% of understory shrubs. They can reach up to 3 m in height after many years of establishment. However *Arctostaphylos manzanita* has difficulty in resprouting from remnants of below-ground roots [Peterson, 1975, Wright and Bailey, 1982] and is mainly established from seeding. According to Fisher et al. [2007], shrubs reached 1 m height and a LAI of 0.7 in the spring of 2003. In september of 2003 they reached a maximum LAI of 1.6 which is higher than the LAI of 1 reported in 1998 before they were cut [Goldstein et al., 2000]. This suggests that the shrubs were not fully established in 2002. Available information for *Arctostaphylos patula* shrubs in the Sierra Nevada region suggests that at full establishment the rooting depth can be up to 160 cm [Plamboeck, 2008]. For our study we have assumed a maximum rooting depth of 85 cm (during the year 2002) and performed sensitivity analyses for the range 60 cm to 140 cm and included in the discussion. The 50^{th} (z_{50}) and 95^{th} (z_{95}) percentile of the root depth for shrubs used in this study were obtained by scaling those reported in Schenk and Jackson [2002]. The maximum root distribution for ponderosa pine was found to reach 10 m. However most of the root biomass is allocated in the first 2 m with z_{50} and z_{95} 0.37 m and 2.60 m, respectively [Amenu and Kumar, 2008].

The MLCan model, thus modified to incorporate multiple species interactions, can be used to study the ecohydrologic consequences of the coexistence of multiple vegetation species. Our preliminary investigations with the MLCan model at the Blodgett Forest site indicated that the litter present on the soil surface could play a significant role in both the surface energy balance and the water balance of the system. Ogee and Brunet [2002] and Wilson [2000] have also emphasized the role of litter on the estimation of soil evaporation and energy balance. A litter layer can act to decrease the conductivity of water vapor between the soil surface and the atmosphere. This effect, therefore, reduces the latent heat flux (LE_{soil}) from the soil surface. Furthermore, the thermal conductivity of a litter layer is considerably smaller than that of the soil, causing the ground heat flux (G) to also be reduced. The net result of these effects is an increase in the sensible heat flux and emitted long wave radiation due to an increase in temperature at the surface.

Given the potential importance of litter at the Blodgett Forest site, we have included a

litter model for this study, which is described in Appendix B. Its implementation requires parameters such as the thickness, thermal conductivity, and thermal diffusivity, which are obtained from existing literature and are listed in Table 2.3.

Throughout the study we contrast the impact of including or excluding a litter layer. Figure 2.3a shows the ground heat flux at the surface computed for the year 2001. The red and the blue lines show the predicted G at the surface when a litter layer is excluded and included, respectively. It can be seen that the incorporation of a litter layer has a significant impact on the magnitude of the ground heat flux. Figure 2.3b shows the same fluxes but now G is computed at 8 cm below the surface, a depth at which measured ground heat flux is available (black dots in Figure 2.3b). The simulation, when a litter layer is included, matches better the fluxes observed at the Ameriflux site. Also the inclusion of the litter layer increases the release of sensible heat from the surface and decreases the release of latent heat (not shown). Figures 2.3c and 2.3d show the sensitivity of the ground heat flux to the litter layer thickness and the thermal conductivity, respectively. When the litter layer is thicker (Figure 2.3c) or the thermal conductivity is lower (Figure 2.3d) the ground heat flux decreases. The litter layer thickness is specified as 3 cm (which is within the range reported by Black and Harden [1995] at Blodgett), and the thermal conductivity is set as 0.15 W/m/K (which is within the range of values reported by Ahn et al. [2009]). Figures 2.3a and 2.3b are illustrated using these values.

2.3 Results and Analysis

2.3.1 Latent Heat Flux and Water Uptake

The extraction of soil moisture to satisfy the transpirational demand is regulated by the interplay of different variables such as leaf phenology, vertical distribution of root biomass, ecophysiological properties and the available soil moisture. The contrasting characteristics of tall and understory vegetation will result in signature differences in soil water extraction in time and space, making their coupled dynamics complex, with the potential for both competitive and mutualistic interactions. In this section we present the results from a set of sensitivity analyses designed to disentangle the relative roles of HR, the coupled interactions of different species, and the presence of a litter layer, on the ecohydrological functioning of the land surface. Our focus here is on the surface energy balance and below-ground water

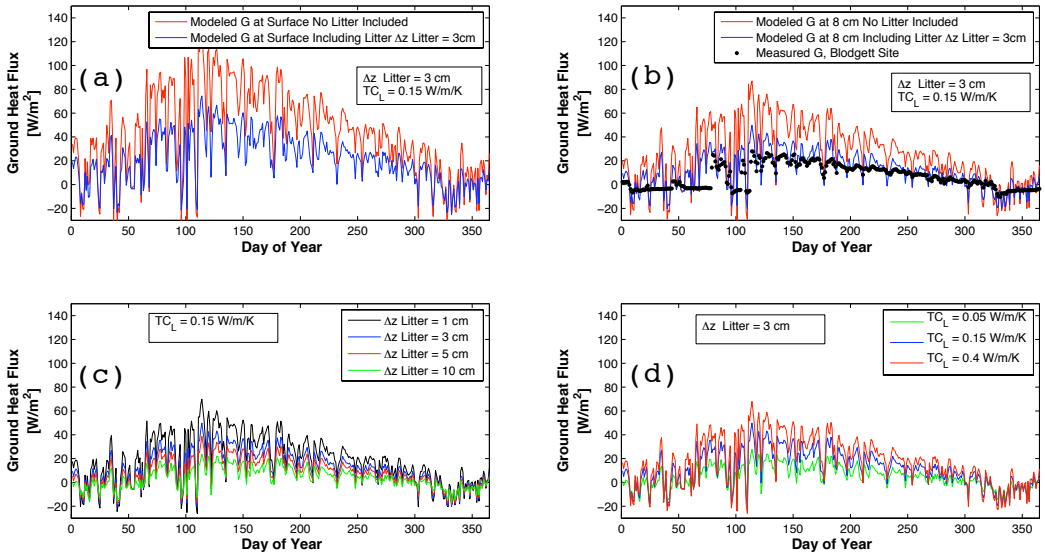

Figure 2.3: Sensitivity of ground heat flux (G) to litter layer thickness (Δz) and thermal conductivity (TC_L) at the Blodgett site for year 2001. **(a)** Modeled G at the ground surface with and without litter layer. **(b)** Measured G at 8 cm below the surface compared with modeled response with and without litter layer. **(c)** Modeled G at 8 cm below the surface for different litter layer thicknesses, **(d)** and for different thermal conductivities.

uptake patterns and resulting soil moisture states. We contrast the situations in which only tall vegetation is present (year 2001) and when both tall and understory vegetation are present (year 2002). We also investigate the role of the hydraulic fuse mechanism, that is, the hydraulic disconnection between roots and soils under extremely dry situations, on the latent heat flux.

Single Species Analysis

For the year 2001, when no understory shrubs are present, Figure 2.4 shows the daytime (7:00 a.m. to 7:00 p.m.) average latent heat flux from the ecosystem (LE_{eco}), consisting of contributions from PP (LE_{PP}) and soil evaporation (LE_{soil}):

$$LE_{eco} = LE_{PP} + LE_{soil}. \tag{2.2}$$

As illustrated in Figure 2.4, four different cases are examined involving the presence or absence of HR and litter which are compared to observations obtained from the flux tower. Comparing Figures 2.4a and 2.4b we see that LE_{soil} is higher when the litter layer is absent. The presence of the litter layer reduces the radiation that reaches the soil underneath, thereby reducing soil evaporation (Figure 2.4b). This increases the available soil-moisture for PP, resulting in increased transpiration. The trade-off between transpiration and soil evaporation in these plots demonstrates that PP will make use of available moisture, and that a litter layer suppresses soil evaporation, increasing available water for transpiration.

When HR is switched off (Figure 2.4d) soil evaporation becomes negligible by the middle of the summer as the shallow layer dries up in early summer and there is no source of moisture replenishment due to the lack of rainfall through the summer. This lack of moisture sources together with the atmospheric demand have been observed to trigger HR [Warren et al., 2007]. Here in the absence of HR we observe that PP transpiration is also reduced during this period. Although the deep roots of PP are able to tap into the deeper reservoirs of moisture in the soil column, the transpiration remains suppressed without HR. As a consequence of the dry near-surface soil layers, most of the energy absorbed by the soil is dissipated in the form of sensible heat flux and longwave radiation emission as the surface warms.

When compared to the observations we see that the absence of litter results in an overestimation of the fluxes of LE during the summer period (Figure 2.4a). When litter is present there is a better agreement with the measurements during the summer period, (Figure 2.4b), however it still overestimates the fluxes in the late summer and autumn (days 250 - 300).

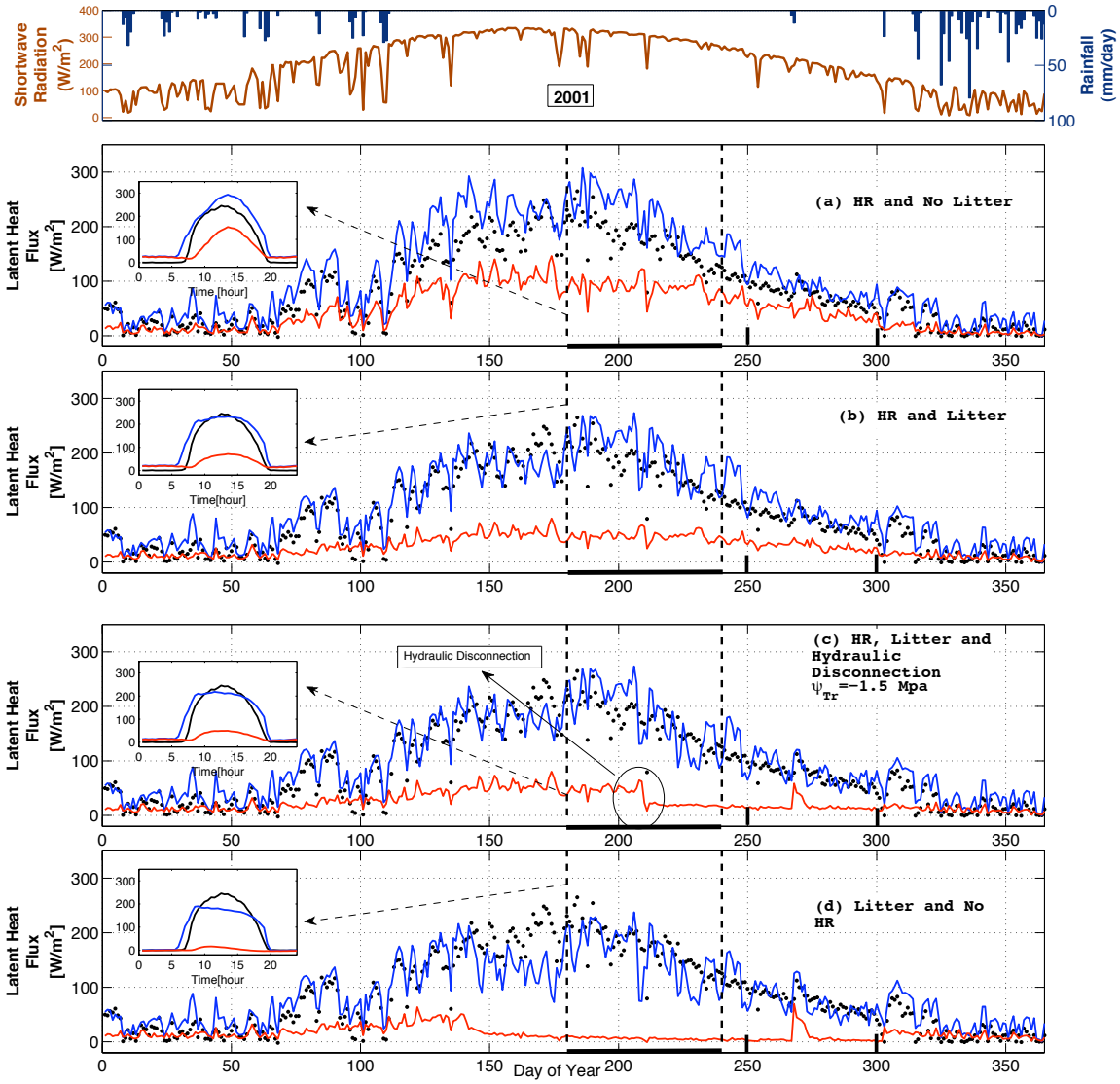

Figure 2.4: Illustration of the annual variation of the daytime (7:00 a.m. to 7:00 p.m.) average latent heat flux from ponderosa pine for four different scenarios. **(a)** HR is included but there is no litter layer above the soil column. **(b)** HR is included and there is a litter layer above the soil. **(c)** HR is included, a litter layer lies above the soil column and hydraulic disconnection between the roots and the soil occurs when $\bar{\psi}_s \leq \psi_{Tr}$, where $\bar{\psi}_s$ is the daily average of soil water potential. **(d)** HR is not included and there is a litter layer above the soil. Blue line indicates the total ecosystem flux consisting of the sum of transpiration and soil evaporation, the red line shows soil evaporation only, and black color indicates observed values. Left insets show the diurnal cycle of the the latent heat flux averaged for July and August. For reference the top panel shows the daily average downward shortwave radiation and daily total rainfall for 2001. The coefficient of determination R^2 between simulated and observed latent heat flux for the four cases (a) through (d) are 0.71, 0.81, 0.82 and 0.75 respectively

In the absence of HR the ecosystem LE flux is underestimated during most of the summer period (Figure 2.4d) although there is a better match in the late summer and autumn period. The observations show a pronounced decrease in LE in the late summer which seems to be produced by water stress.

As the soil column becomes dry and the soil moisture potential drops, an efflux of water from the root to the soil can occur. To prevent such situations a hydraulic disconnection between the roots and the soil is triggered when the daily average $\bar{\psi}_s$ falls below a threshold ψ_{Tr}. This threshold indicates the onset of the hydraulic disconnection. However, the threshold is species specific [Espeleta et al., 2004] and relies on several physiological variables which are difficult to obtain for a particular site and species. The standard value for the wilting point is $\psi_{Tr} = -1.5$ MPa. Although other studies have adopted different values for the wilting point (e.g. Rose et al. [2003] uses $\psi = -2.2$ MPa as a threshold for Jeffrey pine and manzanita shrubs) we use $\psi_{Tr} = -1.5$ MPa in this study. Once the daily average soil matric potential in any layer reaches the wilting point the root radial hydraulic conductivity is set to zero, that is, it is modeled as a threshold mechanism, which prevents both uptake and release of water in the layer. This disconnection remains until the daily average soil matric potential increases again above the threshold.

Figure 2.4c shows the LE fluxes resulting from the simulation in the presence of litter, HR and hydraulic disconnection. Simulations showed that hydraulic disconnection occurs only in the topmost layer. The immediate consequence of this is a significant reduction in soil evaporation. The inclusion of hydraulic disconnection, along with the HR and litter layer dynamics, produce simulated LE fluxes that resemble better the observations from Blodgett during the late summer (Figure 2.4c) and do not show the early shut off of soil evaporation characteristic of the absence of HR (Figure 2.4d). This leads us to conclude that each of these components has an important role to play in this ecosystem.

Multispecies Analysis

The presence of shrubs in the year 2002 adds an additional complexity to the moisture dynamics. The total ecosystem latent heat flux now includes a contribution from shrubs, LE_{shrubs}, and is given as

$$LE_{eco} = LE_{shrubs} + LE_{PP} + LE_{Soil}. \tag{2.3}$$

Figure 2.5 shows the components of LE_{eco} for the same set of sensitivity simulations presented in Figure 2.4, but for the year 2002 with the inclusion of shrubs. The simulations for 2002 were started from the conditions at the end of the 2001 simulation runs. HR has been observed in different shrub species [Muñoz et al., 2008, Prieto et al., 2010], and so we allow for HR to be present in shrubs for these simulations. In Figures 2.5a, 2.5b and 2.5c, HR is enabled in both PP and shrubs while in Figure 2.5d HR is switched off for both PP and shrubs.

Soil evaporation during summer in the presence of shrubs (Figure 2.5a and 2.5b) is smaller compared to that without them (Figure 2.4a and 2.4b). Shrubs rely more on near surface moisture than PP due to their more shallow root profile, making soil evaporation a process that significantly impacts the energy balance of shrubs. In Figure 2.5a the summer soil evaporation is higher than in Figure 2.5b due to the absence of the litter layer. As in Figure 2.4d, Figure 2.5d shows that in the absence of HR soil evaporation drops during the middle of the summer because there are no sources of water to replenish the depleted near-surface soil moisture. The total latent heat flux released by the ecosystem is higher in the presence of HR.

Although the rate of transpiration in shrubs is considerably smaller than PP (Figure 2.5) the strong dry conditions during summer create water stress in the near-surface domain. Since the roots of shrubs are more confined to the near-surface zone of the soil column they are more vulnerable to this drying. HL by PP during the summer plays an important role in supporting both shrub transpiration and soil evaporation. It is interesting to note that in 2002 the presence of shrubs avoids the triggering of hydraulic fuse by reducing the moisture loss due to soil evaporation.

The dynamics observed in Figures 2.4 and 2.5 are a strong function of the processes occurring below-ground. Figure 2.6 shows the monthly mean values of root water uptake through the soil column for year 2001 and 2002 for the four scenarios analyzed above. Figure 2.6a shows that when no litter is included, the evaporative demand from the soil-surface during summer establishes a steep gradient between the soil and root water potential and results in a significant release of moisture from the roots in the near-surface zone, i.e. negative uptake values. This moisture, supplied by moisture taken up from the deeper layers by PP, contributes to high values of LE_{soil}. By comparing the year without shrubs (2001) to that with shrubs (2002), we see that the presence of shrubs results in an increased uptake by PP from the deeper layers, and a reduced release in the near surface zone. This is in part due to the increased shading of the ground surface by the shrub cover. We also note the presence

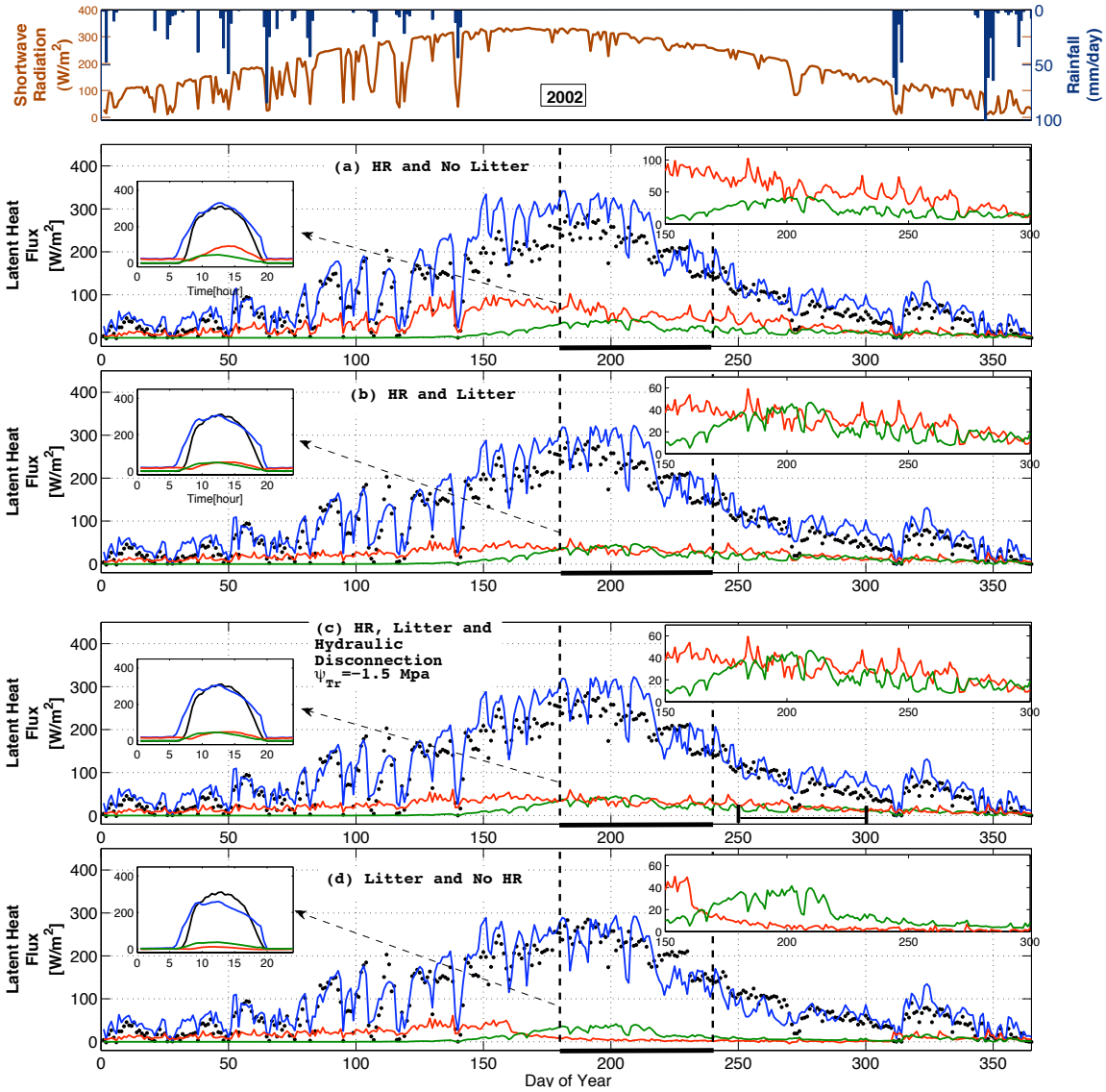

Figure 2.5: Same as Fig. 2.4 but for the presence of two vegetation species, PP and shrubs, during 2002. Green lines represent the flux from the shrubs and the inset on the right shows the comparative details between the latent heat from soil evaporation (red) and shrub transpiration (green). The coefficient of determination R^2 between simulated and observed latent heat flux for the four cases (a) through (d) are 0.72, 0.80, 0.80 and 0.82, respectively.

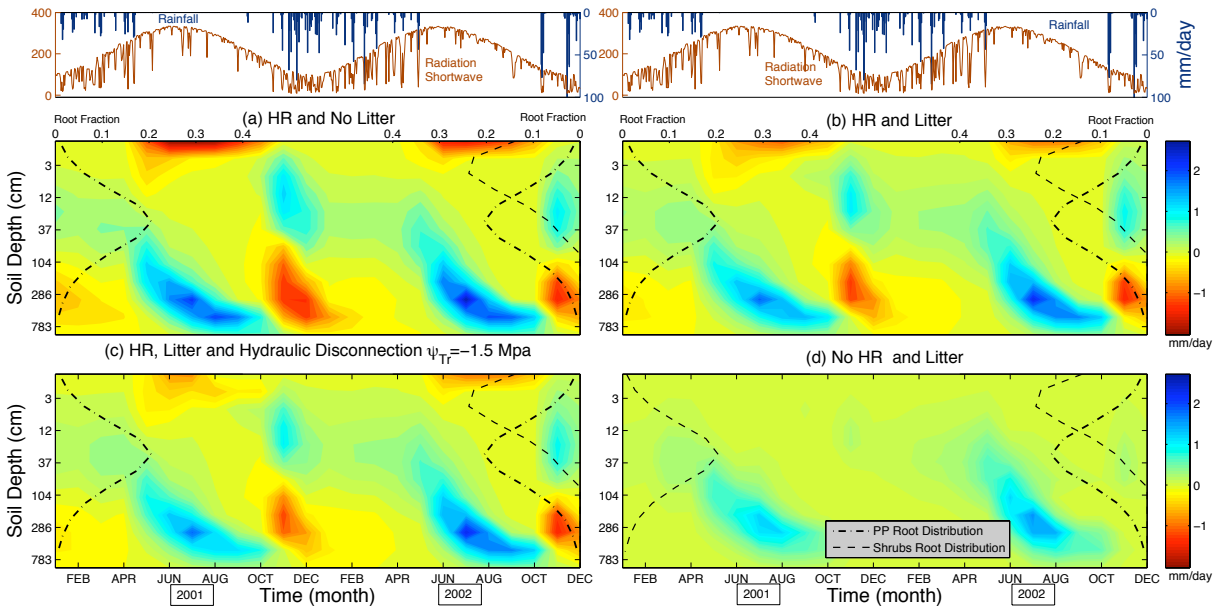

Figure 2.6: Water uptake patterns by vegetation in 2001 and 2002 corresponding to the four scenarios presented in Fig. 2.4 and 2.5 (negative values imply moisture release from the vegetation roots to the soil). The dashed and dot-dashed lines overlaid on the color panel indicate the root distribution for shrubs and PP, respectively. **(a)** HR is included but there is no litter layer above the soil column. **(b)** HR is included and there is a litter layer above the soil. **(c)** HR is not included, a litter layer lies above the soil column and hydraulic disconnection between the roots and the soil occurs when $\bar{\psi}_s \leq \psi_{Tr}$, where $\bar{\psi}_s$ is the daily average of soil water potential. **(d)** HR is not included and there is a litter layer above the soil. For reference the top panel shows the daily average of downward shortwave radiation and daily total rainfall for 2001 and 2002.

of hydraulic descent during the rainy periods. Comparing Figure 2.6b with 2.6a we see a similar pattern but the presence of litter reduces soil evaporation and this is reflected in a reduction in the release of moisture from the roots in the near-surface zone. Again we note higher uptake of water by PP and reduced moisture release near the surface in the presence of shrubs.

In Figure 2.5c hydraulic fuse is not reached and therefore there is a continuous efflux of moisture from the roots to the soil surface during the summer of 2002. The rate of this efflux is smaller in comparison to year 2001 when shrubs were absent. This efflux of water helps to sustain the water potential in the soil surface above the threshold ($\psi_{Tr} = -1.5$ MPa). In the absence of HR shown in Figure 2.6d, the water uptake shows less complex dynamics where the water uptake during the summer is from the deeper layers but at much reduced levels due to the absence of nighttime transport to dry shallow layers. These results,

although qualitatively similar to earlier studies (e.g. [Amenu and Kumar, 2008]), extend our understanding with regards to the role of shrubs, soil evaporation and a litter layer in the HR dynamics.

2.3.2 Summer Season Diurnal Dynamics

The results presented above have revealed interesting patterns of seasonal dynamics based on the analysis of daily average values. In this section we analyze the interaction between different vegetation species and moisture transport at the diurnal time scale using the half-hour observed and simulation data. We analyze the same four scenarios as illustrated in Figures 2.4, 2.5 and 2.6.

In Figure 2.7, the top panel shows the mean diurnal water uptake dynamics by PP in 2001, when shrubs are not present. In Figures 2.7a, b there is a continuous redistribution of water to the top layer throughout the day by PP, indicated by negative uptake values. The top layer is the thinnest layer in the numerical simulation (1.7 cm of thickness) and is in direct contact with the atmosphere unless a litter layer is present. The radiative energy reaching the surface in summer creates a high evaporative demand for moisture. Apart from moisture due to HL and dew in the night, there is no other source of moisture replenishing the surface layer. As a consequence, $\psi_s \leq \psi_r$ for the top layer throughout the day. Note that the moisture released by the roots is highest in the afternoon. There is HL in the night also, albeit at lower volumes, that moves the water to the near surface layer which in turn supports the evaporative demand during the day. Some experimental studies have reported daytime redistribution [Burgess et al., 2000, Espeleta et al., 2004, Scholz et al., 2002]. HR is enhanced by the low water potential that arises in shallow soil layers during dry periods. The importance of HR in regulating soil moisture in this critical zone during prolonged droughts has been indicated in recent studies [Warren et al., 2011].

When litter is considered in the simulation (Figure 2.7b), the flux of water redistributed to the top layer is reduced considerably but not eliminated. Figure 2.7c shows the dynamics in water uptake when hydraulic disconnection is also enabled. Although the average shown in Figure 2.7c for July and August includes several days before the hydraulic disconnection is triggered, we see that the efflux of water in the top layer is reduced.

In Figure 2.7, the middle and bottom rows show the diurnal average water uptake by PP and shrubs, respectively, in 2002 when both species are present. Shrubs uptake water from the shallow (up to 100 cm depth) soil layers. Thus the presence of shrubs generates a new

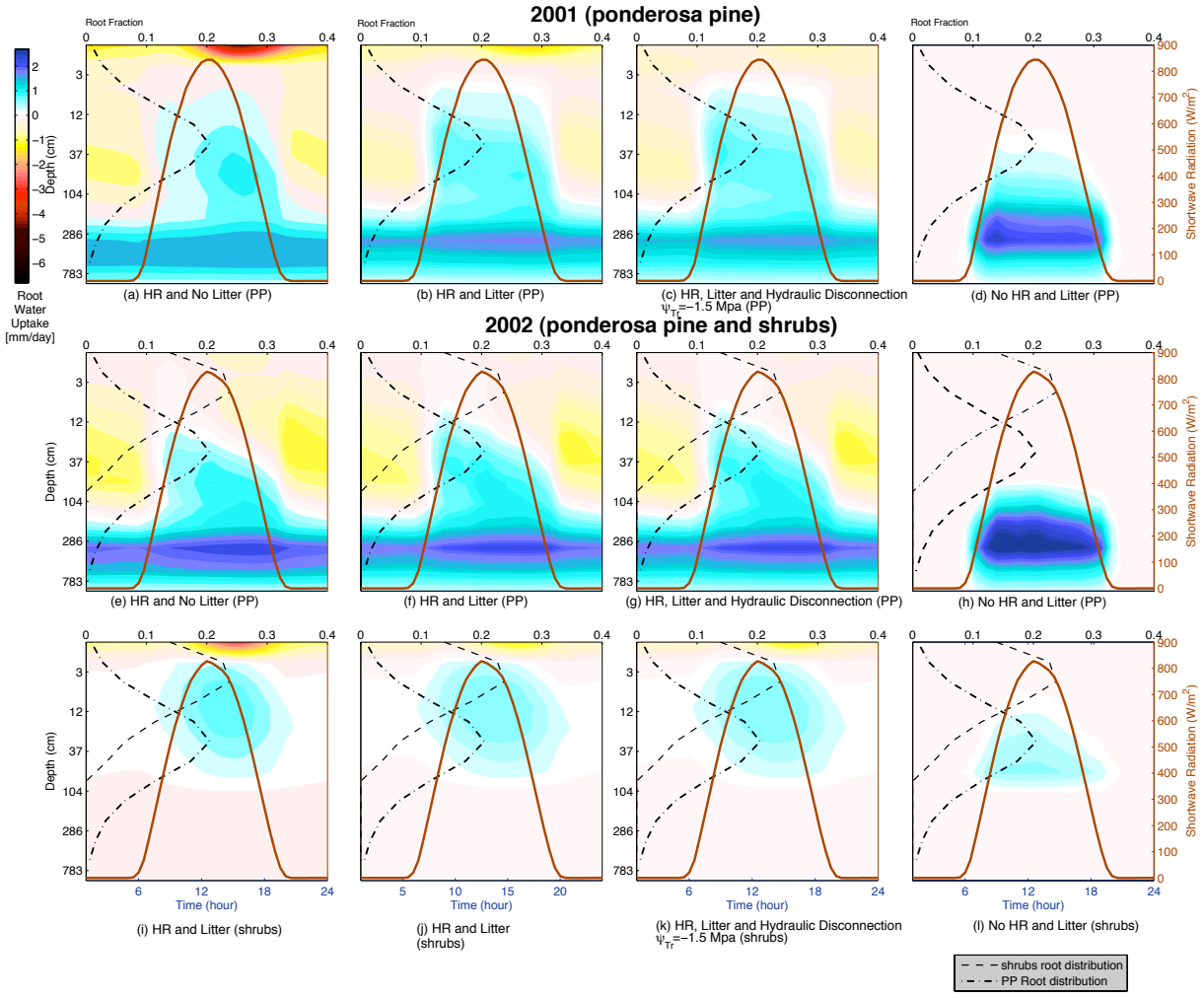

Figure 2.7: Diurnal pattern of water uptake by PP and Shrubs in summer (July-August) for the four scenarios discussed in Figures 2.4 and 2.5. **(a, e, i)** HR is included but there is no litter layer above the soil column. **(b, f, j)** HR is included and there is a litter layer above the soil. **(c, g, k)** HR is not included, a litter layer lies above the soil column and hydraulic disconnection between the roots and the soil occurs when $\bar{\psi}_s \leq \psi_{Tr}$, where $\bar{\psi}_s$ is the daily average of soil water potential. **(d, h, l)** HR is not included and there is a litter layer above the soil. First row shows the water uptake in 2001 by PP. Second row and third row shows water uptake by PP and shrubs, respectively, during 2002 when the two species are present. The presence of litter and shrubs influences the dynamics of water uptake in the soil. Redistribution of water to the soil surface occurs during the daytime also due to the gradient created from the high evaporative demand. The presence of litter and shrubs decreases the efflux of water observed at the surface.

demand that competes with soil evaporation for hydraulically lifted water. The water uptake patterns by PP are different in 2002 as compared to 2001. In 2002, under the presence of shrubs, the water released by PP to the surface is reduced. Instead PP release increases in deeper layers located between 6 and 80 cm where the transpiration use by the shrubs creates a water potential gradient that results in efflux of water out of the pine roots.

In the shallow soil layers both PP and shrub roots are present and compete for water uptake during the daytime. The competition for water is dictated by equation (2.1) and the capacity of each plant species to uptake water at a given layer is determined by the root radial conductivity, which in turn is a function of the root distribution and fine root biomass [Amenu and Kumar, 2008]. In the shallow layers shrubs have higher root radial hydraulic conductivity and, therefore, are more efficient in the uptake of water. The deeper distribution of root biomass makes PP more efficient in water uptake from the deeper layers. The patterns of water uptake and release by shrubs are less prominent than the ones by PP as the redistribution of water by HR in shrubs is found to be small in comparison with those by PP. As seen already, the presence of litter reduces the near-surface evaporative demand. Figure 2.7g also shows the uptake pattern when the hydraulic disconnection mechanism is implemented, but as mentioned before hydraulic fuse is not triggered in this case, suggesting that the presence of shrubs reduces near-surface drying that would occur for PP alone. Note that under No HR scenario (Figure 2.7h) the water uptake patterns are not significantly different from that of the single species case. The third row in Figure 2.7 shows the water uptake pattern for shrubs. We see that, as expected, most uptake is supported in the middle layers where the release by PP during the night provides the moisture to support the transpiration demand of shrubs during the day.

Figures 2.8a,c and d show observed data of soil moisture from a single point measurement and model results for year 2002 at three different depths (10, 30 and 50 cm). The model with both HR and No HR capture the general trend quite well. We should not expect an exact match between modeled and observed soil moisture since observations are at a specific point under the vegetation whereas the model represents the spatial average behavior. Figure 2.8b shows the soil moisture dynamics at 10 cm between days 150 to 166 which are located at the beginning of the summer with no rainfall occurring during this period. In this figure the diurnal cycle of soil moisture can be observed in more detail showing the oscillating pattern which is characteristic of HR. Note that the No HR simulations does not show this behavior. The inset figure shows the diurnal cycle of soil moisture averaged between days 150 to 166 for the observed and the model result in the presence of HR. In both cases it can be seen

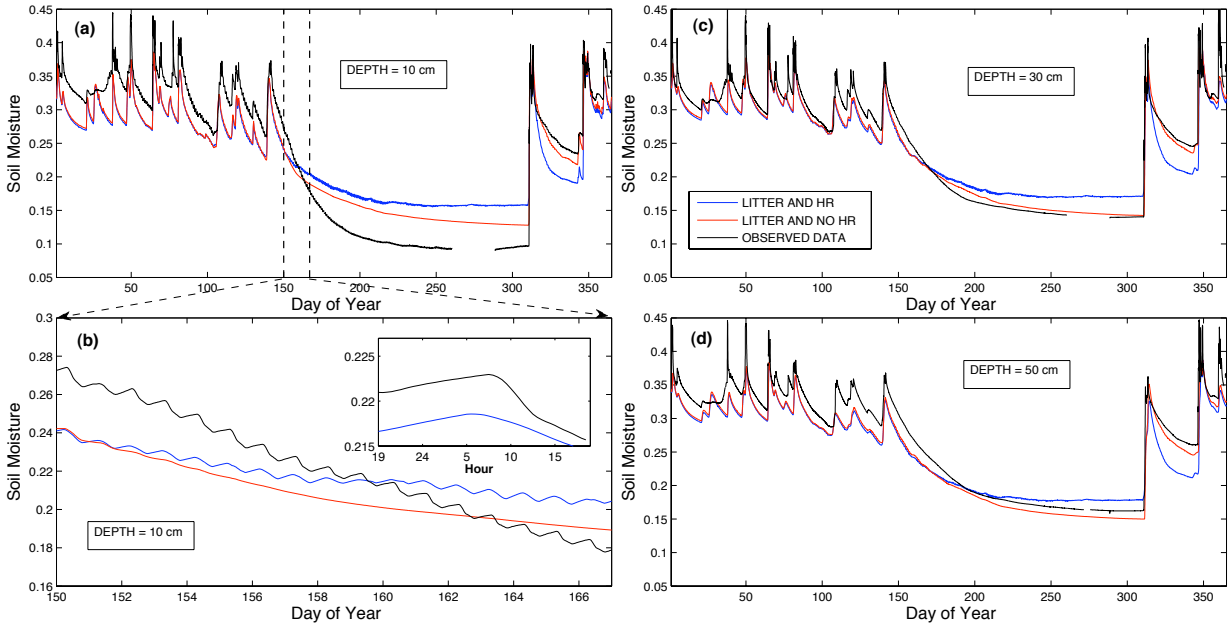

Figure 2.8: Soil moisture dynamics at the Blodgett site during the year 2002 at depths of 10 cm **(a)**, 30 cm **(c)** and 50 cm **(d)**. Observed data is compared with the model simulation in the presence and absence of HR. **(b)** Soil moisture at 10 cm is shown in more detail for days 150 to 166 which correspond to the beginning of the dry summer period. The inset figure shows the diurnal cycle of the observed and modeled (HR presents) soil moisture averaged over days 150 to 166. Since No HR simulations do not show an increase in nighttime soil moisture, they are not plotted in the inset figure.

that there is an increase of soil moisture during the night due to efflux from roots and a reduction during the day due to transpiration.

2.3.3 Competitive and Mutualistic Dependencies

The above results suggest that the dynamics of the multi-species composition at the Blodgett site are best represented through considerations of HR and litter dynamics along with the hydraulic disconnection mechanism. The set of sensitivity simulations that selectively incorporate different subsets of these functions have helped us understand the significance of each component on the latent heat flux and below-ground water uptake, release, and transport patterns. Figure 2.9 sheds more light on the trade-off between the different components of water use. When there is No HR, LE_{soil} is small and LE_{shrubs} can reach over 40 W/m^2 (triangles in the Figure 2.9a). Note that the color of the symbols in Figure 2.9a are associated with the total vegetation LE while the size of the symbols are associated with LE_{PP}. The transpiration for PP and shrubs is supported by soil moisture uptake from the middle and deeper layers (Figure 2.7, 4$^{\text{th}}$ column). Together they increase the LE_{eco} (darker green color). However, when HR is considered (squares and stars in Figure 2.9a), both LE_{soil} and LE_{shrubs} are higher and there is a trade-off between them as characterized by the dotted line obtained from the regression on the largest 10% of the values. That is, LE_{shrubs} increases as LE_{soil} decreases. However, it is noteworthy that the high values of LE_{shrubs} are larger than the case when there is No HR. We also note that LE_{PP} increases (larger boxes and stars) as LE_{shrubs} increases and LE_{eco} is higher (darker green color) as a result. This is a result of higher uptake of water by PP and shrubs (Figure 2.7, column 1 and 2). When we compare the presence (boxes) and absence (stars) of litter in Figure 2.9a, we see that by reducing the energy reaching the soil surface, the litter has the net effect of increasing LE_{shrubs}. Also the presence of litter enhances the fluxes LE_{PP} and productivity for PP. These are further exemplified in Figures 2.9b and 2.9c where the presence of litter results in higher latent heat as captured by the points which trend upwards of the $|:|$ line. This analysis establishes that the trade-off in water use occurs in a way that benefits both the tall and understory vegetation and facilitates increase in total ecosystem productivity. The role of litter layer in nutrient cycling and its impact on ecosystem productivity is presently being studied.

Figure 2.10a shows the total net carbon assimilation A_n from the model and that reconstructed from Blodgett observations for 2002. Comparison of model predictions in the presence and absence of HR (see Figure 2.10b,c and d) capture the expected higher pro-

ductivity of shrubs in the presence of HR. However, the dependence of shrubs on water redistributed by PP trees is regulated by their root depth and therefore their capacity to reach deeper layers. Due to the uncertainties in maximum shrub root depth during 2002 three different maximum shrub root depths, ranging from 60 to 140 cm, were analyzed (Figure 2.10b,c and d). For the 85 cm depth, the presence of HR results in an additional C uptake of 2 mol/m^2 in 2002 which comprises 28% of the net C uptake by the shrubs in that year. For the case of 140 cm depth, the presence of HR results in an additional C uptake of 0.9 mol/m^2 in 2002 which comprises 13% of the net C uptake by the shrubs in that year. As expected, the difference in net shrub productivity between HR and No HR is reduced as the shrub root system becomes deeper. Although the differences in shrub C uptake in the presence or absence of HR is small compared to the PP net uptake ($\sim$ 45 mol/m^2), these numbers comprise an important fraction of the shrub budget at this stage.

2.4 Summary and Discussion

In this study we analyzed the roles of three potentially important ecohydrological processes and their interactive effects. The three processes were hydraulic redistribution, the modulation of soil fluxes by a litter layer, and hydraulic disconnection in the context of a single and multi-species vegetation composition. Our goal was to disentangle the role of each of these processes in root water uptake and vertical soil moisture distribution through a resolved soil column, providing insight into the impacts on land-atmosphere energy partitioning and carbon dioxide exchange. The Ameriflux site at the Blodget Forest in the Sierra Nevada region of California provided an ideal setting to examine the impacts of these ecohydrologic processes in a multi-species system forced by a Mediterranean climate, in which water plays a dominant role in controlling ecosystem function.

Previous studies have indicated the potential for HR to enhance soil evaporation [Caldwell et al., 1998], and numerical studies have shown the impact of HR in soil evaporation [Lee et al., 2005, Wang, 2011]. These studies turn off HR in the near-surface layer during dry periods. Although there is experimental evidence that fine roots die at low soil water potentials and the response to drought is species and site specific [Espeleta et al., 2004], the interaction between different variables such as wilting point, the presence or absence of litter, hydraulic redistribution, and soil evaporation regulate the redistribution of water to the surface which is a critical process that merits further study. To our knowledge these interactions between the hydraulic redistribution of moisture through the soil system by

roots, and soil evaporation (see Figures 2.4 and 2.5) have not been analyzed and quantified in experimental or numerical studies. Our results show that as the summer progresses, the available moisture at the soil surface decreases such that the soil potential in near-surface layers drops below the water potential of the coincident roots. This potential gradient drives the uplift of moisture from moister lower layers to the shallow soil layers through HL (Figures 2.6 and 2.7). This upward transport of moisture is nearly continuous in time during extensive dry periods (Figure 2.7). Simulations conducted without HR show a reduction in soil evaporation during these periods, indicating that HR supplies moisture to near surface layers, which is then evaporated, effectively resulting in an enhanced loss of moisture from the system. Previous simulations have focused mainly on transpiration and have neglected soil evaporation [Amenu and Kumar, 2008, Mendel et al., 2002, Siqueira et al., 2008]. When soil evaporation was not considered (results not shown) the results obtained by our simulations resembled the general dynamics of water uptake reported previously [Amenu and Kumar, 2008].

In natural ecosystems, the presence of a litter layer affects energy and mass balance at the surface [Ogee and Brunet, 2002, Park et al., 1998] with impacts on soil evaporation. Here we introduced a litter layer above the soil column in the numerical model to analyze these dynamics. The inclusion of a litter layer reduces the radiation flux reaching the soil surface, thus reducing the soil evaporative demand. This reduces the potential gradient between the soil and the roots which in turn decreases the efflux of moisture from the roots to the soil (Figures 2.4 and 2.5). Despite the reduction in soil evaporation due to the existence of a litter layer, HR moves moisture from deeper soil layers to shallow soil layers throughout the summer months (Figure 2.6). It has been argued that this enhances fine root longevity [Caldwell et al., 1998, Pregitzer et al., 1993] in those layers, resulting in enhanced moisture uptake once precipitation recommences. It is also possible that higher moisture levels support decomposition of organic matter [Caldwell et al., 1998, Caldwell and Richards, 1989, Dawson, 1993, Horton and Hart, 1998]) as well as facilitating nutrient mass transport and the diffusion of ions in the soil [Caldwell and Manwaring, 1994, Nye and Tinker, 1977].

Under moisture stress plants seek to meet the transpirational water demand while avoiding critical negative water potentials that may cause cavitation [Alder et al., 1996, Tyree and Sperry, 1988]. When shrubs are present, the trigger for hydraulic fuse is dependent upon the depth of the shrubs roots. Shallower shrubs roots prevent hydraulic disconnection as shown in our results, but sensitivity studies showed that as the root density of shrubs go deeper, the hydraulic fuse is triggered resulting in disconnection. Domec et al. [2004] found that the

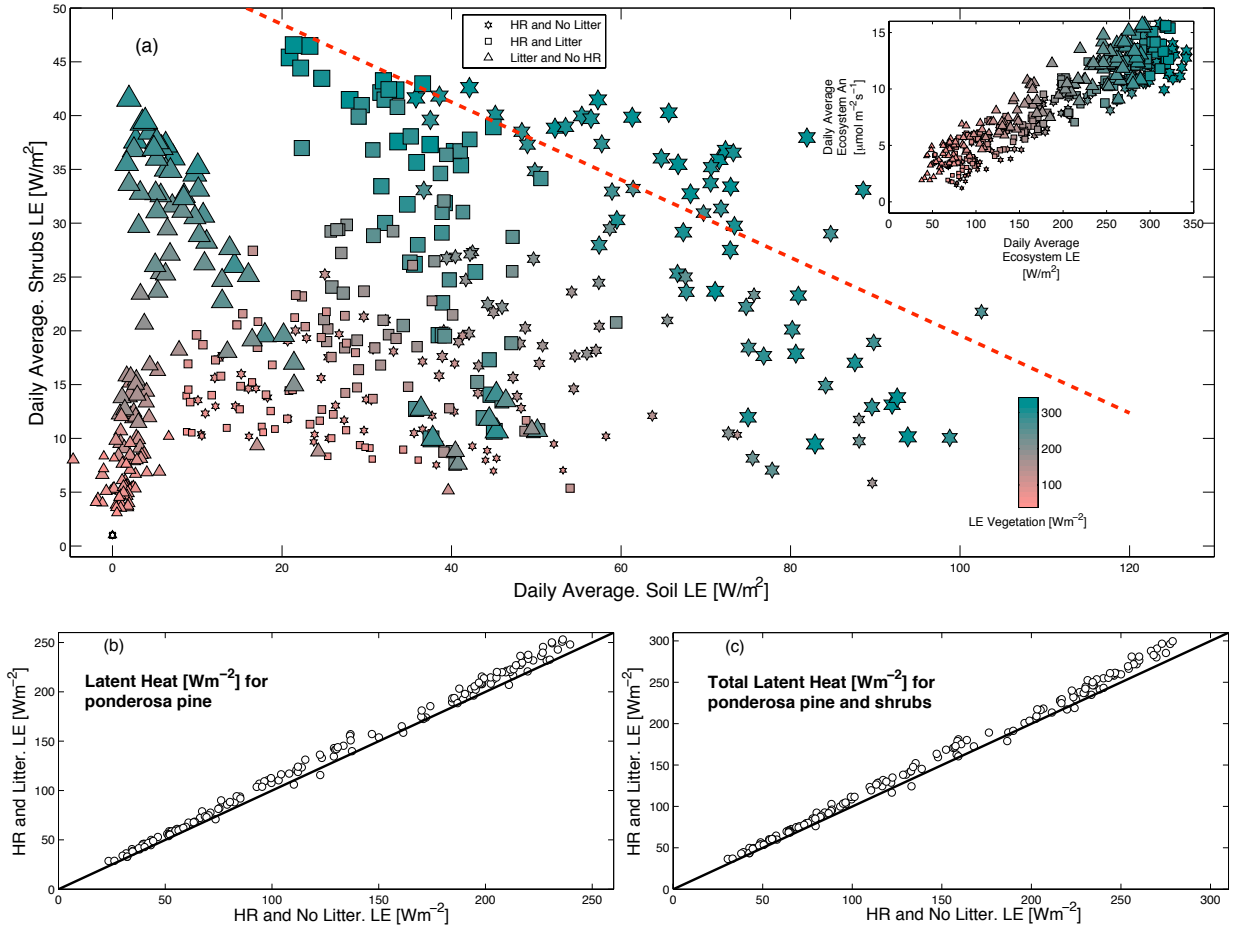

Figure 2.9: **(a)** Illustration of the trade-off between soil evaporation and shrub transpiration. This trade-off is influenced by the presence of HR and litter. In the absence of HR, soil evaporation fluxes are small (triangles). When HR is enabled, the presence of litter damps the radiative energy reaching the soil (compare stars and boxes), thereby reducing the soil evaporative demand and therefore reducing the efflux of water from the roots to the near-surface soil. This enhances shrub transpiration. Larger symbols indicate higher latent heat from ponderosa pine, and greener color indicates higher total vegetation latent heat flux. The dotted red line is the regression line for the highest 10% of the values showing the trade-off. The inset figure shows the relationship between daytime average transpiration and photosynthetic CO_2 assimilation. **(b)** Scatter plot of LE release by the ponderosa pine in the presence and absence of litter. **(c)** Scatter plot of LE release by the ponderosa pine and shrubs in the presence and absence of litter.

presence of HR in two different tree species (ponderosa pine and Douglas fir) helps to mitigate embolism because it sustains higher levels of soil water potential in shallow layers (20-30 cm). However, under extreme stress, plants may develop specific strategies to reduce the hydraulic connection with the soil [Caldwell et al., 1998, Espeleta et al., 2004], for example, death of fine roots [Espeleta et al., 2004]. To explore the role of such strategies, we incorporated hydraulic fuse as a threshold mechanism. When the hydraulic fuse is triggered there is a sharp reduction in the latent heat flux during the middle of the summer and captures the signature of the observed fluxes during this period when shrubs are not present. These results demonstrate that the stomatal control on transpiration, or even standard approaches to modeling root moisture uptake, may not be sufficient to accurately predict water fluxes in protracted dry situations.

Figures 2.4, 2.5, 2.6 and 2.7 show only one scenario of hydraulic disconnection that corresponds to a threshold $\psi_{Tr} = -1.5$ MPa corresponding to a standard value for wilting point. As mentioned in section 2.3, it is challenging to estimate a specific value of wilting point for a particular place and species. When the threshold was established as $\psi_{Tr} = -2.2$ MPa (adopted in Rose et al. [2003]) hydraulic fuse does not occur if litter and HR are present. However this threshold is exceeded if litter is absent. In the absence of litter and presence of HR the daily average of soil water potential reaches $\bar{\psi}_s = -3.8$ MPa. Although there is an uncertainty regarding the wilting point at the surface, the presence of litter has a significant impact on the soil water potential on the surface, and therefore in triggering hydraulic fuse. We believe that these results may have important implications for drought studies where extended dry periods may have implication for root longevity, water uptake, and ecosystem resilience.

Natural ecosystems are characterized by the coexistence of multiple vegetation species which have different above- and below-ground structural and ecophysiological characteristics. Several studies have pointed to the importance of HR in multi-species ecosystems [Brooks et al., 2006, Dawson, 1993, Emerman and Dawson, 1996, Espeleta et al., 2004, Moreira et al., 2003]. The inclusion of shrubs in the model modified the water uptake dynamics (Figure 2.7), by altering the water potential gradient in the vicinity of the shrub roots, resulting in more water being redistributed to layers below the surface that contain the roots of the shrubs while reducing that in the surface layer. The deeper root system of PP moves water upward to shallower soil layers where it is utilized to satisfy the transpiration demand of the shrubs throughout the summer (Figure 2.5). The shrubs in turn reduce the soil evaporative demand during the day.

Several previous studies have detected the presence of hydraulically redistributed water by trees with deeper root systems in understory plants [Brooks et al., 2002, 2006, Dawson, 1993, Emerman and Dawson, 1996, Espeleta et al., 2004, Moreira et al., 2003]. Dawson [1993] found that HR by overstory trees plays an important role in the water dynamics of understory shrubs influencing their growth which is an indirect indicator of productivity. Similarly, Zou et al. [2005] found that in some situations HR facilitates shrub performance in a subtropical savanna composed of tree-shrubs communities. On the other hand Ludwig et al. [2004] found that competition between plants reduces the facilitative effects of HR. Also Meinzer et al. [2004] claimed that the extent to which HR benefits understory shrubs is regulated by the water potential differences in the soil which is the mechanism that triggers HR. They indicate that this mechanism may start at some point where water requirements have been reduced. Furthermore, Emerman and Dawson [1996] found labeled water from HR in understory species but the amount was relatively small which suggests that it is unlikely that this source is causing an effect on shrub performance. The impact of hydraulically redistributed water from overstory trees in understory vegetation is a complex phenomenon that may vary from place to place. The model implemented here is a useful tool to analyze these interactions between different vegetation types. The simulation results obtained in Blodgett suggest that HR is an important mechanism facilitating shrub productivity throughout the long and dry summer. However, the extent to which this mechanism impacts shrub productivity is regulated by shrub root depth. The impact of HR in understory vegetation is stronger as the understory root system is closer to the surface.

The results presented here are based on a numerical model designed to resolve a broad range of physical and ecological functioning through the canopy-root-soil continuum [Amenu and Kumar, 2008, Drewry et al., 2010a] in the spirit of exploring novel relationships [Kumar, 2011]. The simulations are based on the assumption of passive control on the flow of moisture between the roots and soil driven only by potential gradients. In augmenting the MLCan model with a litter layer and implementing the hydraulic disconnection phenomena, as well as allowing for multiple species interactions, we have been able to confirm that each of these processes plays an important role, at least under specific climatic conditions, in the eco-hydrological functioning of a mixed-species Mediterranean system. This study has likewise presented an attempt to represent multiple, interacting species in a detailed ecohydrological model that represents the process of hydraulic redistribution. Our analysis has demonstrated both competitive and mutualistic interactions between the two simulated species, and opens the door to future studies that will further examine the hydrology and biogeochemistry of

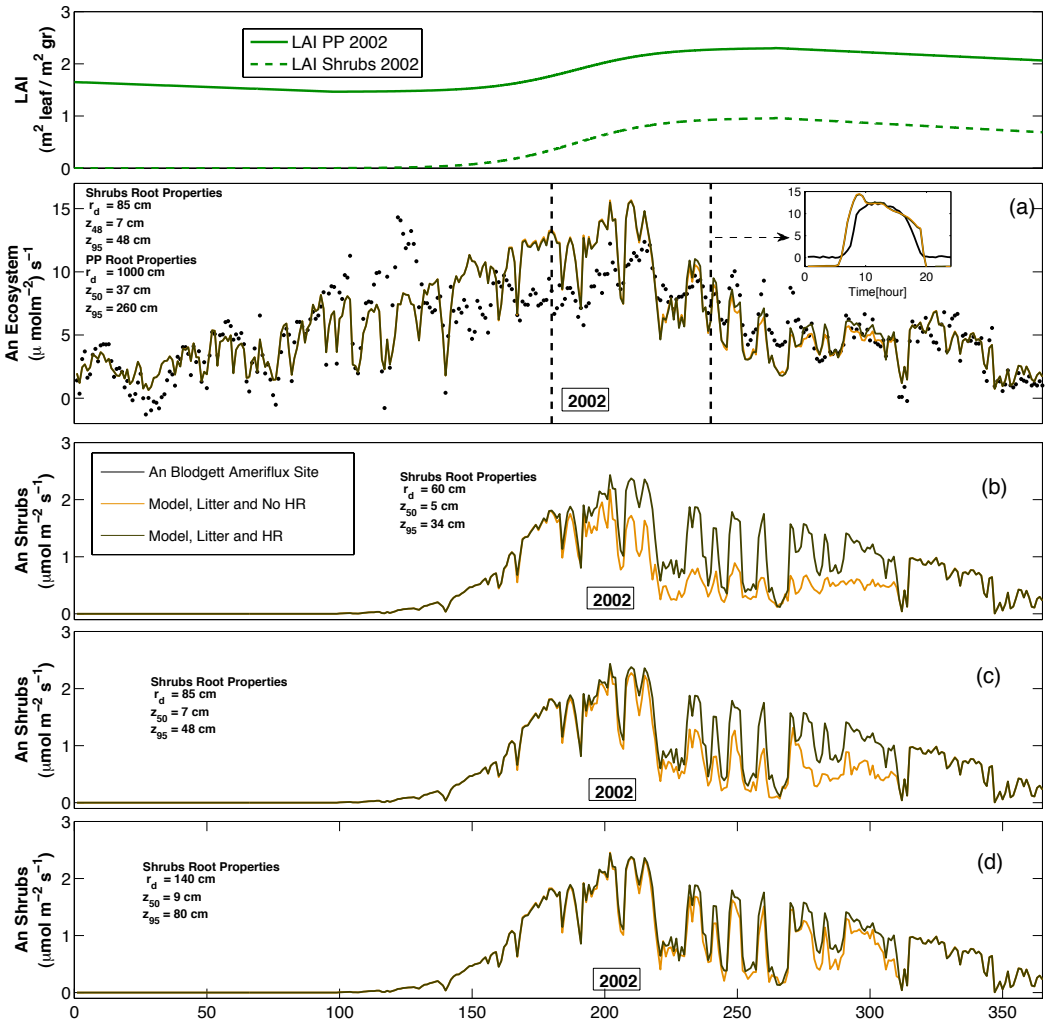

Figure 2.10: Illustration of the annual variation of carbon assimilation in the presence and absence of HR in 2002. **(a)** Gross ecosystem productivity GEP. Daytime (7:00 a.m. to 7:00 p.m.) Net carbon assimilation by shrubs with maximum root depth equal to 60 cm **(b)**, 85 cm **(c)** and 140 cm **(d)**. The presence of HR enhances the net carbon assimilated by shrubs. Top panel shows the LAI of ponderosa pine and shrubs.

mixed species systems.

Table 2.1: List of symbols for Multi-Species MLCan implementation in Blodgett.

Symbol	Description
A_n	Net uptake of CO_2 through photosynthesis
C_p	Specific heat of air
C_{LS}	CO_2 concentration at the leaf surface
b	Ball-Berry intercept
f_{sv}	Tuzet-Ball-Berry parameter for the stomatal conductance
G_{L1}	Ground heat flux into the litter layer
G_{L2}	Ground heat flux from the litter layer into the soil-litter interface
G_s	Ground heat flux into the soil
g	Acceleration due to gravity
g_s	Stomatal conductance
h_{LS}	Relative humidity at the leaf surface
J_{max}	maximum rate of electron transport
K_s	Soil water conductivity
K_{rad}	Total conductivity in the root system in the radial direction
$K_{r_i}^R$	Root conductivity in species i in the radial direction, obtained for each layer from K_{rad} according to the root distribution [Amenu and Kumar, 2008]
K_{ax}	Total conductivity in the root system in the axial direction
$K_{r_i}^A$	Root conductivity in species i in the axial direction, obtained for each layer from K_{ax} according to the root distribution [Amenu and Kumar, 2008]
LE_L	Latent heat emitted from the litter layer to the atmosphere
LE_{eco}	Latent heat emitted from the total ecosystem
LE_{shrubs}	Latent heat emitted from the shrubs
LE_{PP}	Latent heat emitted from ponderosa pine, PP
L_v	Specific heat of vapourisation
m	Ball Berry slope
q_{s1}	Air specific humidity in the soil in the top most layer
q_{a1}	Air specific humidity in the atmosphere in the closest layer to surface

Continued on Next Page...

Table 2.1 – Continued

Symbol	Description
r_a	Aerodynamic resitance
r_s	Additional resistance of litter layer to transport of vapor
R_w	Gas constant for water vapor
RH_{Ln}	Relative Humidity in the litter layer
s_f	Sensitivity parameter, Tuzet model
T_L	Temperature in the litter layer
T_{LSS}	Temperature at the litter-atmosphere interface
T_{Ln}	Temperature at the center of the litter layer
T_{SL}	Temperature at the litter-soil interface
T_{s1}	Soil temperature in the first (top most) layer
T_{a1}	Temperature in the atmosphere in the layer closest to the surface
TC_L	Thermal conductivity of the litter
TC_{s1}	Soil thermal conductivity in the top most layer
V_{cmax}	maximum carboxylation velocity
α_L	Litter thermal Difussivity
θ	Soil moisture
ψ_s	Soil water potential
ψ_l	Leaf water potential
ψ_f	Reference water potential in the Tuzet-Ball-Berry model
ψ_{ri}	Root water potential in i^{th} vegetation species
ψ_L	Litter water potential
ψ_{LL}	Litter water potential for a liter moisture of $1 kg kg^{-1}$[Ogee and Brunet, 2002]
ψ_{Tr}	Soil water potential threshold for hydraulic disconnection
$\bar{\psi_s}$	Daily average soil water potential
$\rho_{b,L}$	Litter bulk density [Ogee and Brunet, 2002]
Δz_L	Litter Layer Thickness

Continued on Next Page...

Table 2.1 – Continued

Symbol	Description
Δz_{s1}	Top soil Layer Thickness
ρ_d	Density of dry air
ρ_w	Density of liquid water

Table 2.2: List of parameters used in the simulations for the Blodgett Ameriflux Site.

Description	**Symbol**	**Units**	**Ponderosa Pine**	**Shrubs**
Photosynthesis				
Fraction absorbed Q available to photosystem II	B_f	-	0.5^a	0.5^a
Conductance and Leaf States				
Ball Berry slope	m	-	$13^{\ b}$	13
Ball Berry intercept	b	$\frac{\text{mol}}{\text{m}^2\text{s}}$	0.001^*	0.001^*
Stomatal sensitivity parameter for m	s_f	MPa^{-1}	1^b	1
Ψ_l at which half potential for m is lost	Ψ_f	MPa	-2^b	-2
Leaf forced convection parameter	c_f	-	$4.3 \cdot 10^{-3\ g}$	$4.3 \cdot 10^{-3}$
Leaf free convection parameter	c_f	-	$1.6 \cdot 10^{-3\ g}$	$1.6 \cdot 10^{-3}$
Canopy Structural				
Canopy Height	hc	m	$5^{\ l}$	1^l
Displacement Height	d	m	2/3 hc	2/3 hc
Leaf width (Needle diameter)	do	m	0.001^e	0.02^c
Shoot diameter for Conifers	wo	m	0.07^e	-

Continued on Next Page...

Table 2.2 – Continued

Description	**Symbol**	**Units**	**Ponderosa Pine**	**Shrubs**
Maximum H_2O storage capacity of a leaf	S_m	$\frac{\text{mm}}{\text{(LAI)}}$	0.2	0.2
Foliage drag coefficient	C_d	-	0.5^d	0.5^d
Mixing Length coefficientt	α	-	0.13^d	0.13^d
Decay Coefficient for Leaf Nitrogen Content	k_n	-	0.5	0.5
Radiation and Energy Balance				
Leaf emissivity	ϵ_l	-	0.95^f	0.95
Leaf Reflectance in the Visible Wavelength	ϵ_{rv}	-	0.09^e	0.09
Leaf Transmittance in the Visible Wavelength	ϵ_{rt}	-	0.06^e	0.06
Leaf Reflectance in the near Infrared Wavelength	ϵ_{ri}	-	0.52^e	0.52
Leaf Transmittance in the near Infrared Wavelength	ϵ_{ti}	-	0.35^e	0.35
Leaf angle distribution parameter	x	-	0.6^k	0.6
Root Structure				
Maximum Root depth	r_d	m	10	0.85
50th percentile rooting depth. Logistic Equation.	z_{50}	m	$0.37^{h,j}$	0.07^h
95th Percentile Rooting Depth. Logistic Equation.	z_{95}	m	$2.60^{h,j}$	0.48^h
Radial Conductivity.	K_{rad}	s^{-1}	$5.0\text{x}10^{-8}.^{hij}$	$2.5\text{x}10^{-8}.^{hij}$

Continued on Next Page...

Table 2.2 – Continued

Description	**Symbol**	**Units**	**Ponderosa Pine**	**Shrubs**
Axial Conductivity.	K_{ax}	mm^2/s	0.2 [hij]	0.1 [hij]

[a]Bernacchi et al. [2003], Bernacchi et al. [2005], [b]Misson et al. [2004] see also Appendix C,
[c]Smith [2005], [d]Katul et al. [2004], [e]Kurpius et al. [2003]
[f]Campbell and Norman [1998], [g]Nikolov [1995],
[h]Jackson et al. [1997], [i]Huang and Nobel [1994], [j]Amenu and Kumar [2008]
[k] Assuming more tendency towards vertical leaf angle distribution [Schade, 2002]
[l] Fisher et al. [2007],*From sensitivity analysis

Table 2.3: List of parameters for the soil and litter model.

Description	**Symbol**	**Units**	**Value**
Soil Parameters			
Atmospheric Emissivity	ϵ_a	-	0.94[a]
Soil Surface Emissivity	ϵ_s	-	0.85 [a]
Litter Parameters			
Saturated Litter Moisture	θ_{Ls}	-	0.8[b]
Litter Moisture at Field Capacity	θ_{Lfc}	-	0.025
Litter Moisture at which r_s (resistance to LE	θ_{Lr}	-	0.2 [c]
due to litter) becomes zero		-	
Litter Moisture at which evaporation (LE_{soil})	θ_{Le}	-	0.0001
becomes negligible		-	
Exponent for Litter Matric Potential	b_l	-	2.42 [d]
Matric Potential for Litter Moisturised	ψ_{1l}	m	35.3 [d]
at 1 kg/kg			
Litter Thickness	Δz	cm	3
Litter Thermal Conductivity	TC_L	$W/m/K$	0.15 [e]
Litter Thermal Diffusivity	α_L	m^2/s	$5.7 * 10^{-7}$ [e]

[a]Campbell and Norman [1998], [b]Park et al. [1998], [c]Schaap et al. [1997]
[d]Ogee and Brunet [2002], [e]Ahn et al. [2009]

CHAPTER 3

Role of Climate and Species Composition on Hydraulic Redistribution

3.1 Introduction

Plant roots are complex systems that uptake water and nutrients necessary for the plant to perform different metabolic activities such as photosynthesis. The ability of plant roots to meet this demand allows vegetation, the major form of life on the planet, to function. Besides sustaining the above-ground demand, the uptake of water by plant roots regulates the distribution of moisture in the subsurface which influences several below-ground processes. The uptake of moisture by plant roots is therefore a critical process that influences water, energy and biogeochemical cycles at different scales. In this study we use a numerical model to analyze different factors that regulate the uptake of moisture by plant roots.

The role of the root system as a water and nutrient supply to the plant is well known [Passioura, 1988, Tyree and Zimmermann, 2002]. In recent decades there has also been an increasing amount of evidence that plant roots release moisture back into the soil [Caldwell et al., 1998, Mooney et al., 1980]. This mechanism seems to be driven by water potential gradients that occur in the soil. Through this process, plant roots are able to transport moisture from wet regions to dry regions in the subsurface. This phenomenon has been observed in the horizontal [Brooks et al., 2002], downward [Burgess et al., 1998, Hultine et al., 2003], and upward [Caldwell and Richards, 1989, Emerman and Dawson, 1996] directions, and has been termed hydraulic redistribution (HR) [Burgess et al., 1998, 2001, 2000, Hultine et al., 2003, 2004].

Previous studies have analyzed the role of water uptake and HR in different ecosystem dynamics. Numerical and empirical experiments have demonstrated the role of HR in enhancing transpiration [Amenu and Kumar, 2008, Ryel et al., 2002, Scott et al., 2008] and net productivity [Dawson, 1993, Quijano et al., 2012]. It has additionally been recognized that HR may mediate ecological functions [Caldwell et al., 1998] such as species interactions [Dawson, 1993, Querejeta et al., 2007, Quijano et al., 2012, Wang and Bras, 2011] or soil

microbial dynamics [Egerton-Warburton et al., 2008, Querejeta et al., 2007, 2003]. Also, the impact of HR on soil moisture may influence biogeochemical processes by modifying decomposition and mineralization rates [Aanderud and Richards, 2009, Armas et al., 2011, de Kroon et al., 1998, McCulley et al., 2004, Quijano et al., 2013].

Although HR is recognized as a critical process that may impact several dynamics at various scales and has been observed in an wide domain of plants species and climates [Caldwell et al., 1998, Neumann and Cardon, 2012, Prieto et al., 2012], there is still high uncertainty regarding the magnitudes of the fluxes released by plants through HR. HR is believed to to occur passively, driven by gradients in water potential. Therefore it is likely that rainfall and energy inputs are the main processes that impact HR fluxes. Although HR has been recorded in sites with clear precipitation seasonality, there are no experimental or numerical approaches that examine the role of climate on the magnitude of HR. Additionally, several other physiological variables related to plant roots such as the hydraulic conductivities regulate the magnitude of these fluxes. A recent review study [Neumann and Cardon, 2012] on the magnitude of HR fluxes revealed the inconsistencies between fluxes obtained from experiments ($\sim$ 0.04 to 1.3 mm day^{-1})and fluxes obtained from models ($\sim$ 0.1 to 3.23 mm day^{-1}). According to this study, differing factors influenced numerical simulations and experiments. One advantage of the modeling approach is the implementation of several numerical models at widely varying sites. However, the experiments did not cover the full annual spectrum, missing periods where HR could potentially be important. Experimental methods have been unable to capture reliable measurements of hydraulic lift at points near the surface and hydraulic descent in deep soil horizons.

In Chapter 2 we have explored the role of HR to mediate interactions between different species and impact the surface energy balance and productivity of the ecosystem. We analyzed these dynamics in Blodgett Ameriflux Site which is located in the Sierra Nevada, California. In this chapter we now focus in the analysis of the most important factors that regulate the magnitude of HR fluxes such as climate, root hydraulic conductivities, and the composition of different species. In this analysis we include three Ameriflux Sites that have different species composition and experience different climates. We use the same numerical model for three Ameriflux Sites and implement a common parameterization of root hydraulic conductivities based on experimental information. This approach allows us to compare the dynamics of HR fluxes across ecosystems that are subject to different climatological conditions.

3.2 Methods

3.2.1 Model

In this study we use Multi-Species MLCan model for the simulation of the ecohydrological dynamics. This model is described in detail in Appendix A. In addition we parameterize root hydraulic conductivities by scaling root measurements of hydraulic conductivities at a single root to the entire root system (see Appendix D Section 1).

3.2.2 Study Sites

The simulations are performed using forcing data from three Fluxnet sites that exhibit different seasonal dynamics of rainfall and incoming energy. The three sites are Blodgett Ameriflux Site in California (US), Tapajós Km 67 in Para (Brazil), and Harvard Forest in massachusetts (US). These sites are briefly described below.

(i) Blodgett Ameriflux Site:

This site is located in the Sierra Nevada near Georgetown, CA, USA, at 1315 above the sea level. The mean annual precipitation is around 1200 mm. The site is characterized by a mediterranean climate with wet winters and dry long summers that may last up to 5 months. More details about this site were presented in Chapter 2 or can be obtained from previous publications such as Fisher et al. [2005], Goldstein et al. [2000], Quijano et al. [2012].

The sierra nevada mountains in the area close to Blodgett presents a vegetation composed by a variety of different understory and overstory species. However the Blodgett Ameriflux site is located over a controlled area of ponderosa pine (*Pinus ponderosa L.*) trees that were planted in 1990. Therefore the ecosystem in this site is dominated by ponderosa pine trees and two major understory shrubs Arctostaphylos manzanita (Mazanita) and Ceonothus cordulatus (Ceanothus) [Misson et al., 2005]. The simulations performed in this study are implemented with two PFTs: (1) Understory shrubs, and (2) Overstory Ponderosa Pine Trees.

(ii) Tapajós KM67 Mature Forest Ameriflux Site:

This site is located on the Tapajós National Forest, 50 to 150 km south of the city of Santarm, Para, Brazil. The mean annual temperature is 25 °C and the mean annual precipitation

is 1920 mm with a recognized dry season of 5 months between July and November where the average monthly precipitation is lower than 100 mm. The reduction in precipitation during the dry season impacts other climatic variables such as global radiation, temperature, and humidity, and therefore it generates a strong seasonal variation at this site. In addition, this site, as most of the Amazon basin, is affected by El Nio Southern Oscillation (ENSO). Although the impact of ENSO may vary from once occurrence to the next, at some point it could reduce considerably the amount of precipitation at this site [Saleska et al., 2003, Silver et al., 2000].

Although three main eddy covariance towers operate in the Santarém-Tapajós region, for the simulations performed in this study we only use data from KM67 because it represents the measurements over the most unaltered forest which is classified as primary [Clark, 1996]. The site is composed of many different plant species with an uneven age distribution and the presence of some emergent trees [Hutyra et al., 2007]. Although there is a high plant biodiversity, previous studies have recognized some main plant functional groups in this site based on life form, species distribution and within canopy profile [Domingues et al., 2007]. According to these studies there are four main functional groups: (1) over-story trees, (2) over-story Lianas, (3) mid canopy tree and (4) understory tree. In this study we perform the numerical simulations considering these same functional groups. However in order to facilitate numerical simulations we combined the two over-story PFT (Lianas and Trees) in one. We use available specific ecohysiological and structural information within each functional group from previous publications [Carswell et al., 2000, Domingues et al., 2007].

(iii) Harvard Forest Ameriflux Site:

This site is located 110 km west of Boston, MA, USA. According to Urbanski et al. [2007] this is the eddy covariance site with the longest running records in the world. The mean annual temperature is 6.5 °C. The mean annual precipitation is about 1000 mm and it is distributed more homogeneously throughout the year than the other two sites described above.

The forest is about 70 years old, the canopy height is close to 23 m and the stand is composed of several deciduous and conifer species. Deciduous species are dominant and represents about 70% of the total basal area. The simulations performed in this study were implemented using three main functional groups, (1) deciduous, (2) conifers, and (3) under-story plants [Bassow and Bazzaz, 1997, Richardson et al., 2009].

The availability of detailed information from these Ameriflux sites allows us to perform

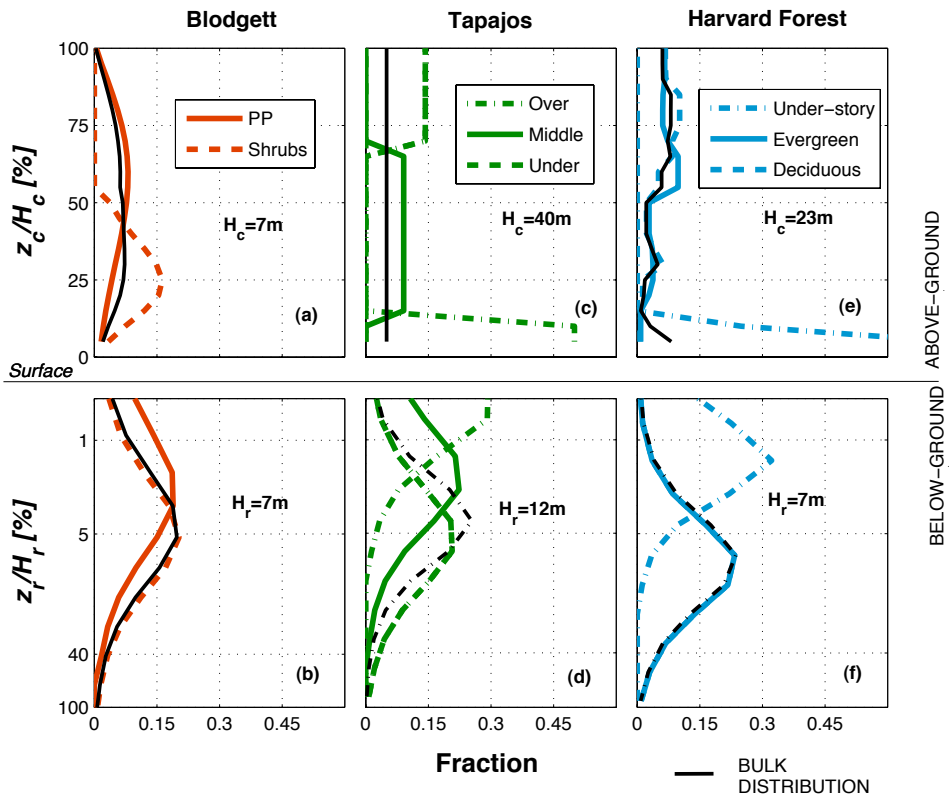

Figure 3.1: Normalized root and leaf area distributions for each PFT at all the three sites analyzed in this study. These distributions were calculated with available information gathered from different sources. The black lines show the distributions implemented in the bulk simulation. The Appendix D shows in more detail the parameters used in this study to calculate these distributions.

numerical simulations using the Multi Species MLCan model. Each site exhibits different rainfall and incoming radiation patterns, in addition to distinct compositions of natural PFTs. Therefore, we believe that numerical simulations at these three sites represents a good experiment to analyze the effect of different variables on the HR fluxes and transpiration in a variety of natural ecosystems. Figure 3.1 shows normalized distributions of roots and leaf area distribution (LAD) in each PFT used in this study. It can be observed that the understory and overstory PFTs allocate roots and leaves closer to the surface than overstory PFTs. It can also be noted that canopy heights and root depths vary between the three sites.

3.2.3 Simulation Period

For each site, we base our simulation period on the three years with the best available Ameriflux Towers records that allow us to extract reliable forcing data and validate latent heat (LE) fluxes. The years selected in Blodgett and Tapajós are 2002, 2003, and 2004. In Harvard Forest the years selected were 2004, 2005, and 2006. All the simulations performed are initialized with soil moisture and temperature values from a spin up process performed one year before the simulations.

3.3 Results and Analysis

3.3.1 Validation of Latent Heat Fluxes

Figure 3.2 shows the fluxes of LE during the simulation's period for the three sites as described above. The LE fluxes from the model simulation match the main diurnal pattern and the daily totals throughout the year recorded at the Ameriflux Towers. The seasonal pattern is clearly apparent in Blodgett and Harvard Forest. Note that the LE fluxes in Blodgett are considerably higher than those in Harvard Forest. In Blodgett, the summer season is dry and the incoming short wave (SW) radiation is much higher than that of Harvard Forest. The availability of hydraulically redistributed water helps to support the high transpiration demand. Contrastingly, the LE in Tapajós display a tropical imprint pattern with more homogeneously distributed fluxes throughout the year.

3.3.2 Seasonal Patterns of Water Uptake

Figure 3.3 shows the fluxes of transpiration and hydraulic redistribution during the simulation period for the three sites. The fluxes in this figure are presented for all the PFTs in different colors. As expected, the fluxes of transpiration follow the same dynamics as observed in Figure 3.2.

In Blodgett, the highest fluxes of LE are from PP trees. Although the leaf area index (LAI) in the understory shrubs is higher than 1 during the summer period, shrubs are shaded by PP trees and therefore receive less direct SW radiation. The Mediterranean climate in Blodgett creates a strong seasonality, with a long dry period during the summer season. This dry period coincides with the time at which plants are able to perform photosynthesis

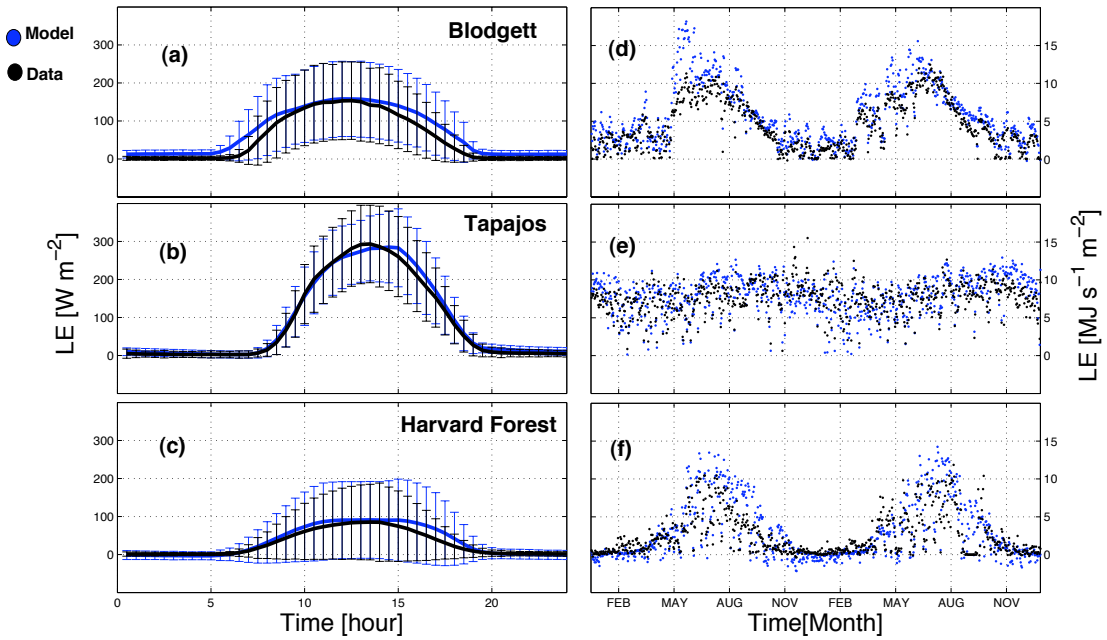

Figure 3.2: Fluxes of Latent Heat (LE) recorded (black) and simulated (blue) in **(a,d)** Blodgett, **(b,e)** Tapajós, and **(c,f)** Harvard Forest. The left panel (a,b,c) shows the diurnal pattern computed by averaging the three years of simulation. The right panel shows the total daily fluxes throughout the period of simulation. It can be observed that the model matches the general recorded patterns. The simulation results were performed with a specific hydraulic root axial conductivity of $K_{axs} = 10^{-}1[m^4 MPa^{-1}\ s^{-1}\ m^{-2}_{root,cs}]$ and root radial conductivity $K_{rad} = 10^{-7}[m^3\ MPa^{-1} s^{-1} m^2_{root,sa}]$.

and transpire more water. During this time the role of deep roots in reaching deep wet layers is critical. During this dry period plant roots redistribute moisture upwards (hydraulic lift, HL). These fluxes can be observed in Figure 3.3c in which HR fluxes are dominant during the summer period. The rainfall season starts around october when transpiration is reduced. The first month of the rainy season is associated with a prominent flux of HR (Figure 3.3c). When the first rainfall event occurs, it creates significant gradients in water potential in the soil that induces redistribution of moisture to deeper dry layers in the soil (hydraulic descent, HD). However, after a couple of months of rainfall and low transpiration fluxes, the gradients in water potential in the soil column are reduced and the HR fluxes become negligible. Note that the HR fluxes between February and April are considerably low. As expected, the HR fluxes are higher in the PP trees compared to shrubs because they have deeper root systems. The HR fluxes between June and January can reach up to 2 mm d^{-1} on average. However, for the rest of the year the magnitude is much lower (< 0.1mm d^{-1}) resulting in annual average of about 0.82 mm d^{-1}.

The transpirational fluxes in Tapajós (Figure 3.2e) are distributed more homogeneously than in Blodgett and Harvard Forest. However, there is a mild seasonality with transpirational fluxes that are slightly higher during the dry season. During the rainy season, clouds reduce the incoming SW radiation (as can be observed in the right panels in Figure 3.2e), constraining the LE fluxes. The highest fluxes of transpiration in Tapajós are from the upper canopy trees. Although LAI is higher for the mid-canopy trees, the amount of radiation that is absorbed is lower.

The pattern of HR fluxes in Tapajós (Figure 3.3) shows a strong seasonality due to a similar mechanism as that observed in Blodgett. During the high transpiration period between June and November, rainfall is scarce and therefore moisture is redistributed towards the surface from deeper layers (HL). Similarly to Blodgett, the first events of the rainy season are associated with high HR fluxes (Figure 3.3d) due to redistribution of moisture from the surface to deeper layers (HD). In contrast to Blodgett, in Tapajós, transpirational fluxes are present throughout the year. This pattern accentuates the water potential gradients and increases the HR fluxes. During certain periods the fluxes of HR in Tapajós reach a magnitude of over than 4 mm d^{-1}. However, as mentioned above, the HR seasonality is strong and the mean annual magnitude of HR is about 1.9 mm d^{-1}. The redistribution fluxes are mostly controlled by the mid canopy and the upper story trees. Although Lianas transpire a significant amount of water, the fluxes of HR are lower in comparison to midcanopy and upper canopy trees because Lianas have lower effective root hydraulic conductivities due

to lower basal area and LAI (see Appendix D). Although transpiration is an important driving factor in HR, HR fluxes are also mediated by other variables such as root hydraulic conductivities.

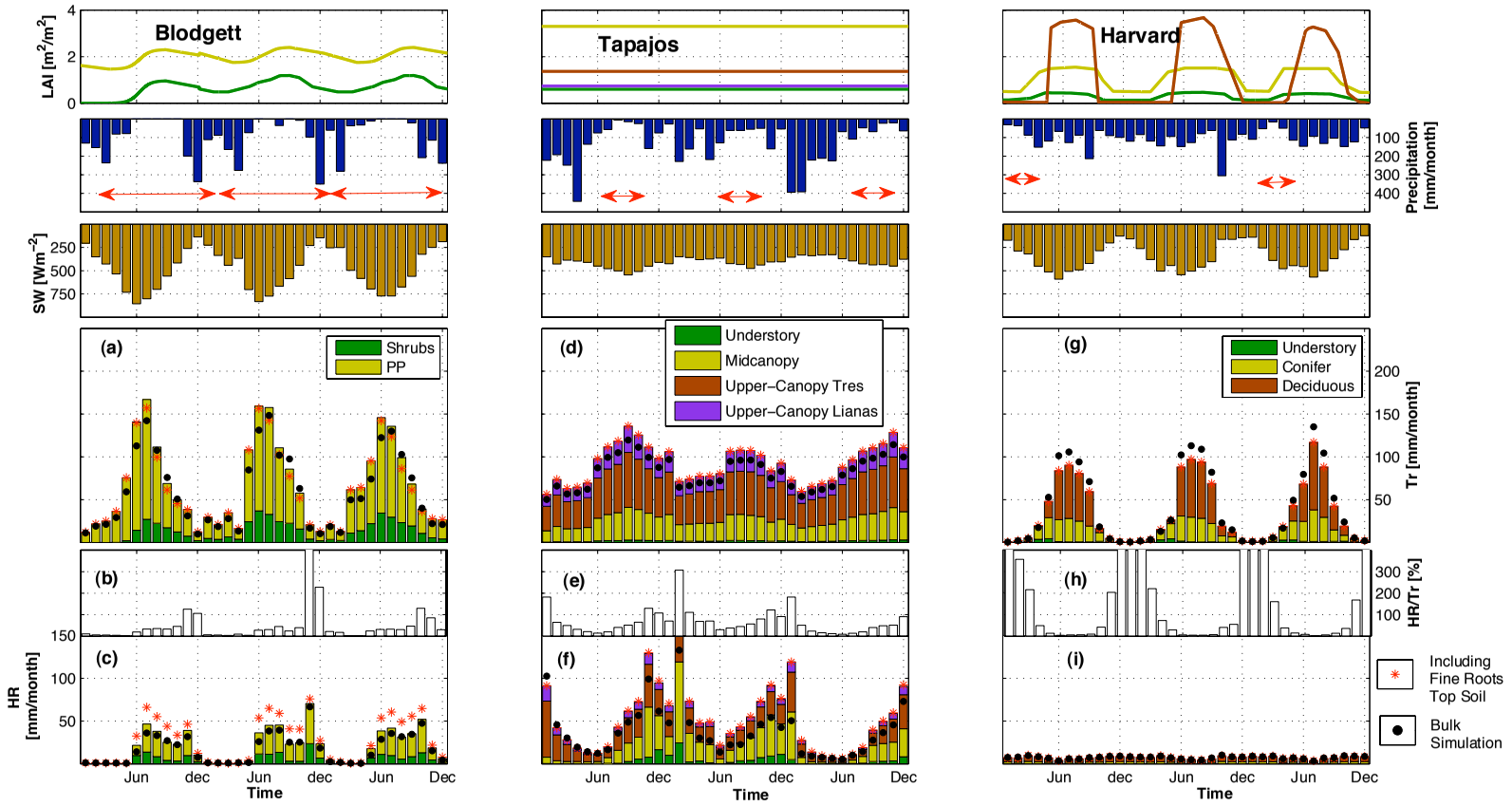

Figure 3.3: Monthly fluxes of water uptake in **(a,b,c)** Blodgett, **(d,e,f)** Tapajós, and **(g,h,i)** Harvard Forest during the period of simulation. The top panels show the leaf area index, precipitation, and incoming shortwave radiation, respectively. The fourth panel displays (a,d,g) the fluxes of transpiration. The fifth panel shows the ratio of (b,e,h) hydraulic redistribution to transpiration, and the sixth panel shows the (c,f,i) fluxes of hydraulic redistribution. The simulation results shown in this figure were computed with an specific hydraulic root axial conductivity of $K_{axs} = 10^{-}1[m^4 MPa^{-1}\ s^{-1}\ m^{-2}_{root,cs}]$ and root radial conductivity $K_{rad} = 10^{-7}[m^3\ MPa^{-1} s^{-1} m^{-2}_{root,sa}]$. The red arrows at the top panels represents the extent of the dry period.

Figure 3.3g shows the LE fluxes in Harvard Forest. The difference in LE fluxes bewteen Blodgett and Harvard Forest can be most clearly observed when Figure 3.3g is compared with Figure 3.3a. As expected, the LE fluxes are more prominent in the deciduous plants since their LAI is significantly higher. Also, the more homogeneous distribution of rainfall throughout the year in Harvard Forest can be observed in the top panel of Figure 3.3. Both the low transpirational fluxes and the lack of rainfall seasonality hinder HR fluxes in Harvard Forest. Figure 3.3i shows the HR fluxes in Harvard Forest. It can be seen that HR fluxes are negligible throughout the year with a mean daily value lower than 0.05 mm d^{-1}.

The rainfall seasonality enhances water potential gradients in the soil. However, the magnitude of transpiration is also an important factor that enhances soil water potential gradients and HR fluxes. Since transpiration is regulated by the incoming SW radiation, the seasonal distribution of SW radiation is an important climatic variable that affects the fluxes of HR. The role of incoming SW radiation on HR fluxes can be observed when Blodgett and Tapajós are compared. The incoming SW radiation at Tapajós allows for a more stable production of LE that induces higher fluxes of HR. This suggests that regardless of the amount of rainfall, a more seasonal distribution of SW radiation will enhance HR fluxes.

3.3.3 Strong Water Potential Gradients at the Surface

Previous numerical simulations have shown that during dry periods the water potential at the soil surface can become extremely low. Low water potential at the surface magnifies the gradient between the roots and the soil and therefore enhances HL fluxes. There is no resolved conclusion on how plant roots will react to this situation. Most experimental studies measure water potential or soil moisture by implementing thermocoupled psychrometers or soil water content sensors. However, the use of these sensors in locations close to the soil surface is unreliable because of high sensitivity to temperature. Although different corrections have been suggested [Brown and Bartos, 1982], still there is high uncertainty, and few studies have installed probes at shallower than 15 cm depths [Domec et al., 2010, Smart et al., 2005].

Numerical studies facing this issue have opted to not include the top layer of fine roots [Lee et al., 2005], assuming that fine roots in the top surface would die under extremely dry conditions. However, the available empirical information regarding the response of fine roots to dry conditions is still inconclusive. Some studies suggest that during dry conditions, fine roots could release moisture and HR could actually enhance the survival or prolong the life of roots [Espeleta et al., 2004, Valizadeh et al., 2003]. Although there is a not a clear

understanding of this process, the most plausible hypothesis is that a reduction of hydraulic conductivity between the soil and the roots is caused by many factors such as root shrinkage, curvature of water menisci, and high salt concentration which tends to reduce the rhizosphere conductivity [Vetterlein and Marschner, 1993].

Quijano et al. [2012] noted that the presence of a litter layer over the soil damps the radiative energy reaching the surface and reduces the water potential gradient. Litter layer over the soil are ubiquitous in natural ecosystems and likely play a role in the HR flux resultant. In this study, all simulations were performed with the presence of a litter layer of 3 cm over the soil column. This is a good estimate for all three ecosystems analyzed. In addition, the fine roots in the topmost layer of 2.5 cm are assumed dead following the same approach as previous models Lee et al. [2005].

To test this assumption, we perform a sensitivity analysis of the roots in the near surface. The red star symbols in Figures 3.3c,f and i show the total magnitude of HR if the fine roots in the top 2 cm of the soil are considered active. It can be observed that there is a strong impact at Blodgett. The presence of fine roots in this top layer would induce a higher HR flux during the summer period. High fluxes of SW combined with a lower LAI than Tapajós and Harvard Forest allow a significant amount of radiation to reach the soil surface and create a strong water potential gradient between the roots and the soil even in the presence of a litter layer [Quijano et al., 2012]. On the other hand the impact of active fine roots in the top 2.5 cm is negligible in Tapajós. In Tapajós, a high LAI damps the incoming energy. In addition, the incoming SW is distributed homogeneously throughout the year and never reaches the values experienced at Blodgett during the summer season. Therefore, the presence of a litter layer in Tapajós will be enough to avoid a strong release of water during dry periods. Similarly, the inclusion of fine roots in the top 2.5 cm in Harvard Forest does not induce a difference in HR fluxes. In Harvard Forest, the fluxes of HR are low, the LAI is high and the incoming SW radiation is damped by clouds during the summer season.

High HR fluxes in top soil layers may be underestimated. According to Quijano et al. [2012] HR can result in significant differences in carbon and nitrogen cycling. However, the simulations presented in this study show they become relevant only in ecosystems where strong radiative energy reaches the surface during dry periods.

3.3.4 Plant Species Composition

The presence of different coexisting and interacting species is ubiquitous in natural ecosystems. Inter-species interactions impacts the dynamics of water and energy. The inherent complexity of interactions poses a challenge in ecosystem analysis. In this study, we use PFTs as a proxy to species diversity. Although this assumption omits important species that are found in natural ecosystems, it is useful to simplify the problem and analyze how the presence of different plant groups with characteristic properties impacts the fluxes of mass and energy.

The simulation results displayed in Figure 3.3 are performed under the presence of several PFTs. The PFTs considered in each site were described in section 3.2.2. In order to observe the impact of the interaction between coexisting PFT, we perform additional simulations with a single compound species (bulk simulation) instead of individual PFTs. The bulk simulation is performed by adding the total LAI and considering the total basal area of the ecosystem as only one single species. This results in a unique PFT having the total LAI and root hydraulic conductivity capacities from all the PFTs combined. The distribution of below-ground roots and above-ground leaves in the bulk simulation is computed by performing a linear weighted average of the distribution present in each species. The linear weighted average is performed according to the respective LAI in each PFT. Figure 3.1 shows the distribution of roots and LAI used in the bulk simulation. Using the same approach, the photosynthetic parameters (V_{cmax} and J_{max}), the stomatal conductance parameters (g, m), and the response to dry conditions in the soil (s_f, Ψ_f) are averaged according to the LAI (see Appendix D, Tables 1 and 2).

Black circles in Figures 3.3 a,d and g represent the fluxes of transpiration obtained for the simulation performed with single compound species (bulk simulation). Note that transpirational fluxes under the bulk simulation (black points in Figure 3.3a,d an g) are different than the fluxes obtained when the simulations are performed with coexisting PFTs. This difference suggests that the coexistence of different PFTs and their interactions impact the ultimate transpirational fluxes. In Blodgett and Tapajós the presence of different PFTs results in a net higher transpiration flux from the ecosystem. In contrast in Harvard Forest the presence of different species decreases the fluxes of transpiration. In Harvard Forest the two most important PFTs considered (Deciduous and Evergreen) have the same root distributions while in Tapajós and Blodgett the PFTs have different root distributions. This suggests the presence of similar PFTs enhances the competitive dynamics and causes a reduction in transpiration.

Figures 3.3 c, f, and i show the HR fluxes at each site. The black circles in this figure shows the total HR that obtained under the bulk simulation. In Blodgett and Tapajós the bulk simulation results in higher HR fluxes. This difference is more prominent in Tapajós where the coexistence of several species results in significantly higher HR fluxes. According to these simulations, the coexistence of several PFTs with different structural properties enhances HR fluxes. During nighttime periods the fluxes of HR from one PFT can enhance the fluxes of HR in the other PFTs, generating a positive feedback.

In a multi-species ecosystem, different species interact to compete for and facilitate resources. It is important to quantify these interactions. Figure 3.4 shows the fluxes of HR and transpiration in Blodgett and Harvard under different overstory scenarios . The green bars show the fluxes in the understory if all the PFTs are present (the same as in Figure 3.3). The open bars show the fluxes in the understory if the overstory PFT were not present, and the red and blue circles show the fluxes in the understory if the overstory were present but unable perform HR.

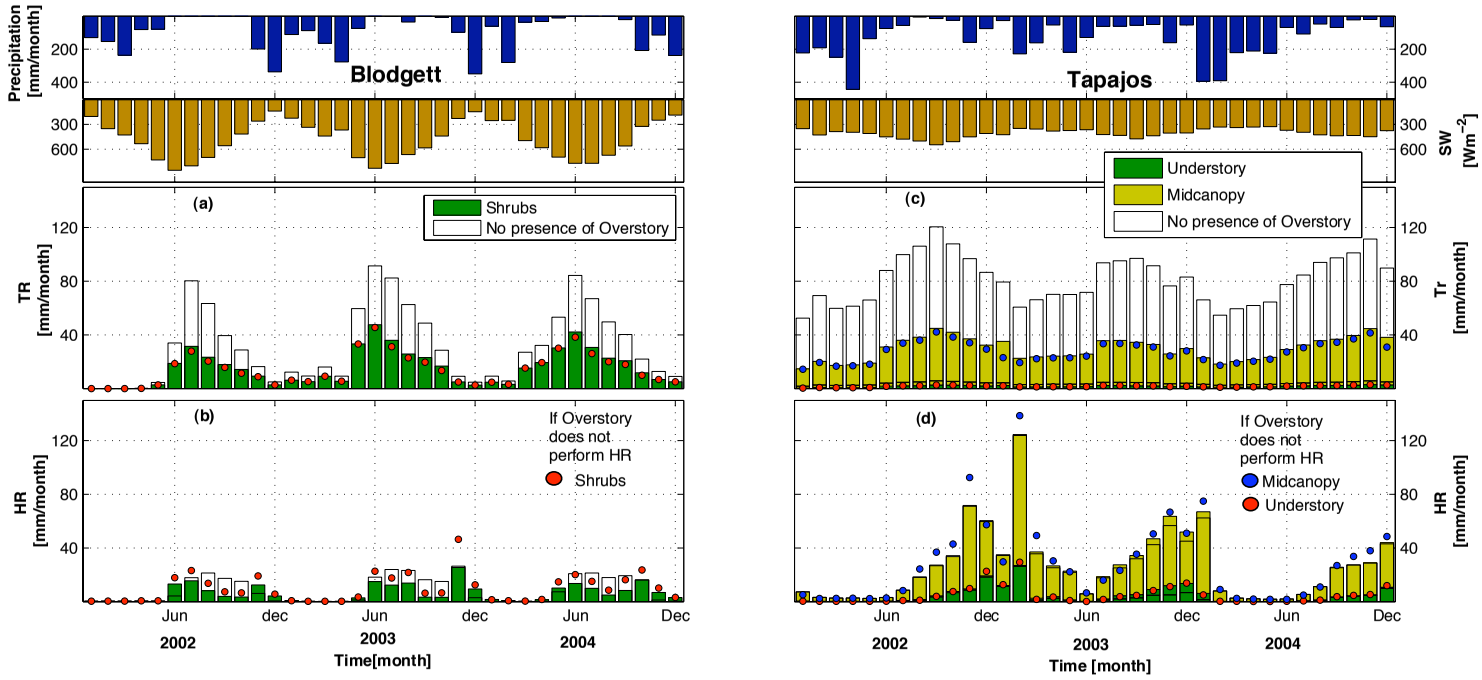

Figure 3.4: Effect on understory transpiration and HR fluxes if overstory species were unable to redistribute moisture by HR. Top plots show the patterns of rainfall and SW radiation during the years of simulation. The plots on the left shows the fluxes of **(a)** transpiration and **(b)** hydraulic redistribution Blodgett shrubs. The plots on the right shows the fluxes of **(c)** transpiration and **(d)** hydraulic redistribution in understory and midcanopy trees in Tapajós. The dashed bars show the fluxes if the overstory species were not present at all. All the the simulation results shown in this figure were computed with a specific hydraulic root axial conductivity of $K_{axs} = 10^{-}1[m^4MPa^{-1}\ s^{-1}\ m^{-2}_{root,cs}]$ and root radial conductivity $K_{rad} = 10^{-7}[m^3\ MPa^{-1}s^{-1}m^{-2}_{root,sa}]$

As expected, the absence of overstory PFTs induces a much larger transpirational flux from the understory. This occurs because there is a higher flux of incoming SW radiation to the understory and because the absence of overstory species allows understory to more freely use the water resources from the soil. In the end, the absence of overstory enhances productivity in the understory (not shown). This outcome is expected and has been observed in experimental studies such as Ludwig et al. [2004] over wooded savanna ecosystems composed of trees and grasses.

The most relevant scientific question is not whether the presence or absence of overstory enhances the understory productivity species since is evident that absence of overstory species results in more availability of resources to understory species. Instead, the more important question is whether mechanisms such as HR enhance the dynamics of these species when they coexist. Overstory species facilitate moisture through HR to the understory. During dry periods this facilitation can enhance transpiration and productivity in the understory. Figures 3.4a and c show that absence of HR in the overstory may result in higher transpirational fluxes in the understory during the dry season and a facilitation in productivity (not shown). This phenomenon was reported in Quijano et al. [2012] and is regulated by the root depth of understory species. Enhancement through HR is expected to be higher under severe droughts during which availability of moisture in shallower layers is scarce.

Note that absence of HR in the overstory species results in higher fluxes of HR by the understory (red and blue circles, Figures 3.4b and d). When overstory species redistribute moisture through HR, the gradients in water potential in shallower layers are reduced. This reduction hinders the HR flux by understory species. Conversely, in the absence of HR from the overstory, the gradients in water potential along the understory roots are higher, and therefore, understory HR is enhanced.

3.3.5 Root Hydraulic Conductivities

The capacity of roots to uptake and transport moisture is a main factor that impacts several ecohydrological processes. Different physiological properties influence the ability of roots to transport moisture. In this study and other modeling and experimental approaches [Amenu and Kumar, 2008, Huang and Nobel, 1994, Mendel et al., 2002] these properties are incorporated in terms of radial and axial conductivities that represent the ability of roots to uptake and transport water, respectively. In this study we calculate the entire root system capacity to uptake and transport moisture using available measurements of root specific hydraulic

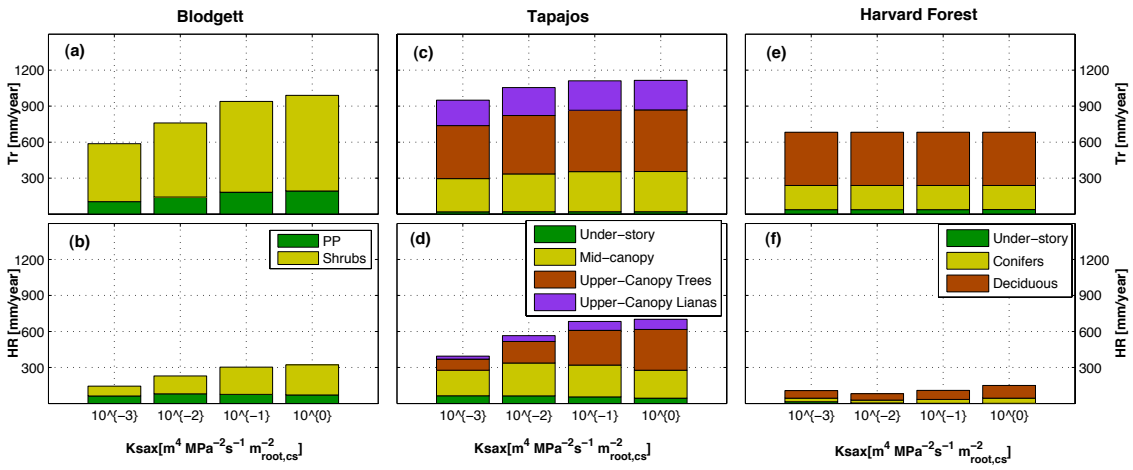

Figure 3.5: Effect of specific root axial hydraulic conductivity on the fluxes of transpiration and hydraulic redistribution.

conductivities (conductivities per unit root area) that have been determined for isolated roots and scaled here to the entire root system. We assume that all the roots and all the PFTs in the ecoystem have the same specific conductivities. In this section we explore the role of these conductivities in regulating the fluxes of water.

Specific Root Axial Conductivity

Figure 3.5 shows the influence of the specific root axial conductivity K_{sax} on the water fluxes for each site. As expected the conductivities influence transpiration fluxes. However, the impact varies in each site. In Blodgett the influence of K_{sax} is stronger than in Tapajós and Harvard Forest. Blodgett experiences a mediterranean climate, so the role of deep roots is critical during the summer period. Although Tapajós also relies on deep roots and the moisture transport by the roots is important, transpiration fluxes are more homogeneously distributed throughout the year. In addition, the dry period is not as strong as that of Blodgett. Therefore, the impact of K_{sax} is weaker in Tapajós compared to Blodgett (Figures 3.5 a,c). In Harvard Forest the effect of K_{sax} is negligible (Figures 3.5 c). In Harvard Forest, rainfall is more evenly distributed during the year and the transpirational fluxes are lower. These patterns result in a lower dependency of K_{sax} on transpiration.

A similar pattern is observed for HR fluxes. In Tapajós and Harvard Forest, the fluxes of HR are reduced for decreased K_{sax}. However, in Harvard Forest the reduction of K_{sax} may induce a slight increment in HR fluxes (Figure 3.5f). Low values of K_{sax} in Harvard Forest enhance the gradients in water potential because water uptake preferentially occurs

at shallower layers, increasing the water potential gradient in the soil.

Although the effect of K_{sax} on transpiration and HR is similar, there are some relevant differences in the main patterns that should be noted. Reduction of K_{sax} in Tapajós and Blodgett results in lower fluxes of both transpiration and HR. However, the impact on HR is more prominent (Figures 3.5 a,b). In addition, the impact of K_{sax} on transpiration follows the same pattern in all the PFTs while the impact on HR fluxes is stronger for the deep rooted PFT (Compare the reduction in each PFT between Figures 3.5 a,c and Figures 3.5 b,d). In Harvard Forest the effect of K_{sax} is only evident in the HR fluxes (Figure 3.5 e,f), since it does not affect the transpiration values.

Specific Root Radial Conductivity

Figure 3.6 shows the effect of the specific root radial conductivity on transpiration and HR. The pattern observed at all the three sites is consistent. Reduction of K_{srad} decreases transpiration and HR fluxes. Similar to the effect of reducing K_{sax}, the effect of reducing K_{srad} is significantly more prominent in HR fluxes than transpiration. For instance, note that reduction in K_{srad} from 10^{-7} to 10^{-8} $[m^3_{H2O}MPa^{-1}s^{-1}m^{-2}_{root,sa}]$ considerably reduces the fluxes of HR (Figures 3.6b,d) but it does not cause a strong reduction of transpirational fluxes (Figures 3.6a,c).

The differences between HR and transpiration are even more noticeable as K_{srad} increases. There is a threshold at which transpiration reaches a peak and incrementally increasing K_{srad} ceases to increase transpiration. At this point transpiration is not water limited. Instead other variables such as energy, or physiological controls such as stomatal conductance limit the transpirational fluxes. In contrast to the effect of K_{srad} on transpiration, increments in K_{srad} are always associated to higher HR fluxes even at very high values of K_{srad}. Furthermore, this phenomenon also occurs in Harvard Forest where the gradients in water potential in the soil are not as prominent. In Harvard Forest, HR fluxes increases significantly when K_{srad} values are equal to 10^{-8} $[m^3_{H2O}MPa^{-1}s^{-1}m^{-2}_{root,sa}]$.

Prominent HR fluxes induced by high conductivity values are only evident in the radial case (K_{srad}). It seems that at high values of both radial and axial conductivities, the former is the limiting factor regulating the fluxes of HR.

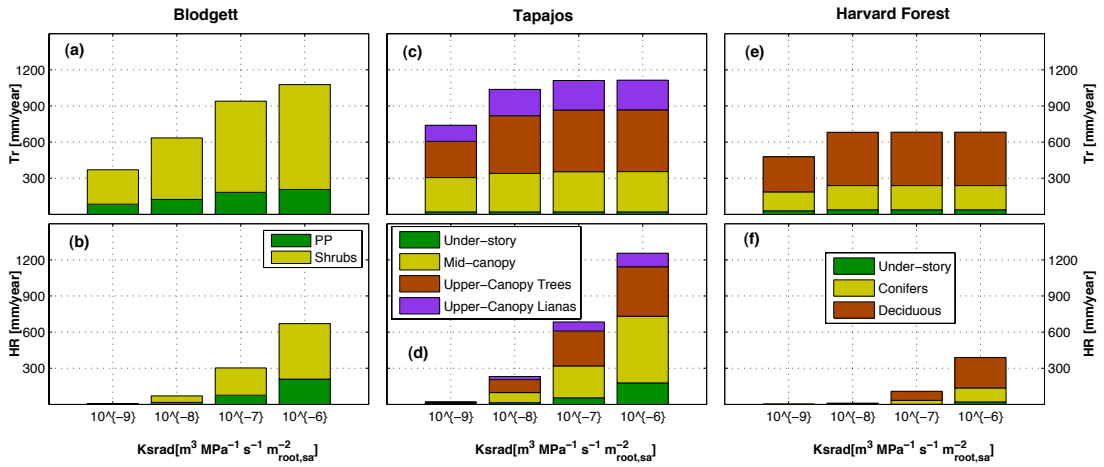

Figure 3.6: Effect of specific root radial hydraulic conductivity on the fluxes of transpiration and hydraulic redistribution

3.3.6 Amount of Precipitation

Precipitation is by far the most important flux of water to ecosystems and therefore is likely an important factor that influences transpiration and HR. In this section, we discuss a sensitivity analysis of precipitation amount on water fluxes. We perform numerical simulations using different values of mean annual precipitation. Each simulation is performed over 10 years. Inter-annual and intra-annual precipitation dynamics where made proportional to those observed in the Ameriflux towers but they were scaled to match the desired mean precipitation. Since fewer than 10 years of data were available at Tapajós, we repeat sequences to obtain 10 years of data. Although the amount of precipitation would impact productivity, ecosystem dynamics, and LAI, it is challenging to predict the LAI for each precipitation condition. Therefore, we assume the current LAI (Figure 3.3) for all the precipitation scenarios and analyze the impact of precipitation under such LAI.

Water availability limits productivity in several ecosystems around the world [Fay, 2009]. In these cases, transpiration is regulated by precipitation. In energy limited ecosystems, productivity is not limited by water availability and increments in precipitation will not result in higher transpirational fluxes. This behavior can be observed in Figures 3.7 a,c, and f. In these figures, transpiration increases with precipitation. However, there exists a point where the system is no longer water limited and further increments in precipitation do not cause increments in transpiration.

The role of precipitation on HR is unknown. According to Neumann and Cardon [2012]

HR has been reported for different ranges of precipitation and there is no direct relationship between the magnitude of HR fluxes and annual precipitation. Figures 3.7 b,d, and e show the fluxes of total annual HR for different values of mean annual precipitation. It is possible to recognize a bell shape pattern where HR peakes at a particular value of mean annual precipitation. At low precipitation, the availability of water reduces and HR flux decreases. At high precipitation values, the magnitude of HR is also reduced. High precipitation creates an excess of moisture that reduces water potential gradients in the soil, causing a reduction of HR. At both very high and very low precipitation, HR converges to zero.

According to Figures 3.7b,d, and f, the highest fluxes of HR under a given LAI occur at a precipitation value below that at which the maximum transpiration is reached (Figures 3.7 b,d, and f). This pattern is present in all three sites analyzed in this study. However, different mean annual precipitations may induce differences in the vegetation structure (LAI, K_{srad} and K_{sax}) and function which is not considered here and may affect the results shown in Figure 3.7.

3.4 Summary and Discussion

We examined the role of climate in HR fluxes though analysis of three ecosystems that exhibit different climatic conditions and vegetation composition. The simulations show that seasonality in precipitation and incoming SW radiation (effect on transpiration) are the most relevant variables that regulate the gradients in water potential in the soil. According to the simulations, the interplay between these two variables impacts the magnitude of HR fluxes. The model shows significant differences in the HR fluxes between the three sites. Specifically, in Harvard Forest the fluxes were much lower due to an homogeneous distribution of rainfall throughout the year. The HR fluxes in Blodgett and Tapajós also showed a significant variation throughout the year following the rainfall seasonality and transpirational fluxes.

The simulations performed in this study included different coexisting PFTs. However, we also run the simulations with a single bulk PFT generated by the combinations of all PFTs. The bulk simulation was performed using a linear weighted average of the parameters of each species and adding the LAI and basal area. The results obtained from the bulk simulation demonstrate different transpirational fluxes than the simulations performed in the presence of several PFTs. These results suggest the role that plant species composition may play in transpirational fluxes. There could be a set of parameters for a bulk simulation that matches the transpirational fluxes of different species. However, it is not a simple weighted averaged.

Additionally, the presence of different PFTs results in higher fluxes of HR than the bulk simulation. Different PFTs redistributing moisture simultaneously enhances the fluxes of HR. We believe that such dynamics could be relevant in the simulation of ecohydrological processes.

In this study we analyze the effect of specific root hydraulic conductivities on the fluxes of HR and transpiration. We explore different magnitudes of specific root radial conductivities K_{sax} and specific root axial conductivities K_{srad}. The simulation results show that both conductivities impact the fluxes of transpiration and HR. However, HR was more sensitive to these conductivities than transpiration. Specifically HR was strongly influenced by K_{srad}. At high values of K_{srad}, incremental increases in K_{srad} result in higher fluxes of HR, but not of transpiration. Therefore the values of K_{srad} (also K_{sax}) selected for the simulations may significantly impact the fluxes of HR. Similar parameters to K_{srad} and K_{sax} can be found in other models. For instance in the model developed by Ryel et al. [2002], the radial flow is controlled by the maximum radial conductance C_{RT} and a parameter c that reduces this conductance based on specific conditions. The computation of such conductivities regulates the net flux of HR. The discrepancy between models and experiments in the HR flux can be attributed to this conductivities. In this study we compute conductivities by performing a bottom-up scaling from isolated root measurements. However, more reliable estimates of root conductivities must be developed in coming years to capture more realistic patterns of HR fluxes with modeling.

Although the seasonal pattern of precipitation impacts the HR fluxes, the impact of mean annual precipitation on HR was unclear. We analyzed the response of HR under different mean annual precipitation values. We found that mean annual precipitation does affect HR. However, the pattern is different than the pattern observed for transpiration. The response of HR to different mean precipitation levels is a bell shape with the tails approaching zero at extremely high or extremely low mean annual precipitation. HR reaches a peak at a precipitation level between these values. However, this HR peak does not match the point of maximum transpiration. In addition, the pattern observed is different for transpiration. Instead of a bell curve transpiration is asymptotically increasing. Our analyses of conductivities and mean annual precipitation suggest that transpirational fluxes and HR are not directly correlated and increase (decrease) transpiration does not necessarily imply an increase (decrease) in HR [Neumann and Cardon, 2012].

In this study, we attempted to examine different factors that influence transpiration and HR fluxes. We considered climate, plant species composition, and root conductivities. We

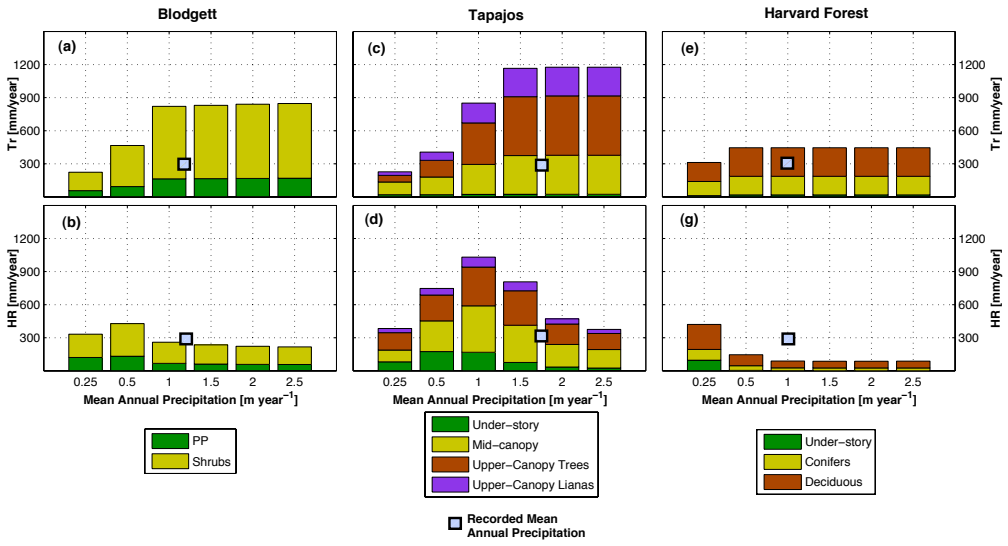

Figure 3.7: Effect of mean annual precipitation on the fluxes of transpiration and hydraulic redistribution

selected three different Ameriflux sites under natural forest that are exposed to different climatic conditions. Although our simulations are controlled by parameters that may be subjective, we made an effort to gather all the available information from previous experimental studies at these Ameriflux Sites. In addition we calculated the root hydraulic conductivities using a bottom up approach with clear assumptions and applied the same criteria to all the sites and PFTs. Therefore, we believe that the results from this study provide important insights into factors that regulate the fluxes of transpiration and HR in natural ecosystems.

CHAPTER 4

Passive Regulation of Soil Biogeochemical Cycling by Root Water Transport

4.1 Introduction

[1] Plant root systems provide the pathway for moisture uptake required by above-ground vegetation, and therefore are a critical component of the terrestrial hydrologic cycle. In addition to water uptake, the ability of plant roots to passively transport moisture throughout the soil column following water potential gradients has been widely observed and is generally referred to as *Hydraulic Redistribution* (HR) [Amenu and Kumar, 2008, Burgess et al., 1998, 2001, 2000, Quijano et al., 2012]. Three main types of redistribution have been observed: (i) hydraulic lift (HL) where water is transported upward from wet deep to dry shallow layers [Dawson, 1993, Espeleta et al., 2004, Ishikawa and Bledsoe, 2000, Ludwig et al., 2003], (ii) hydraulic descent (HD) where water is transported downward from shallow wet layers to deep dry layers [Burgess et al., 1998, Hultine et al., 2003, Schulze et al., 1998, Smith et al., 1999], and (iii) lateral redistribution (LD) where water is transported horizontally from patches of wet to dry soil [Brooks et al., 2002, 2006, Nadezhdina et al., 2010]. The importance of characteristics such as root biomass distribution, and associated processes such as HR in subsurface moisture dynamics has led to several studies that have analyzed the role of plant roots in regulating soil-moisture patterns and associated impacts on vegetation water and energy balances as well as ecosystem productivity [Amenu and Kumar, 2008, Brooks et al., 2002, Quijano et al., 2012, Ryel et al., 2002, Scott et al., 2008]. However, the potential influence of HR on below-ground biogeochemical cycling of carbon and nitrogen has been suggested [Caldwell et al., 1998, Caldwell and Richards, 1989, Dawson, 1993, Hawkins et al., 2009, Horton and Hart, 1998, Jackson et al., 2000, Liste and White, 2008, Richrads and Caldwell, 1987] and is the focus of the present work using a modeling approach.

Water uptake and HR regulate the distribution of soil-moisture at the ground surface,

[1]This chapter is under review as: Quijano, J.C., P. Kumar, D. Drewry. Passive regulation of soil biogeochemical cycling by root water uptake. *Water Resources Research,* submitted February 2013

influencing the release of latent heat from the soil (soil evaporation) [Quijano et al., 2012], and the surface energy balance. As a result, the input of heat into the ground and the near surface soil-temperature is also regulated by root functioning. Soil- moisture and temperature affect the biochemical reactions and microbial activity in the soil [Kieft et al., 1993, Lundquist et al., 1999, Sylvia et al., 2005, Zogg et al., 1997], influencing processes such as decomposition of organic matter and nutrient mineralization [Kätterer et al., 1998, Manzoni and Porporato, 2009]. On the other hand the availability of soil moisture impacts the transport of ions in the subsurface. Higher soil moisture enhances diffusion of ions in the soil [Caldwell and Manwaring, 1994, Nye and Tinker, 1977], and soil moisture fluxes induced by gradients in water potential can carry soluble ions such as nitrate (NO_3^-) and dissolved organic carbon. Furthermore the redistribution of moisture to dry layers can increase the life span of fine roots [Caldwell et al., 1998, Matzner and Richards, 1996] extending the period of plant nutrient uptake during dry seasons.

de Kroon et al. [1998] observed NO_3^- translocation by the root systems of *carex flacca*. Nitrate translocation was more prominent where the NO_3^- concentration gradient and water potential gradient were in the same direction. McCulley et al. [2004] observed a high availability of several nutrients (particularly P, Ca^{2+}, Mg^{2+}) at deeper layers which explain the presence of deep roots in arid and semiarid ecosystems and propose HD as a mechanism that facilitates the formation of this pool. Aanderud and Richards [2009] studied the role of HR in decomposition rates in a field experiment with two different shrub species, *Artemisia* and *Sarcobatus*. They observed higher decomposition rates under the presence of HR. In a recent experiment with Buffalo grass, Armas et al. [2011] observed higher rates of organic matter decomposition and mineralization of nitrogen in the presence of HL. They also observed that the presence of HL enhanced plant nitrogen uptake.

Other experimental studies have shown indirect influence of HR by its capacity to prolong root and microbial activity. Matzner and Richards [1996] ran an experiment with *Artemisia tridentata* to analyze the role of HL in enhancing phosphorus and nitrogen uptake. They found that HL plays an important role because it maintains higher levels of soil water potential enhancing root longevity. The influence of HL to increase root longevity during dry periods, together with the capacity of *Artemisia tridentata* to uptake nutrients under low water potentials, allow this species to sustain a stable uptake of phosphorus and nitrogen during the dry period. Querejeta et al. [2007, 2003] and Egerton-Warburton et al. [2008] observed that the presence of HL enhances mycorrhiza fungi function during dry periods. Egerton-Warburton et al. [2008] observed that efflux of HL from mycorrhizal hyphae in

seedlings of *Quercus agrigolia* enhanced soil processes such as bacterial growth and soil enzyme activity. In a field experiment with Ponderosa Pine, common mycorrhizal networks connecting different plants were found to transport HL water, enhancing the survival of shallow rooted plants during drought Warren et al. [2008].

In this study, we use a detailed muti-species process-based numerical model of the coupled canopy-root-soil systems [Quijano et al., 2012] to examine the interplay between HR and multiple plant species that coexist, and analyze how this interplay influence the carbon and nitrogen dynamics throughout the vertical soil column. Specifically, we address the following questions: (i) What is the influence of HR on soil carbon decomposition and how does it influences the long term concentration and distribution of carbon in the soil column? (ii) How does the presence of different species composition influence the impact of HR on the carbon dynamics? (iii) what is the influence of HR on the the long term concentration, distribution, and fluxes of mineral nitrogen (nitrate NO_3^- and ammonium NH_4^+) in the soil column? and (iv) how does the presence of multiple vegetation species composition influence the impact of HR on the nitrogen dynamics? A list of all symbols used is included in the Appendix E.1.

4.2 Methods

4.2.1 Model Formulation

In order to capture the interactions between different plant species that coexist we use a multi-species model presented in Quijano et al. [2012] which was an extension of the multi-layer canopy-root-soil system model (MLCan) presented in Drewry et al. [2010a,b]. In this study we further extend this multi-species model to include carbon and nitrogen dynamics drawing upon and extending the framework initially proposed by Porporato et al. [2003], see also [D'Odorico et al., 2003, Manzoni and Porporato, 2007]. The multi-species model simulates the ecohydrological dynamics in the presence of several vegetation species that share common resources such as below-ground soil-moisture or above-ground incident radiation. Co-existing species can have different ecophysiological and structural features that result in different abilities to exploit the common resource.

Above-ground, the model solves the longwave and shortwave radiation regimes for each layer of the canopy using a compound leaf area distribution (LAD). The compound LAD is

computed as a linear sum of the LAD of each vegetation species in each layer. The absorbed radiation for each species is then computed as the fraction that species contributes to the compound LAD at each layer. The model then solves the energy balance for all the different canopy layers for each species independently as a function of this absorbed energy. Through this approach the model is able to predict photosynthetic carbon uptake, and latent and sensible heat exchange with the atmosphere for each of the species considered.

Below-ground each species can exploit different parts of the soil column as a function of their unique rooting depths and root biomass distributions. Hydraulic redistribution is represented using a coupled set of differential equations [Amenu and Kumar, 2008] that describes moisture flow through the root system as a function of uptake capacity and potential gradients in the coupled soil-plant system. This framework allows us to simulate the presence of different species sharing the same soil column, effectively allowing for competitive or mutualistic interactions. The model simulates the effect of dry conditions in water uptake and water release (HR) by reducing the radial conductivity of the root system. This reduction is simulated by the implementation of a fine root conductivity loss function (FRCL) (Appendix E Section 1). We believe that this model, therefore, provides an effective tool with which to analyze the hydrological controls on sub-surface carbon and nitrogen dynamics when more than one species coexist and share resources.

The C-N model simulates the main processes that control the carbon and nitrogen dynamics in the soil, such as decomposition, mineralization, immobilization, nitrification, water uptake and leaching using equations based on mass balance and C:N ratios [Manzoni and Porporato, 2007, Porporato et al., 2003]. In this study we extend this initial framework to include multiple soil layers, the effect of soil temperature on decomposition and the vertical flux of carbon from bioturbation. Figure 4.1 shows a schematic representation of this model which includes the coupling between the multi-species MLCan and the C-N model. In this approach roots from different plant species share both soil-moisture and soil mineral nitrogen (NO_3^- and NH_4^+) resources. This approach captures both facilitative and competitive interactions between plant species as influenced by HR.

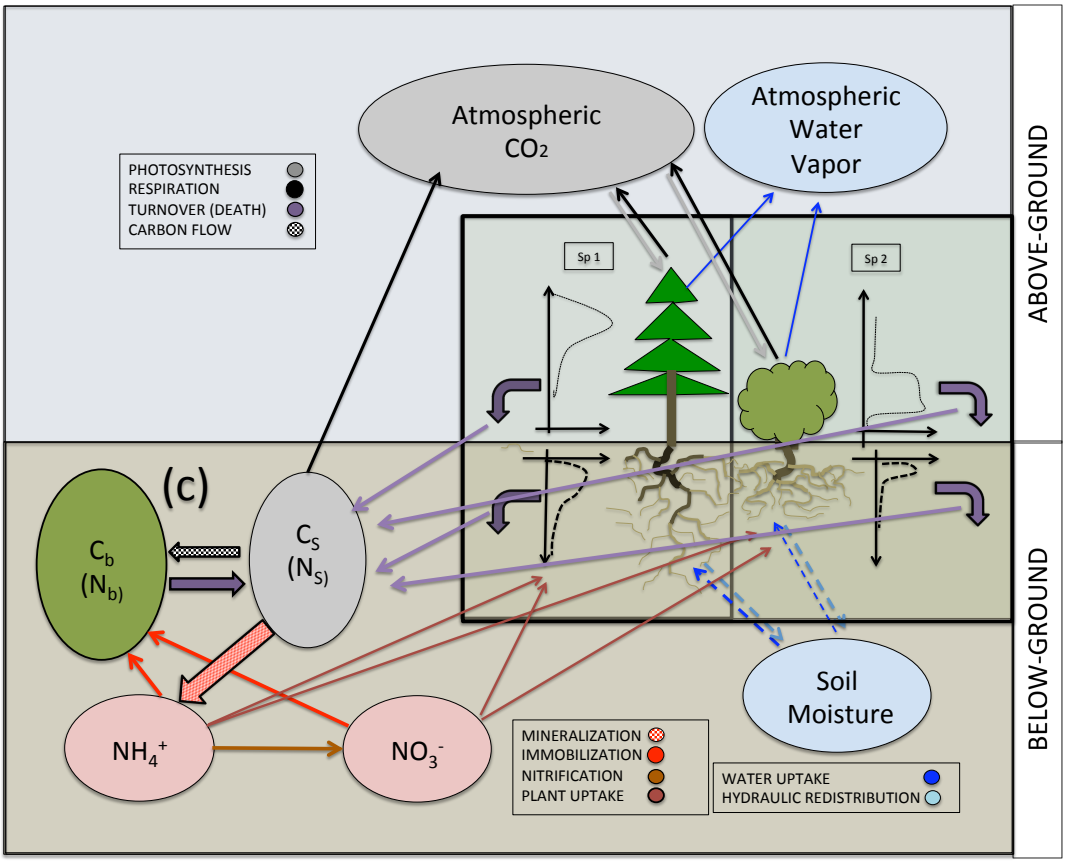

Figure 4.1: Schematic representation of the coupling between the multi-species MLCan model and the C:N model. Above-ground the radiative energy coming from the sun is absorbed by each species according to their leaf area distributions. In addition, each species has different eco-physiological properties resulting in distinct transpiration fluxes. Below-ground the same pools of water and mineral nitrogen are shared by all the species. The uptake of water and mineral nitrogen in the soil is computed independently for each species as a function of the distribution of fine roots.

The bioturbation model allows for the transport of organic matter from the litter layer to horizon O and deeper horizons in the soil column. This is simulated using a diffusive process where the flux of organic carbon is proportional to the vertical carbon concentration gradient [Braakhekke et al., 2011, Dam et al., 1997, Elzein and Balesdent, 1995, Kaste et al., 2007]. Figure 1 in the Appendix E shows a schematic representation of the vertical carbon fluxes in the soil system, including bioturbation and the model equations are given in Appendix E (Section 2).

4.2.2 Simulation Scenarios

The simulations are run with data from Blodgett Forrest Research Station and Blodgett Ameriflux site located in the Sierra Nevada near Georgetown, California. This site is characterized by wet winters and dry summers, typical of a Mediterranean climate. More details of site characteristics and Ameriflux data are presented in Fisher et al. [2005], Goldstein et al. [2000], Panek [2004], Quijano et al. [2012], Xu and Qi [2001] and Misson et al. [2004, 2006]. Although there is evidence that natural vegetation at this location is composed of a variety of understory and overstory species [Fisher et al., 2005, Stephens and Moghaddas, 2005], for the simulations performed in this study we only consider the most dominant vegetation types: (i) *Pinus Ponderosa* (hereafter PP) and (ii) understory shrubs (herafter shrubs) which are composed by two dominant species *Arctostaphylos manzanita* (hereafter manzanita) and *Ceanothus Cordulatus* (hereafter ceanothus).

To test the hypothesis that HR will result in differences in soil carbon and nitrogen cycling, and therefore modify the long-term accumulation of organic and mineral pools, we perform simulations for 500 years and analyze the equilibrium dynamics of soil hydrological and biogeochemical processes. The four different scenarios considered in this study are **(I)** Presence of PP and shrubs with HR, **(II)** Presence of PP and shrubs without HR, **(III)** Presence of only PP with HR, and **(IV)** Presence of only PP without HR.

4.2.3 Data Description

Since Ameriflux data is available for only a limited period (2000-2006) and the carbon and nitrogen dynamics evolve over a much longer time scale, the forcing used in our study is derived from a stochastic weather generator [Ivanov et al., 2007] parameterized using the observed Ameriflux data.

Figure 4.2 shows the ensemble of 500 unique years of daily rainfall, annual cumulative rainfall, daily air temperature, daily global radiation, and daily incoming longwave radiation. The mediterranean climate at this site is characterized by the out-of-phase rainfall and global radiation (also air temperature) throughout the year. The weather generation is performed for each year independently and does not consider inter-annual correlation. The same ensemble (and sequence) of atmospheric forcing (shown in Figure 4.2) is used for the simulations performed for all four scenarios.

Other variables needed to run the model include species composition, leaf area index (LAI), foliage specific carbon leaf area index (SCLA), foliar C:N ratios, and ecohydrological

parameters. These variables were assumed to exhibit the same intra-annual behavior for all the years of simulation. Within the year variability of these parameters were obtained from measurements made at the Blodgett Forest. In addition we also assume that the soil structure (thickness of the different horizons) remains constant in time.

Table D.2 displays a list of the most relevant parameters and the values implemented in this study. The details of the input data used in this model are briefly presented below.

LAI: Figure 4.3a shows the seasonal dynamics of PP and shrub LAI. LAI was constructed using previous studies and available measurements that have been collected at the Blodgett site [Bouvier-Brown, 2008, Goldstein et al., 2000, Misson et al., 2005].

C:N ratios: The foliage C:N ratio varies seasonally throughout the year. Figure 4.3b shows the seasonal dynamics of the C:N ratio of the foliage for each species considered [Misson et al., 2005]. Ceanothus has the smallest C:N ratio because of its symbiotic fixation of nitrogen [Misson et al., 2005]. The C:N ratio in PP and manzanita are similar in magnitude but out of phase. The C:N ratio for manzanita and ceanothus is weighted using the corresponding LAI to calculate the net shrubs C:N ratio. We assume that the fine root C:N ratio is the same as that of the the foliage. Figure 4.3b also shows the critical C:N ratio, $(\mathrm{C{:}N})_{\mathrm{cr}}$, which is the maximum C:N ratio required in the organic matter at which microorganisms can sustain decomposition without immobilizing mineral nitrogen from the soil and is defined as the ratio between the C:N ratio in the microbial pool, $(\mathrm{C{:}N_b})$, and the fraction of decomposed organic matter that goes into respiration, r_r $\left((\mathrm{C{:}N})_{\mathrm{cr}} = (\mathrm{C:N})_{\mathrm{b}}/r_{\mathrm{r}}\right)$ [Manzoni and Porporato, 2007]. It can be observed that for half of the year the foliage C:N ratio of PP is observed to be below $(\mathrm{C{:}N})_{\mathrm{cr}}$. However the C:N in the soil is lower than the $(\mathrm{C{:}N})_{\mathrm{cr}}$ for the entire year and, therefore, the system is under a net mineralization regime throughout the year.

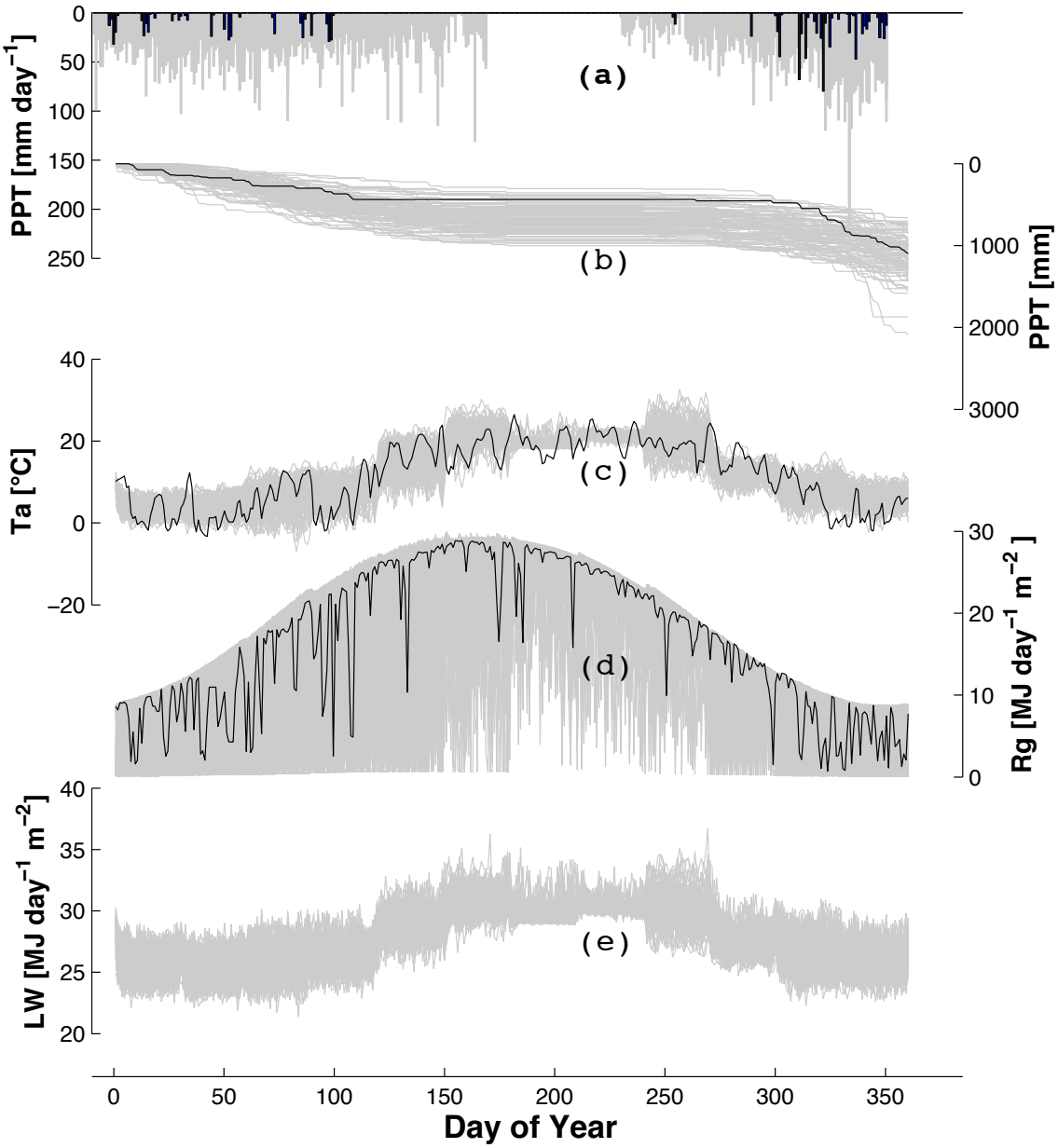

Figure 4.2: Annual time series of atmospheric variables used to force MLCan eco-hydrological model used to conduct the simulations. Variables including daily precipitation (a), annual cumulated precipitation (b), air temperature (c), global radiation (d) and incoming long-wave radiation (e) were stochastically generated. Each figure displays an ensemble of 500 years of generated data. The realization in black corresponds to the observed variables at the Blodgett Ameriflux site in year 2001.

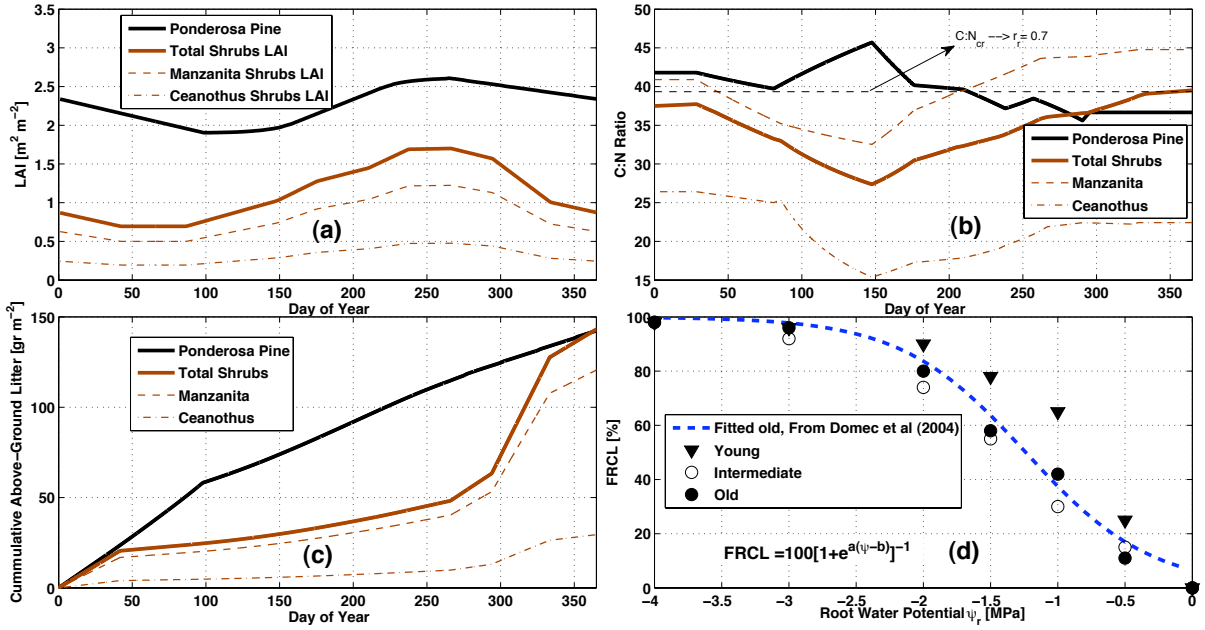

Figure 4.3: Annual time series of biogeochemical variables observed in Blodgett Forest such as **(a)** leaf area index (LAI), **(b)** C:N foliar ratio and **(c)** annual cumulative above-ground input of carbon to the soil (Appendix E, Section 3). This information is used to forced the biogeochemical C:N model. In this study we assume that the time series of LAI, plant C:N ratios and carbon input in the soil is the same for all the simulated years. This figure shows the time series for manzanita and ceanothus shrubs individually. However the simulations are performed considering all the shrubs as a one group where manzanita and ceanothus are integrated by using a representative set of parameters and a combined LAI. Panel **(d)** shows the fine root conductivity loss (FRCL) function for different ages of PP trees according to Domec et al. [2004]. In this study we use the fitted line for old trees that is displayed. FRCL of 100 % corresponds to no loss in conductivity.

Carbon Input: Figure 4.3c shows the annual cumulative input of organic carbon to the soil from above-ground foliage deposition. These values are calculated using the available information on seasonal variation of LAI (Figure 4.3a), specific carbon leaf area (SCLA) [Misson et al., 2006], and foliar C:N ratios in PP and shrubs (Figure 4.3b). The equations used to compute the above-ground loss of foliage are given in Appendix E (Section 3).

Soil Horizon Structure: Black and Harden [1995] analyzed the organic matter composition and thickness of the litter layer and horizons O, A1 and A2 for ecosystems with different ages at the Blodgett Forest site. As expected the soil structure changes with time in Blodgett. The main difference is observed in the thickness of the litter layer and the thickness of the organic horizon. We use a representative structure with a litter layer of 4 cm and a organic horizon of 2 cm that are fixed in time. This structure represents an old

growth ecosystem (Black and Harden [1995]).

Fine Roots Near the Surface: The presence of fine roots in the near surface zone is a critical variable that impacts the energy and water balance at the surface [Quijano et al., 2012]. Previous studies at Blodgett reported no evidence of fine roots in the litter layer and organic horizon [Walker et al., 2010]. Thus, in the simulations performed in this study we assume absence of fine roots in either of these two layers. Walker et al. [2010] reported the presence of fine roots in horizon A at Blodgett. However the dry conditions during the summer could trigger death of fine roots located in horizon A, which could be a mechanism to reduce the hydraulic conductivity with the soil and avoid the loss of water to soil evaporation [Espeleta et al., 2004, Quijano et al., 2012]. We simulate the response of fine roots to dry conditions using a function that considers fine root conductivity loss (FRCL), Figure 4.3d, Appendix E, Section 1). The same FRCL function was implemented for both PP and shrubs.

Initial Conditions for carbon and nitrogen pools: The initial concentrations of carbon in the organic matter pool (C_s) and the microbial biomass pool (C_b) were established according to available information observed and reconstructed in Blodgett Forest for the entire soil column (Appendix E, Section 4). Figure (4.4) shows the Blodgett Forest observations [Bird and Torn, 2006, Black and Harden, 1995] and the profiles reconstructed using an exponential model for vertical variation based on available data from other locations [Fierer et al., 2003, Jobbágy and Jackson, 2000]. Due to high uncertainty in the available records of NO_3^- and NH_4^+ at Blodgett we decided to set the initial concentrations in these pools to zero and perform the analysis once these pools reach equilibrium.

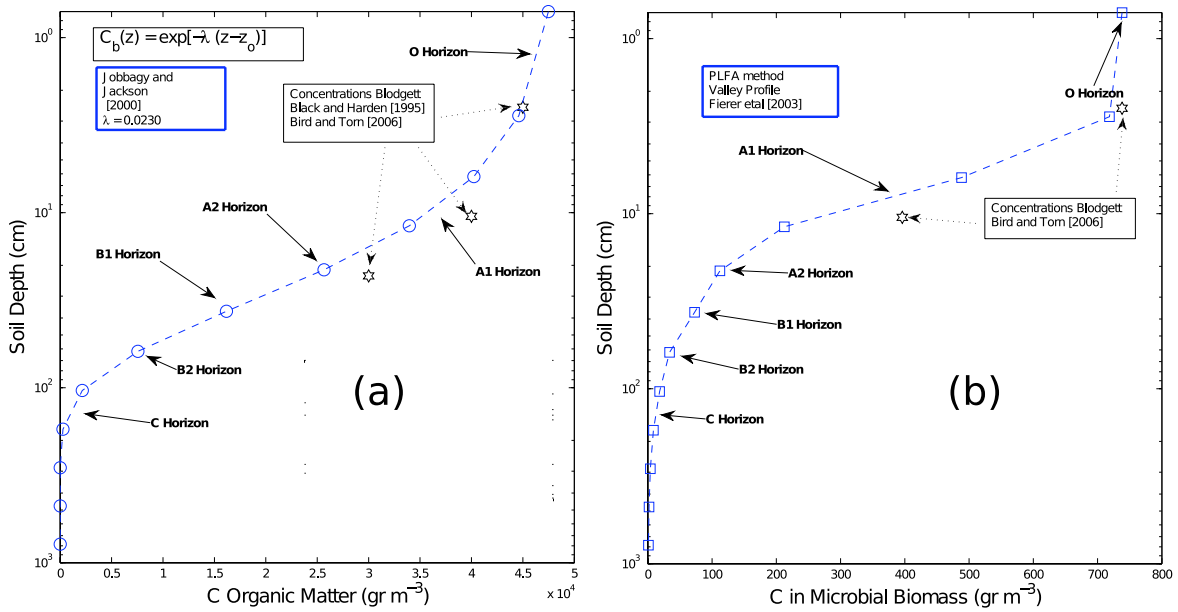

Figure 4.4: Initial conditions in the vertical distribution of **(a)** soil carbon in the organic matter C_s, and **(b)** soil carbon in the microbial biomass C_b. These profiles were derived from a combination of data collected at the Blodgett Forest (stars) and detailed profiles of C_s and C_b from other sites [Fierer et al., 2003, Jobbágy and Jackson, 2000]

.

4.3 Results and Analysis

4.3.1 Moisture and Temperature Dynamics in the Soil Column

Long and pronounced dry periods, such as those observed in Blodgett during summer, enhance the occurrence of strong gradients in water potential between the dry surface and deeper wet layers. The presence of a litter layer above the soil and the response of fine roots to dry conditions such as fine root conductivity loss are mechanisms that may prevent the loss of moisture from the roots to the soil destined to feed soil evaporation under extreme dry conditions [Espeleta et al., 2004]. A litter layer helps reduce considerably the efflux of water from the root to the soil under such situations and prevents root-soil hydraulic disconnection [Quijano et al., 2012]. However, even in the presence of litter there is a flux of moisture from the roots which enhances soil evaporation [Quijano et al., 2012].

In the simulations performed under the no HR case (scenarios II and IV) we imposed

a complete hydraulic disconnection between the soil and the roots by setting the radial conductivity of the root system to zero (FRCL=1) whenever $\psi_{root} > \psi_{soil}$. This condition satisfies the no water flux from the roots to the soil following the definition of No-HR and has been implemented in previous studies to perform the No-HR simulations [Amenu and Kumar, 2008, Quijano et al., 2012].

Figure 4.5 shows the FRCL for the topmost mineral soil layer located in horizon A1 (below horizon O). This figure shows the ensemble of FRCL for all the 500 years of simulation with dark line corresponding to year 100 which has been selected arbitrarily for illustration. Figures 4.5a,b show the FRCL function for HR and No-HR ,respectively, in the presence of shrubs (scenarios I and II). Figures 4.5c and d show the results for the case when shrubs are not present (scenarios III and IV). It can be seen that the hydraulic loss patterns differ in the HR and No-HR cases. When HR is present (Figures 4.5a and c), fine roots undergo a strong reduction in conductivity only during the summer period. The ensemble also shows that there is a considerable year to year variability as a result of variation in atmospheric forcing. In the absence of HR there is a total hydraulic conductivity loss (FRCL=1) during the sumer period that manifests after rainfall ceases at the beginning of the summer. In winter the FRCL function is characterized by fluctuations between one and zero that follows the rainfall patterns and the availability of moisture at the surface.

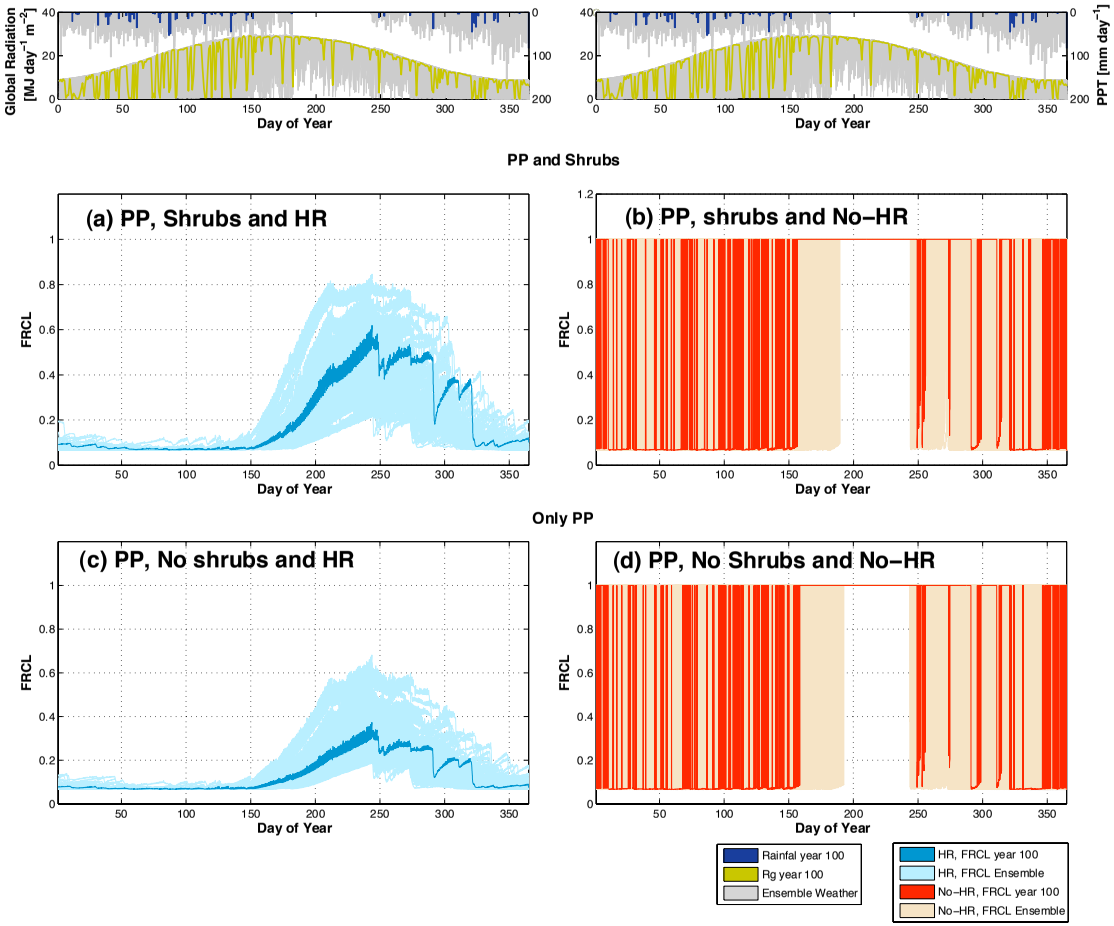

Figure 4.5: Fine root conductivity loss functions (FRCL) at the top 3 cm of horizon A1. FRCL represents the fraction of conductivity loss in fine roots as a response to dry conditions. The figures show the ensemble of FRCL for all the 500 years of simulation for the case when **(a)** shrubs are present and HR is active, **(b)** shrubs are present and HR is not active, **(c)** shrubs are not present and HR is active and **(d)** shrubs are not present and HR is not active. The darker lines show the FRCL for the simulations in year 100. This year was chosen arbitrarily to illustrate the dynamics in a particular year. The top panels show the realizations of rainfall and global radiation in blue and yellow respectively for year 100 and the ensemble of rainfall and radiation for 500 years in grey.

As observed in Figures 4.5a and c, in the presence of HR, FRCL never reaches 1. Although the uptake (or release) of moisture is reduced considerably there is a continuous flux of moisture between the soil and the roots. Furthermore it can be observed that FRCL is consistently higher in the presence of shrubs. This is because the presence of shrubs involves a more aggressive water uptake from plants in the shallow soils that accelerates the reduction of soil-moisture at the surface and therefore the impact fine root water potential.

Understanding the fine root dynamics at the top of horizon A described above helps us examine in more detail the energy balance in the soil profile. Figure 4.6 shows the fluxes of moisture, and states of temperature and moisture in the shallow soil (horizon O, A1 and A2) during the summer period.

The absence of fine roots in the organic horizon results in no water uptake or release in this horizon. There is a prominent release of water from the roots to the soil in the top 2-5 cm of horizon A1. The release of moisture in this thin layer is higher than the release that takes place in the 5-10 cm domain. This pattern is observed both in the presence and absence of shrubs and is induced by the higher water potential gradients that occur between the root and the soil which tend to increase toward the surface due to the evaporative demand. The efflux of water enhances the availability of moisture in these layers and supports soil-evaporation. Figure 4.6b shows higher levels of soil-moisture in the HR case for all the depths displayed. Increases in soil evaporation during the summer reduces ground heat flux, and surface and subsurface temperature. Therefore, the immediate result of No-HR is an increase in the soil-temperature (See Figure 4.6c) where mean soil-temperature in the No-HR case is consistently higher). Therefore the net effect from the HR is a cooling effect with a reduction in soil ground heat flux.

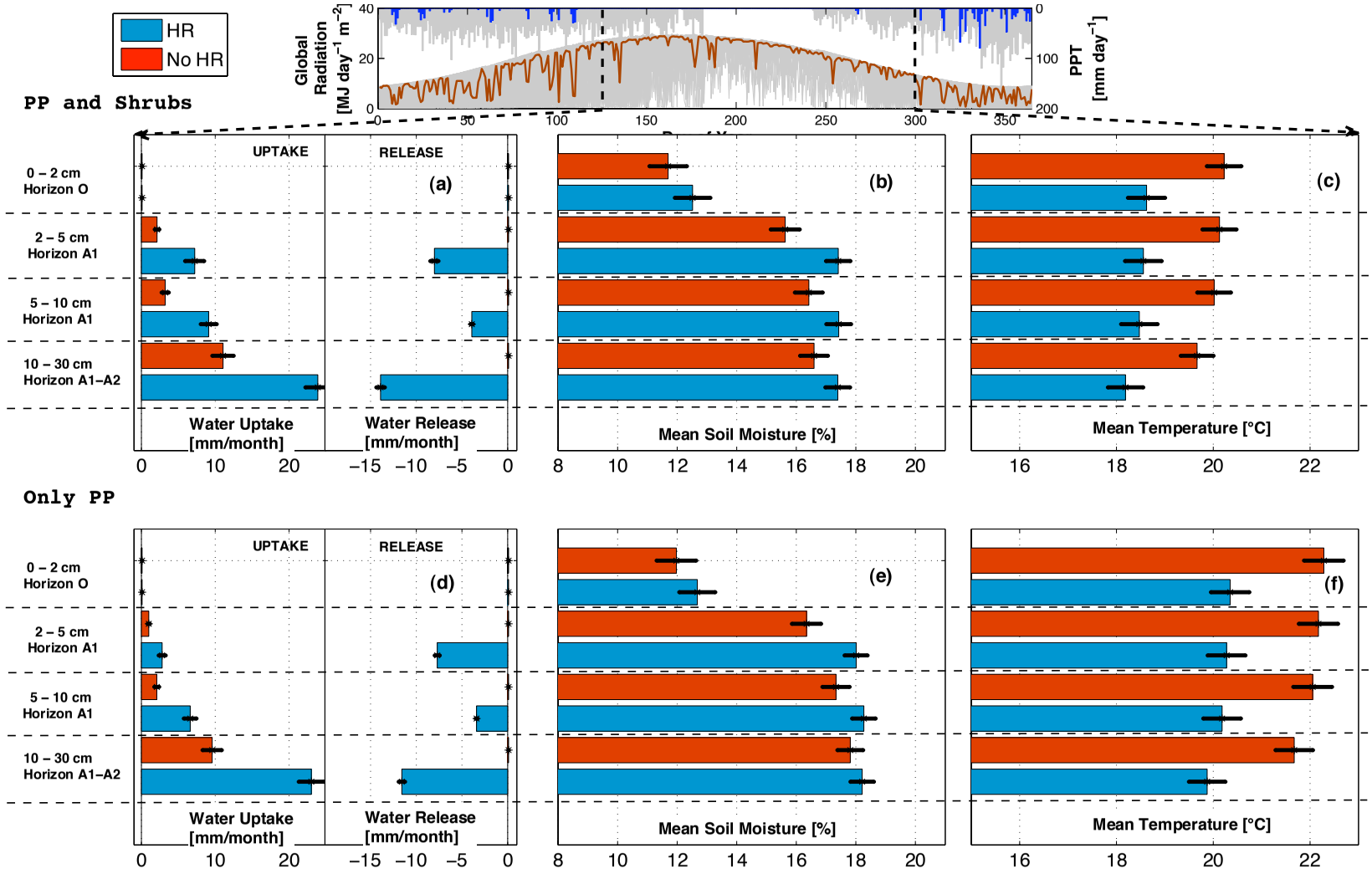

Figure 4.6: Energy balance at the surface and implications on water fluxes **(a and d)**, soil-moisture states **(b and e)** and soil-temperature **(c and f)** in the shallow layers during the summer period. The upper panel shows the simulations in the presence of shrubs and the bottom panel shows the simulations in the absence of shrubs. The small panel at the top displays the ensemble of 500 years of precipitation and global radiation. The bar sizes represent the mean values involved during years 250 to 500 of simulation and the standard deviation is represented by the black line.

When shrubs are absent (Figure 4.6d,e and f) lower LAI values allow higher radiative energy to reach the soil. Although the amount of water released in the 2-5 cm of soil is similar in the absence and presence of shrubs, the net root uptake of moisture is higher when shrubs are present. In the presence of shrubs there is a higher plant water demand and fine root biomass that compete with soil evaporation for available water in the soil. Therefore, in the absence of shrubs HR enhances more soil evaporation compared with the case when shrubs are not present. As a result the cooling effect caused by HR is more prominent in the absence of shrubs.

The magnitude of the net release and uptake fluxes of moisture from plant roots at deeper layers (5-30 cm) are consistently higher in the presence of shrubs, which is expected due to gradients created from the large demand of water by the shallow rooted plants [Quijano et al., 2012].

These differences in moisture and temperature stated between HR and No-HR and the presence and absence of shrubs affect the carbon and nitrogen dynamics as discussed below.

4.3.2 Steady State Analysis of Carbon Dynamics

The net impact of HR on organic matter decomposition can be explained as an interaction between soil-moisture and soil-temperature. This is conceptualized in the form of a simple product between $f_D(\psi)$ and $f_D(T)$ which are the net effects of soil water potential and soil temperature on organic matter decomposition respectively (Appendix E). Similarly, the net effect of HR in organic matter decomposition is represented by two main mechanisms: (i) redistribution of water in the soil column that enhances soil moisture in horizon A1 during the summer period and therefore enhances the organic matter decomposition in horizons O and A1 where concentrations of organic carbon are the highest; and, (ii) HR diminishes the ground heat flux and therefore reduces the temperature in the soil column (*a cooling effect*) resulting in a net decrement of organic matter decomposition.

Figures (4.7a, b) show the long term annual decomposition rates of organic carbon (DEC) from the total soil column. The inset plots in Figures 4.7a, b show in more detail the first 30 years of simulation. During this transient period, both HR (blue) and No-HR (red) simulations diverge from the same initial conditions. For example, in the presence of shrubs it can be observed (inset in Figure 4.7a) that from year 1 to year 17 the decomposition rates are higher when HR is active. The enhancement in soil-moisture at the top of horizon A1 overcomes the cooling effect when HR is active resulting in higher decomposition rates.

However, different decomposition rates impact the mass balance of carbon differently and after 17 years, the soil organic carbon pools (C_s) diverge from the same initial condition and become different ($C_{s,HR} < C_{s,No-HR}$). Higher carbon content when HR is not active enhances decomposition in the following years. Thus, decomposition rates during years 18 to 23 become higher when HR is not active (inset in Figure 4.7a). In the long term decomposition rates when HR is active (blue curves in Figure 4.7a and b) or not (red curves in Figure 4.7a and b) fluctuate around the same mean.

Figures 4.7c, d show the dynamics of total C_s in the entire soil column. In the presence of shrubs (Figure 4.7c) the total C_s diverges from an initial condition of 22 kg/m^2. In the long term it oscillates around a mean value close to 26.8 kg/m^2. The same dynamics are observed in the phase-space plot displayed in Figure 4.7e. On the other hand, Figures 4.7b, d, f show the same information but in this case the simulations are performed in the absence of shrubs. As expected, C_s converges to a lower value in the absence of shrubs fluctuating around a mean close to 23.2 kg/m^2.

The dashed lines in Figures 4.7c, d represents the percentage difference in C_s between HR and No-HR, calculated as $\Delta C_s = [(C_{s,HR} - C_{s,No-HR})/C_{s,HR}] \times 100\%$. In the presence of shrubs (Figures 4.7c) this difference oscillates below zero with a mean value of $\overline{\Delta C_s} = -1.1\%$ which suggest that there is a slighly higher accumulation of carbon in the absence of HR. Therefore HR has a slightly net positive effect on decomposition that results in a lower carbon content. Although the difference is small, it suggest that the net enhancement of soil-moisture in horizon A1 during the summer period overcomes the cooling effect when HR is active.

In the absence of shrubs there is a positive accumulation of carbon when HR is active (Figure 4.7d) with a mean $\overline{\Delta C_s} = +1.9\%$. In this case, the decomposition is higher when HR is not active which suggest that the cooling effect is overcoming the enhancement due to moisture in horizon A1. As shown in section 4.3.1, the differences in soil evaporation and soil temperature when the simulations are performed with HR or without HR are more prominent in the absence of shrubs. These results suggest that the impact of the cooling effect translated as the difference in decomposition of organic matter between the simulations performed with HR and without HR is more prominent in the absence of shrubs. Lower LAI and lower plant transpirational demand in the absence of shrubs results in a higher soil evaporation water demand that enhances the cooling effect from HR. Therefore, in very dense canopies the impact of the cooling effect from HR may become insignificant even during periods of high global radiation. If the cooling effect becomes insignificant the only

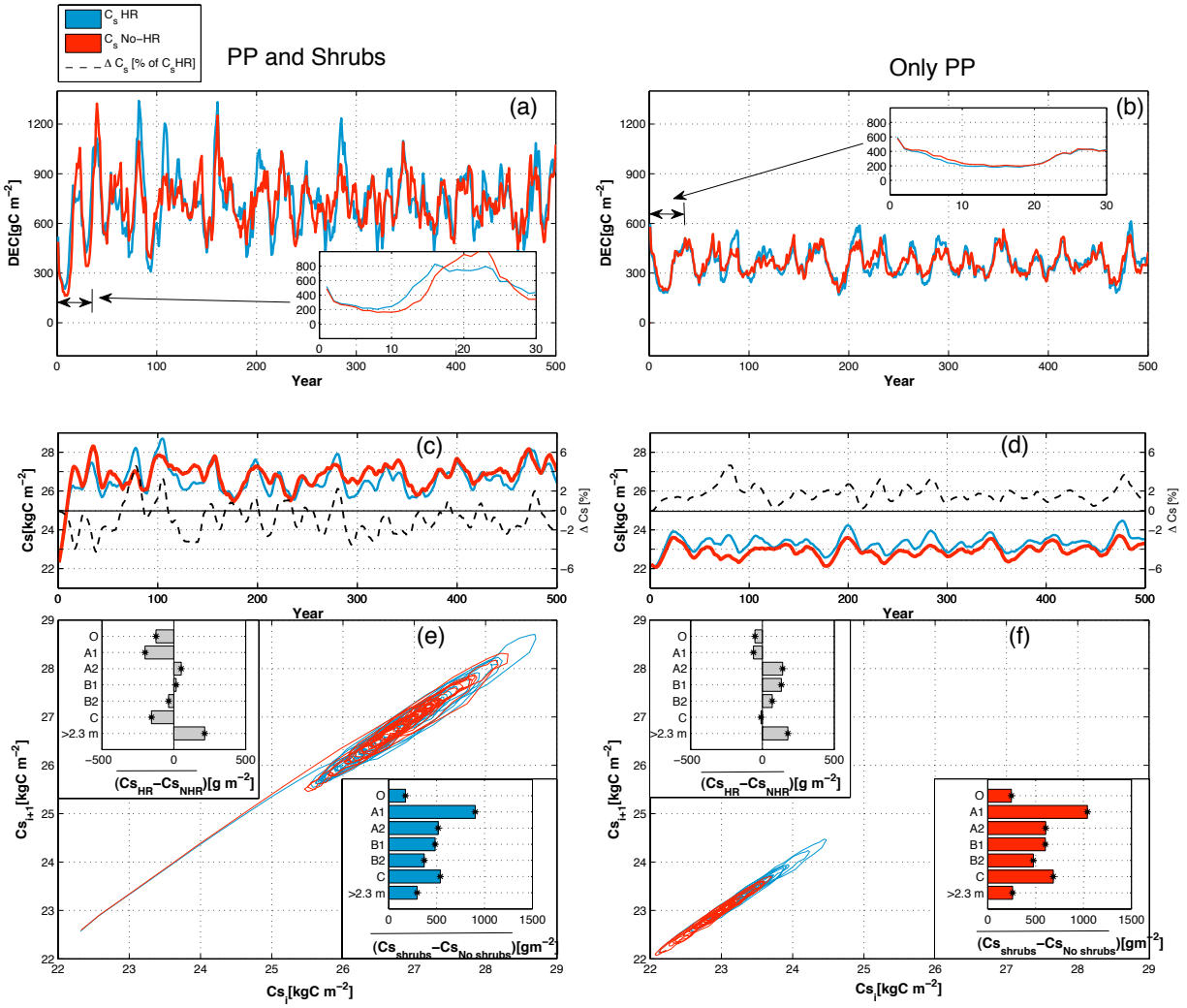

Figure 4.7: Long term dynamics of carbon in the soil organic matter. Top panels (**(a) and (b)**) display the long-term simulation results of soil decomposition in [gC m^{-2}]. Middle panels (**(c) and (d)**) show the long term simulation results of carbon in the soil organic matter C_s in [kgC m^{-2}]. Bottom panels (**(e) and (f)**) displays the phase-space of carbon in the organic matter ($C_{s,i+1}, C_{s,i}$) in [kgC m^{-2}]. The inlet figures in grey color on the bottom panels show the mean carbon differences in C_s between HR and No-HR at each horizon. Similarly the inlet figures in blue and red color on the bottom panels show the mean carbon differences in C_s between the simulations when shrubs are present or absent. The blue and red colors in the figure reflect the simulations in the presence or absence of HR respectively.

effect of HR on decomposition of organic carbon is only moisture dependent.

The presence of HR also influences the distribution of C_s in the soil column. HL efflux to horizon A1 during the summer period and HD efflux to horizon C1 during winter periods enhance decomposition in these horizons. Deeper layers (> 2.3 m) see a lower mean annual soil moisture in the presence of HR as a result of decreased drainage [Amenu and Kumar, 2008] (this is discussed further in section 4.3.3). The inset plots in grey colors in Figures 4.7e,f show the mean differences in C_s for each horizon. The presence of HR results in lower C_s in horizons O, A1, and C. There is a higher accumulation of C_s at depth greater than 2.3 m. In deep horizons the input of organic matter as well as the rates of decomposition and mineralization are much lower compared to the surface. In the long term these horizons may play a role, particularly when we compare the simulations between HR and No HR (Figures 4.7e, f).

The inset plots in blue (HR) and red (No-HR) in Figures 4.7e,f show the difference in C_s in the presence and absence of shrubs ($C_{s,\text{shrubs}} - C_{s,\text{No shrubs}}$). The most prominent difference occurs in horizon A1. Also note that the differences are notably higher in the No-HR case. The net difference in soil temperature between the simulations performed with and without HR are stronger when shrubs are absent because the impact of the cooling effect is more prominent. Higher differences in soil temperature results also in higher differences in decomposition between HR and No-HR cases.

The magnitude of the cooling effect produced by HR is regulated by the presence and functioning of fine roots at the surface. The results displayed in Figure 4.7 were simulated using the soil structure described in section 4.2 with no fine roots in the litter layer and no fine roots in horizon O. Figure 4.8 shows a sensitivity analysis comparing the simulations for different locations of fine roots. The simulations in green color were performed by assuming the presence of fine roots in the organic horizon, while the simulations in yellow assume that there are no fine roots either in the organic horizon or in the top 3 cm of horizon A1. When shrubs are present (Figure 4.8a), fine roots located in the organic horizon enhance the cooling effect when HR is active. Therefore, it produces a negative effect on decomposition throughout the soil column resulting in a considerable accumulation of C_s with a mean annual $\overline{\Delta C_s} = +8.2\%$. The absence of fine roots in the top 3 cm of horizon A1 reduces considerably the cooling effect and the net impact of HR on decomposition is only due to redistribution of moisture in the soil column. The reduction of the cooling effect creates a net positive effect on decomposition when HR is active and this results in a lower C_s in the long term with a mean annual $\overline{\Delta C_s} = -3.5\%$.

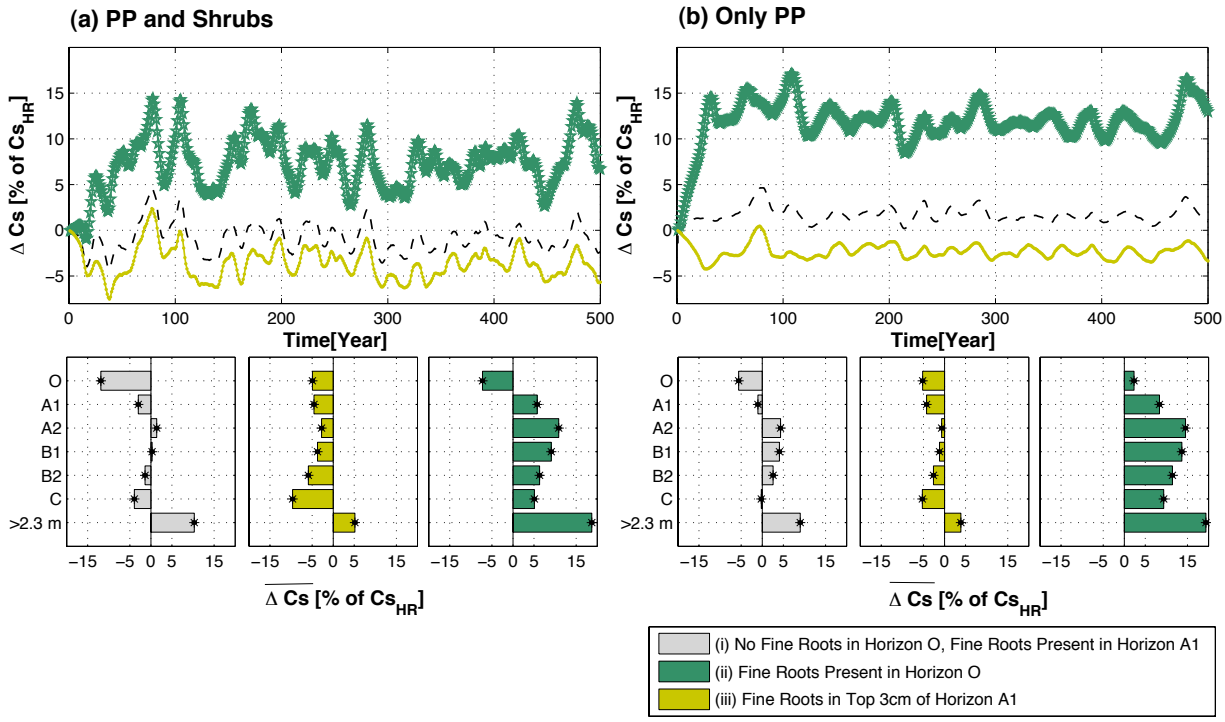

Figure 4.8: Sensitivity analysis on fine root functioning and presence at the top surface. Three different simulations are compared (i) In grey color: no fine roots in horizon O and fine roots present in horizon A1 (as observed in available information documented at Blodgett Forest), (ii) In green color: fine roots present in horizon O and fine roots present in horizon A1, (iii) In yelow color: no fine roots present in horizon O and no fine roots present in top 3 cm of horizon A1. The top panels show the results for the long-term percentage difference in carbon accumulation between the presence and absence of HR. This difference is defined as $\Delta C = \frac{C_{s,HR} - C_{s,No-HR}}{C_{s,HR}}$. The bottom panels show the mean carbon percentage difference $\overline{\Delta C}$ for each horizon for each of the three simulations considered.

Figure 4.8b displays the sensitivity analysis in the absence of shrubs. As mentioned before, in the absence of shrubs the impact of the cooling effect by HR is more prominent and consequently the difference in carbon content with and without HR (ΔC_s) is higher in the absence of shrubs. The sensitivity analysis in the absence of shrubs shows that for the case when fine roots are located in the horizon O there is a mean annual $\overline{\Delta C_s} = +9.7\%$. On the other hand, the absence of fine roots at the top of horizon A1 results in a mean annual $\overline{\Delta C_s} = -2.5\%$.

Bottom panels in Figure 4.8 show mean percentage difference in $\overline{\Delta C_s}$, for each horizon in the soil. The results displayed in these panels suggest that the cooling effect regulated by the presence or absence of fine roots in horizon O and horizon A1 impact the long term accumulation of carbon in the entire soil column. The results in Figure 4.8 suggest that fine roots and their interplay with HR have important implications on the soil carbon cycle not only by their biomass contribution [Jackson et al., 1997, Richter et al., 1999] but also by their control on the energy and moisture dynamics at the surface. Figure 4.9a, c shows the annual cycle for soil-temperature at 5 cm and heterotrophic respiration from the entire soil column (Figure 4.9b and d). Numerical simulations of temperature show a good agreement most of the year except in the late summer where the model overestimates. However, we note that the model temperature corresponds to average values over the canopy footprint while the observation was recorded from a single point measurement during years 2000-2005.

According to the results presented in this section, the net annual decomposition (also the heterotrophic respiration) at equilibrium is similar between the simulations performed with and without HR (Figure 4.7a,b). However, at equilibrium the content of carbon in the soil varies between the simulations performed with and without HR (Figures 4.7 and 4.8), and these dynamics depend on the presence and absence of shrubs and are highly sensitive to the location and functioning of fine roots in the surface. The inter-annual patterns of decomposition (also heterotrophic respiration) at equilibrium are consistently different when the simulations are performed with and without HR. Figure 4.9 shows the inter-annual fluxes of heterotrophic respiration for the scenarios when shrubs are present (Figure 4.9b) and absent (Figure 4.9d). During the dry summer period the heterotrophic respiration is higher when HR is active (blue curves in Figure 4.9b,d). However, heterotrophic respiration is higher in the rest of the year for the simulations without HR (red curves). These differences are more prominent in the presence of shrubs (Figure 4.9b) because there is a higher amount of fine roots in shallow layers that enhances the redistribution of moisture to horizon A1 and the impact of the cooling effect is less strong in the presence of shrubs. These processes allow the

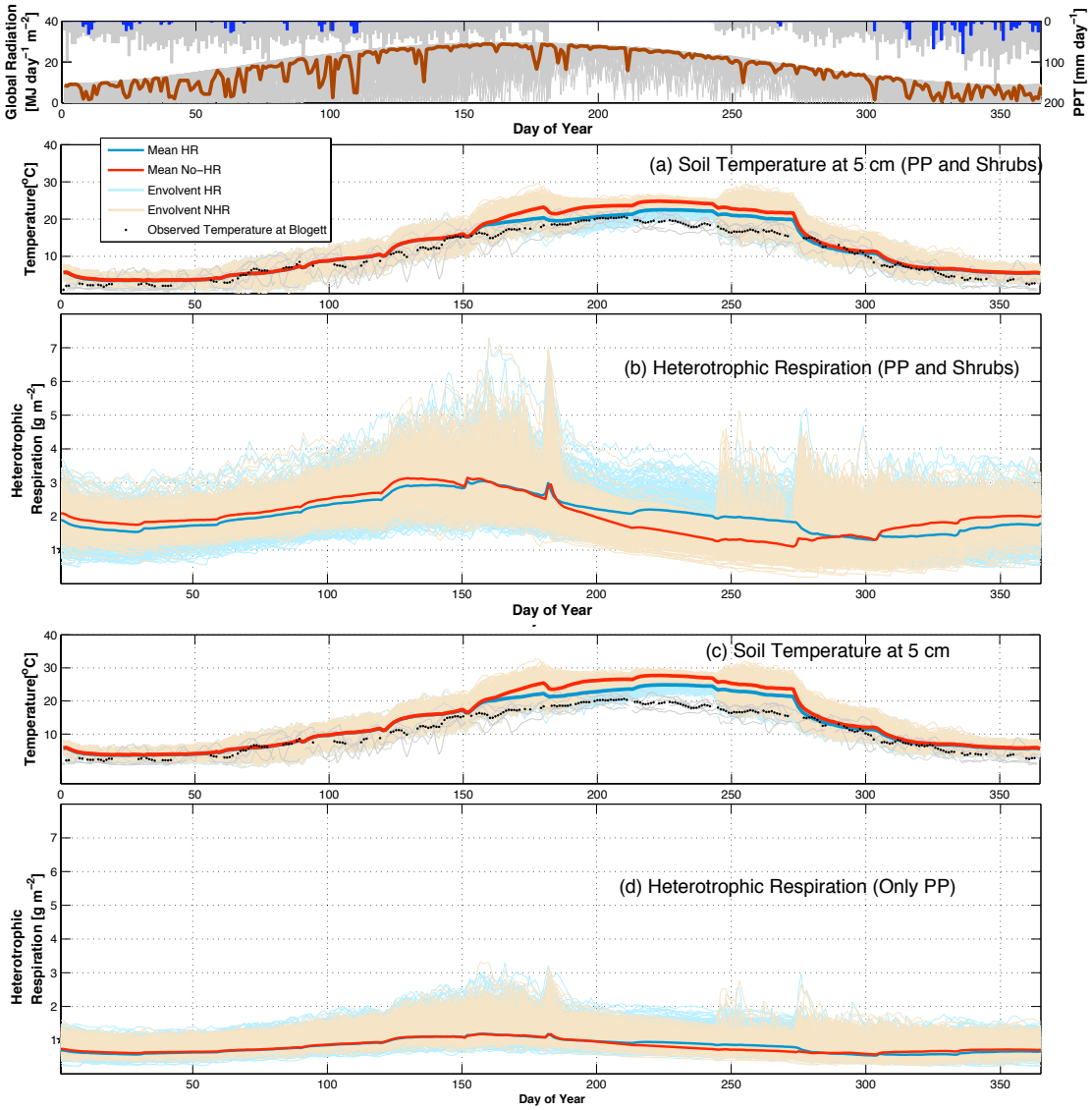

Figure 4.9: Panels **(a)** and **(c)** show the simulation of soil-temperature at 5 cm, and panels **(b)** and **(d)** show the simulation of soil respiration. The uppermost panel show the simulations of precipitation and global radiation. The pattern of global radiation is observed in the temperature and heterotrophic respiration plots. Lighter lines in (a), (b), (c) and (d) shows the ensemble of simulations results during years 250 to 500. On the other hand, the thicker lines represent the average over all these years of simulation.

simulations with HR to have a considerable higher heterotrophic respiration (decomposition) during the summer dry period compared with the simulations performed without HR.

4.3.3 Steady State Analysis of Nitrogen Dynamics

The dynamics of nitrogen in the subsurface includes mineralization, immobilization, nitrification and leaching, and is tightly coupled to subsurface carbon cycling [D'Odorico et al., 2003, Manzoni and Porporato, 2007, Porporato et al., 2003]. In this section we examine how HR and the presence or absence of shrubs impact the fluxes of mineral nitrogen (NH_4^+, NO_3^+).

The uptake by plant roots is the most important flux that depletes the mineral nitrogen from the soil and, therefore it plays an important role in the mass balance of nitrogen in the soil. In this study the uptake of mineral nitrogen by plant roots is simulated by the consideration of two main mechanisms of nitrogen uptake: (i) uptake of mineral ions that are brought toward the roots with the water flux (passive uptake), and (ii) uptake of mineral ions that are brought toward the roots by a diffusion pathway in the soil (active or diffuse uptake, [Porporato et al., 2003]). The passive uptake flux is computed as the advective flux of mineral nitrogen that is transported by the transpirational current. On the other hand the active uptake is computed according to the capacity of roots per unit of dry biomass to uptake mineral nitrogen from a diffusive pathway, F_{factor} (Table D.2) which is based on the initial approach of Porporato et al. [2003] and modified here in the light of a multi-layer and multi-species framework. The equations used to simulate these processes are described in more detail in the Appendix E(Section 2).

Figure 4.10 shows the mean annual water and NO_3^- fluxes, and NO_3^- concentration in different horizons. The uptake of water is enhanced in the presence of HR (blue lines in Figure 4.10). Similarly, the presence of shrubs enhances the uptake of water because they increase the transpirational demand. As a result the lowest mean water drainage from all the different scenarios considered occurs in the presence of shrubs and when HR is active. The fluxes of mineral nitrogen, particularly NO_3^-, are coupled with those of moisture. However the highest uptake of NO_3^- occurs in horizon A1 while the highest uptake of water occurs from the deepest layers. During the dry summer period this ecosystem sustains a high transpiration rate that relies on deep root water uptake [Quijano et al., 2012] . However plant roots are able to uptake NO_3^- from the soil by a diffusive pathway (active) even during periods of low soil moisture and no water uptake. The highest allocation of roots occurs in

shallow horizons and therefore the highest uptake of NO_3^- takes place from these horizons by an active uptake. These results show the relevance of the active uptake of NO_3^- in ecosystems experiencing long and prolonged dry periods such as Blodgett.

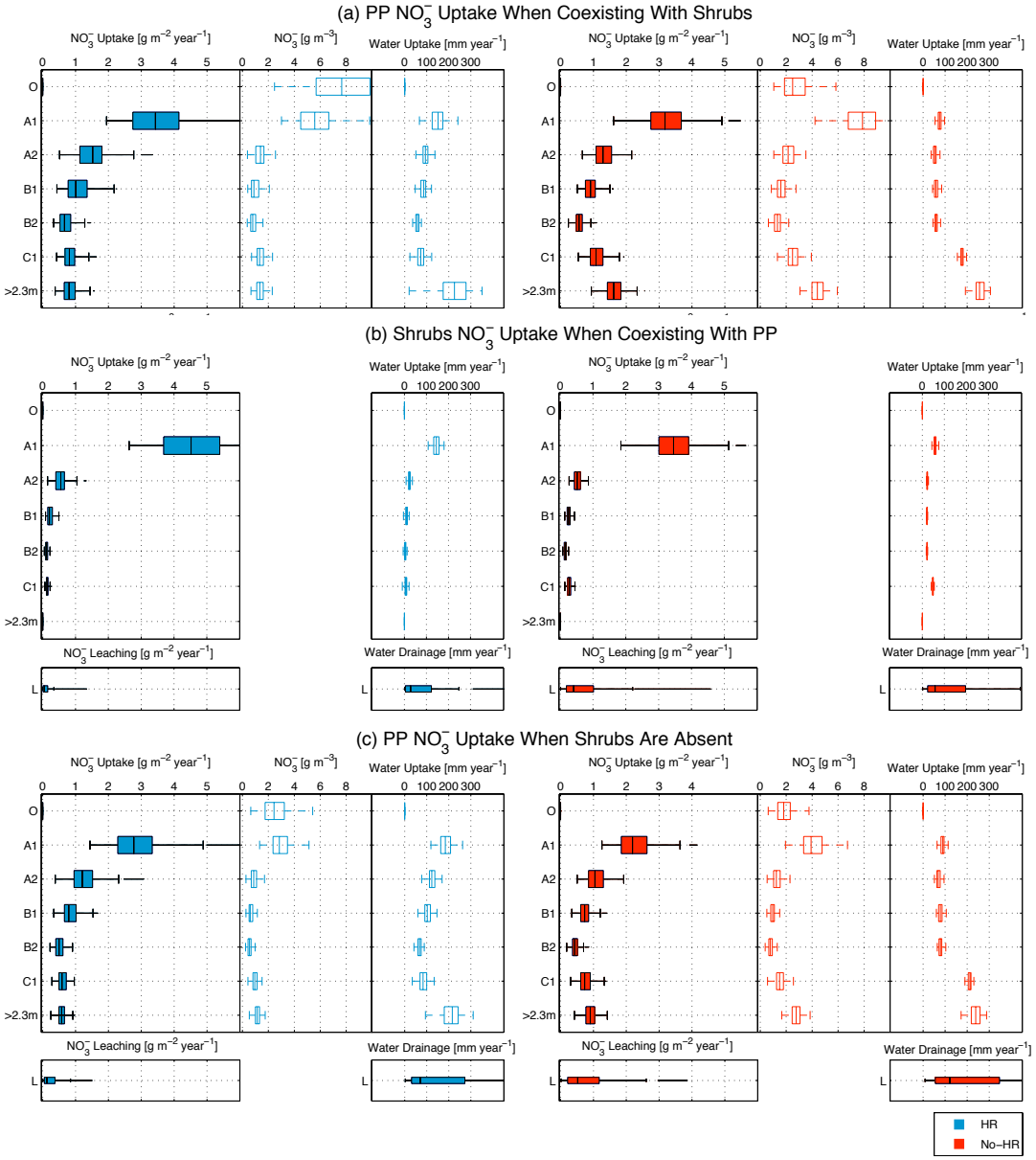

Figure 4.10: Dynamics of water and NO_3^- uptake in the presence and absence of shrubs. The variables displayed are mean annual NO_3^- uptake, mean annual NO_3^- concentration and mean annual water uptake. The box plots show the summary for all the simulations performed between years 250 and 500 which is considered a period where steady solutions have been already reached. Top **(a)** and middle **(b)** panels shows the simulation results for the case when both species, PP and shrubs, coexist. The top panel **(a)** shows the uptake of NO_3^- and water by only PP while the middle panel displays the uptake of NO_3^- and water only by shrubs. The bottom panel **(c)** shows the simulation results in the absence of shrubs (PP being the only species).

Although the active mechanism plays a critical role in the net uptake of mineral nitrogen, the passive mechanism is also important. The NO_3^- concentration in the soil column (Figure 4.10) is highest at the top in horizon A1. This is expected since mineralization occurs mostly in horizon A1 and the input of mineral nitrogen from atmospheric deposition is allocated to horizon O. However, there are some differences in the distribution of the NO_3^- concentration between the simulations performed with (blue boxes) and without (red boxes) HR. When HR is active, the distribution of NO_3^- follows an exponential decay with a maximum value at the top that decreases with depth. On the other hand, when HR is not active the vertical distribution of NO_3^- presents a C shape that is maximum at the top but it also increases at the bottom. The high uptake of water from shallow layers when HR is active, reduces the drainage of moisture in the soil column and enhances the passive uptake of NO_3^- from these layers. When HR is not active there is a higher leaching of NO_3^- and therefore a higher accumulation in deeper horizons.

Note also that the vertical distribution of NO_3^- in the soil column influences the dynamics of NO_3^- uptake since the uptake from both mechanisms (passive and active) is concentration dependent. This is observed in the vertical distribution of NO_3^- uptake (Figure 4.10) that follows a similar shape as the distribution of NO_3^-. However the uptake of NO_3^- in the top horizons is more accentuated since in these horizons there is greater root biomass.

The presence of shrubs increases the pool of nitrogen in the soil due to lower C:N ratios in the foliage in comparison to PP. As a result, in the presence of shrubs the concentration and uptake of NO_3^- is higher. Although the presence of shrubs increases the pool of nitrogen in the soil it does not increase the net leaching of NO_3^- out of the root zone. In the case of HR, the introduction of shrubs results in lower leaching of NO_3^- out of the root zone. This arises because shrubs uptake NO_3^- and also because the enhanced transpiration reduces the net drainage of water from the root zone (Figure 4.10).

Table 4.2 summarizes the net magnitude for each of the uptake and leaching fluxes described above. It also shows in parenthesis the respective values of the diffuse uptake fraction (f_{diff}) which is defined as the ratio between the uptake flux that originates from a diffusive pathway and the total uptake flux (Appendix E, Equation 20). f_{diff} ranges between 0.3 to 0.7. This fraction varies according to the type of flux and also with the presence of HR. As expected, the fraction from a diffuse pathway is higher for NH_4^+ compared to NO_3^- uptake. Also, when HR is active, the percentage of mineral nitrogen uptake fluxes from a diffuse pathway is lower compared to the simulations when HR is not active. These results suggest plants may rely more on a diffuse pathway when HR is not active.

When shrubs and PP coexist there is a higher uptake of mineral nitrogen from PP compared to the scenario when shrubs are absent. The leaching of NO_3^- lost out of the root zone is around 0.6 [g/yr] lower when HR is active. This difference may become an important amount in the long term, particularly in the absence of shrubs where the only external input of nitrogen is from atmospheric deposition.

Figure 4.11 shows the long term dynamics of mineral nitrogen content in the entire soil column. Top panels display NO_3^- and bottom panels display NH_4^+ dynamics. The patterns observed are similar to those observed in the carbon dynamics. The initial conditions are established as no mineral nitrogen content in the soil column. After about 250 years the concentrations of NH_4^+ and NO_3^- reaches equilibrium with oscillations around a mean value. As observed in all of the plots in Figure 4.11, the absence of HR results in a higher content of mineral nitrogen in the soil. Shrubs increase the input pool of nitrogen in the soil. However, there is no significant difference in mineral nitrogen content between the presence or absence of shrubs when HR is active (compare blue lines in Figures 4.11a and 4.11b), which suggest that plants are able to enhance their uptake under higher nitrogen when shrubs are present. On the other hand in the No-HR case, higher increments in the nitrogen pool that occurs in the presence of shrubs results in higher mineral nitrogen content in the soil (Figure 4.10).

According to the results in Figure 4.10 and 4.11, and Table 4.2, the presence of both shrubs and HR reduces the leaching of nitrogen from the soil column. However these results may be sensitive to other external processes, such as:

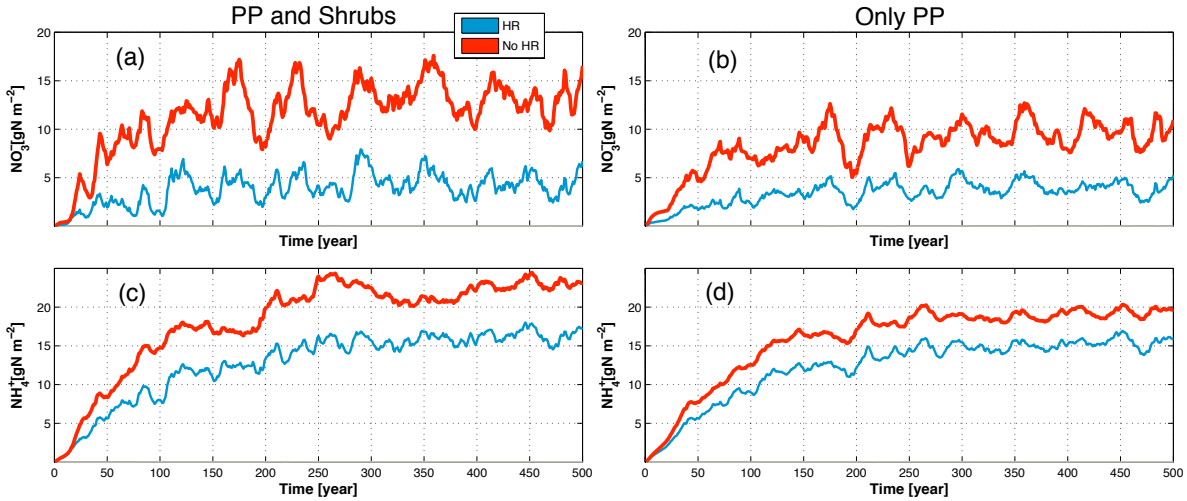

Figure 4.11: Long term simulation results of **(a,b)** total NO_3^- content and total **(c,d)** NH_4^+ content in the soil column.

(i) The rate of transformation from NO_3^- to NH_4^+ (nitrification rate): If there is less NO_3^- production, the retention time of mineral nitrogen in the root zone will increase and therefore the rate of leaching will be lower. This process is regulated by the nitrification factor k_n (See Appendix E, Section 2, Equation 14).

(ii) The ability of roots to uptake nitrogen by a diffusive pathway: If roots increase their capacity to uptake water by diffusion they will become less vulnerable to loss of mineral nitrogen by leaching. This process is regulated by parameter F_{factor} (See Appendix E, Section 2, Equation 18).

All the simulation results displayed in this document were performed with the values of F_{factor} and k_n shown in Table D.2. Figure 4.12 displays a sensitivity analysis showing the influence of k_n, and F_{factor} on the net leaching of nitrogen out of the root zone. In Figure 4.12 the stars represent the simulation results when shrubs are present while the circles represent the case at which shrubs are absent. Similarly the blue color represents the simulation results when HR is active and the red represents the simulation results when HR is not active. The size of the circles represents the fraction from the total mineral nitrogen uptake that comes from a diffusive pathway (f_{diff}). Each point in Figure 4.12 was generated with an independent simulation of 500 years with a unique combination of F_{factor} and k_n. The values displayed in this figure represent the mean annual average leaching of mineral nitrogen out of the root zone during years 250 to 500.

As expected, higher F_{factor} and lower k_n results in lower leaching of NO_3^-. The movement of nitrogen ions in the soil can be conceived as a trade off between *horizontal fluxes* such as the water uptake stream (forced by gradients in soil water potential) and diffusion (forced by gradients in soil ion concentration) that pulls ions toward the fine roots, and *vertical fluxes* such as drainage that are produced by the effect of gravity. The trade off is supported by the fact that stronger horizontal fluxes result in weaker vertical fluxes, or vice-versa. This effect can be seen in Figure 4.12 where the presence of HR and different plant species enhances horizontal fluxes (water uptake) and reduce the vertical flux represented by NO_3^- leaching. Moreover, higher diffusion capacities (higher F_{factor}) also enhance horizontal fluxes causing a reduction in NO_3^- leaching.

However, the effect of increasing the diffusion capacity is more sensitive when HR and shrubs are absent. If HR and shrubs are present, their ability to intensify the water uptake flux is able to capture the amount of nitrogen utpake that is missed by a reduction in diffussion if the difussion pathway uptake capacity from the roots (which is conceptualized in terms of F_{factor}) was reduced. In Figure 4.12 the magnitude of f_{diff} is represented by the

size of the symbols. It can be observed that under low values of F_{factor}, the presence of shrubs and HR results in small sizes that indicates a low fraction from a diffusive pathway. Under the same values of F_{factor}, the NO_3^- leaching is considerably higher in the absence of both shrubs and HR. The simulations results presented in Figure 4.12 suggest that the presence of HR and different species enhances the ability of ecosystems to uptake ions such as NO_3^- and reduces the dependence of plant roots to uptake mineral nitrogen by diffusive pathways from the soil.

4.4 Summary and Discussion

In this study we analyze how the interplay between multiple vegetation species affect the below-ground dynamics of carbon and nitrogen. The analysis enabled the assessment of the long-term impact of this interplay in the pools of carbon and nitrogen in the soil.

Findings indicate that the presence of HR influence decomposition of organic matter by two mechanisms. First, it modifies soil-moisture throughout the soil column and favors decomposition in horizons A1. Second, HR reduces the soil temperature (cooling effect), resulting in reduced decomposition rates throughout the soil column. Decomposition rates are also a function of the total soil carbon, C_s, and the microbial pool, C_b. After a transient response there is convergence toward different states of C_s concentration but with nearly the same decomposition rates. Therefore, in the long term, HR impacts the size of C_s pools rather than the decomposition rates.

The cooling effect observed in the presence of HR varies according to the amount of energy that reaches the soil. We found that it is more prominent when shrubs are absent. In the presence of shrubs the reduction of radiation reaching the ground surface due to higher LAI reduces the soil evaporation. As a result HR is less influential in affecting the soil evaporation and the ground heat flux. These dynamics suggest that in dense canopies the cooling effect may not be seen. In addition the cooling effect is a function of the location of fine roots and their functioning. The presence of fine roots that release water through HR magnifies the cooling effect resulting in higher accumulation of C_s. On the other hand if fine roots are located deeper into the soil the cooling effect is less prominent.

Presence of shrubs increases the flux of organic matter in the soil resulting in higher concentrations organic carbon. The most prominent enhancement of C_s in the presence of shrubs is observed in the near-surface soil horizons. Furthermore, under the presence of shrubs heterotrophic respiration from the soil is considerably higher.

The presence of shrubs also increases the input fluxes of nitrogen in the soil. Co-existing species such as PP are able to uptake more nitrogen from the soil and therefore are favored by the presence of shrubs. The simulations show an interesting interplay between shrubs and HR. HR reduces the leaching of mineral nitrogen by enhancing the ability of plants to capture available nitrogen in shallow horizons with the transpirational stream through passive uptake. Shrubs also extend the ability of the system to capture nitrogen by allocating roots in shallow layers and also by increasing water uptake from the soil for transpiration which in turn reduces drainage. The lowest leaching of NO_3^- was attained when both shrubs and HR were present. These results suggest that HR and coexistence of different species reduce leaching of NO_3^- from the root zone. In addition, the net content and the distribution of mineral nitrogen along the soil profile is influenced by HR. Higher leaching of nitrogen to deeper layers results in more nitrogen allocated in deeper layers in the absence of HR. This phenomenon is more prominent when shrubs are present.

In temperate natural ecosystems nitrogen is often a limited nutrient. The results in this study show that under the presence of HR the ecosystem is more efficient in reducing the leaching of nitrogen from the root zone resulting in a lower mean NO_3^- leaching flux of 0.6 [$g/m^2/yr$]. The capacity of the ecosystem to reduce NO_3^- leaching, even in low magnitudes could be an important trait. Further, the uptake of mineral nitrogen under the same conditions of fine root biomass, fine root distribution and diffusion uptake factors (F_{factor}) are higher when HR is active.

Previous studies have mentioned two relevant processes that enhance the retention of nitrogen in the soil: (i) microorganisms [Vitousek and Matson, 1984] and (ii) species diversity [Hobbie, 1992]. Our results provide support for the latter where the interplay between different species as a proxy of plant biodiversity and HR results in positive feedbacks that enhance the net uptake of mineral nitrogen.

Although the numerical model implemented in this study simplifies many of the complex interactions found in natural ecosystems it established that the passive movement of water in the subsurface by plant roots is an important mechanism that influences the below-ground biogeochemical dynamics and should be considered in the analysis of carbon and nitrogen processes that occur in natural ecosystems. This mechanism may be an important element in the understanding of current and long term biogeochemical patterns observed in experimental observations as well as an important variable that should be considered in climate change studies.

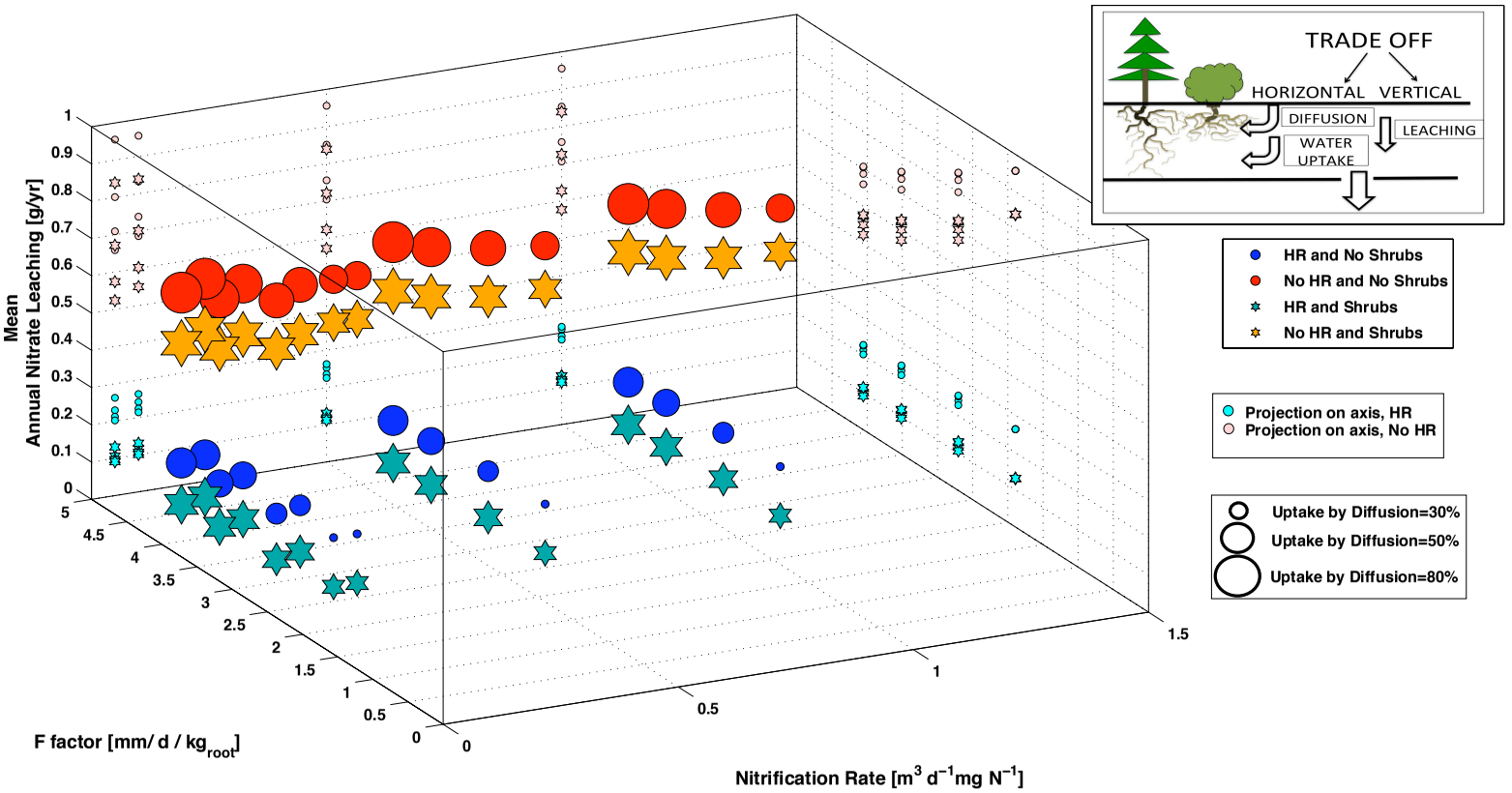

Figure 4.12: Trade off between nitrification rate (k_n), root diffusion nitrogen uptake factor (F_{factor}) and total leaching of mineral nitrogen from the root zone. Higher rates of nitrification enhances NO_3^- leaching while higher F_{factor} reduces NO_3^- leaching. Both the presence of shrubs and the presence of HR reduce the leaching of NO_3^-. The size of the symbols represent the fraction of nitrogen uptake from a diffusive pathway (f_{diff}). Under the same combination of k_n and F_{diff}, this fraction is lower when HR is active. These results suggest the net uptake of nitrogen rely more on a diffusively pathway when HR is absent and therefore this scenario is more sensitive to k_n and F_{factor}.

Table 4.1: Carbon and nitrogen model parameters.

Parameter	Symbol	Units	Value
Foliar Parameters			
Needle life span PP		year	3
Leaf life span shrubs		year	3
Carbon-Nitrogen Dynamics			
Rate of nitrification	k_n	$m^3/d/kgC$	0.5
Fraction of decomposed organic matter going into respiration	r_r	–	0.7
Critical C:N above which immobilization occurs	$(C:N)_{cr}$ Fig 4.3	–	39.3
Microbial biomass C : N ratio	$(C:N)_b$	-	11.8 [a]
Fraction of dissolved NH_4^+	λ^+	%	5
Fraction of dissolved NO_3^-	λ^-	%	100
Water potential below which microbial activity is water limited	ψ_{top}	MPa	-0.1 [h]
Water potential at which microbial activity is considered negligible	ψ_{min}	MPa	-10 [h]
Litter carbon concentration	$C_{s,litter}$	kgC m^{-3}	60 [f,g]
Litter thickness	Δz_{litter}	cm	3 [f]
Litter fragmentation parameter	k_{litter}	d^{-1}	$2.85 * 10^{-7}$ *
Leaves biomass and fine root biomass proportionally constant	km_r	–	0.8
Biotubation diffusion constant at the surface	D_b	cm^2/year	4 [c,d,e]
Depth below which bioturbation is considered negligible	z_{biot}	cm	80
Total annual deposition	N_{dep}	g/yr	0.5
Root diffusion N uptake factor	F_{factor}	$mm/d/kg_{root}$	1.8

Continued on Next Page...

Table 4.1 – Continued

Parameter	Symbol	Units	Units

[a]Bird and Torn [2006], [b]Misson et al. [2005],[c]Elzein and Balesdent [1995], [d]Dam et al. [1997]
[e]Kaste et al. [2007], [f] Black and Harden [1995], [g] Bird and Torn [2006], [h] Andren [1992]
*Found by calibration

Table 4.2: Total annual nitrogen fluxes. The fluxes displayed correspond to multi annual average computed with the simulations results obtained between year 250 and year 500. All the fluxes are in [g $m^{-2}year^{-1}$].

Uptake Form	**HR**		**No-HR**	
	PP	**Shrubs**	**PP**	**Shrubs**
PP and Shrubs				
N Uptake	8.77 (0.38)	5.46 (0.53)	8.98 (0.52)	4.58 (0.70)
NO_3^-Uptake[a]	6.27 (0.37)	4.08 (0.52)	7.03 (0.48)	3.52 (0.70)
NH_4^+Uptake	2.50(0.42)	1.38 (0.53)	1.95 (0.62)	1.06 (0.69)
Total N Uptake	14.24 (0.44)		13.47 (0.54)	
Leaching[a]	0.10		0.70	
Only PP				
N Uptake	6.92 (0.32)	-	6.32 (0.46)	-
NO_3^-Uptake[a]	4.72 (0.30)	-	4.73 (0.43)	-
NH_4^+Uptake	2.19 (0.37)	-	1.59 (0.54)	-
Total N Uptake	6.92 (0.32)		6.32 (0.46)	
Leaching[a]	0.24		0.83	

[a]Same as displayed in Figure 4.10

* Values in parenthesis represent f_{diff}: the fraction of the flux that arrives by a diffusion pathway

CHAPTER 5

Entropy Production in Ecohydrologic Systems

5.1 Introduction

Natural ecosystems are complex systems composed of different species and individuals that coexist and coevolve through mutual interactions. The inherent complexity of ecosystems and the overwhelming amount of interactions and degrees of freedom make these systems challenging to analyze. In particular, fundamental understanding and prediction of structural, functional, and compositional patterns in these systems is difficult. A common approach has been the conceptualization of organizing principles that can give us more insight into the existing structure, composition, and function. These principles have been associated to energy, entropy, or free energy fluxes. In this study we analyze the fluxes of energy and entropy under different structural and functional properties and examine the connection between the organization of ecosystems represented in terms of these properties and the production of entropy.

Principles from classical thermodynamics has allowed us to predict the fate of close and isolated systems. However, in the realm of open systems experiencing no thermal equilibrium with the environment the complexity increases and it is challenging to examine the possible path and the steady state the system will reach. Non-equilibrium systems that exchange fluxes of energy and matter with their environment are present everywhere. The evolution of these systems is complex and it has been a challenge to predict their behavior. One of the most important concepts that have been used to describe and analyze these systems is the second law of thermodynamics and the ubiquitous *production of entropy* that is present in the universe. Entropy and free energy are concepts that are more related to the actual energy that is useful to perform work. Therefore, analysis of these quantities could give us more fundamental insights into the evolution, organization, and functioning of these systems than the traditional approach utilizing energy balances.

Ecological systems are open and are far from equilibrium. Different optimal hypotheses

have been trying to elucidate the fate of these systems by the optimization of a given "universal function" [Martyushev and Seleznev, 2006]. Initial approaches suggested that ecological systems evolved towards maximization of the energy that flows through them [Lotka, 1922]. Further studies recognized the role of the second law of thermodynamics and the importance of the entropy production [Prigogine and Wiame, 1946, Schrodinger, 1944]. These studies suggested that ecological systems evolves toward a state at which they self organize and therefore are able to optimize a given function that is related with the production of entropy or destruction of exergy. For instance, hypotheses such as the maximum entropy production principle (MEPP) [Martyushev and Seleznev, 2006], maximization of the dissipation exergy flows [Schneider and Kay, 1994], and the maximum storage and maximum dissipation principle [Fath et al., 2001] are examples of some of the optimum principles that have been postulated for ecological systems.

There is still a no conclusive validation of any of the optimal principles described above. Such validation is challenging because it would need to prove that a particular optimum principle will hold for all ecological systems experiencing all possible environmental forcing. However, these hypotheses could be useful to have a better insight about ecosystem properties. Some previous studies have taken for granted some of these optimal hypotheses and based on that they have inferred about other ecosystem properties where no information is available. For instance, Schymanski et al. [2010] used the MEPP to elucidate about subgrid heterogeneity in a two box ecohydrological model. They claimed the results following the MEPP were able to match observed biomass patterns. Similarly, Porada et al. [2011] and Wang and Bras [2011] used the MEPP to elucidate parameters of a global ecohydrological model and to obtain an analytical formulation of LE fluxes from the surface, respectively.

On the other hand, other studies have performed entropy budgets on ecosystems with no optimality framework. Therefore, these studies have focused on the quantification of the entropy fluxes in ecosystems or in some specific subcomponents. For instance, the entropy budget of conifer [Aoki, 1989], and deciduous [Aoki, 1987b] leaves were calculated under a constant input of radiation fluxes using the mathematical formulation developed in Aoki [1982]. These studies represented the first preliminary report of the entropy fluxes that are released by vegetation. They found that the entropy fluxes from the leaves increases linearly with the amount of energy absorbed by them and the ratio between the absorbed energy and produced entropy was the same for deciduous and conifer trees. In a more recent study Holdaway et al. [2010] developed a framework to compute the production of entropy from ecosystems using eddy covariance measurements. With this framework they were able to

calculate and compare the production of entropy in ecosystems that present different stages of development in the Amazon. Their analysis concluded that the entropy production from ecosystems was higher at the more advanced stages. Although these studies have estimated the total production of entropy in ecosystems they did not analyze and quantify how this production is controlled by structural and functional ecosystem properties such as root depth, leaf area index (LAI), leaf area distribution (LAD), species composition, and ecophysiological parameters.

Although the validation of the optimality principles mentioned above is challenging, the concepts of entropy production and destruction of exergy are very important and they are very likely associated to the self-organization of ecological systems. Therefore, it will be useful to analyze how different levels of ecosystem organization are associated with the production of entropy (or the destruction of exergy). This approach will allow us to understand in more detail the inherent mechanisms associated with the entropy production and their connection with the organization of ecosystems. This understanding, in turn could bring more insight into functional and structural patterns that have been observed, and also to analyze how the entropy production varies along with the evolution of ecosystems. Moreover, the connection between the organization of ecosystems and entropy production will allow us to comprehend the role of vegetation on the budgets of entropy in the atmosphere and draw inference about the coupled evolution of the surface and the atmosphere.

In this study we analyze how different levels of ecosystem organization impact the production of entropy from the surface. We conceptualize this organization in terms of structural and functional properties such as LAI, LAD, root depth, and species composition. The formulation implemented here to compute the entropy production centers on a detailed, multilayer, canopy model that resolves photosynthetic active radiation, near infrared radiation, and longwave (LW) radiation through the canopy, thus allowing for unique considerations in the calculation of the ecosystem entropy budget. In particular, we address the following questions: (i) Do the different structural and functional ecosystem properties affect their entropy production? (ii) What are the key functional mechanisms that impact the production of entropy? (iii) What components of the entropy budget are affected by these structural and functional ecosystem properties? (iv) How do the interaction between the ecosystem properties and the production of entropy vary under different climatic conditions? In order to address these questions we perform numerical simulations in three ecosystems that are located in different climates.

5.2 Methods

5.2.1 Sites

The numerical simulations are run with data from three different sites that experience different atmospheric forcing conditions: (i) Blodgett Ameriflux Site, (ii) Tapajós KM67 Mature Forest Ameriflux Site, and (iii) Harvard Forest Ameriflux Site. The main advantages of these sites are the availability of eddy covariance information that allow us to validate the energy and heat fluxes, the presence of native vegetation species that have evolved with the climate in the region, and the extensive research that has already been performed facilitating the availability of data to parameterize the model. More detailed information about these sites is described in Section 3.2.2.

5.2.2 Forcing Data

The analysis in this study are accomplished using simulations that are performed over a two year period. The spin up to initialize these simulations was performed by running the model during two years prior to the period of analysis. Therefore, every single simulation was performed over a four year period but all the results reported in this study reflect the simulations during the last two years only.

The two year period was selected based on the information available to force and validate the model. Figure 5.1 shows the years selected for each site along with daily time series of precipitation and solar radiation. Blodgett and Harvard Forest experience a more strong seasonality in global radiation than Tapajos. This is expected because these ecosystems are located over higher latitudes than Tapajos. The mediterranean climate in Blodgett characterized by long dry periods that overlaps with high global radiation during the summer period is evident. On the other hand Tapajos experiences a reduction of rainfall between July and November and the distribution of rainfall in Harvard Forest is homogeneous throughout the year.

In addition Figure 5.1 also shows the LAI for all the three sites. The contribution of LAI from each plant functional type (PTF) at each ecosystem is also displayed in this figure. As expected from the SW radiation the seasonal pattern of LAI is more prominent in Blodgett and Harvard Forest than in Tapajos.

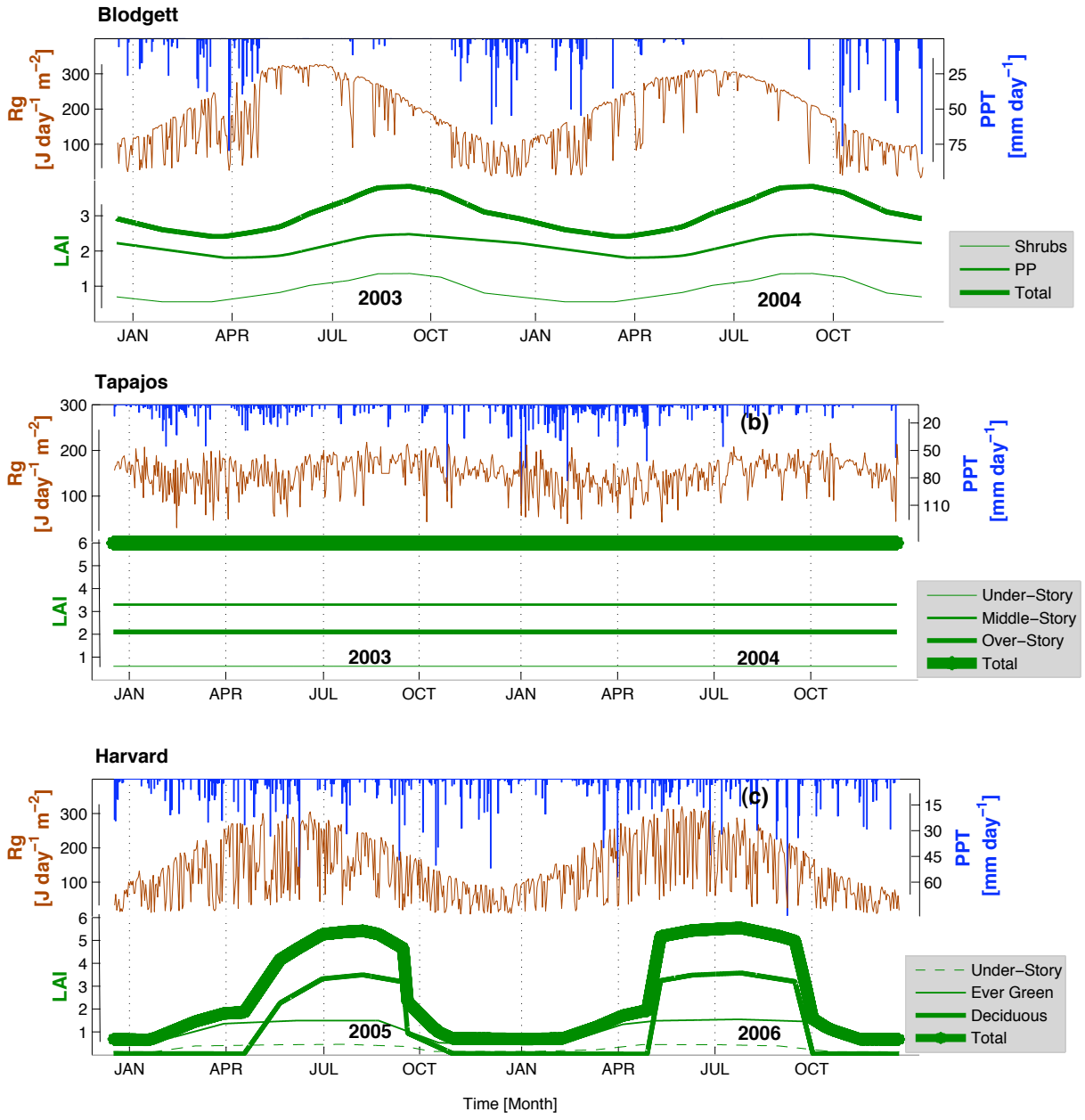

Figure 5.1: Forcing data for (a) Blodgett, (b) Tapajos and (c) Harvard Forest during the period of simulation. Rainfall data is displayed at the top, global radiation in the middle, and LAI for each functional type is shown at the bottom.

5.2.3 Entropy Budget

In this study the control volume used to delineate the ecosystem is displayed in Figure 5.2a. In this control volume we include all the plant functional type and the soil, and exclude the atmosphere that surround the vegetation. The entropy budget in this control volume is defined as:

$$dS_{eco} = dS_{ext} + dS_{int} \tag{5.1}$$

The change in entropy inside the control volume (dS_{eco}) is defined as the the sum of the entropy change associated with fluxes of mass and energy with the environment (dS_{ext}) and the production of entropy within the control(dS_{int}). At steady state, the total change of entropy in the ecosystem on an annual basis is assumed equal to zero, therefore:

$$\int_{year} dS_{eco} = 0 \tag{5.2}$$

and

$$\int_{year} dS_{int} = -\int_{year} dS_{ext}. \tag{5.3}$$

This suggest that the entropy production in the ecosystem under an steady state assumption can be obtained by the calculation of the entropy change associated with the interchange of fluxes of mass and energy with the environment. This rate of change can be expressed as [Kondepudi and Prigogine, 1998] given us:

$$\frac{dS_{ext}}{dt} = [S_{flux,E} + S_{flux,M}] \tag{5.4}$$

In this equation, $S_{flux,E}$ represents the fluxes of entropy associated with energy exchange, while $S_{flux,M}$ represents the fluxes of entropy associated to mass exchange with the environment. Although there is considerable flux of mass related to water, carbon, and several other nutrients, the entropy associated with mass fluxes is significantly lower than that associated with energy fluxes and therefore they are neglected in this study.

$$S_{flux,M} \approx 0 \ . \tag{5.5}$$

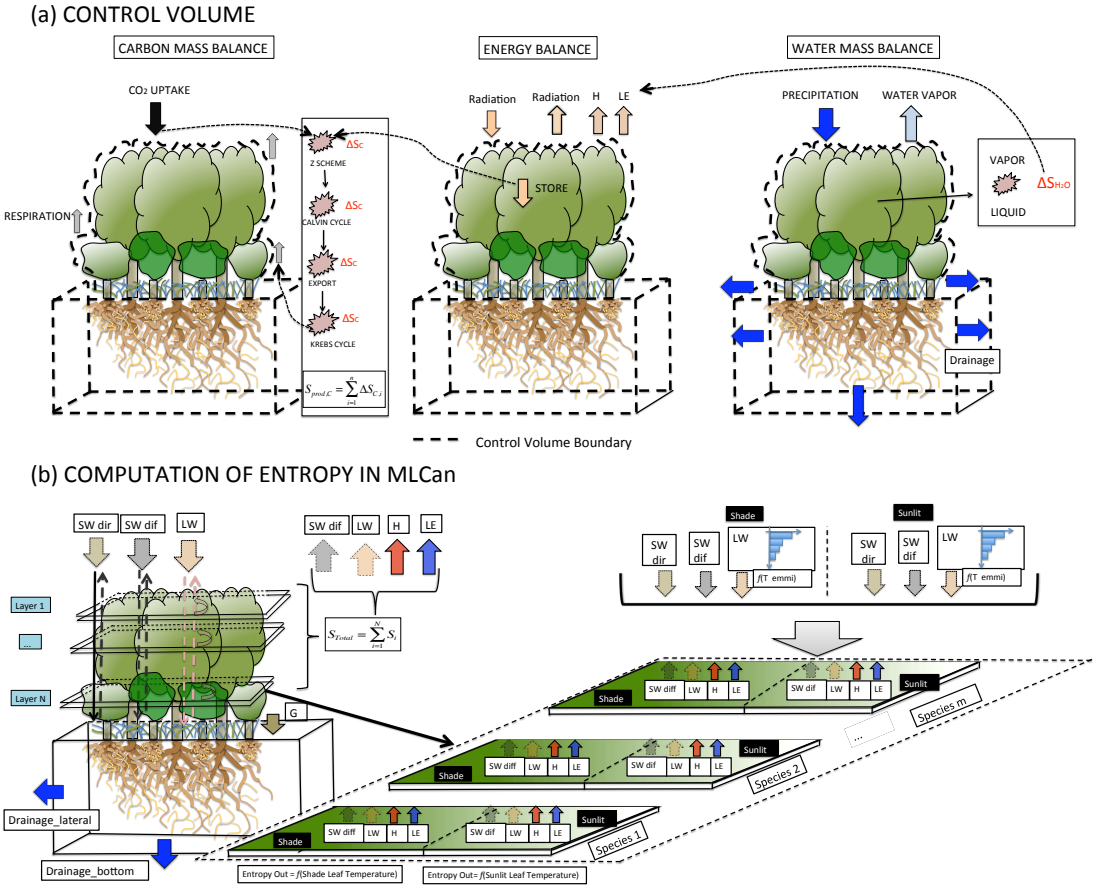

Figure 5.2: Scheme for entropy calculation. The top panel shows **(a)** the control volume utilized in the simulations. Open system experiences fluxes of mass and energy with the environment. The most relevant fluxes of mass between the control volume and the environment are due to carbon and water exchange. In this study we assume steady state conditions and the net annual storage of water and carbon negligible, thus the energy fluxes are the only fluxes that are considered in the entropy budget. The change of phase of water performed inside the control volume is included in the energy budget. Under the steady steady assumption the fluxes of carbon from respiration and carbon uptake are the same. The bottom panel shows **(b)** a schematic representation that illustrates the calculation of entropy in MLCan. Surface temperature is computed at different layers in the canopy (for different species, and for sunlit and shade leaves), and the soil. The computation of surface temperature is performed by solving energy balance at each location independently. Entropy fluxes are computed with all the components of the energy balance. The total entropy flux in the ecosystem is calculated by the sum of all the entropy fluxes in each components.

5.2.4 Model and Computation of Entropy

The model used in this study is Multi-species MLCan. This model is based on the initial approach developed by Drewry et al. [2010a,b]. In Quijano et al. [2012] (see Chapter 2) the model was extended to include the dynamics under the presence of different species that coexist in the same location.

All the different species that are present share a common atmosphere (Figure 5.2). Therefore, atmospheric states such as carbon, temperature and water vapor are mutually influenced by all the species simultaneously. In addition, incoming solar radiation is also shared by the species. In the model the availability of incoming solar radiation for each species is determined by solving the radiation regime using a compound LAD that includes all the species that are present. Below the ground the model includes the presence of different root systems from each PFT with unique ecophysiological and structural properties. These roots share a common pool of soil moisture from where they uptake water to satisfy the above-ground demand (See Chapter 2 for details).

In this study we use the capabilities of multi species MLCan to compute the fluxes of entropy between the ecosystems and their environment. Incoming solar energy in the form of radiation that reaches the ecosystem penetrates the canopy, and goes through absorption, reflection and transmission. Small fraction of the energy absorbed by the leaves is used for photosynthesis while the rest is dissipated in different forms such as latent heat (LE), sensible heat (H) and emission of LW radiation. The closure of the absorbed energy in these forms is what we called energy balance and there is a unique value of surface temperature that satisfies this balance.

Energy balance is solved by a non linear optimizer that finds the optimum temperature that satisfies a specified maximum error in the energy closure. The model solves the energy balance at all the canopy levels and the soil, and is performed for shaded and sunlit fractions separately [Drewry et al., 2010a]. In addition, the energy balance solution is performed independently for each of the PFTs that are present [Quijano et al., 2012] (see Figure 5.2). In the end, the model is able to compute the surface temperature with high accuracy and for different parts of the system. Although these processes involve intensive numerical computations at each time step, this level of detail to compute the temperature is particularly useful in the analysis of the thermodynamic entropy where the fluxes are highly sensitive to surface temperature.

The entropy associated to energy fluxes at a single discrete area ΔA_k of the system boundary surface area at which energy balance is solved (canopy or soil) is given by:

$$S_{flux,E,\Delta A_k} = \Bigg[\underbrace{[S_{SWdif,in} + S_{SWdir,in} + S_{LW,in}]}_{S_{in}} - \underbrace{[S_{SWdif,out} + S_{SWdir,out} + S_{LW,out} + S_{H,out} + S_{LE_{out}}]}_{S_{out}} \Bigg] \Bigg|_{\Delta A_k} \tag{5.6}$$

.

In this equation the terms S_{SWdir} and S_{SWdif} refers to the fluxes of entropy in the direct and diffuse shortwave (SW) radiation respectively, S_{LW} are the fluxes of entropy in the LW radiation, S_H and S_{LE} are the fluxes of entropy associated to sensible and latent fluxes respectively. Section 5.2.5 shows the approach implemented in this study for the computation of entropy in each of the energy forms that are considered.

Following the energy balance solution, the entropy fluxes are computed in the canopy for both, the shaded and sunlit fractions, at every layer, and for each PFT independently. Additionally, the entropy flux is also computed at the soil surface. Thus, the total rate of change in entropy associated with the fluxes of energy exchanged with the environment ($dS_{E,ext}$) is given by:

$$\frac{dS_{E,ext}}{dt} = \underbrace{\sum_{j=1}^{M_{PFTs}} \sum_{i=1}^{Nlayers} \sum_{shd,sun} S_{flux,E,\Delta A_{i,j}}}_{Canopy} + \underbrace{S_{flux,E,\Delta A_{soil}}}_{Soil} \tag{5.7}$$

The total entropy production over a period of time is calculated by the integration of $dS_{E,ext}$. For instance the total annual entropy production is given by:

$$S_{prod,yr} = S_{ext,yr} = \int_{year} dS_{E,ext} \tag{5.8}$$

5.2.5 Computation of Entropy in Heat and Radiation Fluxes

This section describes the methodology implemented for the computation of the entropy for different energy forms. The calculation of entropy in heat fluxes such as H and LE is performed by following a Clausius approach. In this approach the entropy flux is computed by the ratio between the energy flux and temperature of the surface boundaty (Equation 5.9). This approach is adopted from several previous studies [Aoki, 1982, Holdaway et al.,

2010].

$$S_Q = \frac{Q}{T_{surf}}. \tag{5.9}$$

In this equation Q is the heat flux and T_{surf} is the temperature of the surface boundary of the control volume. The calculation of entropy in direct and diffuse solar radiation is computed using the approach developed in Aoki [1982]. In this approach the entropy in direct SW radiation is given by:

$$S_{SW,dir} = E_{SW,dir}\frac{s1}{e1}. \tag{5.10}$$

In this equation the term e1 is the solar constant, s1 is the solar constant of second kind and E_{SW} is the energy in form of SW radiation reaching the control volume. In order to compute the entropy in SW diffuse radiation it is assumed that it behaves as a grey-body radiation with emissivity δ and emitted from a surface with temperature T_{sun}. A similar approach was used by [Wu and Liu, 2010]. Parameter δ is denominated scattering ratio of the SW diffuse radiation. According to Aoki [1982] this parameter can be computed as:

$$\delta = K_1/K_o. \tag{5.11}$$

In this equation, K_o is the extraterrestrial solar radiation per unit of solid angle, and K_1 is the radiance of diffuse solar radiation energy incident on the surface. The solution of entropy in a non black body radiation is performed here by implementing the approximation developed by Wright et al. [2001] where the entropy in non back body radiation is solved by integration of the spectral entropy flux over the solid angle and frequency [Wright et al., 2001, Wu and Liu, 2010]. This approximation has shown good results to solve the non linearity that arises in the entropy calculation of non black body radiation [Wu and Liu, 2010]. Following this approach the entropy in diffuse solar radiation is given by:

$$S_{SW,dif} = \left(\frac{45}{4\pi^4}\ln(\delta)\left(\delta C_2 - C_1\right) + 1\right)\frac{4}{3}\delta\sigma\frac{{T_{sun}}^4}{T_{sun}}. \tag{5.12}$$

In this equation the terms C_1 and C_2 are constants that were determined by Wright et al. [2001], σ is the Stefan-Boltzman constant, and T_{sun} is the sun temperature. Equation 5.12 can also be written as:

$$S_{SW,dif} = \underbrace{\left(\frac{45}{4\pi^4}\ln(\delta)\left(\delta C_2 - C_1\right) + 1\right)\frac{4}{3}}_{RF_{SW}} \frac{E_{SW,dif}}{T_{sun}} \tag{5.13}$$

where $E_{SW,dif}$ is the energy in the diffuse shortwave radiation. Note that RF_{SW} is a factor that controls the ratio between the flux of energy and the flux of entropy. RF_{SW} is denominated radiation factor for diffusion SW energy. Also, note that $RF_{SW,dif}$ is the proportion that represents the difference between the entropy computed using the approximation of Wright et al. [2001] and the entropy that would have been computed by following a straight analogy of Clausiuss entropy (as a ratio of energy flux to temperature) used for conduction or convection based heat transfer and apply it directly for radiative tansfer fluxes. The factor $RF_{SW,dif}$ and the difference in the entropy of radiation and the Clausius method arises from an entropy contribution from radiation pressure [Wu and Liu, 2010] and should not be omitted.

Again using the approximation of Wright et al. [2001] the entropy in the LW radiation is given as [Aoki, 1982, Wu and Liu, 2010]:

$$S_{LW} = \left(\tfrac{45}{4\pi^4}\ln(\varepsilon)\left(\varepsilon C_2 - C_1\right) + 1\right)\tfrac{4}{3}\varepsilon\sigma\tfrac{{T_{emi}}^4}{T_{emi}}. \tag{5.14}$$

In this equation the term ε is the emissivity and the term T_{emi} is the temperature of emission. This entropy can also be expressed as:

$$S_{LW} = \underbrace{\left(\frac{45}{4\pi^4}\ln(\varepsilon)\left(\varepsilon C_2 - C_1\right) + 1\right)\frac{4}{3}}_{RF_{LW}} \frac{E_{LW}}{T_{emi}} \tag{5.15}$$

where E_{LW} is the LW radiation energy and the term RF_{LW} is the radiation factor for the LW radiation flux.

5.2.6 Analysis Scenarios

In this study we analyze three scenarios that represent different levels of ecosystem organization. These levels of ecosystem organization are conceptualized with different structural and functional ecosystem properties. The following scenarios are considered:

(i) Scenario I Full Canopy, which includes the presence of all the PFTs.

(ii) Scenario II Understory, which considers only the understory PFTs, considering only shrubs in Tapajos, shrubs in Harvard Forest, and under and mid canopy trees in Blodgett.

The LAI is lower and roots are shallower than *Scenario I.*

(iii) Scenario III No Vegetation, which excludes all the vegetation and simulates the dynamics assuming a bare soil only.

5.3 Results and Analysis

5.3.1 Energy Fluxes Validation

The simulation results are validated with information of energy fluxes recorded at the Ameriflux towers. The period of simulation was selected according to the available record of measurements that present the more reliable information in a two year time frame. Figures 5.3a, b and c show diurnal fluxes of LE+H. These fluxes represent the average over two year period of simulations for each site. The fluxes of LE+H represent a good indicator for validation of the model because they are the main components in which the net radiation is dissipated $R_n = LE + H + G$. In Figure 5.3 we did not include ground heat flux G because there is no available records of this variable for all the three sites that are examined in this study.

Looking at Figures 5.3a,b and c, we observe that simulation results obtained from the model resemble the diurnal patters from the records and follows the same order of magnitude. The closest match between the model results and the observation occurs in Harvard Forest. In Blodgett the model matches the net diurnal fluxes with a small overestimation of about 40 Wm^{-2} in the morning that is compensated in the afternoon. In Tapajos, the model underestimates the fluxes throughout the day. The numerical mean energy balance errors in all the three sites were low ($< 4\mathrm{W/m}^2 \sim 1\%$). In addition, the ground heat fluxes simulated in Tapajos were significantly lower than the LE and H suggesting that the underestimation in the net radiation obtained in Tapajos might be produced by differences in the incoming energy that forces the model. In particular there is a high uncertainty in the incoming LW radiation which is computed by the Brutsaert approximation [Brutsaert, 1975].

The fluxes of LE and H displayed in Figures 5.3a,b and c correspond to the total heat that is dissipated by the ecosystem. This total is computed by the sum of all the heat fluxes (LE and H) dissipated by the different components such as all the PFTs and the soil. These components can be observed in more detail in Figures 5.3d, e and f where for illustrative purposes we select three days of August to display the dissipation of heat from all the PFTs.

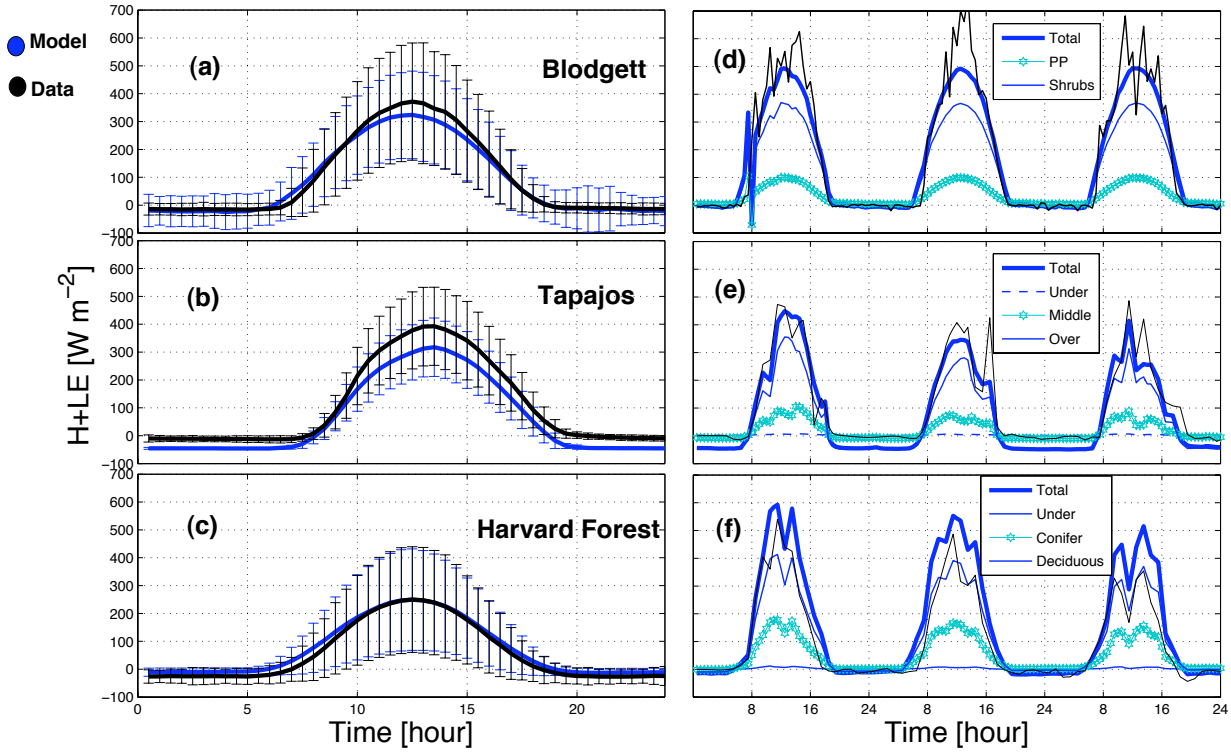

Figure 5.3: Fluxes of latent heat (LE) and sensible heat (H) in Blodgett **(a, d)**, Tapajos **(b, e)**, and Harvard Forest (**c, f**). The figures to the left (a,b,c) show the diurnal fluxes of LE+H calculated during the two years of simulation. Figures on the right display the fluxes during days 210, 211 and 212 selected to illustrate the contribution from each PFT.

As expected, in Blodgett and Tapajos the dissipation of LE and H from the over story is significantly larger than from the under story plants. In Harvard Forest, the dissipation of LE from deciduous trees was considerably higher than from evergreen plants. Although deciduous and evergreen plants are both distributed vertically through the canopy, there is a considerably higher LAI in the deciduous plants that accounts for their higher dissipation of heat.

5.3.2 Energy Fluxes

Figure 5.4 shows all the different energy fluxes for each site independently. All the information displayed in Figure 5.4 correspond to annual fluxes calculated by averaging the two year simulation. Figures 5.4 (i.a), (ii.a) and (iii.a) show the total annual fluxes of energy into the ecosystem. During daytime there are periods where income SW (direct + diffuse) radiation is higher than income LW radiation. However, LW is the dominant energy component during the night. Although the same pattern is observed in all the three sites the magnitudes differ. In the case of incoming LW radiation, the magnitude is strongly influenced by the atmospheric temperature where on annual average is higher in Tapajos. Moreover, the highest input of direct SW radiation occurs in Blodgett that experiences a mediterranean climate with little clouds during the summer period.

As expected the input of energy is the same for all the three scenarios. However, the dissipation of energy is affected by the surface structure and the outgoing energy varies with the scenario. Figures 5.4 (i.b), (ii.b) and (iii.b) show the energy fluxes in all the different forms in which the incoming energy is dissipated. Similar to the input energy, the highest dissipation flux is in the form of LW radiation. These are the most important differences:

- The dissipation of energy in the form of LE and H is higher in *Scenarios I and II*. Plants are able to reach into the deeper soil layers with available soil moisture and therefore they enhance the LE fluxes.

- The dissipation of energy in the form of LW radiation is higher in *Scenario III*. Although the net surface area of the control volume is reduced (not LAI) the temperature of the soil surface is significantly higher inducing higher fluxes of LW.

- The dissipation of energy in the form of SW radiation is lower in *Scenario I* and *II*. The SW radiation flux that is absorbed is related to the albedo of the surface and is affected by many processes including photosynthesis.

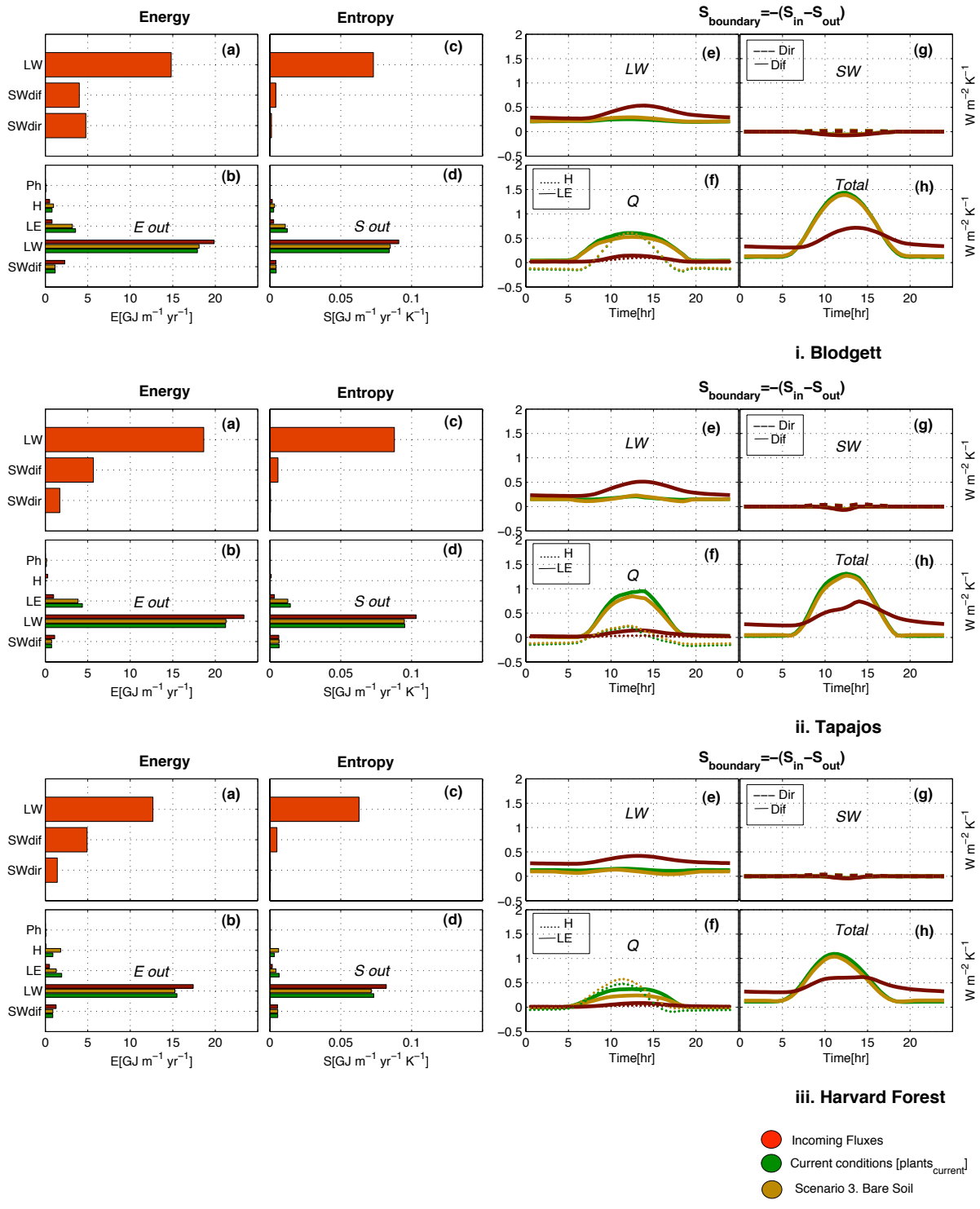

Figure 5.4: Fluxes of energy and entropy at (i) Blodgett, (ii) Tapajos, and (iii) Harvard Forest Sites. Panels on the left show the total fluxes of incoming **(a)** energy, **(b)** outgoing energy, **(c)** incoming entropy, and **(d)** outgoing entropy for each site separately. Panels on the right display the average diurnal fluxes of entropy in the form of **(e)** longwave, **(f)** heat, **(g)** shortwave, and **(i)** the total.

5.3.3 Entropy Fluxes

Figures 5.4 (i.c), (ii.c) and (iii.c) show the incoming fluxes of entropy. Again, incoming fluxes of entropy are independent of the structure at the surface and is the same for all the scenarios. The direct SW radiation is the most pure energy and has the lowest content of entropy. On the other hand the entropy content in LW radiation is significantly higher than the entropy in SW radiation. In addition, the highest incoming energy is in the form of LW. As a result there is a significant difference in the incoming entropy between LW and SW radiation (Figures 5.4 (i.c), (ii.c) and (iii.c)). This difference is more notable than in the energy case (Figures 5.4 (i.a), (ii.a) and (iii.a)). The same pattern is observed at the three sites.

Figures 5.4 (i.d), (ii.d) and (iii.d) show the entropy fluxes associated with the dissipation of energy at the surface. The highest flux of entropy dissipated from the system is in the form of LW. At all the sites the fluxes of entropy in the LW are highest in *Scenario III* while the fluxes of entropy in form of LE are highest in the presence of plants (*Scenario II* and *III*). The main difference observed between *Scenario I* and *Scenario II* is a higher flux of LE in *Scenario I* that is compensated by a reduction in H.

5.3.4 Diurnal Cycles

Figures 5.4(e), (f), (g) and (h) show the diurnal fluxes of entropy production ($S_{E,ext} = S_{E,int}$). These fluxes are displayed for the three sites and are computed by performing an average over the two years of simulation. As mentioned above for Figures 5.4c,d the highest fluxes of entropy are associated to LW radiation. However, large input and output fluxes of LW cancel out and the net magnitude of the net entropy associated with LW is on the same order of magnitude of the entropy associated to the other forms of energy (Figure 5.4e). During daytime periods the surface becomes warmer and there is a higher emission of LW from the surface. This process is more prominent in the absence of vegetation.

The net entropy fluxes associated with heat in *Scenario III* remains constant throughout the day with some small increments produced during the day associated with soil evaporation. On the other hand, in the presence of vegetation (*Scenario I* and *Scenario II*) there is a significantly higher flux of entropy associated with heat (LE and H) as compared with LW. As expected, entropy fluxes of SW are zero during nighttime. In general the levels of entropy associated to SW are significant lower than the entropy associated to heat and LW (Figure 5.4g).

The total flux of entropy is displayed in Figure 5.4h. There are clear differences between the patterns observed in the scenarios that are considered. In the presence of vegetation there is a higher flux of entropy during daytime that is sustained by the emission of LE. On the other hand, in the absence of vegetation there is a more homogenous pattern throughout the day with significant fluxes of entropy production during nighttime.

5.3.5 Seasonal Entropy Fluxes

Figure 5.5 shows the total entropy production for each month of the year at the three sites and for the three scenarios. The entropy production reflects a similar dynamics as the incoming SW radiation (See Figure 5.1). This pattern is expected since SW is the form of incoming energy to the system that has the lowest entropy. Therefore, the capacity of the system to maximize the production of entropy rely on the incoming SW radiation. Following the patterns of SW radiation, the entropy production in Blodgett and Harvard Forest have a prominent seasonality with higher values during summer and lower during winter. In Tapajos, the entropy production is relatively constant during the year. However, the production of entropy from July to November are slightly higher than the production of entropy during the rest of the year. The period between July and November coincides with the dry season and therefore the time of the year with highest SW radiation reaching the ecosystem.

Note that the entropy production in Blodgett during the summer period (May to September) shows the highest levels of entropy production per month in all the three sites. The mediterranean climate in Blodgett are characterized by dry summers and wet winters. Dry summer allows for a clear sky during the time of the year when most SW is present. Therefore at Blodgett the dry conditions during the summer enhances the production of entropy. This situation does not occur at Harvard Forest where rainfall is present all the year around. Figures 5.1a and c shows that Blodgett and Harvard Forest have the same daily maximum SW radiation during the summer but the SW radiation in Harvard Forest fluctuates more resulting in a net lower income of SW radiation when compared with Blodgett. These dynamics are reflected in Figure 5.5a,c where the entropy production in Blodgett during the summer period is considerably higher than in Harvard Forest.

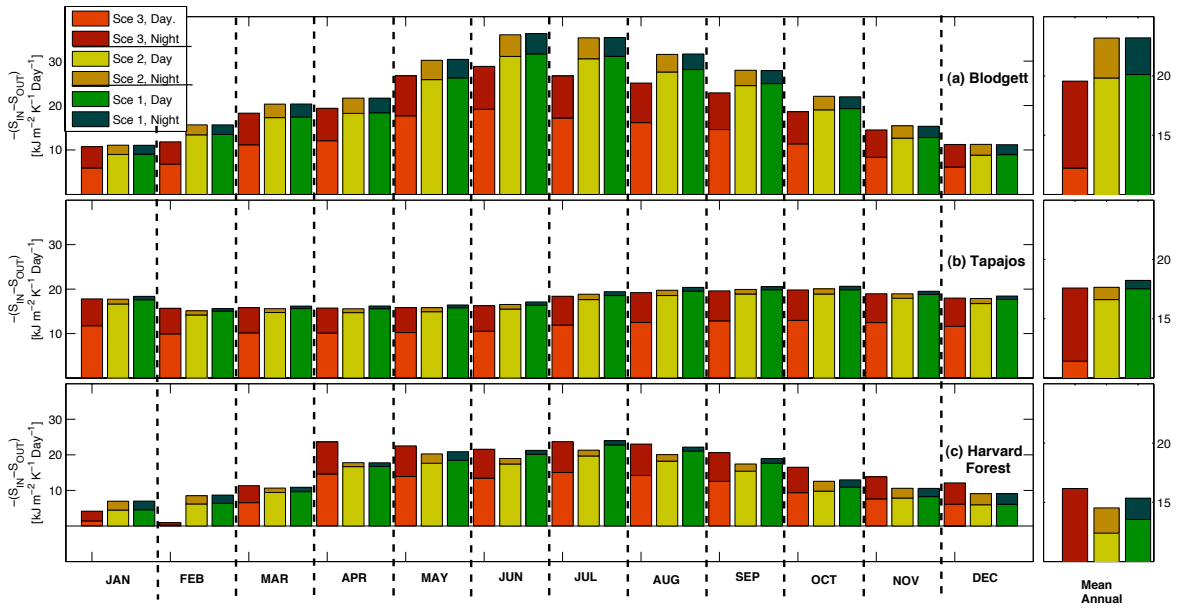

Figure 5.5: Seasonal fluxes of entropy in **(a)** Blodgett, **(b)** Tapajos, and **(c)** Harvard Forest. The figure shows the mean monthly fluxes of total entropy produced in units of $[\mathrm{kJm^{-2}K^{-1}Day^{-1}}]$. The total entropy is composed of entropy produced during nighttime and daytime periods. Fluxes of entropy are displayed for each scenario independently. Total entropy production is higher in the presence of platns (*Scenario III*) in Blodgett and Tapajos. On the other hand, the fluxes of entropy production in Harvard Forest is higher in the absence of plants. The fluxes of entropy production in Blodgett are higher than in Tapajos and Harvard Forest due to a higher availability of incoming shortwave radiation during the summer period.

5.3.6 Radiation and Effective Temperature

Figure 5.5 shows that the entropy production under the presence of vegetation is higher in Blodgett and Tapajos. However, in Harvard Forest there is a higher production of entropy in the absence of vegetation during most of the year. In Harvard Forest, the higher entropy production observed in April, May and November in the absence of vegetation is explained by a longer period of snow cover in the presence of vegetation. Vegetation reduces the fluxes of radiation that reaches the soil surface. Therefore, the amount of energy available to melt the snow is lower than if plant were absent. Lower radiation reaching the soil surface prolongs the period with snow.

From section 5.3.2 we observed some important differences in the entropy produced by the surface under the presence and absence of vegetation. These differences can be useful to analyze the patterns observed in Figure 5.5. The flux of diffusive SW energy emitted by the surface is higher in *Scenario III* (Figure 5.4b). However, the fluxes of entropy in SW emitted by the surface are very similar for all the scenarios. Although *Scenario III* emits a higher energy flux of diffuse SW, the entropy in the diffuse SW is inversely proportional to its flux. This pattern is expected since a lower flux of SW reflects a higher level of transformation from its original state. Therefore, in *Scenario III* the higher emission of energy in the form of SW radiation is damped by a lower amount of entropy per unit of energy. In the end, the differences of entropy in the diffuse SW between *Scenarios I*, *II*, and *III* are negligible.

The difference in the amount of entropy per unit of energy in the emission of diffuse SW between *Scenarios I* and *II*, and *Scenario III* can be observed clearly in terms of $\mathrm{RF_{SW,dif}}$ (Equation 5.13). Figure 5.6a shows the mean diurnal pattern for the diffuse shortwave radiation factors ($\mathrm{RF_{SW}}$) for all the scenarios and sites. The values of $\mathrm{RF_{SW,dif}}$ are higher in *Scenarios I* and *II* than in *Scenario III* reflecting a higher entropy per unit of energy in the diffusive SW flux emitted in the presence of plants.

Figure 5.6a shows also the diurnal patterns for the LW radiation factor ($\mathrm{RF_{LW}}$). Note that $\mathrm{RF_{LW}}$ is constant throughout the day. This is expected since $\mathrm{RF_{LW}}$ is only a function of the emissivity (ε) of the surface that is emitting LW which is assumed constant. Also, note that $\mathrm{RF_{LW}} \sim 1.34 > 1$ which implies that the entropy per unit of energy is higher in LW radiation than in heat.

In order to facilitate the analysis we compute an effective temperature $\mathrm{T_{surf}}$ by performing an entropy budget at the entire ecosystem:

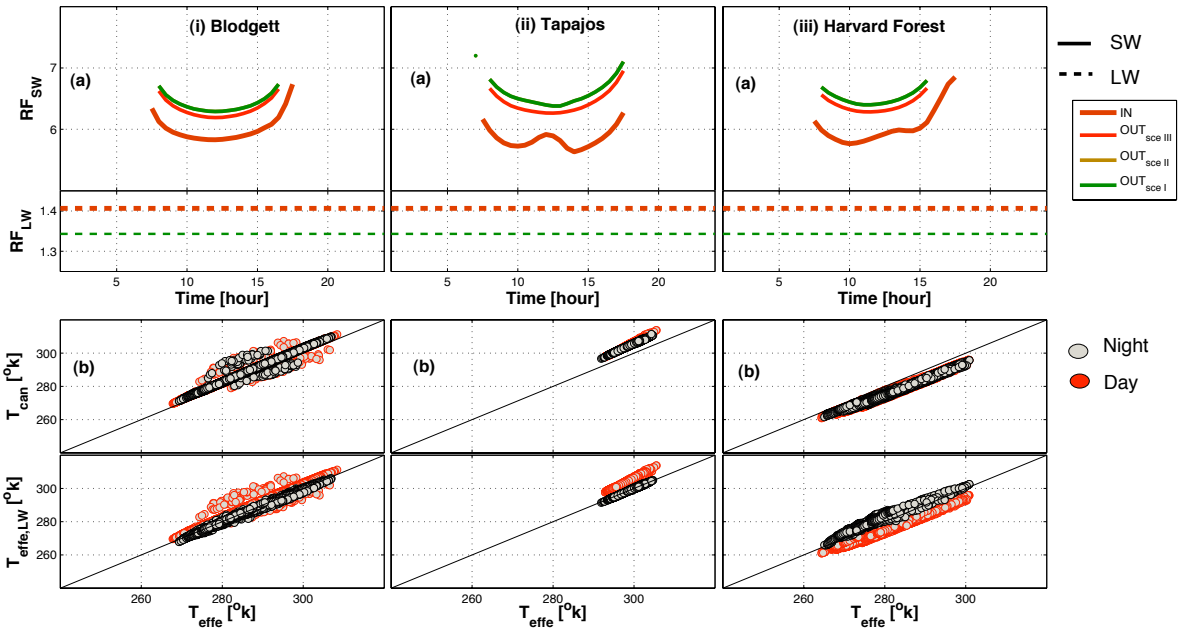

Figure 5.6: Figures on the top show **(a)** the mean diurnal patterns of radiation factors for diffuse shortwave (RF_{SW}) and longwave (RF_{LW}). It can be observed that RF_{SW} is lower in the incoming diffuse shortwave. In addition, the outgoing diffuse shortwave RF_{SW} is higher in the diffuse shortwave emitted from the surface in the presence of plants resulting in a higher fraction of entropy per unit of diffuse energy in *Scenario I* compared to *Scenario III*. On the other hand, RF_{LW} is higher in the incoming longwave compared to the outgoing. RF_{LW} is function of the surface emissivity and therefore there are no significant differences in the outgoing RF_{LW} between *Scenarios I* and *II*, and *Scenario III*. The bottom panels **(b)** show scatter plots between the effective temperature T_{effe} computed with the production of entropy, and temperatures obtained from the longwave emission ($T_{effe,LW}$) and the mean temperatures in the canopy T_{can}.

$$
\begin{aligned}
S_{NET,ECO} \quad = \quad & [S_{SW,dir} + S_{SW,dif} + S_{LW}]_{IN,ECO} \\
& - \left[S_{SW,dif} + \frac{E_{LW}}{T_{effe}} + \frac{LE}{T_{effe}} + \frac{H}{T_{effe}}\right]_{OUT,ECO}.
\end{aligned}
\tag{5.16}
$$

In this equation the subscript ECO represents fluxes at the entire ecosystem, subscript IN refers incoming fluxes (computed with the forcing information recorded in the Ameriflux Towers) and subscripts OUT and NET refer to outgoing and net fluxes respectively in the system (computed by aggregating all the results obtained from the model including all the components in the canopy and the soil). From Equation 5.16 it is possible to compute T_{effe}. Therefore, this effective temperature is computed in order to satisfy the entropy budget. There are other different alternatives to compute the effective temperature of the surface under the presence of plants. For instance, a simple approach is to consider the mean canopy temperature (T_{can}) as the effective temperature of the surface. Other approach that has been implemented in previous studies is to perform a back calculation of the Stefan−Boltzmann law ($T_{effe,LW}$) using the LW radiation emitted by the surface. Figure 5.6 shows scatter plots of (T_{effe} vs $T_{effe,LW}$) and (T_{effe} vs T_{can}). Although T_{effe}, $T_{effe,LW}$, and T_{can} are very similar there are some slighly differences. The scatter plot T_{effe} vs T_{can} shows a divergence from the 45° line throughout the day. On the other hand there is a good match between T_{effe} and $T_{effe,LW}$ during nighttime. However, $T_{effe,LW}$ is calculated with only fluxes of LW while T_{effe} is obtained with both LW and sensible and latent heat fluxes. This difference is accentuated during daytime because the heat fluxes are more prominent. In this study we use T_{effe} because is the effective temperature that matches the fluxes of entropy.

Figure 5.7a shows T_{effe} for all the scenarios and sites. It can be observed that T_{effe} is significantly higher in the absence of vegetation. Furthermore, T_{effe} is lower in *Scenario I* than *Scenario II*. As expected the presence of overstory species reduces the effective temperature.

From Figure 5.7a we observe that the higher emission of LW under bare soil is associated to a much higher surface temperature. Although the surface area of emission is higher in the presence of plants (from leaves, $1 <$ LAI) the emission of LW is proportional to the temperature of emission to the power of four and therefore the magnitude of temperature might become more relevant than the area of emission for the emission of LW.

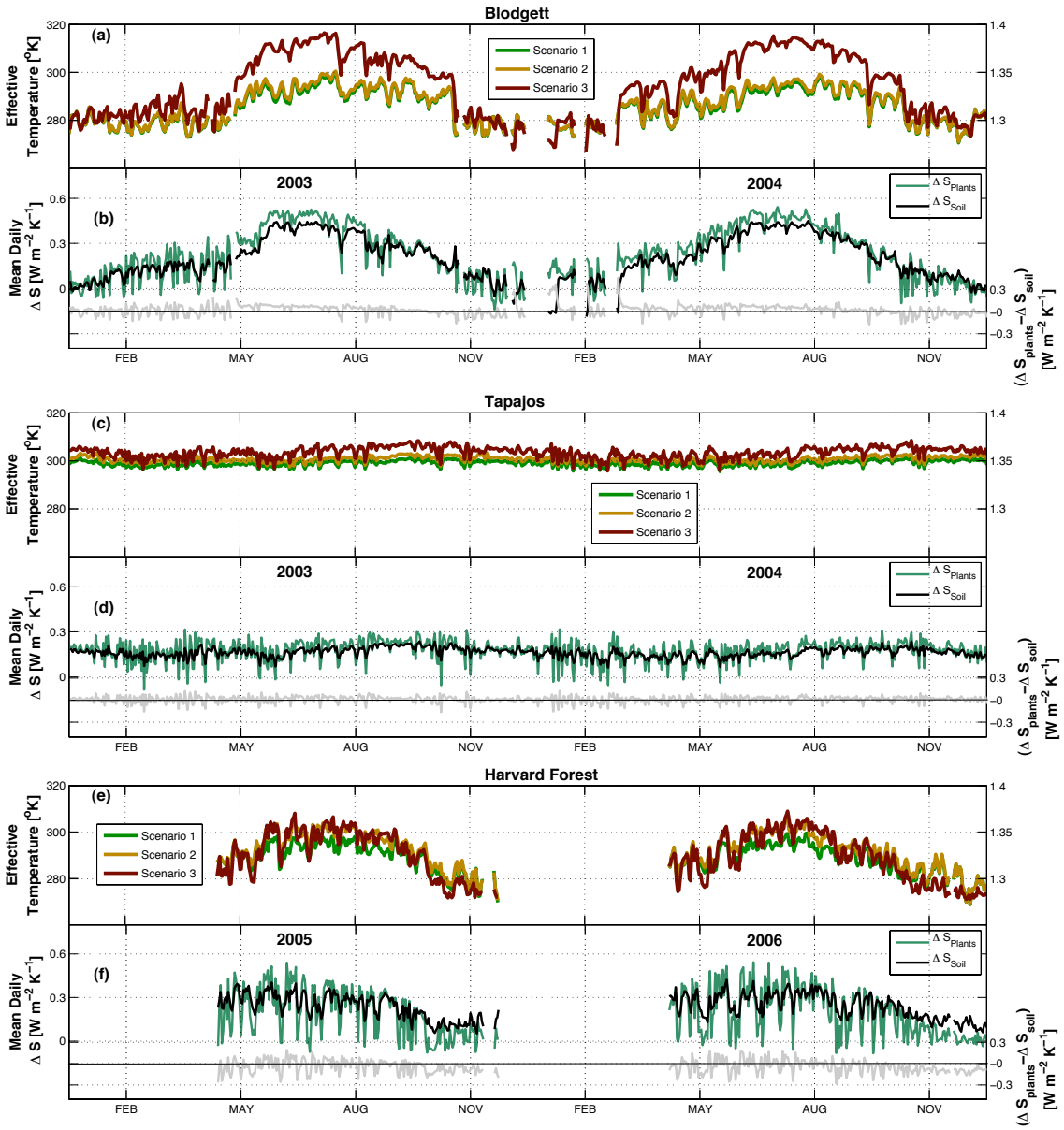

Figure 5.7: Top figures **a,c,e** show the effective temperatures for all the different scenarios. The presence of vegetation results in a significant lower temperature in Blodgett. In Harvard Forest the difference is not as significant. The bottom figures **b,d,f** show the Trade off between a lower temperature in the presence of vegetation (*Scenario I*), and a higher emission of longwave radiation from a bare soil (*scenario III*).

5.3.7 Comparisson of Entropy Production from Plants and Soil

The lower T_{effe} in the presence of plants displayed in Figure 5.7b is caused by two main mechanisms: (i) higher surface area, that reduces the amount of radiation absorbed per unit of surface area, and (ii) higher fluxes of LE that cools the surface. In the end, the reduction of effective surface temperature in the presence of plants allows to enhance the production of entropy because all the outgoing fluxes of entropy are inversely proportional to the temperature of the surface.

On the other hand the factor RF_{LW} (Equation 5.14) influences the amount of entropy per unit of energy flux in the LW. This factor is very similar in all the scenarios because it is function of the surface emissivity (ε). From Figure 5.6 we observed that $RF_{LW} > 1$ implying there is more entropy per unit of energy in the LW compared to heat. Therefore, more emission of LW radiation instead of heat (as in the bare soil, *scenario III*) will maximize the production of entropy from the surface.

There is a trade off in the production of entropy from the surface. In the presence plants the surface temperature is reduced, therefore there is an enhancement of entropy production that is given by:

$$\begin{aligned} \Delta S_{plants} = & \left(\frac{SW_{out}}{T_{effe}} + \frac{LW_{out}}{T_{effe}} + \frac{LE_{out}}{T_{effe}} + \frac{H_{out}}{T_{effe}} \right)_{plants} - \\ & \left(\frac{SW_{out}}{T_{effe}} + \frac{LW_{out}}{T_{effe}} + \frac{LE_{out}}{T_{effe}} + \frac{H_{out}}{T_{effe}} \right)_{BareSoil} \end{aligned} \tag{5.17}$$

On the other hand, in the absence of plants there is a higher emission of LW which contains higher entropy than heat. Therefore, there is an enhancement of entropy production in the absence of plants which is given by:

$$\Delta S_{baresoil} = RF_{LW} \left[\left(\frac{LW}{T_{effe}} \right)_{baresoil} - \left(\frac{LW}{T_{effe}} \right)_{plants} \right]. \tag{5.18}$$

Figure 5.7b shows the plot of ΔS_{plants} vs $\Delta_{baresoil}$. The trade off between ΔS_{plants} and $\Delta_{baresoil}$ resembles the same pattern as that displayed in Figure 5.5. In Blodgett and Tapajos ΔS_{plants} is higher for most of the period of simulation. On the other hand, in Harvard Forest $\Delta S_{baresoil}$ is slightly higher during the summer period. These results confirms that T_{effe} and LW are the most relevant factors regulating the emission of entropy from the surface. In the case of Harvard Forest, the reduction in the surface temperature under the presence of vegetation is not enough to compensate the entropy it would have produced under a bare soil scenario.

5.3.8 Entropy Production in the Absence of Vegetation

In the absence of vegetation the entropy production is maximized by increasing the absorption of SW and increasing the emissivity of LW. There is ample evidence that the reflectance of shortwave by the soil is inversely proportional to soil moisture. In this study we implement the exponential shape function suggested by Gascoin et al. [2009] to simulate the role of soil moisture in the albedo. Figure 5.8a shows the albedo throughout the year, for the three sites and for *scenarios I* and *III*. The simulations results show a higher albedo in the presence of vegetation for all the scenarios. As expected, in Harvard Forest (also in less magnitude in Blodgett) the albedo increases during the winter due to the presence of snow. During no winter periods the highest difference in the albedo between *scenario I* and *scenario III* occurs in Blodgett during the summer period. During the summer period the rainfall in Blodgett is very scarce with no events at all resulting in significant dry conditions in the top surface. Therefore, during this period soil albedo increases significantly.

Figure 5.8b illustrates the effect of soil moisture and albedo on the entropy produced under a bare soil scenario in Blodgett. When albedo is not affected by soil moisture (remain constant as 0.15) the entropy produced under the bare soil scenario is significantly higher during the dry period.

Another important mechanism that impacts the entropy produced by a bare soil is the ability to emit LW which is regulated by the soil emissivity ε_{soil}. A higher magnitude of ε_{soil} will allow for a higher emission of LW under a given soil temperature. The values utilized in the simulations are $\varepsilon_{soil} = 0.85$ and $\varepsilon_{veg} = 0.95$ for the soil and vegetation leaves respectively which are on the range reported by previous studies [Galantowicz et al., 1999, Humes et al., 1994, Njoku and Entekhabi, 1996]. However, soil emissivity depend on several factors such as soil moisture content, soil organic composition, soil structure, and soil color [Jin and Liang, 2006] and therefore there is an uncertainty associated to these values.

5.3.9 Entropy Production in the Presence of Vegetation

The presence of vegetation reduces the net effective temperature of the surface enhancing entropy production. According to the trade off introduced in Section5.3.7 the presence of vegetation will produce more entropy than the bare soil scenario if the effect from a lower T_{effe} overcomes the effect of a higher LW emission from a bare sol. In Blodgett and Tapajos the lower T_{effe} results in a higher entropy in the presence of plants. However in Harvard Forest the higher emission of LW from the soil overcome the reduction in T_{effe} from the

plants. It seems the reduction in T_{effe} in Harvard Forest is not enough to overcomes the high emission of LW from the bare soil.

The most relevant mechanism to increase the production of entropy in the presence of vegetation is by reducing T_{eff}. This mechanism is attained by increasing the LAI and increasing the fluxes of LE. The inclusion of the overstory species in *scenario I* resulted in a lower net temperature compared with *scenario II* for the three scenarios.

In Figure 5.9 we perform a sensitivity analysis of LAI on the production of entropy. This figure illustrates the evolution of the entropy production as LAI increases, starting from a bare soil situation where LAI= 0. Increase of LAI induces a gradual reduction in the entropy produced from LW (S_{LW}), and there is a gradual increment in the entropy produced from LE (S_{LE}). These patterns are consistent in all the sites. Also, there is a consistent increment in the production of entropy as the LAI increases. However, in Harvard Forest lower T_{effe} in the presence of plants under high LAI never overcomes the entropy production obtained under a bare soil scenario. In addition Figure 5.9 displays the values of T_{effe} along the gradient in LAI. As expected higher LAI results in lower T_{effe} because it induces a higher flux of LE.

5.4 Summary and Discussion

In this study we have analyzed the production of entropy under three scenarios that consider different structural and functional properties emulating different levels ecosystem organization. We found that the total production of entropy from these scenarios is on the same orders of magnitude. However, the diurnal patterns of entropy fluxes varies between the three scenarios. In the presence of vegetation the highest amount of entropy is produced during daytime periods, and this pattern is more prominent when overstory plants were present (*Scenario I*). On the other hand, the production of entropy in the absence of vegetation (*Scenario III*) is distributed more homogeneously throughout the day.

The production of entropy is affected by the capacity of the surface to dissipate the incoming energy in the form of LE flux. This mechanism is enhanced in the presence of plants because they have the capacity to reach a higher pool of moisture that is present in deeper layers of the soil. The numerical simulations performed in this study show that the immediate effect of a higher LE flux is a reduction of the effective surface temperature. Therefore, the effective temperature is lower in the presence of vegetation and the reduction was more prominent when the overstory vegetation was present because they enhance the fluxes of LE. Similar patterns of effective surface temperature under the presence of vege-

tation were obtained in previous studies using experiments over terrestrial ecosystems with Infrared Multispectral Scanner (TIMS) [Luvall et al., 1990].

Lower effective temperature in the presence of vegetation (*Scenario I*) enhances the production of entropy from the surface because all the entropy fluxes are inversely proportional to temperature. However, in the absence of vegetation the lower flux of LE is compensated with a higher flux of LW radiation emitted from the surface. The amount of entropy per unit of energy in the LW radiation is higher than heat fluxes. Therefore, in the absence of vegetation higher dissipation of energy in the form of LW enhances the production of entropy. Thus, the net difference in entropy production under a surface with different levels of organization is regulated by the trade off between a reduction of T_{effe} when LE is maximized (more developed ecosystems), and a higher emission of LW when LE is lower (less developed ecosystems). The simulations results show that the total entropy production in the different scenarios analyzed in this study are on the same order of magnitude. The main differences between the scenarios that are considered lies in the effective temperature of the ecosystem and in the distribution of the entropy production in the different components of the energy balance.

In this study we analyzed the dynamics for three sites that experience different climatic conditions. We found that the main patterns described above are present in these three sites. However there are some differences that are worth to mention. Although the total fluxes of entropy were similar for the three different scenarios, in Blodgett and Tapajos the reduction in T_{effe} under the presence of overstory PFTs (*Scenario i*) overcome the higher LW in the absence of vegetation and results in a slightly higher production of entropy. On the other hand in Harvard Forest the reduction of temperature in *Scenario I* was not enough to overcome the higher emission of LW in the absence of vegetation resulting in a higher entropy production in the absence of vegetation.

We observed that the pattern of total entropy production resembles the patterns in the incoming SW. Therefore, the total entropy production presents a clear seasonality in template ecosystems such as Blodgett and Harvard Forest, and a more homogenous distribution throughout the year in tropical ecosystems such as Tapajos. Moreover, the highest production of entropy fluxes occurs in Blodgett Forest and is associated with a net high flux of incoming direct SW radiation that takes place in this site.

In this study we have made an attempt to quantify the link between different levels of ecosystem organization and the production of entropy from the surface. We have conceptualized this organization in terms of functional and structural properties. The calculation of

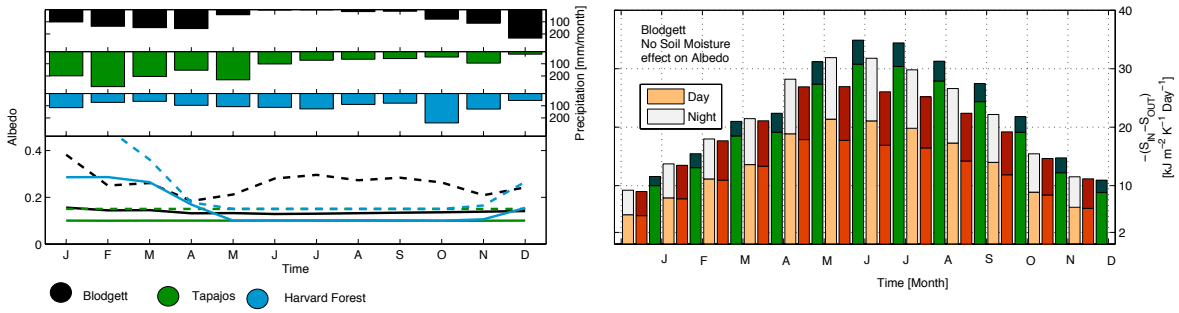

Figure 5.8: Influence of soil albedo on the production of entropy under the absence of vegetation. The figure to the left **(a)** shows the soil albedo during one year of simulation for all the three sites including in the analysis. Top panels in (a) display the mean monthly precipitation. The figure to the right **b** shows the influence of soil moisture in the production of entropy from Blodgett Forest.

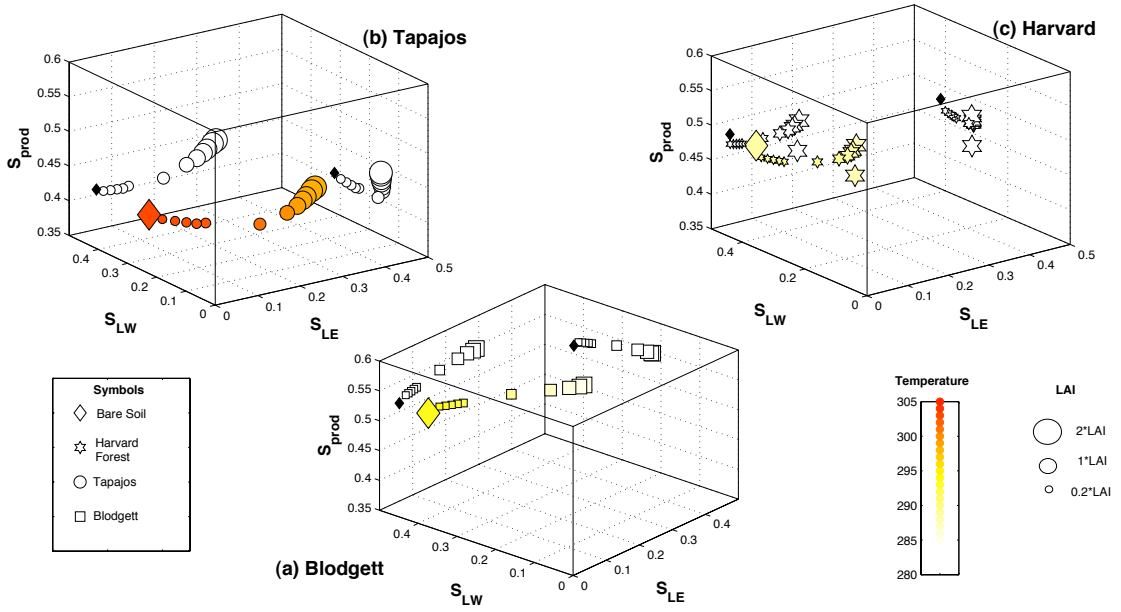

Figure 5.9: Sensitivity analysis of LAI on the entropy production. The analysis is displayed for each site independently. Each plot is showing the tradeoff between the total entropy produced S_{prod}, the entropy produced from LW (S_{LW}) and the entropy produced from LE (S_{LE}) along the gradient in LAI. In addition T_{effe} is displayed as a color gradient. The values of entropy associated to a bare soil scenario are shown by the diamond symbol.

entropy production were performed with numerical simulations implemented with a detail multi layer above- and below-ground model. We are aware that the numerical approach followed in this study is sensitive to some parameters and site specific information. However, we have made an effort to include the most realistic information and use the fluxes recorded in Ameriflux Sites to validate the model. On the other hand the numerical approach has allowed us to investigate the production of entropy from the surface under different conditions and therefore improve our understanding regarding the role of vegetation in the production of entropy from the surface.

CHAPTER 6

Conclusions

This study focused in the analysis of the above- and below-ground interactions that occurs in the Critical Zone. The main objective was to understand better these interactions in the light of different processes that they influence. In this chapter we present the conclusions and findings from this work. Initially, we describe briefly the most representative results from each chapter separately. Later, we analyze all the results in a holistic perspective that integrates across different processes. In the last part of this chapter, we provide some possible future avenues of research that can be achieved after this study.

6.1 Research Summary

Competitive and Mutualistic Dependencies in Multi-Species Vegetation Dynamics Enabled by Hydraulic Redistibution

In this study we have explored the first and second research questions exposed in the introduction. We analyzed the role of multiple coexisting species in the above-and below ground interactions and how they impact the energy and water balance in the surface. Traditional approaches in Ecohydrology have examined the role of vegetation on the water and energy fluxes but have not included interacting multiple vegetation species. In this study we analyzed these interactions under the presence of different species that coexist. In particular, we examine how the interactions between plant species influence the energy and water balance, and in turn how these processes impact the ecosystem productivity. The solution of energy and water balance is performed for both, the canopy and the soil. The numerical solution includes the presence of a litter layer that lies over the soil. Litter layer is ubiquitous in natural ecosystems and is an important element that regulates the energy and water balance. This was the first numerical study that examined the ecohydrological dynamics mediated by HR under the presence of different interacting species and that included litter layer in the simulations. The most important findings are:

- Several experimental studies have pointed to the importance of HR in multi-species ecosystems as processes that mediates mutualistic feedbacks between plants [Brooks et al., 2006, Dawson, 1993, Emerman and Dawson, 1996, Espeleta et al., 2004, Moreira et al., 2003]. However, the previous modeling exercises involved a single species neglecting the competitive or mutualistic interactions between species. This study represents the first modeling attempt to analyze the below-ground water dynamics under the presence of different plant species. This modeling approach provides a framework for the predicting distribution and use of resources by different species. In addition it quantifies the contribution from each species to the fluxes of water and energy.

- Previous numerical studies have indicated the potential for HR to induce significant fluxes of soil evaporation during dry periods [Lee et al., 2005, Wang, 2011]. These studies turn off HR assuming death of fine roots in the near-surface layer during dry periods. However, experimental studies examining the response of fine roots during dry periods have shown a gradual reduction of root conductivity and have reported that HR is a mechanism that can help to prolong root survival. We analyze these dynamics under different scenarios including the presence of litter. The presence of litter represents an important factor in the balance of energy and water [Ogee and Brunet, 2002, Park et al., 1998]. We found that the presence of litter layer reduced the incoming radiative energy reaching the soil and hinders the demand of moisture by the atmosphere. Our simulations results show that both, HR, and the presence of litter helped to prolong the functioning of fine roots by maintaining higher levels of water potential in the near surface layer. In addition, we found that litter layer influence the ecohydrological dynamics in shallow soils by maintaining moisture in the soil that otherwise would have been evaporated. This moisture is an important resource for shallow rooted plants.

- The simulations performed in this study show that facilitation of water resources in the below-ground by ponderosa pine trees with deep roots enhances productivity of shrubs during the summer period. Although the significance of this process is sensitive to the maximum root depth of shrubs, still these results support the hypothesis that plant interactions could be an important missing mechanism that is not included in current ecohydrological and climatological models. Specifically, in the long term the survival of some species could be supported by the coupled interactions with other species.

Role of Climate and Species Composition on Hydraulic Redistribution

In this study we have explored in detail the secong and third research questions exposed in the introduction. We analyzed the water fluxes in the presence of coexisting species in different sites that experience different climates. In particular, we explored the role of climate and species composition on the fluxes of hydraulic redistribution.

Uptake and release of water by plant roots in the soil is an important component of the hydrologic cycle. Uptake of moisture by roots maintains the rates of transpiration. On the other hand, release of water through HR modifies the distribution of soil moisture and impact several processes the below the ground. The magnitude of transpirational fluxes has been studied for long time with experiments and models. This is not the case with HR where numerical and experimental evidence is limited and report different orders of magnitude [Neumann and Cardon, 2012]. In this study we performed numerical simulations to analyze the implication of different factors on the fluxes of transpiration and HR simultaneously. We analyzed three ecosystems that experience different climatic conditions. Although there are several uncertainties related to below-ground processes, this comparative examination provided important insights about these fluxes along a range of climates and vegetation types. The most important findings are:

- Seasonal variation of precipitation and incoming shortwave are the most important factors for the fluxes of HR because in the end they are the regulators of water potential gradients in the soil. Seasonal precipitation with long dry periods enhances HR while temporally uniform rainfall reduces HR. In contrast, a homogeneous distribution of shortwave radiation, such as in the tropics, enhances HR because it supports a constant rate of transpiration throughout the year.

- Previous studies of HR assumed a single vegetation. In this study we use multi species MLCan to analyze whether different vegetation species releasing and taking up water simultaneously from a common pool of soil moisture would impact the net flux. By comparing a simulation performed with several co-existing species, and a simulation with a single bulk species we found that the fluxes of HR were significantly affected. HR was enhanced under the presence of different species. The interaction of multiple species also impacts the transpirational fluxes. These results support the hypothesis that species diversity and interactions impact eco-hydrological fluxes.

- We analyzed the effect of root hydraulic conductivities on the fluxes of transpiration and HR. We found that both axial and radial conductivities are limiting factors of these fluxes. However, the magnitude of HR fluxes were more sensitive to the root

radial conductivity since it regulates the connectivity between the root system and the soil. This analysis showed the sensitivity of numerical modeling to root hydraulic conductivities.

- Previous studies have considered transpiration as a method for the validation of HR fluxes. In this study we observed that transpirational flux impacts the water potential gradients in the soil and therefore it enhances HR. However, the effects of climate, root hydraulic conductivities, and vegetation composition induces different patterns in the magnitude of HR and transpiration, and these patterns are not always correlated. Therefore, we posit that the measurement of transpirational fluxes are not sufficient for the validation of HR.

Passive Regulation of Soil Biogeochemical Cycling by Root Water Uptake

In this study we have explored the second and third research questions exposed in the introduction. In particular we analyzed the role of water transport in regulating above- and below- ground interactions and how these processes impact the biogeochemical cycling of carbon and nitrogen.

We examined the role of different vegetation species in the cycling of nitrogen and carbon in the soil. Specifically, we analyzed how different composition of species influence the dynamics of carbon and nitrogen by: (i) modification of the energy and water balance at the surface thereby impacting the states of soil moisture and temperature, (ii) regulation of decomposition by the quantity and quality of nitrogen content in litter drop, and (iii) impact on soil moisture due to uptake and redistribution of moisture in the soil. The study was conducted with information from Blodgett Ameriflux site by contrasting two different species that coexist, overstory ponderosa pine, and shrubs. The most important findings from this study are:

- The co-existence of the two species showed a larger long-term pool of organic matter and nitrogen in the soil. Specifically the presence of shrubs increases significantly the pool of nitrogen because of their low C:N ratio.

- The energy balance solutions differ between the simulations performed with only one species and that with two species. The presence of two species increases the LAI, and less amount of radiation reaching the surface. Soil temperatures were lower when the two species were present reducing the rates of decomposition. However, in the presence of two species the amount of organic matter was higher and supported a larger microbial

pool that counteracted the effect of lower temperature. Steady state solution in the long-term showed higher decomposition when the two species were present. This study represents the first numerical attempt to simulate the implications of multiple species in the cycling of carbon and nitrogen that includes dynamics associated with both, (i) the effect of litter drop, and (ii) the regulation of energy balance at the surface inducings changes in soil moisture and temperature.

- This study developed the first numerical approach to analyze the role of HR in the biogeochemical cycling of carbon and nitrogen. The simulations performed here support the results from previous experimental studies that have reported enhancement of decomposition by hydraulic lift (HL) at near surface horizons. However, we also found HL could impact the energy balance by releasing moisture to the soil and enhancing evaporation. Under such situation the temperature in the soil would become lower and the positive effect on decomposition is damped. A sensitivity analysis showed that functioning of fine roots located in the near surface is a very critical factor that impact the fate of organic matter in the soil.

- Previous experimental studies reported that HR fluxes enhance decomposition rates. However, these studies are performed over short time scales. In this study we perform long term simulations to analyze the accumulation of organic carbon in soils. We were able to show that higher decomposition rates in short time scales induced by HR impact the soil organic matter concentration, which in turn impact processes such as bioturbation and decomposition rates. In the end, the long-term dynamics of carbon show the same decomposition rates in the presence or absence of HR, but the concentrations of organic matter were different.

Entropy Production in Ecohydrologic Systems

In this study we have explored the fourth research question exposed in the introduction. We analyzed the second law of thermodynamics (specifically the production of entropy) and its connection with the organization of ecosystems.

Concepts related to the second law of thermodynamics such as entropy or free energy provide insight of the actual energy available to perform work in an open system and can be used to examine the organization and functioning of ecosystems. It is believed that open ecological systems self organize to attain some specific functions related to the second law of thermodynamics. Previous studies in ecohydrology have computed entropy budgets without linking it with different levels of ecosystem organization. In this study we have made an

attempt to analyze the interaction between the different levels of ecosystem organization and the production of entropy. We conceptualize the organization of ecosystems in terms of structural and functional properties and examine how the production of entropy is affected by these properties.The most important findings from this study are:

- We found that the dissipation of energy in the form of latent heat is an important mechanism that impact the production of entropy. Latent heat fluxes reduce the effective temperature of the surface and therefore enhances the production of entropy.
- We also found that dissipation of energy in the form of longwave maximizes the production of entropy because the entropy content in the longwave is higher than the entropy content in heat fluxes.
- Following the previous results we found there is a trade off between the dissipation of energy in the form of longwave and latent heat. This trade off regulates the link between different levels of ecosystem organization and the production of entropy. We did not find significant differences in the total production of entropy between the levels of organization that we explore through different structural and functional properties. However, the diurnal patterns of entropy production were significantly different.
- We found some differences between the different sites that were analyzed. Although the total production of entropy were similar for all the levels of ecosystem organization considered, there were some differences from site to site. In Blodgett and Tapajos there was a higher production of entropy in the presence of vegetation, while in Harvard Forest the production of entropy was higher in the absence of vegetation. In addition the production of entropy resembles the incoming shortwave and was highest in Blodgett were the mediterranean climate allows for high inputs of shortwave.

6.2 Integrated Examination Across Different Processes

In this work we have studied the above- and below-ground interactions in view of different processes that occur in the Critical Zone. The analysis performed for these processes independently allowed us to obtain specific conclusions, that were described in the previous section. In this section we provide a synthesis of these understanding.

Figure 6.1 shows an schematic representation of the synthesis of above- and below-ground interactions characterized through this study. We can observe different ecological, biogeo-

chemical, hydrological, and thermodynamical processes occurring the CZ. All these processes are connected and are mutually regulated, and should be examined under an integrated framework.

From Figure 6.1 we can observe the role of water as the primary resource that is responsible for competitive and facilitative intra- and inter-specific interactions; in biogeochemical processes as the main mechanism to transport nutrients and facilitator of biochemical reactions that mediates processes such as decomposition or mineralization; as the main regulator of the energy balance at the surface; and also the main mechanism to maximize the production of entropy.

Previous ecological studies have explored the different interactions that occur between plants and soil biota communities. They have recognized the role of above- and below-ground biodiversity in these interactions and have reported mutual feedbacks between components above and below the ground. The present study adds to these understanding by characterizing the influence of water, energy, and entropy as mediators of these interactions, and how species interactions impact the fluxes of water, energy, and entropy.

An important contribution of this study was quantification of how vegetation is able to influence the below-ground communities not only by providing biochemical energy but also by regulating the dynamics of soil moisture and soil temperature. An important mechanism that mediates these processes is *hydraulic redistribution* where plants can modify the distribution of water moisture in the soil and under some specific conditions it can also impact soil temperature.

Biodiversity and species richness are fundamental variables in Ecology. However, the development of ecohydrology has overlooked biodiversity and has been more focused in the understanding of water and energy fluxes. In this study we have explored the role of biodiversity using species composition as its surrogate in these interactions by a simple approach where we have examined the coexistence of different plant species that are in the same location and share resources. Another important outcome of this study is the recognition of plant biodiversity as a factor that impact the fluxes of mass, energy, and entropy. Therefore, the feedbacks between biodiversity, and water and energy dynamics should be considered and analyzed in detail. Specially in the light of climate change where alterations of biodiversity will impact water and energy dynamics and vice-versa.

We are aware that the approach we implemented in this study oversimplifies the complexity that is present in plant species interactions. However, this study represents an important attempt to link ecological, biogeochemical, hydrological and thermodynamical processes. We

hope these results lead to new avenues of research oriented to understanding the coupled interactions between all these processes.

6.3 Future Research

In this study we have examined above- and below-ground interactions in the CZ. The approach we have followed is based on numerical simulations that have been performed in different ecosystems. We have provided an integral framework to analyze these interactions in view of different processes, and the main purpose has been to complement experimental studies in our goal to analyze these interactions in the CZ.

This study is part of a multidisciplinary effort oriented to understand different processes that occur in the CZ at different time, and spatial scales. The numerical developments implemented in this study, and the results obtain can open new avenues of research that can elucidate new patterns in the CZ. In this section I describe some of these research avenues.

6.3.1 Modeling of plant-mycorrhizal symbiosis

In this work we have not considered direct interactions between plants and microorganisms. However, these interactions have been recognized as main mechanisms that impact the composition and structure of above- and below-ground processes. In particular, important advances have been reported in the interaction between mycorrhizal fungi and plants which is a symbiotic interaction that occurs in roughly 80% of plants in the planet. There is evidence that this interaction is an important mechanism that supply nutrients to plants and structure the composition of plant species [Grime et al., 1987].

Although these interactions have been mainly recognized as important suppliers of nutrients, recent studies have also reported their connection to water functions in plants. There is evidence that myccorrizae fungi can enhance water uptake [Marulanda et al., 2003, Ruiz-Lozano, 2003]. In addition, mycorrhizal symbiosis can include different individual trees from the same species creating a common network which has been denominated as 'common mycorrhizal network' (CMN). It has been reported that CMN can facilitate water from mature trees to seedlings through HR [Warren et al., 2008]. These findings suggest the capacity of mycorrhizal symbiosis to enhance vegetation dynamics not only by supply of nutrients but also water. This lead to the following hypothesis: *Interactions between plant roots and mycorrhizal fungi impact the cycling of water and nutrients below the ground and impact the*

fluxes of water and energy from the surface, as well as the productivity of plants Although the role of mycorrhizal symbiosis to enhance nutrients and water uptake in plants has been tested in experimental studies, still there are few modeling efforts that have quantified the implications of these interactions on the fluxes of energy and water from ecosystems. This is an open problem that can be explore through numerical simulations.

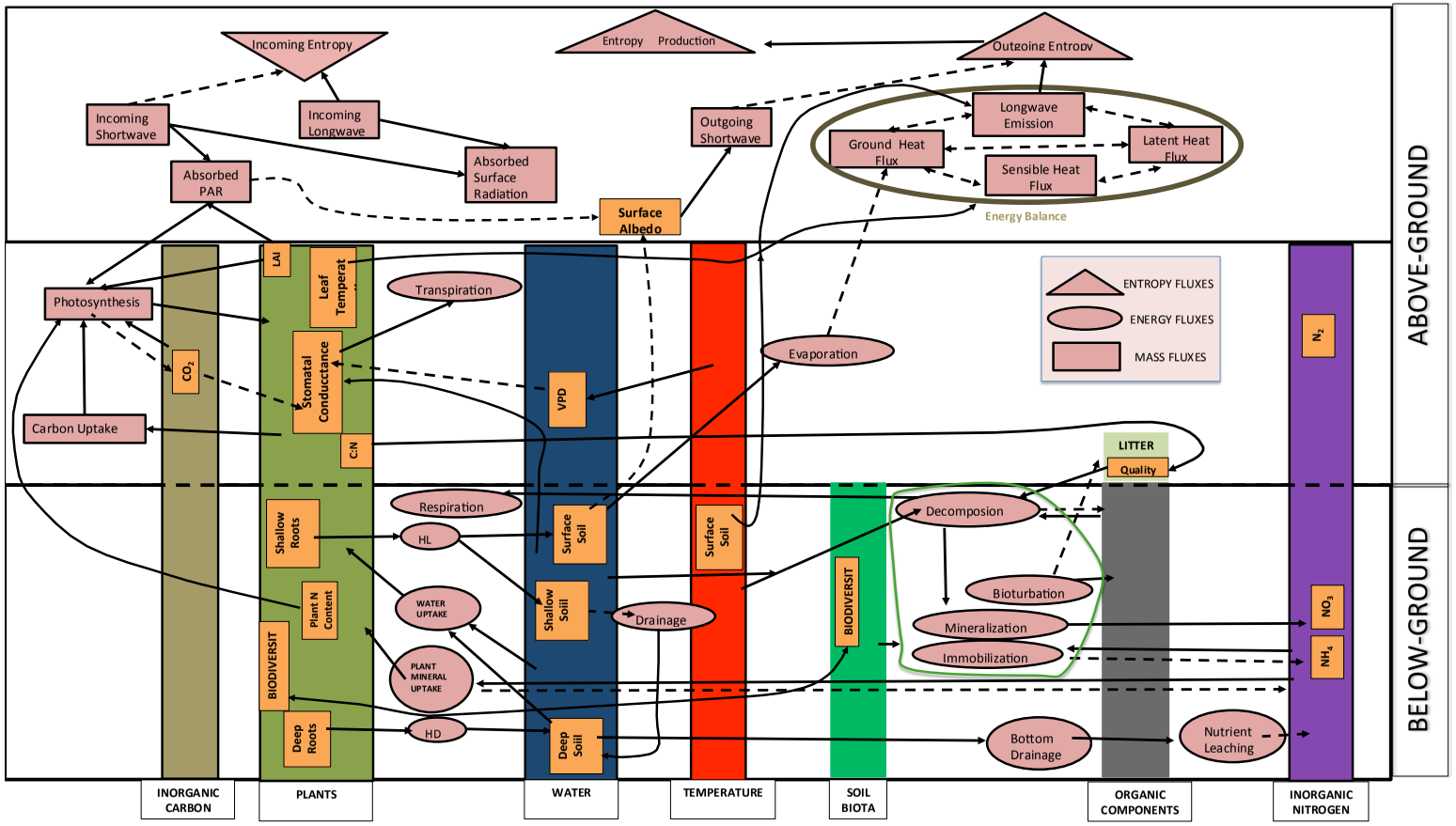

Figure 6.1: Illustrative Figure of the Above- and below-ground feedbacks in the Critical Zone. Solid lines represent positive feedbacks, and dash lines represent negative feedbacks.

Previous experimental studies have observed functional differences between arbuscular and ectomycorrhizal mycorrhizal symbiosis. In addition there is increasing evidence showing some degree of plant specificity [Eom et al., 2000, Molina and Trappe, 1982] in these interactions. Simulation of mycorrhizal symbiosis could be performed in the light of different species using Multi Species MLCan. Ectomycorrhizal and arbuscular symbiosis must be simulated independently following our current understanding from the experiments that have been performed in the last twenty years in different ecosystems and plant species. Simulation of these symbioses should consider the effect they have in the uptake of nitrogen, and water from the soil. Modeling of ectomycorrhizal and arbuscular symbiosis can be performed by extending root properties. The formulation must be performed using available experimental evidence that quantify the capacity of this interaction to enhance nutrient and water uptake.

Once, we have different formulations for ectomycorrhizal and arbuscular symbiosis, it is possible to utilize the specificity formulation in Multi Species MLCan to perform simulations of these symbiosis under different plant hosts. This approach would allow to perform comparative studies of ectomycorrhizal and arbuscular symbiosis in different ecosystems, and under different situations such as the presence of both symbiosis or only one of the two. This approach will allow us to understand the role of this symbiotic interaction on the water, energy, and carbon fluxes following a similar approach as that performed in this study.

6.3.2 Large-Scale- Spatial Modeling: Role of Plant Biodiversity

The simulations in this study have been performed in different Ameriflux Sites separately. The numerical formulation implemented includes the dynamics in the vertical domain only, and the spatial scale comprise only the footprint of an Ameriflux tower. In addition, we have not considered several ecological dynamics such as growth, dispersal, and external disturbance mechanisms such as fire.

Simulations at larger spatial scales than those implemented in this study may provide more fundamental answers regarding the role of biodiversity in the cycles of water, and energy in the planet. In addition, the consideration of species dynamics will enable us to have a more clear understanding of the species interactions at longer time scales. This leads to the hypothesis that: *Facilitative and competitive interactions between coexisting plant species serves as an important regulatory mechanism.*

In order to accomplish this research we need to perform numerical simulations at larger spatial scales, and by considering species dynamics. Although Multi Species MLCan could

be modified in order to perform such large scale simulations, the most optimal option would be to incorporate the capabilities that are present in Multi Species MLCan into an existing numerical model that is able to perform large scale simulations. There are several numerical models that can perform large scale simulations. The most known is the Community Land Model (CLM), which is able to perform ecohydrological and biogeochemical simulations at high spatial scales. CLM model is the result of an collaborative work of different scientists and has been used for different studies in the last decade to analyze the connection between soil, land surface and atmosphere processes. The model includes the concept of ecological climatology which is an important framework that allows to examine the role of vegetation on climate. This framework suggest that terrestrial ecosystems can influence climate by their impact on the cycling of energy, water, and biogeochemical elements. This conceptualization is particular useful and therefore we believe CLM 4 would be an appropriate choice to examine the objective that has been proposed.

There is a important modification to CLM 4 that will increase its potential to examine the feedbacks between climate change and vegetation biodiversity.

CLM 4 uses PFTs as a proxy to biodiversity. The implementation of PFTs in CLM 4 is an adequate form to include vegetation composition while reducing the level of complexity to deal with biodiversity. Although in CLM 4 all the PTFs are represented in a grid cell, they are separated into independent patches. Therefore, under this formulation species do not coexist in the same location. We can use the same formulation developed in Multi Species MLCan to consider overlapping of PFTs that share resources and coexist in the same location. This formulation is consistent with ecological observations and could be incorporated following the experience from Multi Species MLCan.

6.3.3 Role of soil structure in the above- and below-ground interactions

The development and formation of soils occurs from different processes occurring at different time scales. The soil structure and fertility are relevant regulators of above- and below-ground processes. The implications of soil structure on hydrological processes have been studied for a long time. Today, it is well known that soil properties such as the hydraulic conductivity controls the flux of water in the soil [van Genuchten and Leij, 1992]. In addition, the structure of the soil has been associated to the net primary production (NPP) of ecosystems [Lvovich, 2004], the cycling of biogeochemical elements [McClain et al., 2003], and plant nutrition [Chiarini et al., 1998]. Furthermore, some studies have reported on the

role of soil type on microbial communities [Chiarini et al., 1998]. In some cases, soil type was reported as the most important factor influencing the distribution and composition of microbial communities in the rhizosphere [Singh et al., 2007].

The studies mentioned above suggest the strong influence that soil type has on the composition of vegetation and soil communities in natural ecosystems. However, soil, plants, micro flora, and fauna have been co-evolving for long time. Therefore, it is likely that the living component is making an imprint on the soil properties a well. There is evidence of soil structure modification by additions of soil organic matter (SOM) in the presence of plants and microorganisms. SOM enhances the aggregation and stabilization of the soil [Golchin et al., 1994, Oades, 1993, Rillig and Mummey, 2006]. In addition, the presence of biotic structures such as roots may induce the generation of macropores [Beven and Germann, 1982] in the soil matrix which in the end will modify the porosity and hydraulic conductivity of the soil matrix.

At long time scales the living component may also impact other soil properties such as the mineral composition, and therefore the ultimate soil type. The magnitude of the time scale over which such feedbacks occur creates a challenge for the generation of a proper hypothesis to be tested. Some hypotheses have been postulated and they have been very useful to improve our conceptualization of the co-evolution of soils within natural ecosystems. For instance, Albretcht suggested the evolutions of soil may be explained by a curve [Albrecht, 1940, Huston, 2012] where different soil properties (such as clay content, exchange capacity, base saturation, and organic matter) change along time. Soil evolution occurs at long time scales and is regulated by climate. An important variable of soil evolution is weathering which is an important process that over time changes the mineral composition of soils. According to Albrecht the curve reaches a peak at which evapotranspiration becomes equal to precipitation.

Another important hypothesis of soil evolution in the light of ecohydrological interactions is Eagleson′s third Hypothesis [Eagleson, 1982]. This hypothesis suggest that ecosystems evolution in the long term is associated with alterations in the soil in such a way that these alterations occur to increase ecosystem productivity. This lead to the hypothesis that: *In the long term the composition of vegetation will shape the soil structure that impact the energy balance in the surface and the productivity of ecosystems.*

Although, several relevant properties of soils such as exchange capacity, base saturation, and content of minerals impact the fertility of plants, in this research proposal soil structure is associated only to content of clay, sand, and organic matter. In particular, this research

proposal intends to analyze the role of soil organic mater only. We suggest to analyze these interactions in view of different plants functional types using Multi Species MLCan and examine the role of different species in the formation of soils.

This research will improve or understanding of the mutual feedbacks between plants and soil structure. We propose to analyze steady state solutions under different compositions of plant species. We believe that steady state solutions of soil organic content will be different according to the composition of species that are considered. This pattern is supported by the simulations performed in this study. For instance, the long term simulations of carbon and nitrogen performed in Chapter 4 showed different results of soil organic carbon accumulation at steady state in the presence and absence of shrubs. The main implications of soil structure in the ecohydrological fluxes are associated to changes in soil porosity and changes in the saturated hydraulic conductivity of soils. In order to determine the effect of soil organic matter on the hydraulic conductivity of the soil we must implement a pedotransfer function that accounts for organic matter such as the function obtained by Saxton and Rawls [2006]. We suggest to analyze these dynamics in different ecosystems and implement the next simulations in each ecosystems:

- Perform long term simulations for different combinations of PFTs.
- The simulations for every particular combination of PFTs must be performed with a pedotransfer function that includes soil organic matter, and a control simulation when soil organic matter is not considered in the pedotransfer function.

With these simulations we can analyze: (i) the effect of different combinations of coexisting PFTs on soil soil organic matter, and (ii) the role of soil structure on ecohydrological fluxes of carbon, water, and energy such as ecosystem productivity, and transpiration.

This formulation will be an adequate approach to examine the feedbacks between species diversity, soil structure, and ecohydrological fluxes of water and energy in natural ecosystems.

APPENDIX A

Multi-Species Mlcan Model Description

A.1 Previous Models

Ecological Approaches to Model Species Interactions

The existence of different species in natural ecosystems is observed everywhere. Today we know that natural ecosystems are networks of different species that have coevolved and this coevolution has been an important factor in the survival of the species that are observed. The interaction between different species and their role in biodiversity has been an important component of community ecology. To improve our understanding of this concept, experimental studies have been conducted in different communities. In parallel to these studies there have been several modeling attempts oriented to simulate species interactions and to provide further information about their behaviour.

The first models developed to analyze interspecific interactions such as competition or mutualism where based on single species approaches that were expanded to include multiple species. The first approaches used the well known logistic equation (Equation A.1). This equation describes the growth of abundance (N) of a given population at a given exponential rate r and includes a carrying capacity K in such a way that when the abundance in the population approaches the carrying capacity the growth becomes zero. This equation was used initially by Pearl and Reed [1920] to describe dynamics in human populations. Later, it has been implemented in many other different species.

$$dN/dt = rN(1 - N/K) \tag{A.1}$$

The logistic equation was extended by Lotka [1925] and Volterra [1926] to include the competition between different species that share a specific resource. The authors included two species that share resources and have specific growth rates and carrying capacities. This model is composed by two differential equations that are coupled (Equation A.4). The

growth in one species is controlled by the abundance of the other species. There is a new factor $\alpha_{i,j}$ which was denominated as *the competition coefficient* and describes the extent of the competition. This factor quantifies the role of species j into species i by translating the abundance of species j into i using a common currency.

$$\begin{array}{l} \frac{dN_1}{dt} = \frac{r_1 N_1 (K_1 - N_1 - \alpha_{12} N_2)}{K_1} \\ \frac{dN_2}{dt} = \frac{r_2 N_2 (K_2 - N_2 - \alpha_{21} N_2)}{K_2} \end{array} . \tag{A.2}$$

When more than one species is present, Equation A.1 can be extended to include more species that share a common resource. In this case there will a matrix of competition coefficients from all the possible species interactions i, j. These dynamics can be described mathematically using equation A.3

$$\frac{dN_i}{dt} = \frac{N_i r_i \left(k_i - \sum_{j=1}^{n} \alpha_{ij} N_j \right)}{k_i} \tag{A.3}$$

The coexistence of species can have also positive feedbacks in which case there will be a positive interaction. These kind of interactions have been recognized in many communities and were termed mutualism. According to Boucher [1985] there are four basic forms by which this interaction occurs (i) energetic, (ii) nutritional, (iii) protective, and (iv) transport. The first attempts to model mutualism dynamics used the same logistic approach (Equation A.4). However, in this case the coeficiens $\alpha_{1,2}, \alpha_{2,1}$ are positive rather than negative:

$$\begin{array}{l} \frac{dN_1}{dt} = \frac{r_1 N_1 (K_1 - N_1 + \alpha_{12} N_2)}{K_1} \\ \frac{dN_2}{dt} = \frac{r_2 N_2 (K_2 - N_2 + \alpha_{21} N_2)}{K_2} \end{array} . \tag{A.4}$$

The presence of many species could involve both mutualistic and competitive interaction. Therefore the matrix $\alpha_{i,j}$ could have negative and positive elements.

The application of these models was helpful to improve our insight into the competition and mutualistic interactions that arises when species coexist and share common resources. However, these models rely in theoretical parameters such as the carrying capacities and the coefficient factors. Further approaches attempted to have a more realistic quantification of the carrying capacities and coefficient factors by implementing mechanistic models under which these capacities were linked to several other variables such as realistic abilities of the different species to exploit and deplete resources. The implementation of these models allowed to analyze more realistic scenarios. Although the mathematical complexity increased

due to inclusion of more variables and non linear functions describing the carrying capacities, in some cases analytical solutions were still achievable.

The improvements performed to the logistic equations not only allowed to have more realistic conditions but also to understand in more detail the competitive and mutualistic interactions. However, the dynamics described by the model were simple compared to the complexity observed in experiments. Consequently, the field of plant ecologist started to develop models that included more dynamics. Scientist in this field felt the need of modeling each individual tree as unity, observe the variations at the individual level and analyze their connection with other species and their environment. These ideas gave birth to individual base models [Holling, 1964] that simulate and track the changes in each individual in the system. These models were to able to get rid of two important assumptions that were used in previous approaches, (i) all individuals are identical, and (ii) the population is spatially mixed.

From the individual base models different branches with different assumptions and processes were generated. One important approach that contributed to the understanding of competitive interactions is the neighborhood model developed by Pacala in a series of papers [Pacala, 1986a,b, Pacala and Silander, 1990]. In their work they tried to introduce intra and interspecific competitions in plants by generating the concept of neighborhood. They assumed that individual plants respond and are affected by competition only in a neighborhood limited by the specific radius around the plant. This neighborhood impacts individual dynamics such as survival and fecundity. The influence of competition on fecundity is assumed to follow an exponential decay function. The population in a future time step N_{t+1} can be predicted by the population in a current time step N_t using the following equation:

$$N_{t+1} = gPN_tMe^{-gPN_t\gamma}. \tag{A.5}$$

In this equation g is the probability of germination, P is the probability of a germinated seed to survive adulthood, M_t is the number of seeds that an individual plant produces and $\gamma = 1 - exp(-c)$ where c is a parameter that describes the intensity of the neighborhood competition. The same equation can be extended to more species using a similar approach as that obtained with the logistic equation.

$$\begin{aligned} N_{1,t+1} &= g_1P_1M_1N_{1,t}e^{(-g_1P_1N_{1,t}\gamma_{11} - g_2P_2N_{2,t}\gamma_{12})} \\ N_{2,t+1} &= g_2P_2M_2N_{2,t}e^{(-g_2P_2N_{2,t}\gamma_{22} - g_1P_1N_{1,t}\gamma_{21})} \end{aligned} \tag{A.6}$$

The model was also performed with numerical simulations All the individuals at different

stages in a given species, were taken into account in the simulations. Although the analytical model was more exact and simpler to analyze, the numerical solution was able to account for more species.

Another important family of models that branched out from the individual base approach are the Gap Models. In this approach each tree is simulated as an independent entity. The model introduces the concept of mosaic dynamics in the sense that it simulates a small patch of forest. The size of the patch varies according to the simulations but usually it was on the order of 0.1 ha. The first Gap model called JABOWA was presented in Botkin et al. [1972]. The name "GAP" was given some years later [Shugart and West, 1980] as a description that matches both, the individual level and the mosaic concept.

GAP models are computational expensive because they solve processes at a gap level. However, these models beyond been less expensive than solving each individual tree, allow to simulate spatial heterogeneity. The simulations include competition between different trees that share a common environment. The most evident competition factor is light. Light is divided in the canopy according to heigh and LAI of each tree. This competition is simulated by including an attenuation of the radiation regime through the canopy according to the vertical distribution of leaf area index. The vertical distribution of the leaf area index depends on plant growth and carbon allocation. The level of detail considered in the above-ground competition for light varies according to the model. Several GAP model versions with different levels of detail have been created. However, less detail has been considered for the below-ground competition. At that level, the competition is performed by a simple allocation of resources using equations based on root biomass [Wullschleger et al., 2001].

Ecohydrological Modeling

The field of Hydrology is directly involved in the analysis of the water cycle on the Earth. In this regard, hydrological studies are oriented to improve our understanding of the recirculation of water at different time and spatial scales. In the last decades, hydrologists started to notice the role of vegetation in the hydrological cycle. Plants are able to penetrate deeper in the soil and obtain moisture from places where bare soil evaporation would not be able to reach. In the end, the presence of plants results in a significant higher release of vapor in the atmosphere with important relevant consequences in the hydrological cycle.

Hydrology as a field has emerged from engineering. Therefore, modeling and the prediction ability have been important components of this field. The role of vegetation and the high uncertainty in the evapotranspiration term under the standard hydrological models were

important arguments that lead hydrologist to include more detail vegetation processes in the modeling exercise. These fact gave raise to Ecohydrology a subfield of Hydrology which is particularly related to the analysis of interactions between the biological processes and the hydrological cycle. The most relevant and influencing contributions to Ecohydrology are the publications by Eagleson [1978a,b,c,d,e,f,g] where the interactions between soil, climate and vegetation were examined under an analytical framework.

The interactions between the water and vegetation have been investigated by analytical and numerical models. Important contributions to the field of Ecohydrology were presented by Laio et al. [2001a,b], Porporato et al. [2001], Rodriguez-Iturbe et al. [2001]. In these studies the authors were able to find an analytical solution for the probabilistic density function of soil moisture under the presence of vegetation. Additionally, numerical models have been able to add more complexity and simulate the water and vegetation interaction including more dynamics. A diverse set of numerical models have been generated in the last decades to simulate these processes. Today two of the most representative numerical models available are the Soil and Water Assesment Tool SWAT and the Community Land Model(CML). These models simulate soil-plant-atmosphere interactions at small spatial scales or subunits and then scale up to bigger spatial scales by aggregation and integration of the results obtained at the smaller subunits. In the case of SWAT the simulations are performed at small subbasins or watersheds while in CLM the simulations are performed in grids composed of nested subgrids having different properties including: landunits, snow/soil and plant functional types. These models have been utilized to analyze different dynamics at different spatial scales. They have shown potential to perform simulations at big spatial scales and have insights at a regional or global scale. However, there are specific scientific questions and dynamics that can not be solved and are not included in SWAT or CLM. For these cases, several other models have been developed to achieve these goals. For example the distributed hydrological model TRIBS developed by Ivanov et al. [2004] improved the representation of the surface by including a triangular irregular network TIN base real approach. This model has been useful to elucidate the basin response and to improve the capacities to predict runoff response. Another example is MLCan developed by Drewry et al. [2010a,b] to simulate the response of vegetation to climate change. This model improved our capacity to understand the response of vegetation to higher CO_2 concentration and temperature by resolving an explicit coupling between different processes such as the radiation regime and emission of thermal radiation, canopy energy balance, stomatal conductance and photosynthesis.

Ecohydrological models have been able to incorporate different biological and ecological

processes. However, in most cases the canopy is treated as a unique entity and interspecific or infraspecific interactions are not considered. In some cases, different species (proxies) such as plant functional types PFTs have been considered. For example CLM introduced the concept of ecological climatology with the main goal of analyzing the relationship between climate, biological process and human induced changes. In this approach they consider different PFTs and are particularly interested in the interactions of these PFTs with ecohydrological and biogeochemical processes at the earth surface. Although they included different PFTs, the solution of ecohydrological and biogeochemical processes is performed at a sub-grid cell where only *one* PFT is present. This approach therefore neglects all the interspecific interactions between plant species that coexist in the same location because they assume that all the plants in the same subgrid cell behave in the same manner. On the other hand, ecological models that have analyzed the interactions between different plant species are focused mostly in the fate of the interaction and the fate of the species rather than in the ecohydrological and biogeochemical processes. There have been some approaches that have analyzed these processes in a more holistic framework. For example the ED model presented in Moorcroft et al. [2001] scaled the fine scale processes occurring in a gap to a large scale domain. They were able to predict the large scale population and some ecohydrological dynamics by introducing an appropriate approach where the size and ages of the plants are treated by probabilistic functions. This approach allows long scale ecosystem dynamics simulations without the need of focusing in each individual plant. Although this model is a good approach to scale the processes from a gap to a large spatial scale, still the ecohydrological processes computed within a gap are calculated by the assumption of a unique entity. The approach developed by the GAPs models included competition and solves ecohydrological variables for each species independently [Rossiter and Riha, 1999]. These models have result very useful to analyze the competition in agriculture fields. Although these models include competition and solution of ecohydrological states, the competition in the below-ground is solved with a simplistic approach. In addition, the aboveground competition is determined mostly by absorption of radiation and its impact on ecohydrological variables such as transpiration, water uptake of soil moisture is not explicitly solved.

In this study, we develop a numerical model (Multi Species MLCan) which is able to simulate the ecohydrological dynamics in the presence of several coexisting species. The main purpose of this model is to examine the role of plant biodiversity in different ecohydrological processes and also to understand how climate change will influence these dynamics.

A.2 Model Introduction

Multi Species MLCan (multi-MLCan) is a multi layer above- and below-ground model that solves ecohydrological dynamics in the presence of different species. The model development is based upon the multi-layer canopy-soil-root (MLCan) biophysical model of Drewry et al. [2010a,b]. MLCan incorporates explicit coupling between leaf-level ecophysiological processes (photosynthesis and stomatal conductance), physical processes (energy balance and boundary layer conductance), and below-ground water status which incorporates the HR model of Amenu and Kumar [2008]. It resolves the radiation regimes, both direct and diffuse shortwave as well as longwave, throughout the vertical domain of the canopy. Radiation attenuation is determined by the leaf area density (LAD) profile [Drewry et al., 2010a]. It predicts the latent and sensible heat fluxes for each canopy layer through an iterative solution of the leaf energy balance, considering sunlit, shaded, and wet leaf fractions (due to dew or rainfall interception) separately. CO_2 fluxes (assimilation and respiration) are also calculated for each canopy layer, being directly coupled to the energy balance through stomatal dynamics. The details of the MLCan formulation can be found in the online supplement of Drewry et al. [2010a].

In multi-MLCan, the initial formulation from MLCan model is extended to include light dynamics of plant species coexisting in the same environment. As the MLCan model is designed to include both C3 and C4 photosynthetic pathways, it allows the interaction between different tall and understory vegetation combinations: C3-C3, C3-C4 (or in rare cases C4-C4). Therefore, multi MLcan enables the simulation of water, energy, and carbon dynamics when several species with different structural and ecophysiological characteristics interact and share resources.

A schematic of the model is presented in Figure A.1. As illustrated, we assume that several species are able to coexist in the same environment and they are homogeneously distributed in the spatial domain. Above-ground, their coexistence affects the radiation regime. For example, tall vegetation can shade the understory vegetation, thus reducing the radiation available for understory plants. Radiative effects such as this will directly impact the partitioning of energy between ecosystem components, the energy balance of each vegetation type and the soil, and consequently the net photosynthetic productivity of the system. The different root depths as well as the distribution of tall and understory vegetation, impact below-ground resource acquisition. For instance, different species draw from the same resource pool with different strengths and from different locations in the soil profile.

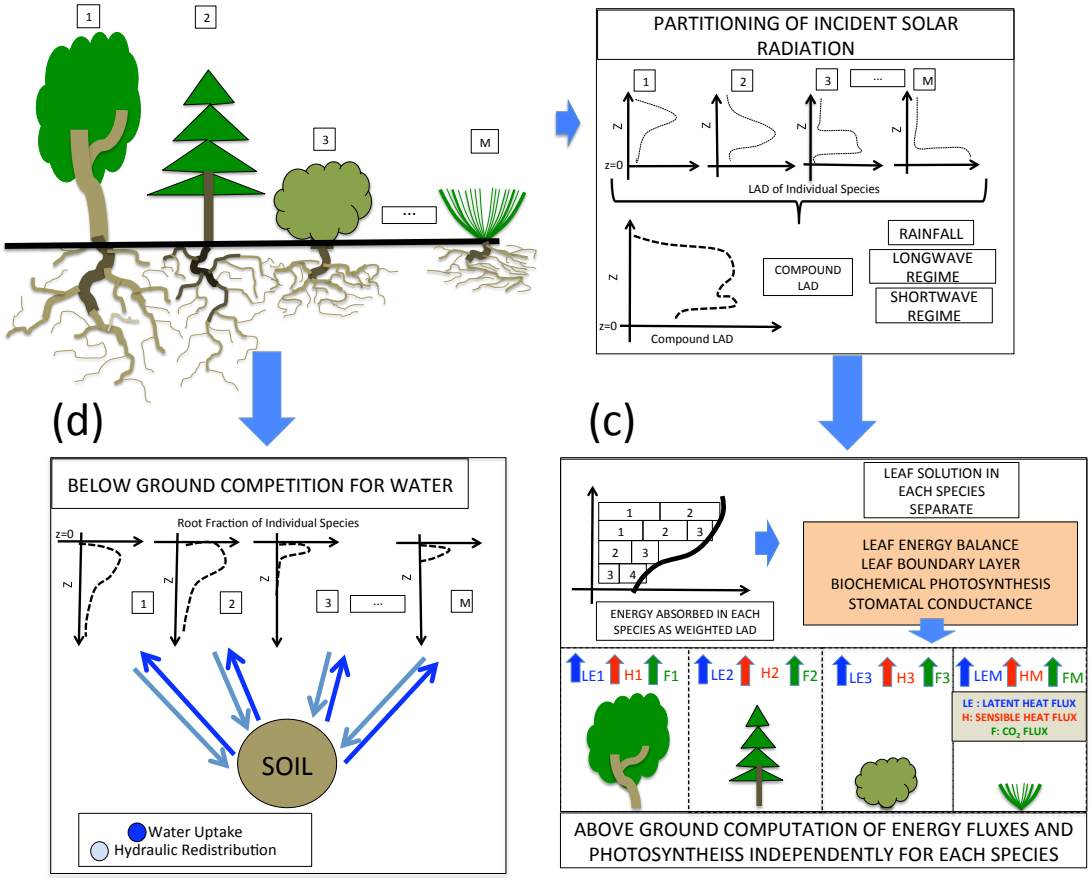

Figure A.1: Schematic representation of the multi-species MLCan model. **(a)** The structure and composition of the above ground canopy involving several vegetation species determines the partitioning of the incident solar radiation and water uptake patterns. **(b)** The combination of the leaf area density (LAD) of each individual species is used to develop a compound LAD. This compound LAD in turn determines the radiation regime through the vertical profile and the radiation reaching the soil. **(c)** The energy absorbed or emitted by each species at different levels is a function of the fraction of the LAD of that species in the compound LAD. **(d)** Below the ground the uptake of water and nutrients by each species is coupled with a common soil pool. The model framework allows the incorporation of different ecophysiological and structural parameters for the vegetation species considered.

In the aboveground the model simulates different processes such as the longwave and shortwave regime, latent heat from leaves and from the soil, photosynthesis, sensible heat and atmospheric turbulent transport of temperature, vapor and CO_2. These processes are interconnected and they have mutual feedbacks. In order to quantify these feedbacks the model solves all these processes simultaneously by an explicit coupling. This approach allows us no only to examine the effects of the coupling between biochemical, ecophysiological and physical functioning at the leaf level, but also to assess how these interactions alter canopy-scale responses to environmental perturbations. This approach is particularly useful to study the ecohydrological and ecophsysiological implications in the light of climate change since it can predict the feedbacks induced by alterations on atmospheric CO_2 concentrations on different ecohpysiological and ecohydrological processes Drewry et al. [2010a,b].

In the below-ground, roots from different species uptake water simultaneously. In multi-MLCan we assume that all the roots from the same species have the same structural and physiological properties. Roots from coexisting species share a common soil pool from where they uptake water. In multi-MLCan all the dynamics are solved only in the vertical domain assuming horizontal homogeneity. Following this assumption the model assumes that all the roots from different species share a common vertical soil moisture pool. This framework allows to simulate the competitive and mutualistic interactions in the below-ground under the presence of HR. More detail about the numerical solution implemented in multi-MLCan can be found in the following sections.

A.3 Above-Ground Interactions

The approach utilized to simulate light competition between different species in the above-ground is similar to the approach implemented in previous GAP models. In addition we solved the energy balance, transpiration and photosynthesis in more detail, and include the dynamics of the atmosphere surrounding the canopy following the same approach developed in MLCan.

A.3.1 Light Competition and Compound Above-Ground LAD For Different Species

The leaf area density (LAD) representing the vertical distribution of leaves in a canopy of species i with height H is given by

$$LAD_i(z) = \nu_i(z) LAI_i, \tag{A.7}$$

where $\nu_i(z)$ is the distribution function ($\int_0^H \nu(z)\, dz = 1$), LAI_i is the total leaf area index and $LAD_i(z)$ is the leaf area index of the i^{th} plant species. Usually $\nu_i(z)$ is assumed to follow a Weibull distribution with species dependent parameters α and β. The cumulative distribution function given as [Coops et al., 2007]:

$$F(z; \alpha, \beta) = 1 - \exp\left(- \frac{1 - z/H}{\alpha} \right)^{\beta} \tag{A.8}$$

By considering N vertical layers, the LAD for the i^{th} species in the j^{th} layer can be obtained by the following equation

$$LAD_{i,j} = \int_{z_i}^{z_{j+1}} LAD_i(z)\, dz \tag{A.9}$$

We define a compound LAD for the entire canopy by adding all the leaf distributions in each species.

$$LAD_{C,j} = \sum_{i=1}^{M} LAD_{i,j} \tag{A.10}$$

Therefore, the fraction from the total leaf area index that belongs to a given species i at a given layer j is given by:

$$f_{i,j} = \frac{LAD_{i,j}}{\sum\limits_{i=1}^{M} LAD_{i,j}} = \frac{LAD_{i,j}}{LAD_{C,j}} \tag{A.11}$$

The light regime for shortwave and longwave radiation is solved for the entire canopy by considering all the canopy as a single species with a compound $LAD_{C,j}$. Once the radiation regime is solved and the total absorption of radiation by the canopy at each layer is known ($R_{abs,C,j}$), the allocation of the the absorption in each species is computed by a linear weight average using $f_{i,j}$.

$$R_{abs,i,j} = R_{abs,C,j} f_{i,j} \tag{A.12}$$

A.3.2 Above Ground Interactions

In MLCan the coupling between the ecophysiological processes and the energy balance is solved by an iterative explicit scheme. The radiation energy absorbed by the leaves forces the energy balances and this energy is dissipated in the form of emitted longwave and heat fluxes. All these fluxes are temperature dependent and there is a unique temperature that satisfies these conditions. This temperature is computed in MLCan by finding the most optimum value that closes the energy balance.

The photosynthetic dynamics are conditioned by leaf temperature. Therefore, the resulting leaf temperature from the energy balance impacts photosynthesis. MLCan uses Farquhar model [Farquhar et al., 1980] to calculate photosynthesis. In addition, the photosynthetic outcome influences the stomatal conductance since the plant regulates the stomata to uptake carbon. In MLCan the stomatal conductance is computed with the Ball Berry model [Ball et al., 1987]. This formulation includes the effect of photosynthesis on the stomata conductance. Furthermore, stomata conductance regulates the rate of transpiration (latent heat) and also affects sensible heat which are the main mechanisms to dissipate energy. In the end, energy balance, photosynthesis, and the fluxes of heat are all coupled and MLCan solves this coupling by an iterative approach at each time step.

In multi-MLCan several coexisting species are considered. The absorption of radiation in each species is solved using a linear weight approximation as mentioned in section A.3.1 based on the fraction $f_{i.j}$ out of the total compound LAD that a particular species has. Once the absorption in each species is computed the coupling between energy balance, biochemical photosynthesis and stomatal conductance is solved for each species independently (Figure A.3). All the species share a common pool of atmospheric CO_2 water vapor and temperature. Therefore the solution of this coupling in one species may influence the others. In multi-MLCan the overall solution is calculated by solving all the species iteratively until a final converge is reached. The steps of multi-MLCan to solve the canopy dynamics in the presence of multiple species is illustrated in the flowchart in Figure A.3.

A.4 Below-Ground Interactions

In the belowground, multi-MLCan simulates the moisture dynamics in the presence of different plant root species that uptake and release moisture simultaneously. Multi-MLCan uses the framework originally developed by Amenu and Kumar [2008]. In this framework, the

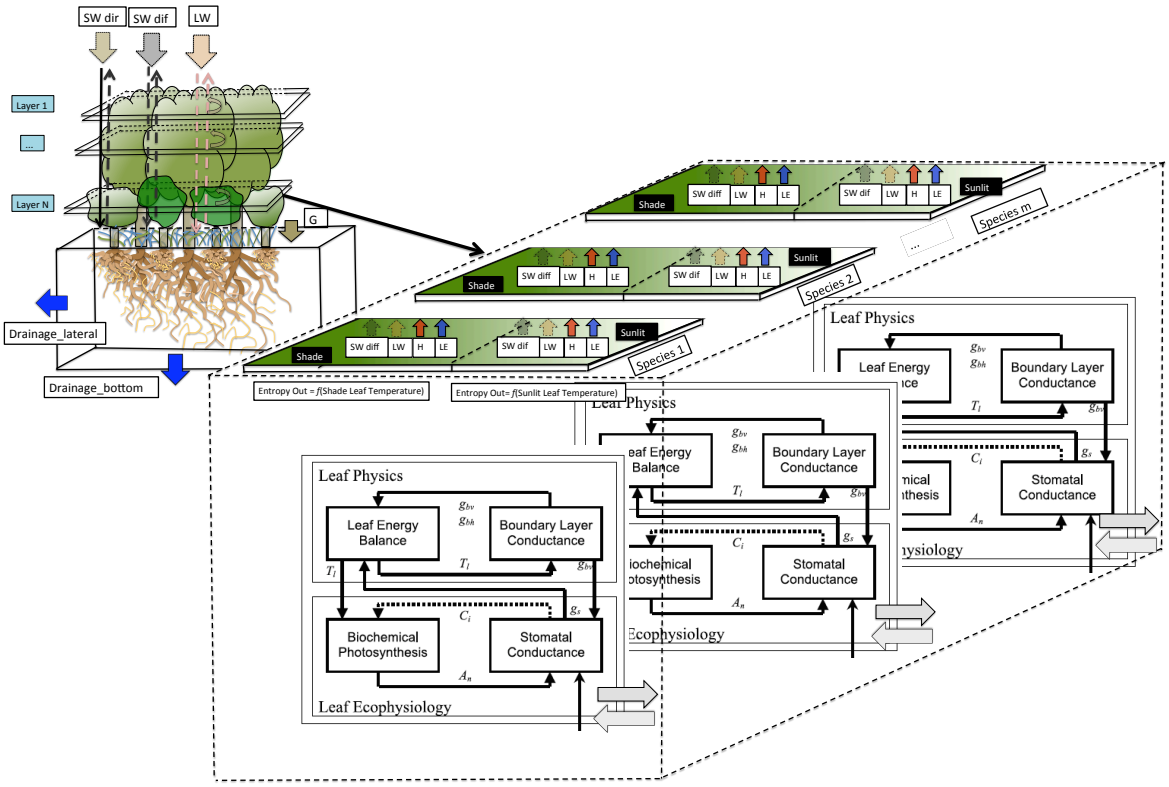

Figure A.2: Schematic representation of above-ground dynamics considered in multi-MLCan. Different species in the aboveground coexist in the same location. The model solves the coupling between energy balance and ecophysiological processes at the leaf level for each species independently. However, all the species share the same atmospheric pool of cabon, water vapor and temperature and the dynamics in one species may influence the others.

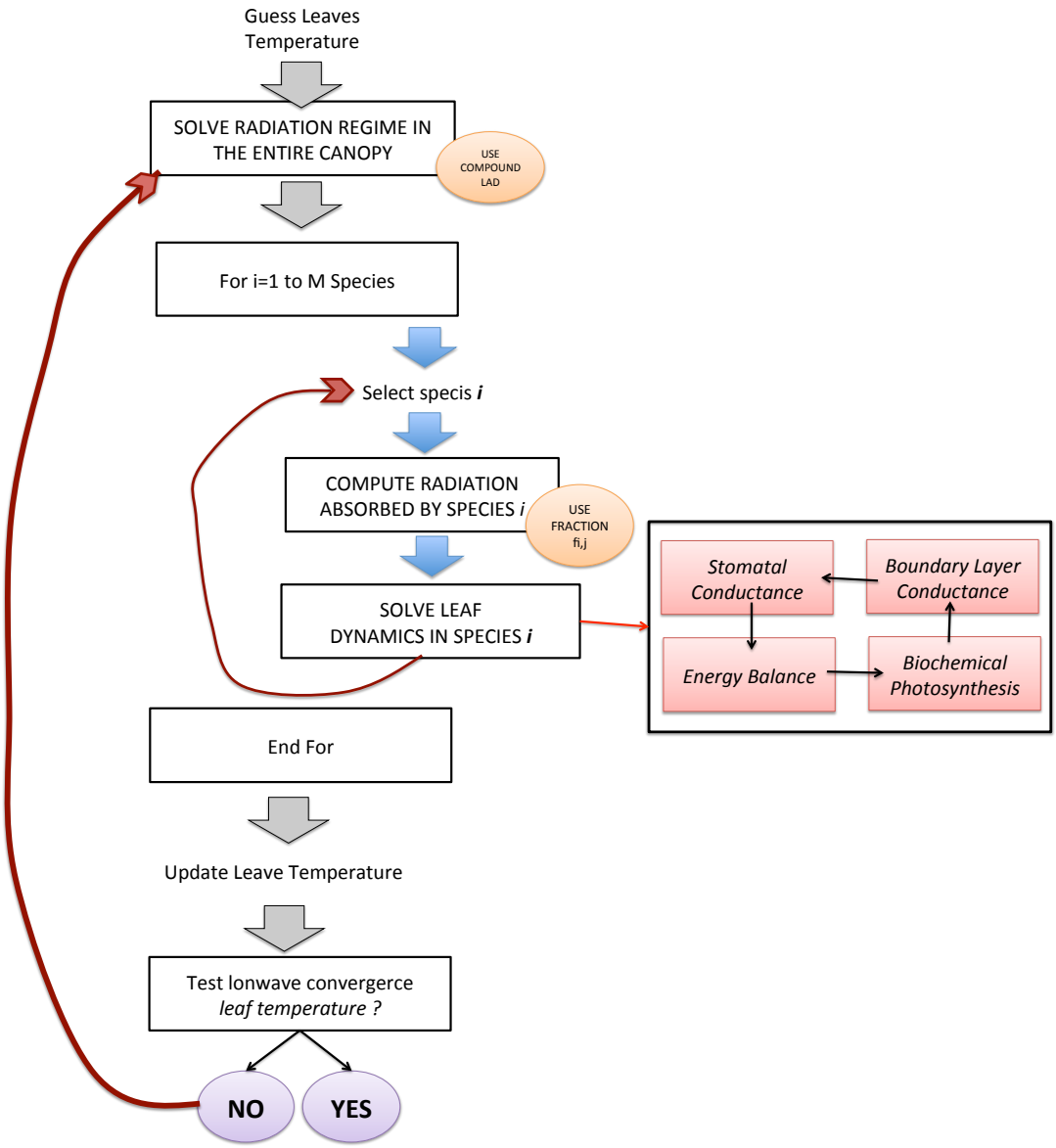

Figure A.3: Flowchart illustrating the numerical solution of the above-ground dynamics in multi-MLcan.

moisture processes in the soil are simulated by the well known Richards Equation while the internal processes inside the roots are simulated by a one dimensional equation that is based on the Hagen-Poiseuille law. The fluxes of moisture within the root and between the root-soil system are quantified in terms of radial (k_{rad}) and axial (k_{ax}) root hydraulic conductivities that are parameterized based on available root measurements. Both, Richards Equation and the equation that solves the dynamics within the roots are solved simultaneously by an approach that allows to quantify the feedbacks that arise in the soil-root system. This framework enables the computation of hydraulic redistribution fluxes which are fluxes from the root to the soil that occur when the water potential within the roots (ψ_r) becomes higher than the water potential in the soil (ψ_s). Similarly, the model can simulate the dynamics in the absence of HR by constraining $k_{rad} = 0$ whenever $\psi_r > \psi_s$.

When different species coexist, their root system can exploit different parts of the soil column as a function of their unique rooting depths and root biomass distributions. These dynamics are emulated in multi-MLCan by an independent root equation for each species. This accounts for their differences in structural and functional properties. The coupled dynamics between the roots and the soil is evaluated by solving simultaneously all the respective root equations and Richards Equation. This framework allows to simulate the presence of different species sharing the same soil column. Competitive or mutualistic interactions through water uptake and hydraulic redistribution are included. Equation A.13 shows the coupled differential equations under the presence of M plant species.

$$\begin{aligned}
&\tfrac{\partial\theta}{\partial t} - \tfrac{\partial}{\partial z}\left[K_s\left(\tfrac{\partial \psi s}{\partial z} - 1\right)\right] = -\textstyle\sum_{i=1}^{M} K_{r_i}^R\left(\psi_s - \psi_{r_i}\right)\\
&-\tfrac{\partial}{\partial z}\left[K_{r_1}^A\left(\tfrac{\partial \psi_{r_1}}{\partial z} - 1\right)\right] = K_{r_1}^R\left(\psi_s - \psi_{r_1}\right)\\
&-\tfrac{\partial}{\partial z}\left[K_{r_2}^A\left(\tfrac{\partial \psi_{r_2}}{\partial z} - 1\right)\right] = K_{r_1}^R\left(\psi_s - \psi_{r_2}\right)\\
&\ldots\\
&-\tfrac{\partial}{\partial z}\left[K_{r_M}^A\left(\tfrac{\partial \psi_{r_M}}{\partial z} - 1\right)\right] = K_{r_M}^R\left(\psi_s - \psi_{r_M}\right)
\end{aligned} \tag{A.13}$$

The top equation is the well known Richards equation and the other M equations represent transport through M different plant species. The terms ψ_s and ψ_{r_i} are the water potential in the soil and the root of the i^{th} plant species, respectively, and θ is the soil-moisture. The vertical coordinate and time are represented as z and t, respectively. Note that each layer has a unique water potential value for the roots of each plant. The term K_s is the soil hydraulic conductivity, and $K_{r_i}^R$ and $K_{r_i}^A$ are the radial and axial root conductivities of the i^{th} plant

species, respectively [Amenu and Kumar, 2008]. These equations are solved simultaneously for N number of layers in the soil domain.

The individual root systems of each species do not directly interact but they share a common soil system, such that θ and ψ_s in each soil layer are the same for all species (see Figure A.1). This conceptualization of shared resource dynamics allowed to capture inter-species interactions, both competition and mutualism. The water uptake or release by one species affects the shared soil moisture state, resulting in an indirect effect of each vegetation species on the dynamics of the others. When plants uptake water from the same layer they compete for available water. The release of water through hydraulic redistribution may, however, benefit the other species that share that layer by increasing available moisture. The model can simulate HR in all plant species and this function can be switched off by setting the root radial conductivity of a species to zero, i.e. $K_{r_i} = 0$, when the water potential in the roots is higher than the water potential in the soil, i.e. $\psi_{r_i} > \psi_s$.

In this study we use an implicit numerical scheme to solve Equation A.13. The iterative procedure to solve the below-ground dynamics is displayed in Figure A.4. In the following section the details of this numerical scheme are presented.

A.4.1 Numerical Solution of Belowground Water Dynamics

This section describes the below-ground solution of moisture under the presence of several coexisting plant root species. Initially Richards equation is introduced. Then details of the implicit numerical solution are first presented for a single species case where one single species interacts with the soil. Finally the details of the numerical simulation of several coexisting species interacting with the soil is described.

Richards Equation

The top equation in A.13 describes the dynamics of moisture in the soil. This equation is known as Richars equation which has been of common use in hydrology to analyze the flow of water in soils. To start, we show how Richards Equation can be obtained from the conservation of mass and Darcys Law equations. Afterwards we explain three different methods, termed θ - ψ - *mixed*, respectively that are used to solve Richards Equation numerically. Finally, the numerical discretization for the mixed method which has shown good mass balance and stability results is described.

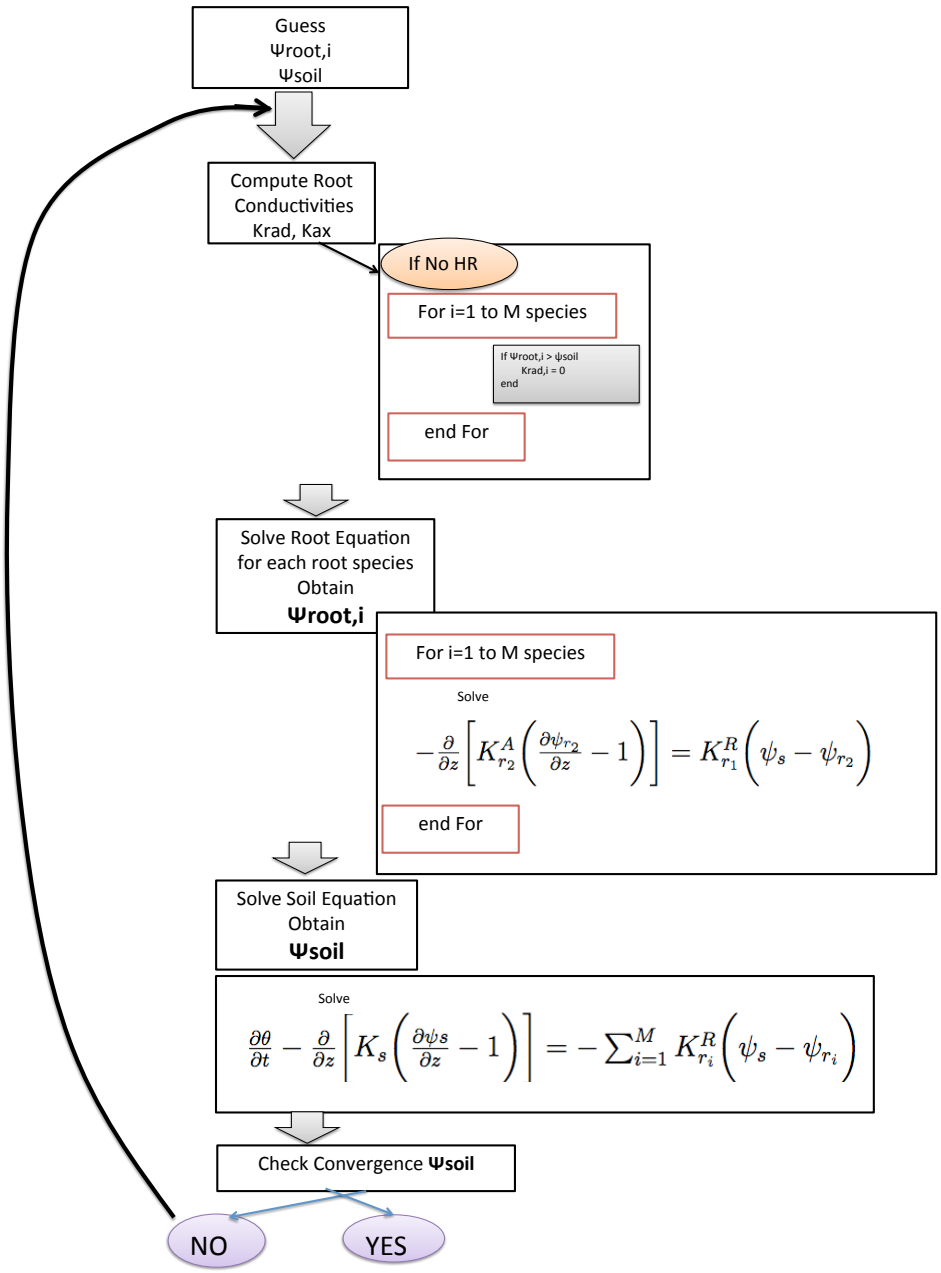

Figure A.4: Flowchart illustrating the numerical solution for the below-ground soil moisture dynamics in multi-MLcan.

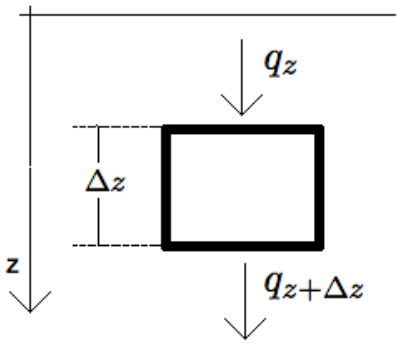

Figure A.5: Representation of Soil Mass Balance.

Starting from the control volume shown in Figure A.5 and applying conservation of mass in one dimension:

$$\frac{\partial \theta}{\partial t} = -\frac{\partial q}{\partial z'} \tag{A.14}$$

The variable z' in equation A.14 refers to a variable that increases downward. Equation A.14 is based on conservation of mass. The total amount of water that goes into the control volume minus the total amount of water that leaves the control volume equals the rate of change in storage inside the control volume.

The term q in equation A.23 represents the flux of water per unit area, and its units are [volume/area/time] = [length/time]. The flow of water in unsaturated porous media obeys Darcys Law. Therefore:

$$q = -K(\theta)\frac{\partial H}{\partial z'} \tag{A.15}$$

The term $K(\theta)$ is the soil hydraulic conductivity and is function of the soil moisture θ. The variable $H(z)$ is the total head of the water at a given z. Equation A.15 is known as Darcys

Law and it implies that the flow of water in an unsaturated porous media is lineraly related with the rate of change of head in space by a constant known as conductivity $K(\theta)$. The total head at a given z is given by:

$$\begin{aligned} q &= -K(\theta)\left(\frac{\partial H}{\partial z'}\right) \\ q &= -K(\theta)\left(\frac{\partial(\psi+z')}{\partial z'}\right) \\ q &= -K(\theta)\left(\frac{\partial \psi}{\partial z'}+\frac{\partial z}{\partial z'}\right) \\ q &= -K(\theta)\left(\frac{\partial \psi}{\partial z'}-1\right) \end{aligned} \tag{A.16}$$

By coupling equation A.16 with equation A.14 we obtain equation A.17

$$\frac{\partial \theta}{\partial t} = \frac{\partial}{\partial z}\left[K(\theta)\left(\frac{\partial \psi}{\partial z'}-1\right)\right] \tag{A.17}$$

θ form, ψ form and *mixed* form of Richard Equation

Equation A.17 is the well known Richards Equation. Let us introduce the term $D(\theta)$ called the unsaturated diffusivity:

$$D = k(\theta)\frac{\partial \psi}{\partial \theta} \tag{A.18}$$

If we substitute $D(\theta)$ in equation $A.17$, then we obtain:

$$\frac{\partial \theta}{\partial t} = \frac{\partial}{\partial z}\left[D(\theta)\left(\frac{\partial \theta}{\partial z'}-1\right)\right] \tag{A.19}$$

Equation A.19 is the θ base Richards Equation. The specific moisture capacity $C(\theta)$ is de-

fined as:

$$C(\theta) = \frac{\partial \theta}{\partial \psi} = \frac{K(\theta)}{D(\theta)} \tag{A.20}$$

Using the specific moisture capacity in equation A.17:

$$C(\theta)\frac{\partial \psi}{\partial t} = \frac{\partial}{\partial z}\left[K(\theta)\left(\frac{\partial \psi}{\partial z'} - 1\right)\right] \tag{A.21}$$

Equation A.21 is the ψ form of Richards Equation. Both forms θ and ψ where implemented for long time as numerical schemes to solve Richard Equation. This is a non linear, since the conductivity is function of soil moisture $K(\theta)$ and therefore its analytical solution is challenging task. Only some particular simplified cases have analytical solutions. In general the solution of Richard Equations under more realistic conditions rely in numerical approximations. The numerical solution of the θ form produces good mass balance results while several studies have detected considerable general mass balance errors for the ψ form. However, the numerical solution under the ψ is more convenient and has several advantages. Moreoever, in the θ form there is a discontinuity in the soil moisture content and its application is limited for unsaturated flow [Rathfelder and Abiola, 1994].

In Celia et al. [1990] the *mixed* form was introduced. Equation A.22 represnt the *mixed* form. This scheme has shown some advantages due to its capacity to obtain good mass balance performances while maintaining the advantages of the ψ form.

$$\frac{\partial \theta}{\partial t} = \frac{\partial}{\partial z}\left[K(\theta)\left(\frac{\partial \psi}{\partial z'} - 1\right)\right] \tag{A.22}$$

In this document all the numerical schemes presented for solving Equation A.13 for Richards Equation are based on the *mixed* form.

Single Species Case

The hydraulic redistribution formulation consists of two coupled differential equations, one of them describes the flow of water in the soil while the other describes the flow of water in the roots. The coupling between both equations is given by the uptake of water by the roots from the soil, which is a sink term in the case of the soil and a source term in the root equation.

$$\begin{aligned} \frac{\partial \theta}{\partial t} - \frac{\partial}{\partial z}\left[Ks\left(\frac{\partial \psi s}{\partial z} - 1\right)\right] &= -Kr_r\left(\psi s - \psi r\right) \\ -\frac{\partial}{\partial z}\left[Kr_a\left(\frac{\partial \psi r}{\partial z} - 1\right)\right] &= Kr_r\left(\psi s - \psi r\right) \end{aligned} \tag{A.23}$$

Equation A.23 describes the flow of water in the coupled soil and root system. Note that z increases downward. The top equation is the Richards Equation in the soil. The bottom equation is the equation that describes the flow moisture in the roots. In this equation no water storage is considered in the roots system. In the equations shown in A.23, the movement of water from the root to the soil is allowed. In the cases where the water potential in the roots is higher than in the soil, $\psi r > \psi s$, there will be a release of moisture from the roots to the soil.

In the absence of hydraulic redistribution, plants will not allow the flux of water from the roots to the soil. There can be several physiological mechanisms in which plants could control the flux of water out of the root system. Here, if the water potential is higher in the roots than in the soil, the root radial conductivity becomes zero.

$$\begin{aligned} \frac{\partial \theta}{\partial t} - \frac{\partial}{\partial z}\left[Ks\left(\frac{\partial \psi s}{\partial z} - 1\right)\right] &= -Kr_r\left(\psi s - \psi r\right) \\ -\frac{\partial}{\partial z}\left[Kr_a\left(\frac{\partial \psi r}{\partial z} - 1\right)\right] &= Kr_r\left(\psi s - \psi r\right) \\ Kr_r = 0, \text{ for } , \psi r < \psi s & \end{aligned} \tag{A.24}$$

Equation A.24 describes the dynamics of water flow in the soil root system for the case in which there is not hydraulic redistribution.

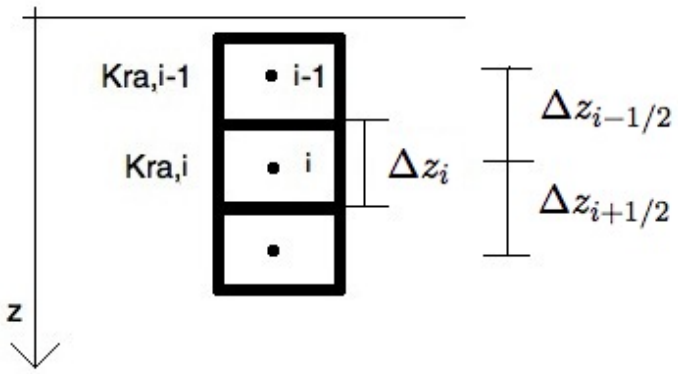

Figure A.6: Schematic representation of root discretization.

Root Numerical Scheme

Figure A.6 shows an schematic representation of the root discretization. The equation that describes the water flow in the root system is given in equations A.23 and A.24.

$$-\frac{\partial}{\partial z}\left[Kr_a\left(\frac{\partial \psi s}{\partial z}-1\right)\right]=Kr_r\left(\psi s-\psi r\right)$$

Using forward finite difference and according to the scheme showed in figure A.6 we can write the root equation using discrete terms as:

$$-\frac{1}{\Delta z_i}\left\{Kra_i\left[\left(\frac{\psi r_{i+1}-\psi r_j}{\Delta z_{i+1/2}}\right)-1\right]-Kra_{i-1}\left[\left(\frac{\psi r_i-\psi r_{i-1}}{\Delta z_{i-1/2}}\right)-1\right]\right\}=Krr_i[\psi s_i-\psi r_i] \tag{A.25}$$

Grouping terms:

$$\psi r_{i-1}\left[\frac{-Kra_{i-1}}{\Delta z_i \Delta z_{i-1/2}}\right]+\psi r_i\left[\frac{Kra_i}{\Delta z_i \Delta z_{i+1/2}}+\frac{Kra_{i-1}}{\Delta z_i \Delta z_{i-1/2}}+Krr_i\right]+\psi r_{i+1}\left[\frac{-Kra_{i+1}}{\Delta z_i \Delta z_{i+1/2}}\right]= \psi s_i Krr_i - Kra_i + Kra_{i-1} \tag{A.26}$$

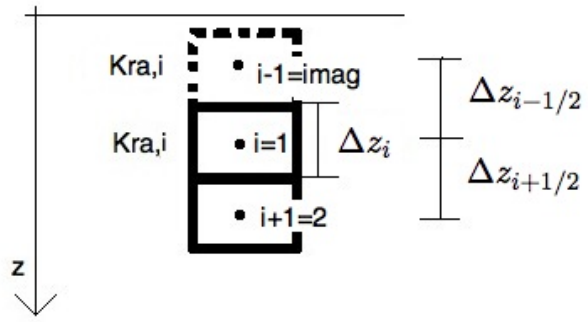

Figure A.7: Schematic representation of root discretization at the top.

Equation A.26 is the general form of the numerical discrete equation for the root system. The terms on the left of the equation that go together with ψ_{i-1}, ψ_i and ψ_{i+1} are the terms that cast the tridiagonal matrix A in the final linear system of equation $A\Psi r = B$.

In order to solve the root equation numerically boundary conditions are needed. There are two boundary conditions, at the top and at the bottom. Figure A.7 shows the schematic diagram at the top of the root system. At the top a flux boundary condition is assumed: the flux at the top is equal to the total transpiration in the canopy (above ground) and is given by:

$$q_{top} = -Et$$

$$\begin{aligned} -Kra_{i-1}\frac{\partial H}{\partial z} &= -Et \\ -Kra_{i-1}\left(\frac{\psi r_i - \psi r_{i-1}}{\Delta z_{i-1/2}} - 1\right) &= -Et \end{aligned} \tag{A.27}$$

Note that z in equation A.27 increases downward. From A.27 it is possible to compute ψ_{i-1} which is an imaginary node over the top of the root system.

$$\psi r_{i-1} = \psi r_i + \frac{Et\Delta z_{i-1/2}}{Kra_{i-1}} - \Delta z_{i-1/2} \tag{A.28}$$

Now substituting A.28 in A.26, and assuming that $K_{i-1} = K_i$ and $\Delta z_{i-1/2} = \Delta z_i$ then we obtain the complete equation for the first node.

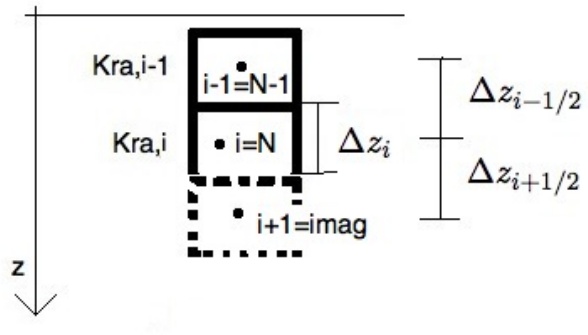

Figure A.8: Schematic representation of root discretization at the bottom.

$$\psi r_i\left[\frac{Kra_i}{\Delta z_i \Delta z_{i+1/2}} + Krr_i\right] + \psi r_{i+1}\left[\frac{-Kra_{i+1}}{\Delta z_i \Delta z_{i+1/2}}\right] = \psi s_i Krr_i - \frac{Kra_i}{\Delta z_i} - \frac{Et}{\Delta z_i} \tag{A.29}$$

Figure A.8 shows a schematic diagram of the bottom layers. After the last bottom layer there is an imaginary layer. The boundary condition at the bottom is a flux boundary condition where the flux is equal to zero. Using this boundary condition we can obtain ψr_{i+1} which is root the water potential at the imaginary node. The flux at the bottom is given by:

$$\begin{gathered} q_{top} = -Et \\ -Kra_i \frac{\partial H}{\partial z} = 0 \\ -Kra_i\left(\frac{\psi r_{i+1} - \psi r_i}{\Delta z_{i+1/2}} - 1\right) = 0 \end{gathered} \tag{A.30}$$

From equation A.30 it is possible to compute ψr_{i+1}.

$$\psi r_{i+1} = \psi_i + \Delta z_{i+1/2} \tag{A.31}$$

Using equation A.26 and equation A.31 we can compute the equation for the last layer in the root system.

$$\psi r_i[\frac{Kra_i}{\Delta z_i \Delta z_{i-1/2}} + Krr_i\Bigg] + \psi r_{i-1}\Bigg[\frac{-Kra_{i-1}}{\Delta z_i \Delta z_{i-1/2}}\Bigg] = \psi s_i Krr_i + \frac{Kra_i}{\Delta z_i} \tag{A.32}$$

Soil Numerical Scheme

The numerical scheme for the soil implemented here is based on the mixed form of Richards Equation. Initially the general numerical solution of the mixed form is given, afterwards the solutions for the boundary conditions are presented. The top boundary condition can be either of type I (constant head in case of saturation of the soil) or type II (flux in case there is infiltration when the top soil is not saturated). The bottom boundary condition is always a constant flux given by the soil hydraulic conductivity in the last layer.

The notation implemented here is the same as the notation implemented for the case of the roots and that notation is taken from Rathfelder and Abiola [1994].

The soil equation as presented in the hydraulic redistribution framework (equation A.23 and A.24) is given by:

$$\frac{\partial \theta}{\partial t} - \frac{\partial}{\partial z}\Bigg[Ks\Bigg(\frac{\partial \psi s}{\partial z} - 1\Bigg)\Bigg] = -Kr_r\Bigg(\psi s - \psi r\Bigg)$$

The discrete form of the soil equation in A.23 and A.24 is shown in A.33. The schematic diagram of the discrete partition of the soil column is shown in figure A.9.

$$\begin{gathered}\Bigg(\frac{\theta_i^{t+1,m+1} - \theta_i^t}{\Delta t}\Bigg) - \\ \frac{1}{\Delta z_i}\Bigg[Ks_{i+1/2}^{t+1,m}\Bigg(\frac{\psi s_{i+1}^{t+1,m+1} - \psi s_i^{t+1,m+1}}{\Delta z_{i+1/2}} - 1\Bigg) - Ks_{i-1/2}^{t+1,m}\Bigg(\frac{\psi s_i^{t+1,m+1} - \psi s_{i-1}^{t+1,m+1}}{\Delta z_{i-1/2}} - 1\Bigg)\Bigg] = \\ -Krr_i^{t+1}\Bigg(\psi s_i^{t+1,m+1} - \psi r_i^{t+1}\Bigg)\end{gathered} \tag{A.33}$$

Note that in A.33 there are three different subindex t, i and m, corresponding to time step,

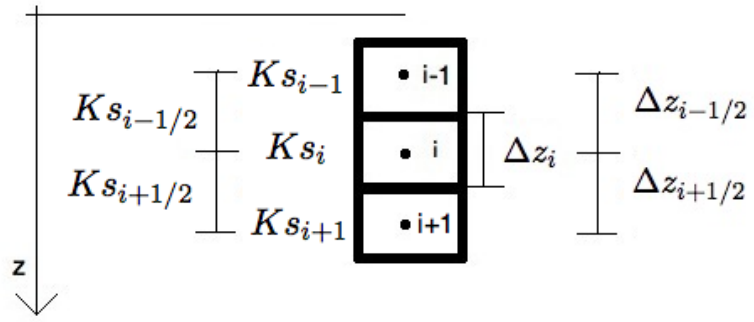

Figure A.9: Schematic representation of soil discretization.

space and iteration, respectively. The numerical scheme in A.33 is implicit. The soil equation A.23 and A.24 is non linear and therefore the implicit solution is reached through the use of iterations.

In Celia et al. [1990] a taylor expansion over the iteration domain was proposed in order to obtain θ_i^{m+1} .

$$\begin{aligned}
\theta_i^{m+1} &\sim \theta_i^m + \tfrac{\partial\theta}{\partial m}|_{i,m}(\Delta m) \\
\theta_i^{m+1} &\sim \theta_i^m + \tfrac{\partial\theta}{\partial\psi}\tfrac{\partial\psi}{\partial m}|_{i,m}(\Delta m) \\
\theta_i^{m+1} &\sim \theta_i^m + \tfrac{\partial\theta}{\partial\psi}|_{i,m}\left(\psi s_i^{m-1} - \psi s_i^m\right) \\
\theta_i^{m+1} &\sim \theta_i^m + C_i^m\left(\psi s_i^{m+1} - \psi s_i^m\right)
\end{aligned} \tag{A.34}$$

If the results in A.34 are substituted in A.33 then:

$$\left(\frac{\theta_i^{t+1,m}+C_i^{t+1,m}(\psi s_i^{t+1,m+1}-\psi s_i^{t+1,m})-\theta_i^t}{\Delta t}\right)-\frac{1}{\Delta z_i}\left[Ks_{i+1/2}^{t+1,m}\left(\frac{\psi s_{i+1}^{t+1,m+1}-\psi s_i^{t+1,m+1}}{\Delta z_{i+1/2}}-1\right)-\right.$$
$$\left.Ks_{i-1/2}^{t+1,m}\left(\frac{\psi s_i^{t+1,m+1}-\psi s_{i-1}^{t+1,m+1}}{\Delta z_{i-1/2}}-1\right)\right]=-Krr_i^{t+1}\left(\psi s_i^{t+1,m+1}-\psi r_i^{t+1}\right) \tag{A.35}$$

Rearranging terms from A.35.

$$\psi s_{i-1}^{t+1,m+1}\left[\frac{-Ks_{i-1/2}^{t+1,m}}{\Delta z_{i-1/2}\Delta z_i}\right]+$$
$$\psi s_i^{t+1,m+1}\left[\frac{C_i^{t+1,m}}{\Delta t}+\frac{Ks_{i-1/2}^{t+1,m}}{\Delta z_{i-1/2}\Delta z_i}+\frac{Ks_{i+1/2}^{t+1,m}}{\Delta z_{i+1/2}\Delta z_i}+Krr_i^{t+1}\right]$$
$$+\psi s_{i+1}^{t+1,m+1}\left[\frac{-Ks_{i+1/2}^{t+1,m}}{\Delta z_{i+1/2}\Delta z_i}\right]= \tag{A.36}$$
$$\left(\frac{C_i^{t+1,m}\psi s_i^{t+1,m}}{\Delta t}\right)-\left(\frac{\theta_i^{t+1,m}-\theta i^t}{\Delta t}\right)-\frac{1}{\Delta z}\left(Ks_{i+1/2}^m-Ks_{i-1/2}^m\right)+\psi r_i^{t+1}Krr_i^{t+1}$$

Equation A.36 is the general form of the numerical discrete equation for the soil system. The terms on the left hand side of the equation that go together with ψs_{i-1}, ψs_i and ψs_{i+1} are the terms that cast the tridiagonal matrix A in the final linear system of equation $A\Psi s = B$.

Note that in equation A.36 all the variables except the state variable are in the future time $t+1$. In the next sections, every time the soil equation is presented it is assumed that all the variables are considered in the future time step.

Figure A.10 shows a schematic representation of the top layers of the soil domain. There are two different types of top boundary condition for the soil equation. In this section I am going to show the numerical solution for the flux boundary condition.

Starting from the flux (q) definition and its connection with conservation of mass.

$$\frac{\partial\theta}{\partial t}=\frac{\partial q}{\partial z}$$

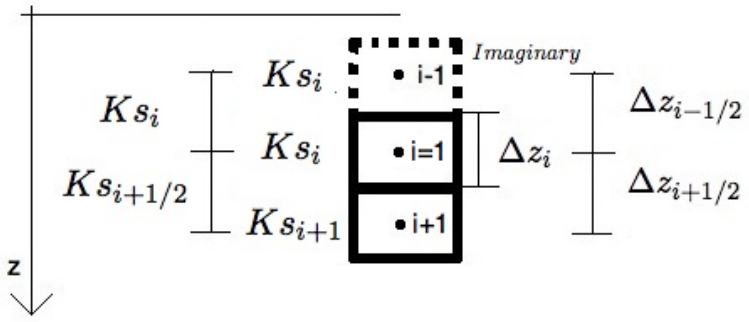

Figure A.10: Schematic representation of soil discretization at the top.

If we substitute the fluxes at the top (figure A.10), then:

$$\left(\frac{\theta_i^m + C_i^m(\psi s_i^{m+1} - \psi s_i^m) - \theta_i^t}{\Delta t}\right) = \frac{1}{\Delta z_i}\left[Ks_{i+1/2}^m\left(\frac{\psi s_{i+1}^{m+1} - \psi s_i^{m+1}}{\Delta z_{i+1/2}} - 1\right) - q_{Inf}^{m+1}\right] \\ -Krr_i\left(\psi s_i^{m+1} - \psi r_i\right) \tag{A.37}$$

The variable q_{inf} is the infiltration flux at the top of the soil column. Note that q_{inf} is also function of θ at therefore it is also changing through the iterations.

Rearranging and grouping terms from equation A.37 we obtain:

$$\psi s_i^{m+1}\left[\frac{C_i^m}{\Delta t} + \frac{Ks_{i+1/2}^m}{\Delta z_{i+1/2}\Delta z_i} + Krr_i\right] + \psi s_{i+1}^{m+1}\left[\frac{-Ks_{i+1/2}^m}{\Delta z_{i+1/2}\Delta z_i}\right] = \\ \left(\frac{C_i^m \psi s_i^m}{\Delta t}\right) - \left(\frac{\theta_i^m - \theta i^t}{\Delta t}\right) - \frac{1}{\Delta z}(Ks_{i+1/2}^m) + \psi r_i Krr_i - q_{inf}^m \tag{A.38}$$

There could be another type of boundary condition defined by a head instead of a flux. This type of boundary condition may occur when there is ponding and a layer of water with a given head is over the soil. Figure A.10 shows an schematic representation of the discrete layers corresponding to the top layer in the soil column. Following figure A.10, knowing that

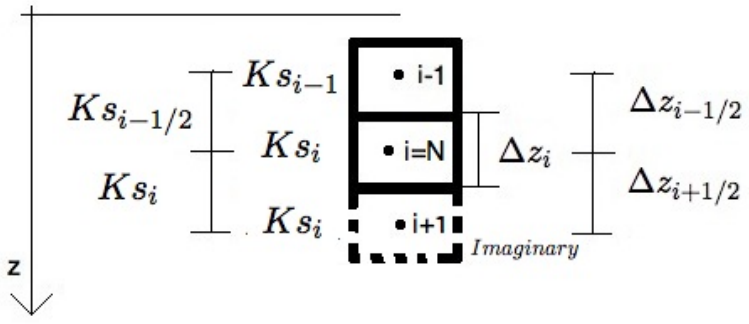

Figure A.11: Schematic representation of soil discretization at the bottom.

$\psi s_0 = \psi s_{i-1} = H_o$ and using equation A.36:

$$\psi s_i^{m+1}\left[\frac{C_i^m}{\Delta t} + \frac{Ks_{i-1/2}^m}{\Delta z_{i-1/2}\Delta z_i} + \frac{Ks_{i+1/2}^m}{\Delta z_{i+1/2}\Delta z_i} + Krr_i\right] + \psi s_{i+1}^{m+1}\left[\frac{-Ks_{i+1/2}^m}{\Delta z_{i+1/2}\Delta z_i}\right] =$$
$$\left(\frac{C_i^m \psi s_i^m}{\Delta t}\right) - \left(\frac{\theta_i^m - \theta i^t}{\Delta t}\right) - \frac{1}{\Delta z}\left(Ks_{i+1/2}^m - Ks_{i-1/2}^m\right) + \psi r_i Krr_i + H_o\left[\frac{Ks_{i-1/2}^m}{\Delta z_{i-1/2}\Delta z_i}\right] \tag{A.39}$$

The boundary conditions at the bottom of the soil are solved similarly as in the top.

Figure A.11 shows a schematic representation of the layers at the bottom of the soil column. A flux boundary condition equal to the soil hydraulic conductivity is assumed.

$$q_{bottom} = Ks_{N+1/2}$$

We start from the concept of flux and its relation with conservation of mass.

$$\frac{\partial \theta}{\partial t} = \frac{\partial q}{\partial z}$$

If we substitute the fluxes at the bottom (figure A.11) and $Ks_{i+1/2} = Ks_{N+1/2}$ then:

$$\left(\frac{\theta_i^m + C_i^m(\psi s_i^{m+1} - \psi s_i^m) - \theta_i^t}{\Delta t}\right) = \frac{1}{\Delta z_i}\left[K_i^m - Ks_{i-1/2}^m\left(\frac{\psi s_i^{m+1} - \psi s_{i-1}^{m+1}}{\Delta z_{i+1/2}} - 1\right)\right] \\ -Krr_i\left(\psi s_i^{m+1} - \psi r_i\right) \tag{A.40}$$

Rearranging and grouping terms from equation A.40 we obtain:

$$\psi s_{i-1}^{m+1}\left[\frac{-Ks_{i-1/2}^m}{\Delta z_{i-1/2}\Delta z_i}\right] + \psi s_i^{m+1}\left[\frac{C_i^m}{\Delta t} + \frac{Ks_{i-1/2}^m}{\Delta z_{i-1/2}\Delta z_i} + Krr_i\right] = \\ \left(\frac{C_i^m \psi s_i^m}{\Delta t}\right) - \left(\frac{\theta_i^m - \theta i^t}{\Delta t}\right) + \frac{1}{\Delta z}(Ks_{i-1/2}^m) + \psi r_i Krr_i + \frac{k_i^m}{\Delta z_i} \tag{A.41}$$

Equation A.41 describes the soil moisture dynamics at the bottom layers under a flux boundary condition.

A.4.2 Numerical Solution. Multiple Species Case

This section provides the numerical solution for the water flow dynamics in the soil - root system for the case of two species. When two different species are considered, it is not only assumed that the demand of transpiration between both is different but also that the root strategy (depth, root distribution, hydraulic conductivity) to uptake water is different. The equations for the water flow dynamics in the soil - root system for the case in which there are two species are:

$$\frac{\partial\theta}{\partial t} - \frac{\partial}{\partial z}\left[Ks\left(\frac{\partial\psi s}{\partial z} - 1\right)\right] = -Kr_{r,1}\left(\psi s - \psi r_1\right) - Kr_{r,2}\left(\psi s - \psi r_2\right)$$

$$-\frac{\partial}{\partial z}\left[Kr_{a,1}\left(\frac{\partial\psi r_1}{\partial z} - 1\right)\right] = Kr_{r,1}\left(\psi s - \psi r_1\right) \tag{A.42}$$

$$-\frac{\partial}{\partial z}\left[Kr_{a,2}\left(\frac{\partial\psi r_2}{\partial z} - 1\right)\right] = Kr_{r,2}\left(\psi s - \psi r_2\right)$$

In A.42 there are three coupled differential equations. Two of them describe the flow of water in the root system while the third equation describes the flow of water in the soil. The two root equations are independent and they are independently coupled with the soil equation. The later has now two different sinks instead of one.

Note that equation A.42 is similar to equation A.23. In the case that hydraulic redistribution is not allowed in the root systems of both species then the coupled set of equations are.

$$\frac{\partial\theta}{\partial t} - \frac{\partial}{\partial z}\left[Ks\left(\frac{\partial\psi s}{\partial z} - 1\right)\right] = -Kr_{r,1}\left(\psi s - \psi r_1\right) - Kr_{r,2}\left(\psi s - \psi r_2\right)$$

$$-\frac{\partial}{\partial z}\left[Kr_{a,1}\left(\frac{\partial\psi r_1}{\partial z} - 1\right)\right] = Kr_{r,1}\left(\psi s - \psi r_1\right)$$

$$-\frac{\partial}{\partial z}\left[Kr_{a,2}\left(\frac{\partial\psi r_2}{\partial z} - 1\right)\right] = Kr_{r,2}\left(\psi s - \psi r_2\right) \tag{A.43}$$

$Kr_{r,1} = 0$, for $, \psi r_1 < \psi s$

$Kr_{r,2} = 0$, for $, \psi r_2 < \psi s$

Note that the numerical solution for the root equations in A.43 are the same as the solution presented before in equations A.26, A.29 and A.32 therefore here we are going to show only the solution for the soil equation. The soil equation in A.42 is similar to the soil equation in

A.23 but now the equations contain two sink terms corresponding to the two different root species. Apart of this small difference both equations are the same.

$$\frac{\partial\theta}{\partial t} - \frac{\partial}{\partial z}\left[Ks\left(\frac{\partial\psi s}{\partial z} - 1\right)\right] = -Kr_{r,1}\left(\psi s - \psi r_1\right) - Kr_{r,2}\left(\psi s - \psi r_2\right)$$

The discrete representation of the soil equation for the case in which there are two species is given by:

$$\left(\frac{\theta_i^{t+1,m} + C_i^{t+1,m}(\psi s_i^{t+1,m+1} - \psi s_i^{t+1,m}) - \theta_i^t}{\Delta t}\right) - \frac{1}{\Delta z_i}\left[Ks_{i+1/2}^{t+1,m}\left(\frac{\psi s_{i+1}^{t+1,m+1} - \psi s_i^{t+1,m+1}}{\Delta z_{i+1/2}} - 1\right) - Ks_{i-1/2}^{t+1,m}\left(\frac{\psi s_i^{t+1,m+1} - \psi s_{i-1}^{t+1,m+1}}{\Delta z_{i-1/2}} - 1\right)\right] = -Krr_{i,1}^{t+1}\left(\psi s_i^{t+1,m+1} - \psi r_{i,1}^{t+1}\right) - Krr_{i,2}^{t+1}\left(\psi s_i^{t+1,m+1} - \psi r_{i,2}^{t+1}\right) \tag{A.44}$$

Rearranging terms in A.36 we obtain:

$$\psi s_{i-1}^{t+1,m+1}\left[\frac{-Ks_{i-1/2}^{t+1,m}}{\Delta z_{i-1/2}\Delta z_i}\right] + \psi s_i^{t+1,m+1}\left[\frac{C_i^{t+1,m}}{\Delta t} + \frac{Ks_{i-1/2}^{t+1,m}}{\Delta z_{i-1/2}\Delta z_i} + \frac{Ks_{i+1/2}^{t+1,m}}{\Delta z_{i+1/2}\Delta z_i} + Krr_{i,1}^{t+1} + Krr_{i,2}^{t+1}\right] + \psi s_{i+1}^{t+1,m+1}\left[\frac{-Ks_{i+1/2}^{t+1,m}}{\Delta z_{i+1/2}\Delta z_i}\right] = \left(\frac{C_i^{t+1,m}\psi s_i^{t+1,m}}{\Delta t}\right) - \left(\frac{\theta_i^{t+1,m} - \theta i^t}{\Delta t}\right) - \frac{1}{\Delta z}\left(Ks_{i+1/2}^m - Ks_{i-1/2}^m\right) + \psi r_{i,1}^{t+1} Krr_{i,1}^{t+1} + \psi r_{i,2}^{t+1} Krr_{i,2}^{t+1} \tag{A.45}$$

Equation A.36 is the general form of the numerical discrete equation for the soil system equation for the case of two or more species.

From equation A.45 and following the same approach as in single species, the equation for two root species for the first layer of soil under a flux boundary condition is:

$$\psi s_i^{m+1}\left[\frac{C_i^m}{\Delta t}+\frac{Ks_{i+1/2}^m}{\Delta z_{i+1/2}\Delta z_i}+Krr_{i,1}+Krr_{i,2}\right]+\psi s_{i+1}^{m+1}\left[\frac{-Ks_{i+1/2}^m}{\Delta z_{i+1/2}\Delta z_i}\right]=$$

$$\left(\frac{C_i^m\psi s_i^m}{\Delta t}\right)-\left(\frac{\theta_i^m-\theta i^t}{\Delta t}\right)-\frac{1}{\Delta z}(Ks_{i+1/2}^m)+\psi r_i Krr_{i,1}+\psi r_i Krr_{i,2}-q_{inf}^m \tag{A.46}$$

Likewise, the top boundary bondition for the soil equation using a flux can be computed from Equation A.45. Following the same approach as in single species, the equation for two root species for the first layer of soil under a given head boundary condition is:

$$\psi s_i^{m+1}\left[\frac{C_i^m}{\Delta t}+\frac{Ks_{i-1/2}^m}{\Delta z_{i-1/2}\Delta z_i}+\frac{Ks_{i+1/2}^m}{\Delta z_{i+1/2}\Delta z_i}+Krr_{i,1}+Krr_{i,2}\right]+\psi s_{i+1}^{m+1}\left[\frac{-Ks_{i+1/2}^m}{\Delta z_{i+1/2}\Delta z_i}\right]$$

$$=\left(\frac{C_i^m\psi s_i^m}{\Delta t}\right)-\left(\frac{\theta_i^m-\theta i^t}{\Delta t}\right)-\frac{1}{\Delta z}\left(Ks_{i+1/2}^m-Ks_{i-1/2}^m\right)+ \tag{A.47}$$

$$\psi r_{i,1}Krr_{i,1}+\psi r_{i,2}Krr_{i,2}+H_o\left[\frac{Ks_{i-1/2}^m}{\Delta z_{i-1/2}\Delta z_i}\right]$$

Similarly it is possible to solve the head boundary condition in the soil when two species coexist by following the results obtained for a single species.

$$\psi s_{i-1}^{m+1}\left[\frac{-Ks_{i-1/2}^m}{\Delta z_{i-1/2}\Delta z_i}\right]+\psi s_i^{m+1}\left[\frac{C_i^m}{\Delta t}+\frac{Ks_{i-1/2}^m}{\Delta z_{i-1/2}\Delta z_i}+Krr_{i,1}+Krr_{i,2}\right]=$$

$$\left(\frac{C_i^m\psi s_i^m}{\Delta t}\right)-\left(\frac{\theta_i^m-\theta i^t}{\Delta t}\right)+\frac{1}{\Delta z}(Ks_{i-1/2}^m)+\psi r_{i,1}Krr_{i,2}+\psi r_{i,2}Krr_{i,2}+\frac{k_i^m}{\Delta z_i} \tag{A.48}$$

APPENDIX B

Litter Model

The litter model uses the framework introduced in previous studies ([Bavel and Hillel, 1976, Chung and Horton, 1987, Haverd and Cuntz, 2010, Ogee and Brunet, 2002, Park et al., 1998]). The following three coupled equations are solve iteratively until convergence is reached (see Figure B.1a for the algorithm and Appendix E.1 for a description of the symbols):

1. Energy Balance at the litter surface

At the litter surface

$$R_n \equiv R_{abs} - LW_s = LE_L + H_L + G_{L1} \tag{B.1}$$

where R_n is the net radiation equal to the total radiation absorbed by the soil (R_{abs}) minus the long wave radiation emitted by the soil (LW_s). LE_L is the total latent heat released by the litter and is obtained as

$$LE_L = L_v \rho_d \Big[\frac{RH_{Ln} q^*_{Ln} - q_{a1}}{r_a + r_s} \Big] \tag{B.2}$$

where r_a and r_L are the aerodynamic resistance and the resistance of litter to vapor transport. These resistances are computed using the methodology developed by Ogee and Brunet [2002], Schaap et al. [1997]. The sensible heat flux (H_L) is obtained as

$$H_L = \rho_d C_p \left[\frac{T_{LSS} - T_{a1}}{r_a} \right]. \tag{B.3}$$

The ground heat flux into the litter (G_{L1}) is obtained as

$$G_{L1} = TC_L \left[\frac{T_{LSS} - T_{Ln}}{\Delta z_L / 2} \right] \tag{B.4}$$

Equation B.1 is solved using a numerical root finding function for the temperature at the

litter surface (T_{LSS}).

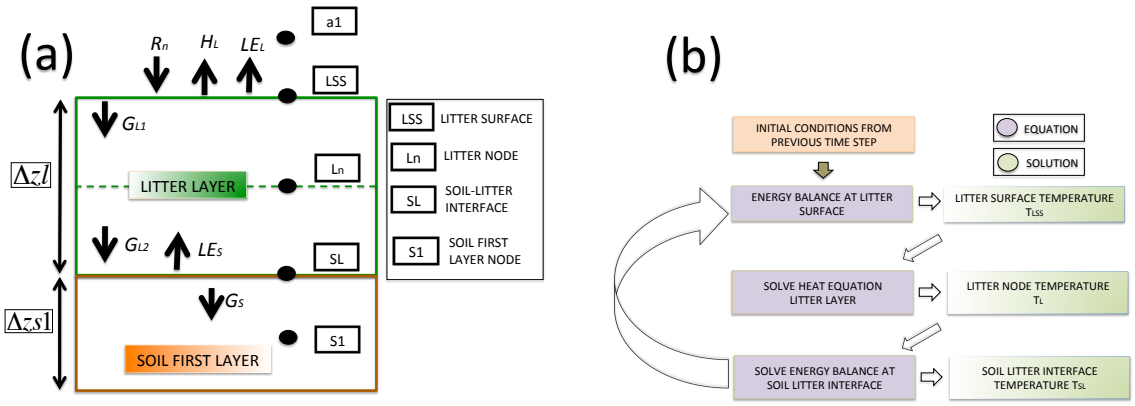

Figure B.1: Schematic illustrating the litter model. **a.** The litter layer is modeled as a single layer. **b.** Iterative Solution flowchart. A numerical implementation is performed to include litter layer dynamics. Energy balance is solved at the litter surface and also at the soil litter interface. Three equations (i. litter surface energy balance, ii. Litter heat equation, iii. litter - Soil Interface energy balance) are solved simultaneously using an iterative framework.

2. Conservation of energy inside the litter layer

Assuming that the thermal conductivity remains constant through the litter layer, the heat equation for the litter layer is given by:

$$\frac{\partial T_L}{\partial t} = \alpha_L \frac{\partial}{\partial z}\left(\frac{\partial T_L}{\partial z}\right) \equiv -\frac{\partial G_L}{\partial z} \tag{B.5}$$

The terms T_L, G_L, and α_L in equation B.5 are the litter temperature, heat flux inside the litter layer and litter thermal diffusivity. We implement a simple numerical solution of the heat equation using an implicit scheme and just one layer to get:

$$T_{Ln}^{j+1} = \frac{\left(4\eta(T_{LSS}^{j+1} + T_{SL}^{j+1}) + T_{Ln}^{j}\right)}{\left(1 + 8\eta\right)} \tag{B.6}$$

where

$$\eta = \frac{\alpha_L \Delta t}{\Delta z_L^2} \tag{B.7}$$

3. Energy Balance at the soil-litter interface

The ground heat flux from the litter layer to the soil (G_{L2}) is given as

$$G_{L2} = LE_s + G_s \tag{B.8}$$

where

$$G_{L2} = TC_L \left[\frac{T_{Ln} - T_{SL}}{\Delta z_L / 2} \right] \tag{B.9}$$

The latent heat emitted from the soil (LE_s) is obtained as

$$LE_s = L_v \rho_d \left[\frac{RH_{S1} q^*_{S1} - q_a}{r_a} \right] \tag{B.10}$$

The ground heat flux into the soil (G_s) is obtained as:

$$G_s = TC_{s1} \left[\frac{T_{SL} - T_{S1}}{\Delta z_{s1} / 2} \right] \tag{B.11}$$

The Relative humidity in the top soil layer is computed as:

$$RH = \exp \left[\frac{-g\psi}{R_w T} \right] \tag{B.12}$$

where R_w is the gas constant for water vapor and ψ is the water potential. In the case of the litter the water potential is computed as [Ogee and Brunet, 2002]:

$$\psi_L = \psi_{LL} \left[\frac{\rho_w \theta_L}{\rho_b} \right] \tag{B.13}$$

where θ_L is the soil water content in the litter layer. The dynamics of water in the litter layer are calculated based on simple mass balance.

APPENDIX C

Solution of Snow-Litter Dynamics

This section describes the numerical approximation implemented in the solution of the snow-litter dynamics in MLCan. The solution of the snow-litter dynamics includes two main components (See Figure C.1):

1. Solution of change of phase between ice and liquid water in the soil column. The heat equation is solved by including an extra sink (or source) of heat energy that is used to melt (or freeze) the water in the soil column under some special circumstances.

2. Solution of the snow-litter dynamics. During winter time snow can be formed over the surface if some conditions such as rainfall and low temperatures are present. In addition, natural ecosystems accumulates a layer of highly decompose organic matter over the soil column. This layer is known as litter. The presence of litter and snow impact the balance of mass (water) and energy in the surface. The numerical solution described in this section solve mass, and energy balance by consider the presence of snow and litter simultaneously.

C.1 Change of Phase in the Soil

The solution of the heat equation in the soil was included in MLCan [Drewry et al., 2010a,b]. The scheme utilized by MLCan to solve the heat equation is based on the formulation developed in the Community Land Model (CLM). This formulation implements a Crank Nicholson method to solve the heat equation in one dimension [Oleson et al., 2010]. The main equations used to solve the heat equations by a Crank Nicholson approximation are not shown here. Instead we focus in the equations used to solve the change of phase between ice and liquid water. Again, the solution of the phase change was implemented following the approximation developed in the CLM. Most of these equations are described in [Oleson

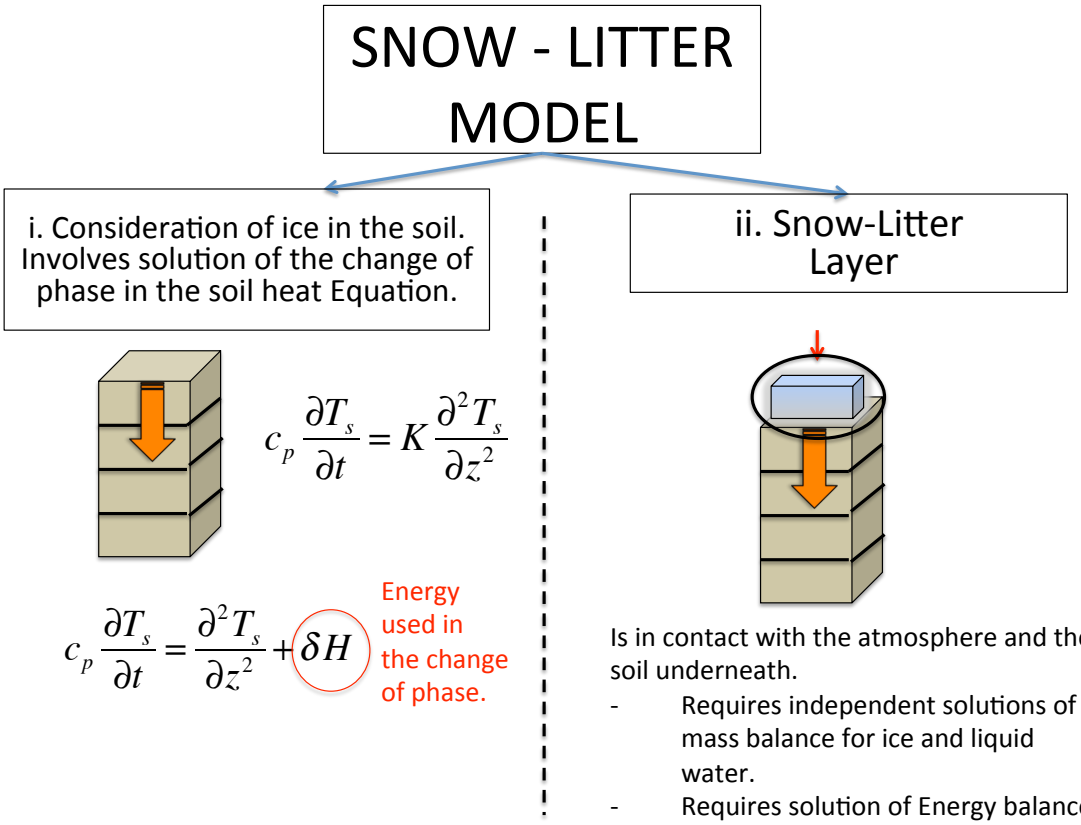

Figure C.1: General description of snow and litter solution. Two main numerical solutions are considered. **(i)** Solution of the heat equation including energy consumed (or released) in the change of phase between liquid and ice that occurs in the soil under some given conditions, and **(ii)** solution of the snow litter layer above the soil column that impacts the energy balance at the surface.

et al., 2010] chapter 7. However, in this document we made some modifications to the original equations in order to show more clarity in the light of MLCan.

The flux of heat in the soil between two layers i and $i+1$ is given by:

$$F_i = -K_i \left(\frac{T_{i+1} - T_i}{z_{i+1} - z_i} \right). \tag{C.1}$$

In Equation C.1 the term T_i refers to soil temperature in layer i, k_i refers to the thermal conductivity between layers i and $i+1$ and F_i is the flux of energy between layers i and $i+1$. The heat equation can be expressed in terms of heat fluxes as shown in Equation C.2

$$c_i \frac{\partial T_i}{\partial t} = -\frac{\partial F}{\partial z} \simeq -\left(\frac{F_i - F_{i-1}}{\Delta z_i} \right) \tag{C.2}$$

Combining Equations C.1 and C.2, and using a Cranck Nicholson method with a factor α it is possible to show that:

$$c_i \frac{\partial T_i}{\partial t} = \left\{ \begin{array}{ll} -F_i^n \alpha - F_i^{n+1}(1-\alpha) + G_s & \text{layer } i = 1 \\ -\left(F_i^{n+1} - F_{i-1}^{n+1}\right)(1-\alpha) - \left(F_i^{n+1} - F_{i-1}^{n+1}\right)\alpha & \text{layer } i > 1 \end{array} \right\} \tag{C.3}$$

Equation C.3 can be solved to obtain the temperature in the future time step T_i^{n+1}. However, note that some fraction of energy could be consumed or releases in change of phase between liquid and ice water. Therefore, the solution of temperature is readjusted to include possible changes of phase between liquid and water. It is possible to compute and extra (or needed) energy H_i that can be used to freeze (or melt) the water in a particular soil layer.

$$H_i = \left\{ \begin{array}{ll} G - \alpha {F_i}^n - (1-\alpha){F_i}^{n+1} - \frac{c_i \Delta z_i}{\Delta t}\left(T_f - {T_i}^n\right) & i = 1 \\ -\alpha\left(F_i^n - F_{i-1}^n\right) - (1-\alpha)\left(F_i^{n+1} - F_{i-1}^{n+1}\right) - \frac{c_i \Delta z_i}{\Delta t}\left(T_f - T_i\right) & i > 1 \end{array} \right\} \tag{C.4}$$

This energy can also be computed in terms of water units, as:

$$H_{mi} = \frac{H_i \Delta t}{L_f}. \tag{C.5}$$

In this Equation, the term L_f is the latent heat of fusion. From Equation C.5 it is possible to compute the new states of ice in the next time step w_{ice}^{n+1} based on the availability of ice and liquid water in the soil.

$$w_{ice,i}^{n+1} = \left\{ \begin{array}{l} w_{ice,i}^{n} - H_{mi} >= 0 \\ \qquad\qquad \textbf{if} \left[T_i^{n+1} > T_f \text{ and } w_{ice,i} > 0 \text{ and } H_{mi} > 0 \right] \text{ (Melting)} \\ \min \left(w_{ice,i}^{n} + w_{liq,i}^{n} - w_{liq,\max}, w_{ice,i}^{n} - H_{mi} \right) >= 0 \\ \qquad\qquad \textbf{if} \left[T_i^{n+1} < T_f \text{ and } w_{liq,i} > w_{liq,\max} \text{ and } H_{mi} < 0 \right] \text{ (Freezing)} \end{array} \right\} \quad \text{(C.6)}$$

The liquid water in the next time step is given by:

$$w_{liq,i}^{n+1} = w_{liq,i}^{n} + w_{ice,i}^{n} - w_{ice,i}^{n+1} = w_{liq,i}^{n} + \Delta w_i \geq 0 \quad \text{(C.7)}$$

Note, that the change of phase is constrained by the availability of energy and also by the availability of ice (or liquid). Therefore the initial available energy H_i must be updated by consideration of available water.

$$H_i^* = H_i - \frac{L_f \left(\Delta w_i \right)}{\Delta t} \quad \text{(C.8)}$$

The temperature in the future time state can be finally calculated by consideration of the energy consumed in the change of phase.

$$T_i^{n+1} = T_f + \frac{\Delta t}{c_i \Delta z} H_i^* \quad \text{(C.9)}$$

C.2 Solution of the Snow-Litter Pack

The snow-litter pack is a conceptualization of a layer of snow and litter that is formed over the soil. This layer influences the mass and energy balances in the surface. During winter periods the availability of moisture and low temperatures can induce the formation of snow. On the other hand, in natural ecosystems is very common the formation of litter which is a layer of highly decompose organic matter over the soil.

In this study we simulate the energy and mass balance of the snow-litter pack considering a layer that is composed of both materials. As expected, in the absence of snow (no winter), the snow litter pack is only formed by litter.

C.2.1 Thermal Properties of the Snow-Litter Pack

In this section I present the equations to compute the thermal properties of the snow-litter pack. The snow-litter pack is composed of different components such as litter, snow and water. Therefore the net thermal properties in the snow-litter pack will depend on each of the individuals properties of these components. The two main properties introduced in this section are the thermal conductivity and the thermal diffusivity.

Thermal Conductivity

The thermal conductivity is assumed to be the same as snow when the snow depth is higher than the litter thickness. In the case that the snow depth is lower than the litter thickness then the net thermal conductivity is computed by considering the thermal conductivities in each of the three components. (Equation C.10).

$$K_{sl} = \begin{cases} K_e K_{sl,sat} + (1 - K_e) K_{litter} \\ \qquad\qquad \text{if} \quad z_{SN} \leq \Delta z_{litter} \\ K_{air} + \left(7.75x10^{-5}\rho_{SN} + 1.105x10^{-6}\rho_{SN}^2\right)(K_{ice} - K_{air}) \\ \qquad\qquad \text{if} \quad z_{SN} > \Delta z_{litter} \end{cases} \tag{C.10}$$

The term K_{litter}, K_{air} and K_{ice} are the thermal conductivities of the litter, air, and ice respectively. The term $K_{SL,sat}$ is the saturated thermal conductivity of the snow-litter pack and is calculated as:

$$K_{sl,sat} = \begin{cases} K_{litter}^{(1-\eta)} K_{liq}^{\eta} & \mathrm{T}_{SL,n} \geq T_f \\ \\ K_{litter}^{(1-\eta)} K_{liq}^{\eta} K_{ice}^{\eta-\theta_{liq}} & \mathrm{T}_{SL,n} < T_f \end{cases} \tag{C.11}$$

Similarly, K_{liq} refers to the thermal conductivity of liquid water. The term K_e in Equation C.10 is given by:

$$K_e = \begin{cases} \log(S_r) + 1 \geq 0 & \mathrm{T}_{SL,n} \geq T_f \\ \\ S_r & \mathrm{T}_{SL,n} < T_f \end{cases} \tag{C.12}$$

where S_r is the effective snow-litter pack moisture, which is defined as:

$$S_r = \left(\frac{\theta_{liq} + \theta_{ice}}{\eta}\right) \tag{C.13}$$

Thermal Diffusivity

The thermal diffusivity of the snow-litter pack is given by:

$$c_{SL} = \begin{cases} c_{litter}(1-\eta) + \frac{w_{ice}}{\Delta z_{litter}} C_{ice} + \frac{w_{liq}}{\Delta z_{litter}} C_{liq} \\ \qquad\qquad\qquad \textbf{if} \quad z_{SN} \leq \Delta z_{litter} \\ c_{litter}(1-\eta)\frac{\Delta z_{litter}}{z_{SN}} + \frac{w_{ice}}{\Delta z_{litter}} C_{ice} + \frac{w_{liq}}{\Delta z_{litter}} C_{liq} \\ \qquad\qquad\qquad \textbf{if} \quad z_{SN} > \Delta z_{litter} \end{cases} \tag{C.14}$$

where that C_{ice} and C_{liq} are the specific heat capacities of ice and liquid water respectively. Note that the product $C\frac{w}{\Delta z}$ is the respective volumetric heat capacity.

C.2.2 Energy Balance in the Snow-Litter pack

Energy balance is solve separately in two different locations: (i) inside the snow litter pack, and (ii) in the snow-litter pack - soil boundary (See Figure C.2). The final solution is obtained by an iterative process of these two calculations. Although these two calculations are performed separately, they are coupled. In this section I describe each of these two energy balance solutions.

1. Energy Balance inside the Snow-Litter Pack Surface

The energy balance in the snow-litter is given by:

$$c_{sl}\frac{\partial T}{\partial z} = R_{abs,sl} - LE_{sl,s} - LE_{sl,v} - H_{sl} - LW_{sl} - G_{sl} - \delta H \tag{C.15}$$

In this equation the term $LEsl,s$ is the latent heat due to sublimation processes, $LEsl,v$ is the latent heat due to evaporation, H_{sl} is the sensible heat flux, and G_{sl} is the ground heat flux into the snow-litter pack. $R_{abs,sl}$ is the absorbed radiation, and LW_{sl} is the long wave radiation emitted by the snow-litter pack. The term δH refer to the energy spent (or released) by melting (or freezing) during change of phase.

In this study I assume that one of both latent heat fluxes is occurring only. The flux of either evaporation or sublimation is controlled by the amount of snow that is present (Equation C.16). The equations to compute the latent heat are given by:

$$LE_{sl,v} = \begin{cases} \frac{L_v(q_{sl}-q_a)}{r_a+r_s} & z_{ice} < \nu\Delta_{litter}\eta_{litter} \\ \\ \frac{L_s(q_{sl}-q_a)}{r_a} & z_{ice} > \nu\Delta_{litter}\eta_{litter} \end{cases} \tag{C.16}$$

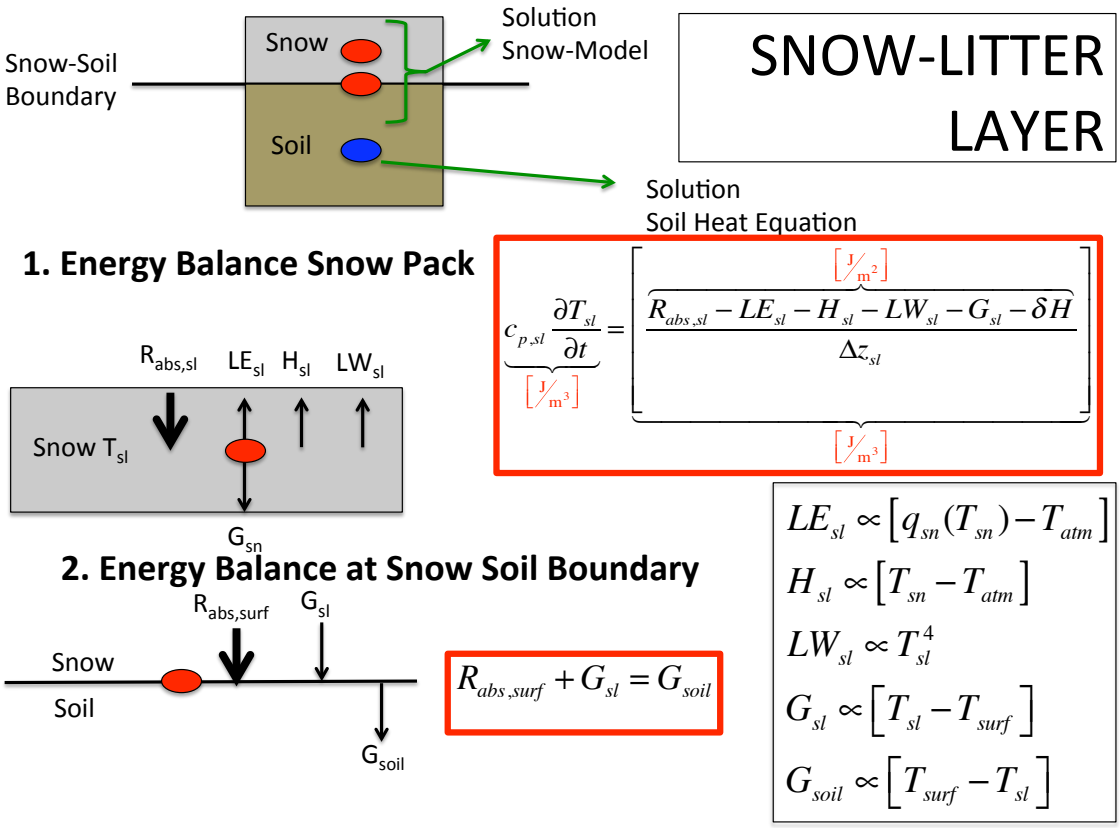

Figure C.2: Representation of the energy solution of the snow-litter pack. Energy balance is solved in the center node of the snow-litter pack, and also at the interface between the snow-litter pack and the soil. The final solutions is obtained by an iterative process between these two solutions.

In Equation C.16 the term ν determines the fraction of ice above which sublimation occurs, q_{sl} refers to the absolute humidity in the soil-litter pack, q_a is the absolute humidity in the atmosphere, r_a is the aerodynamic resistance, r_s is the extra resistance of vapor vapor in the litter layer.

The absolute humidity in the snow-litter layer and also in the atmosphere is computed as:

$$q_{sl} = 0.622 \frac{e_s RH_{sl}}{e_d} \rho_d \tag{C.17}$$

$$q_a = 0.6220 \frac{e_a}{e_d} \rho_d \tag{C.18}$$

The aerodynamic conductivity is given by:

$$r_a = \frac{\left(\log\left[\frac{z1}{zo}\right]\right)^2}{{k_v}^2 U} \tag{C.19}$$

where k_v is the von Karman's constant, U is the wind velocity at a reference height $z1$ and zo is the roughness length.

The ground heat flux into the snow-litter pack is given by:

$$G_{sl,1} = \begin{cases} k_{sl}\left(\frac{T_{sl,n} - T_{surf}}{\Delta z_{litter}/2}\right) & z_{SN} \leq \Delta z_{litter} \\ k_{sl}\left(\frac{T_{sl,n} - T_{surf}}{z_{SN}/2}\right) & z_{SN} > \Delta z_{litter} \end{cases} \tag{C.20}$$

The term $T_{sl,n}$ is the temperature at the central node of the snow-litter pack, T_{surf} is the snow-litter pack temperature at the bottom in the boundary with the soil and k_{sl} is the thermal conductivity in the snow-litter pack (see section C.10).

In order to solve Equation C.15, we need to solve the energy that is involved in the change of phase δH. The approach followed in this study to solve this equation is iteratively. The next steps are performed:

1. Initially it is assumed that the temperature in the snow litter pack $T_{sl} = 0$. Under this assumption it is possible to compute the available energy that will be present to melt (positive) or freeze the soil (negative).

$$\delta H = R_{abs,sl} - LE_{sl,s} - LE_{sl,v} - H_{sl} - LW_{sl} - G_{sl} - c_{sl}\Delta z_{sl}\left[\frac{T_{sl}^n - T_{sl}^{n-1}}{\Delta t}\right] \tag{C.21}$$

2. With δH and knowing the availability of liquid water or ice in the snow-litter pack, it is possible to compute the change in ice content that is occurring from a change of phase. If $\delta H > 0$ there is extra energy and melting occurs if there is ice, on the other hand, if $\delta H < 0$ the system is releasing energy and freezing occurs if there is liquid water. The amount of water that could experience change of phase based on availability of energy only is given by:

$$H_{m,sl} = \left(\frac{H_{SL} \Delta_t}{L_f} \right) \tag{C.22}$$

In this equation L_f is the latent heat of fusion. The amount of w_{ice} in the new time step is then given by:

$$w_{ice}^{n+1} = \begin{cases} \max\left(w_{ice}^{n} - H_{m,SL}, 0\right) \\ \qquad \textbf{if} \quad [w_{ice} > 0, H_{m,sl} > 0] \\ \min\left(w_{ice}^{n} - H_{m,SL}, w_{ice}^{n} + w_{liq}^{n}\right) \\ \qquad \textbf{if} \quad [w_{liq} > 0, H_{m,sl} < 0] \end{cases} \tag{C.23}$$

and therefore the total change of ice from the previous time step is given by:

$$\Delta w_{ice} = w_{ice}^{n+1} - w_{ice}^{n}. \tag{C.24}$$

3. Based on the availability of liquid water (or ice) to freeze (or melt), the final energy spent in the change of phase is updated:

$$\Delta H_{new} = \left(\frac{\Delta w L_f}{\Delta t} \right) \tag{C.25}$$

4. Using the new found energy invested in the change of phase δH_{new}, it is possible to solve Equation C.21 for the temperature in the snow-litter pack using a non linear optimizer that finds the most optimum temperature satisfying equation C.26.

$$0 = R_{abs,sl} - LE_{sl,s} - LE_{sl,v} - H_{sl} - LW_{sl} - G_{sl} - \delta H_{new} - c_{sl} \Delta z_{sl} \left[\frac{T_{sl}^{n} - T_{sl}^{n-1}}{\Delta t} \right]. \tag{C.26}$$

Figure C.3 shows a flow chart that represents the steps described above.

2. Energy Balance at the Bottom of the Snow-Litter Pack

This section shows the equations for the calculation of the energy balance in the boundary between the snow-litter pack and the soil. The solution of these equations allow us to obtain

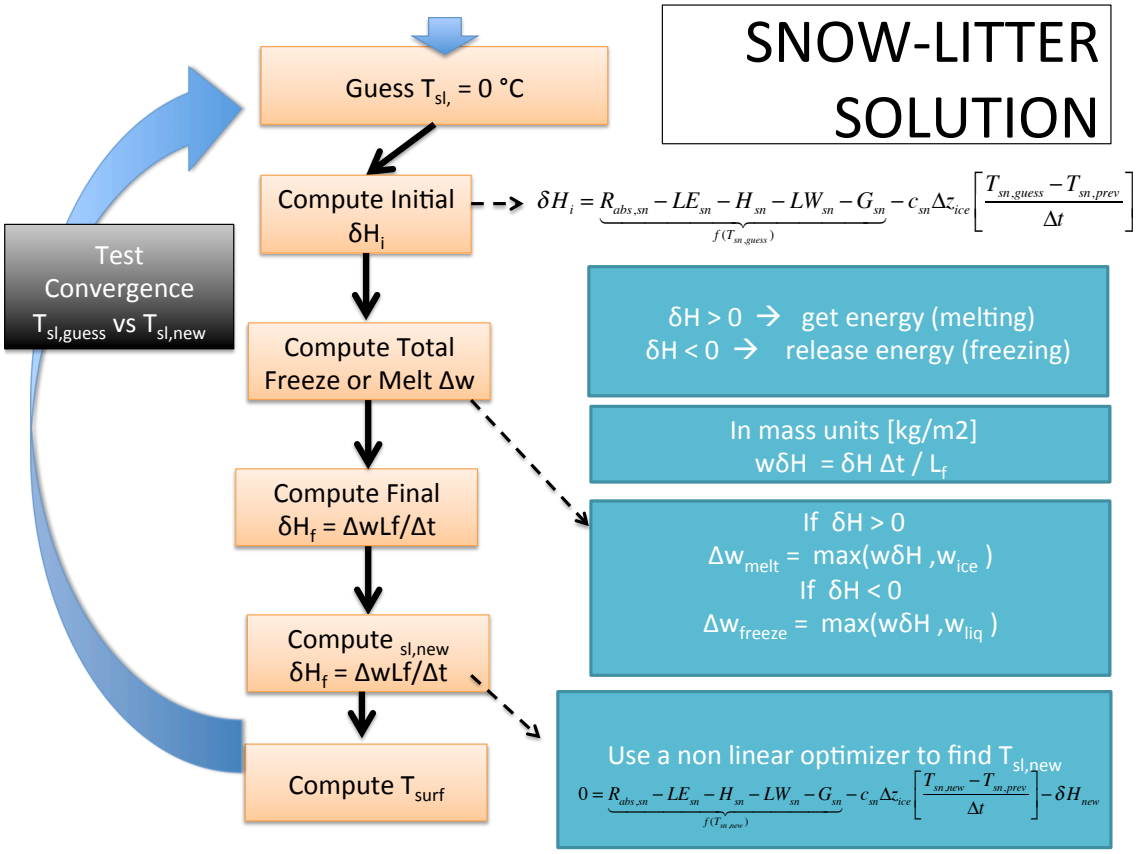

Figure C.3: Flow chart of the different processes involves to solve the energy balance inside the snow-litte pack layer.

the temperature at the interface between the snow-litter pack and the soil (T_{surf}). The energy balance in the snow-litter interface and soil will depend on the amount of snow that is above the soil. When ice content above the soil is thick it will not allow the fluxes of latent heat from the soil.

$$\text{EnergyBalance} \begin{cases} G_{sl} = G_s + LE_s & z_{ice} < \nu\Delta_{litter}\eta_{litter} \\ \\ G_{sl} = G_s & z_{ice} > \nu\Delta_{litter}\eta_{litter} \end{cases} \tag{C.27}$$

In this Equation G_{sl} is the flux of heat from from the snow-litte pack, G_s is the flux of heat into the soil, and LE_s is the latent heat flux from the soil.

These fluxes are given by:

$$G_{sl,2} = \begin{cases} K_{sl}\frac{\left[T_{sl,n} - T_{surf}\right]}{\Delta z_{litter}/2} & z_{SN} \leq \Delta z_{litter} \\ K_{sl}\frac{\left[T_{sl,n} - T_{surf}\right]}{z_{SN}/2} & z_{SN} > \Delta z_{litter} \end{cases} \tag{C.28}$$

$$G_s = K_{s,1}\frac{\left[T_{surf} - T_{s,1}\right]}{\Delta z_{s,1}/2} \tag{C.29}$$

and

$$LE_s = \frac{L_v\left(q_{s,1} - q_a\right)}{r_a} \tag{C.30}$$

The term K_s refers to soil thermal conductivity and $q_{s,1}$ is the absolute humidity in the upper soil layer. Base on the previous equations it is possible to show that the temperature in the interface between the snow-litter pack and the soil ($T_{SL,b}$) is given by:

$$T_{SL,b} = \begin{cases} \left(\frac{T_{s,1}K_{s,1}\Delta z_{sl} + T_{sl,n}K_{sl}\Delta z_{s,1} - \left(LE_s/2\right)\Delta z_{sl}\Delta z_s}{K_{s,1}\Delta z_{sl} + K_{sl}\Delta z_{s,1}}\right) \\ \qquad\qquad \textbf{if} \quad z_{ice} < \nu\Delta_{litter}\eta_{litter} \\ \\ \left(\frac{T_{s,1}K_{s,1}\Delta z_{sl} + T_{sl,n}K_{sl}\Delta z_{s,1}}{K_{s,1}\Delta z_{sl} + K_{sl}\Delta z_{s,1}}\right) \\ \qquad\qquad \textbf{if} \quad z_{ice} > \nu\Delta_{litter}\eta_{litter} \end{cases} \tag{C.31}$$

The final solution in the snow-litter pack is obtained by an iterative process between the energy balance within the snow litter pack (solved for $T_{sl,n}$) and the energy balance at the interface with the soil (solved for T_{surf}) (See Figure C.2).

C.3 Mass Balance in the Snow-Litter Pack

C.3.1 Rainfall

The input of rainfall reaching the ground could be in form of ice or liquid. The state of water reaching the surface is determined according to the atmospheric temperature (T_a). When temperature in the atmosphere is above a critical value (T_c) then the state of water reaching the surface is liquid otherwise it reaches the surface as snow.

$$\begin{aligned} z_{icegr} &= PPT_{gr}; z_{liqgr} = 0; && \text{if } T_a < T_c \\ z_{icegr} &= 0; z_{liqgr} = PPT_{gr}; && \text{if } T_a \geq T_c \end{aligned} \tag{C.32}$$

Similarly, the density of water reaching the ground is also function of the atmospheric temperature.

$$\rho_{sli} \left\{ \begin{array}{ll} 50 + 1.7(17)^{1.5} & T_{atm} > T_f + 2 \\ 50 + 1.7(T_{atm} - T_f + 15)^{1.5} & T_f - 15 \leq T_{atm} \leq T_f + 2 \\ 50 & T_{atm} < T_f - 15 \end{array} \right\} \tag{C.33}$$

Once the density and depth of rainfall water is known it is possible to compute its mass per unit of surface area.

$$w_{si} = PPT_{gr}\rho_{si} \tag{C.34}$$

C.3.2 Mass Balance in the Litter - Snow Pack

The litter and snow configuration is able to retain some amount of liquid water. Here, I assume that if the depth of the snow z_{SN} is higher than a given fraction η of the total litter porosity depth then it behaves as a snow pack, otherwise it behaves as a regular litter layer. Therefore, the calculation of the total depth of drainage is given as:

$$q_{drainli} = \left\{ \begin{array}{ll} k_m \left[\exp(-b_m z_{liq})\right] & z_{ice} < \nu \Delta z_{litter} \eta_{litter} \\ \max\left[0, \left(\frac{w_{liq}}{w_{SN}} - S_{hc}\right)\right] \frac{w_{SN}}{\rho_{liq}\Delta t} & z_{ice} > \nu \Delta z_{litter} \eta_{litter} \end{array} \right\} \tag{C.35}$$

In this equation k_b and b_m are litter parameters, while S_{hc} is the maximum percentage of liquid water than can be retained by the snow.

C.3.3 Update of Snow Density

The snow density is reduced in time due snow compaction and metamorphism. According to Koivusalo et al. [2001], the rate of change snow density is given by two combined equations:

$$\frac{d\rho_{SN}}{dt} = \rho_{SN}\left[c1W^{*}e^{-c2(T^{*}-T_{SN})}e^{-c3\rho_{SN}}\right] \tag{C.36}$$

In this equation the terms $c1$, $c2$ and $c3$ are constants, W^{*} is the snow water equivalent, assumed in this study equal to the load of snow in the current layer w_{SN}, and T^{*} is equal to 0°C.

The second equation that determines the rate of change of density is:

$$\frac{d\rho_{SN}}{dt} = \rho_{sn}\left[c4e^{-c5(T*-T_{SN})}c6\right] \tag{C.37}$$

$$c6 = \left\{ \begin{array}{l} e^{-c7(\rho_{SN}-\rho_{d})}\rho_{\mathrm{sn}}{>}\rho_{\mathrm{d}} \\ 1\rho_{\mathrm{sn}} \leq \rho_{\mathrm{d}} \end{array} \right\} \tag{C.38}$$

In this equation the terms $c4$, $c5$ and $c6$ are constants (Table C.1).

The update of the snow density is computed with Equations C.36 and C.38 in the next form:

$$\rho_{SN}^{n+1,1} = \rho_{SN}^{n} + \rho_{sn}^{t}\left[c1w^{n}e^{-c2(T*-T_{SN})}e^{-c3\rho_{SN}}\right] \tag{C.39}$$

$$\rho_{SN}^{n+1,2} = \rho_{SN}^{n+1,1} + \rho_{SN}^{n+1,1}\left[c4e^{-c5(T*-T_{SN})}c6\right] \tag{C.40}$$

After the snow density has been updated due to processes such as compaction and metamorphisms the general update is computed including the new snow fallen from rainfall and the drainage of liquid water into the soil underneath. The snow density in the new time step is computed using linear weights applied to all the different fluxes involved:

$$\rho_{SN} = \frac{\left[\left(w_{SN}\rho_{SN}^{n+1,2}\right) + \left[\left(w_{SIN}\rho_{SIN}\right) - \left[\left(\overbrace{\rho_{liq}z_{drainli}}^{w_{drainli}}\rho_{SN}^{n+1,2}\right)\right]\right]\right]}{w_{SN} + w_{SIN} + w_{drainli}} \tag{C.41}$$

C.3.4 Compute all the State Variables

The state variables for the snow are computed using the liquid and ice loads respectively.

$$\left\{ \begin{array}{l} w_{SN} = w_{liq} + w_{ice} \\ z_{SN} = \frac{w_{SN}}{\rho_{SN}} \end{array} \right\} \tag{C.42}$$

Note that w_{SN} and z_{SN} are the load and depth of the snow layer respectively. We can also compute the different states of moisture in the snow and the litter.

$$\left\{ \begin{array}{l} \theta_{SN} = \frac{z_{liq}+z_{ize}}{z_{SN}} \\ \theta_{LI} = \frac{z_{liq}+z_{ize}}{\Delta z_{litter}} \end{array} \right\} \tag{C.43}$$

The difference between θ_{SN} and θ_{LI} in only the variable used in the normalization. In θ_{SN} it is normalized with the total depth z_{SN} while in the θ_{SN} it is normalized with the total thickness of the litter Δz_{litter}. Similarly, we can compute the moisture of liquid and ice in the snow litter by normalizing with respect to the total depth of snow or the total litter thickness.

$$\left\{ \begin{array}{ll} \theta_{liq} = \frac{z_{liq}}{\Delta z_{litter}} & \theta_{liq-sn} = \frac{z_{liq}}{z_{SN}} \\ \theta_{ice} = \frac{z_{ice}}{\Delta z_{litter}} & \theta_{ice-sn} = \frac{z_{ice}}{z_{SN}} \end{array} \right\} \tag{C.44}$$

Table C.1: List of symbols used in the snow model.

Description	Symbol	Units	Value
-			
Ground heat flux into the soil	G_s	[$\mathrm{Wm^{-2}}$]	-
Flux of heat in the soil from layer i to i+1	F_i^n	[$\mathrm{Wm^{-2}}$]	-
Flux of heat in the soil from layer i to i+1	F_i^n	[$\mathrm{Wm^{-2}}$]	-
Thermal conductivity in boundary btn layer i and i+1	K_i	[W $\mathrm{m^{-1}}$ $^\circ\mathrm{K^{-1}}$]	-
Thermal conductivity in snow-litter pack	K_{SL}	[W $\mathrm{m^{-1}}$ $^\circ\mathrm{K^{-1}}$]	-
Thermal conductivity of top soil layer	$K_{s,1}$	[W $\mathrm{m^{-1}}$ $^\circ\mathrm{K^{-1}}$]	-
Volumetric heat capacity of layer i	c_i	[J $\mathrm{m^{-3}}$ $^\circ\mathrm{K^{-1}}$]	-
Volumetric heat capacity of snow-liter pack	c_{SL}	[J $\mathrm{m^{-3}}$ $^\circ\mathrm{K^{-1}}$]	-
Soil temperature at layer i	T_i	[°K]	-
Temperature at the center node of the snow-litter pack	$T_{sl,n}$	[°K]	-
Temperature at the bottom of the snow-litter pack	T_{surf}	[°K]	-
Temperature of soil top soil layer	$T_{s,1}$	[°K]	-
Soil moisture in layer i	θ_i	–	-
Total soil moisture in the snow	θ_{SN}	–	-
Total soil moisture in the snow-litter pack	θ_{LI}	–	-
Soil moisture of liquid water in litter	θ_{liq}	–	-
Soil moisture of ice in litter	θ_{ice}	–	-
Soil moisture of liquid water in the snow	θ_{liq-sn}	–	-
Soil moisture of ice in the snow	θ_{ice-sn}	–	-
Amount of liquid water in soil layer i	$w_{liq,i}$	[kg $\mathrm{m^{-2}}$]	-
Amount of ice water in soil layer i	$w_{ice,i}$	[kg $\mathrm{m^{-2}}$]	-
Change of ice water in soil layer i btn time stept n and n+1	$\Delta w_{ice,i}$	[kg $\mathrm{m^{-2}}$]	-
Amount of liquid water in snow litter pack	w_{liq}	[kg $\mathrm{m^{-2}}$]	-
Amount of ice water in snow litter pack	w_{ice}	[kg $\mathrm{m^{-2}}$]	-
Amount of water in snow-litter pack	w_{SN}	[kg $\mathrm{m^{-2}}$]	$w_{ice} + w_{liq}$
Amount of snow reaching the ground	w_{si}	[kg $\mathrm{m^{-2}}$]	-
Change of ice water in snow litter pack btn time stept n and n+1	Δw_{ice}	[kg $\mathrm{m^{-2}}$]	-
Soil water potential in layer i	ψ_i	[mm]	-
Saturated Soil water potential in layer i	$\psi_{sat,i}$	[mm]	-
Minimum amount of liquid water that should remain in the soil	$w_{liq,max}$	[kg $\mathrm{m^{-2}}$]	-
Absolute humidity in the snow-litter pack	q_{sl}	[kg $\mathrm{m^{-3}}$]	-
Absolute humidity in the atmosphere	q_a	[kg $\mathrm{m^{-3}}$]	-

Continued on Next Page...

Table C.1 – Continued

Description	Symbol	Units	Value
Absolute humidity in the top soil layer	$q_{s,1}$	[kg m^{-3}]	-
Relative humidity in the snow-litter pack	RH_{sl}	[kg m^{-3}]	-
Aerodynamic resistance	r_a	[m s^{-1}]	-
Additional litter resistance to vapor transport	r_s	[m s^{-1}]	-
Density of dry air	ρ_d	[kg m^{-3}]	-
Density of water in the snow-litter pack	ρ_{si}	[kg m^{-3}]	-
Density of snow reaching the ground	ρ_{SN}	[kg m^{-3}]	-
Density of liquid water	ρ_{liq}	[kg m^{-3}]	-
Density of ice	ρ_{ice}	[kg m^{-3}]	-
Saturated air pressure	e_s	[MPa]	-
Dry air pressure	e_d	[MPa]	-
Wind velocity at a reference $z1$ height	U	[m/s]	-
Reference height	$z1$	[m]	-
Roughness length	zo	[m]	-
Net Radiation	$R_{n,soil}$	[W m^{-2}]	-
Radiation absorbed by the soil	$R_{abs,soil}$	[W m^{-2}]	-
Longwave radiation emitted by the soil	$LW_{e,soil}$	[W m^{-2}]	-
Latent heat of sublimation emitted by the snow-pack	LE_s	[W m^{-2}]	-
Latent heat of evaporation emitted by the snow-pack	LE_v	[W m^{-2}]	-
Sensible heat emitted by the snow-pack surface	H_{sl}	[W m^{-2}]	-
Ground heat flux into the snow-litter pack	G_{SL1}	[W m^{-2}]	-
Available energy for melting or freezing at layer i	H_i	[°K]	-
Available energy for melting or freezing at snow-litter pack	H_{SL}	[°K]	-
Net energy correction due to melting or freezing at layer i	H_i^*	[°K]	-
Net energy correction due to melting or freezing at snow litter pack	H_{SL}^*	[°K]	-
Amount of water that could be freeze or melt at layer i	H_{mi}	[kg m^{-2}]	-
Amount of water that could be freeze or melt at snow litter pack	$H_{m,SL}$	[kg m^{-2}]	-
Energy consumed in change of phase	δM	[kg m^{-2}]	-
Soil depth at node of layer i	z_i	[m]	-
Liquid water depth in the snow-litter pack	z_{liq}	[m]	-
Ice depth in the snow-litter pack	z_{ice}	[m]	-
Thickness of layer i	Δz_i	[m]	-
Thickness of snow-litter pack, $\left(\max[\Delta z_{litter}, z_{SN}]\right)$	Δz_{SL}	[m]	-

Continued on Next Page...

Table C.1 – Continued

Description	Symbol	Units	Value
Litter thickness	Δz_{litter}	[m]	-
Depth of snow	z_{SN}	[m]	-
Fraction of litter absolute depth above which is considered snow	ν	[m]	-
Porosity of litter	η	[m]	-
Holding capacity of litter	S_{hc}	[m]	-
Thickness of top soil layer	$\Delta z_{s,1}$	[m]	-
Depth of rainfall in form of ice reaching the ground	z_{icegr}	[m]	-
Depth of rainfall in form of liquid reaching the ground	z_{liqgr}	[m]	-
Depth of rainfall reaching the ground	$PPTgr$	[m]	-
Drainage flux from snow-litter pack into the soil	$q_{drainli}$	[mm/s]	-
Flux of rainfall in form of liquid reaching the ground	q_{liqgr}	[mm/s]	-
Flux of rainfall in form of ice reaching the ground	q_{icegr}	[mm/s]	-
Flux of water from liquid phase to ice phase	δ_{ice}	[mm/s]	-
Parameter to compute rate of change of the density	$c1$	[1/m/h]	1.01
Parameter to compute rate of change of the density	$c2$	[1/°C]	0.08
Parameter to compute rate of change of the density	$c3$	[m^3kg^{-1}]	0.08
Parameter to compute rate of change of the density	$c4$	[1/h]	0.01
Parameter to compute rate of change of the density	$c5$	[1/°C]	0.04
Parameter to compute rate of change of the density	$c7$	[m^3kg^{-1}]	0.046
Parameter to compute rate of change of the density	T^*	[°C]	T_f
Parameter to compute rate of change of the density	W^*	[kgm^{-2}]	w_{SN}
Parameter to compute rate of change of the density	ρ_{dc}	[kg m^{-2}]	150
Parameter to compute drainage fro litter	k_m	[1/s]	0.00015
Parameter to compute drainage fro litter	b_m	-	0.1
Von Karman constant	α	-	0.4
Crank-Nicolson Parameter, used to solved Heat Equation	α	-	0.5
Latent heat of fusion	L_f	[J kg^{-1}]	3.337X10^5
Latent heat of sublimation	L_f	[J kg^{-1}]	2.834X10^6
Latent heat of vaporization	L_v	[J kg^{-1}]	2.501X10^6
Freezing temperature of fresh water	T_f	[°K]	273.15
Soil texture-dependent saturated matric potential (mm) in layer i	b_i	[mm]	
Acceleration of gravity	g	[m s^{-2}]	9.80616

APPENDIX D

Estimation Root Conductivities

D.1 Root Conductivities Computation

Experiments conducted on roots usually report two main conductivities: (i) axial conductivity and (ii) radial conductivity [Frensch and Steudle, 1989, Huang and Nobel, 1994, Melchior and Steudle, 1993, Tyree and Zimmermann, 2002]. The radial conductivity represents the capacity of the root to transport water from the surrounding soil into the roots while the axial conductivity refers to the capacity of roots to transport water in the axial direction along the root system.

These conductivities are usually measured in controlled experiments on isolated roots. In order to use this information in numerical or analytical models that simulate processes at the whole-plant (or ecosystem) scale, we must scale these properties from isolated roots to the whole-plant (or ecosystem) level. This section presents a formulation to scale conductivities or resistances measured in isolated roots in order to estimate the conductance of the whole root system. In this formulation, both radial and axial conductivities are used. Although several assumptions as described below are considered, this formulation is a useful approach to determine the transport capacity of whole root systems based on isolated root measurements.

D.1.1 Radial Root Conductivity

Specific root radial conductivities (K_{srad}) is the root radial conductivity per unit surface or root area. Usually the units of K_{srad} are [$ms^{-1}MPa$] and refer to the discharge of water per unit area of roots under a given water potential gradient between the soil and the root. Assuming that this water potential gradient remains constant $\Delta\psi = (\psi_s - \psi_r)$, it is possible to compute the total discharge from the soil to the root as:

$$Q_{sr} = K_{srad} A_{root,sa} \Delta\psi. \tag{D.1}$$

Where $A_{sa,r}$ is the total surface area of roots. As expected the total discharge is proportional to the area and increases as the surface area increases. Based on the international system K_{rad} is expressed in $[m^3 s^{-1} m^{-2}_{root,sa} MPa^{-1}]$, $A_{roots,sa}$ in $[m^2_{root,sa}]$ and Q_{sr} in $[m^3/s]$. The effective root radial conductivity is given by $K_{e,rad} = K_{arad} A_{sa,r}$. Thus:

$$Q_{sr} = K_{e,rad} \Delta\psi. \tag{D.2}$$

The root area index ($A_{sr,g}$) is defined as the ratio between the root surface area per unit ground surface area. Using this concept, we can compute the discharge from the soil to the root per unit of ground area at a given depth as:

$$q_{sr}(z) = \frac{Q_{sr}}{A_{ground}} = K_{srad} A_{sr,g}(z) \Delta\psi(z). \tag{D.3}$$

In this equation $A_{sr,g}(z)$ is the total root surface area and $\Delta\psi(z)$ is the average difference in water potential between the soil and the root at a given depth z.

D.1.2 Estimation of $A_{sr,g}$

The computation of the $A_{sr,g}$ is challenging. It accounts for all the root surface area per unit of ground area, including coarse and fine roots. In this study we follow the approach developed by Noordwijk et al. [1994] to compute the total root surface area from a proximal root. This approximation assumes the root system follows a fractal branching model. The total root surface area of a given tree can be calculated as:

$$A_{sr,tree} = \sum_{i=0}^{Np} A_{sr,p} = \sum_{i=1}^{Np} \{N_{lp} \pi d_p L_p\}. \tag{D.4}$$

In this equation $A_{sr,p}$ is the total root surface area in a given order. The variables d_p, L_p, and N_{lp} are the representative root diameter, root length, and number of roots for a given order p, respectively. N_p is the total number of orders in the root system, and N_k is the branching number. Note that the total number of elements in a given order can be determined from N_k and N_p as:

$$N_{lp} = N_p^{N_k}. \tag{D.5}$$

In this study we follow the relationship of L_p found in Ozier-Lafontaine et al. [1999] to link root length and root diameter:

$$\mathrm{L_p} = 6.5136\ \log(\mathrm{d_p}) + 21.827 \tag{D.6}$$

The total root surface area per unit ground area can be computed if the number of trees per surface area is known (Table D.1):

$$\mathrm{A_{sr,g}} = \mathrm{A_{sr,tree}N_{trees}}. \tag{D.7}$$

The total surface area per unit of ground is distributed vertically following a root distribution function. In this study we use the logistic dose-response curve introduced in Schenk and Jackson [2002].

D.1.3 Axial Root Conductivity

Experiments conducted to measure the axial conductivity of roots are performed on isolated roots that have a particular radious $\mathrm{r_m}$ and a particular length l_m. These experiments determine the discharge transported by the root when exposed to a fixed water potential difference. Equation D.8 describes the discharge along the root occurring during the experiment. In this equation, $\Delta\psi_\mathrm{m}$ is the differential of controlled potential conditions, l_m is the root length used in the experiment, $\mathrm{Q_{rootm}}$ is the experimental discharge and $\mathrm{K_{axm}}$ is the root system conductivity.

$$\mathrm{Q_{rootm}} = \left[\frac{\Delta\psi_\mathrm{m}}{l_\mathrm{m}}\right] \mathrm{K_{axm}}. \tag{D.8}$$

If all the conditions in the experiment are controlled, the discharge $\mathrm{Q_m}$, the difference in potential $\Delta\psi_\mathrm{m}$ and the length of the root $\mathrm{l_m}$ are known. Based on this information, it is possible to obtain the conductivity of the root $\mathrm{K_{axm}}$ using equation D.9. Usually $\mathrm{Q_m}$ is expressed in units of [$\mathrm{m^3/s}$], $\Delta\psi_\mathrm{m}$ in units of [MPa] and l_m in [m]. Based on these units, $\mathrm{K_{axm}}$ is usually presented in [$\mathrm{m^4/MPa/s}$]

$$\mathrm{K_{axm}} = \left[\frac{\mathrm{Q_{rootm}}}{\Delta_\mathrm{m}\psi/l_\mathrm{m}}\right] \tag{D.9}$$

A theoretical approximation to describe the flow in root xylems can be obtained from the Hagen-Poiseuille equation [Tyree and Zimmermann, 2002]. In this case the discharge inside

a vessel may be given by:

$$\mathrm{Q_{vessel}} = \left[\frac{\pi \mathrm{r}_{\mathrm{vessel}}^4}{8\mu}\right]\left[-\frac{\partial \mathrm{H_{vessel}}}{\partial l_{\mathrm{vessel}}}\right] \tag{D.10}$$

In this equation $\mathrm{Q_{vessel}}$ is the discharge in the vessel, $\mathrm{r_{vessel}}$ is the radius of the vessel, $\frac{\partial \mathrm{H_{vessel}}}{\partial l_{vessel}}$ is the rate of change of the total energy difference in the vessel per unit length. The total energy difference can be approximated as the sum of pressure and potential energy.

$$\mathrm{Q_{vessel}} = \left[\frac{\pi \mathrm{r}_{\mathrm{vessel}}^4}{8\mu}\right]\left[-\frac{\partial (\mathrm{P}+\rho \mathrm{gz})_{\mathrm{vessel}}}{\partial l_{\mathrm{vessel}}}\right] \tag{D.11}$$

Note that l_{vessel} is the total length of the vessel (similar to equation D.8). If we combine all the vessels in the root and divide over the root cross sectional area $\mathrm{A_{cs,root}}$ we obtain the discharge per unit area of root:

$$\mathrm{q_{root}} = \frac{\sum_{\mathrm{i=1}}^{\mathrm{N_{vessel}}} \left\{\left[\frac{4\pi {\mathrm{r_i}}^4}{8\mu}\right]\left[-\frac{\partial (\mathrm{P_i}+\rho \mathrm{gz_i})}{\partial \mathrm{l}}\right]\right\}}{\mathrm{A_{cs,root}}} \tag{D.12}$$

Assuming all the vessels have the same P, z and average vessel radius $\mathrm{r_v}$,

$$\mathrm{q_{root}} = \frac{-\frac{\partial (\mathrm{P}+\rho \mathrm{gz})}{\partial \mathrm{l}}\left\{\frac{\mathrm{N_{vessel}} 4\pi \overline{\mathrm{r_v}}^4}{8\mu}\right\}}{\mathrm{A_{cs,root}}} \tag{D.13}$$

The righthand term in Equation D.13 is the axial hydraulic conductivity of the root, $\mathrm{k_{ax}}$.

$$\mathrm{q_{root}} = -\frac{\partial(\overbrace{P+\rho g z}^{\mathrm{H}})}{\partial \mathrm{l}} \frac{\overbrace{k_{ax}}^{\mathrm{k_{sax}}}}{\mathrm{A_{cs,root}}} \tag{D.14}$$

The ratio between $\mathrm{k_{ax}}$ and $\mathrm{A_{root}}$ is called the specific root conductivity, $\mathrm{k_{sax}}$ and gives us information regarding the axial conductivity of roots per root unit of cross sectional area. Experimental studies report the axial root conductivity $\mathrm{k_{axm}}$ and the specific axial root conductivity $\mathrm{k_{saxm}}$ of isolated roots by measuring the discharge under controlled gradients in water potential.

$$\mathrm{q_{root,m}} = -\frac{\partial (\mathrm{P}+\rho \mathrm{gz})}{\partial \mathrm{l}} \frac{\mathrm{k_{axm}}}{\mathrm{A_{cs,root,m}}} = -\frac{\partial (\mathrm{P}+\rho \mathrm{gz})}{\partial \mathrm{l}} \mathrm{k_{saxm}}. \tag{D.15}$$

D.1.4 Pipe Model Assumption

The pipe model assumes there constant ratio α that relates the area of a root order p-1 with the area of all roots of order p that converge to p-1 [Shinozake et al., 1964]. This relationship is given by:

$$A^{p-1} = \alpha \sum_{i=1}^{N_p} (A_i^p) \tag{D.16}$$

Also, by conservation of mass and assuming no water storage in the roots, we know that the water discharge through a root of order p-1 is equal to the sum of all the discharges through roots of order p that converge at p-1.

$$Q^{p-1} = \sum_{i=1}^{N_p} Q_i^p = \sum_{i=1}^{N_p} (A_i^p q^p) \tag{D.17}$$

It is possible to obtain an expression for the discharge per unit area in the roots of order p by assuming that the discharge per unit area in all roots of the same order are equal.

$$q^{p-1} A^{p-1} = q^p \sum_{i=1}^{N_p} (A_i^p) \tag{D.18}$$

$$q^{p-1} = \frac{q^p \sum_{i=1}^{N_p} A_i^p}{A^{p-1}} \tag{D.19}$$

$$q^{p-1} = q^p \alpha^{-1} \tag{D.20}$$

The same principle can be applied for the entire root system. Using the information obtained experimentally in a given root and also knowing its order in the plant root network it is possible to compute the discharge per unit area at the proximal root where p=0.

$$q^o = q_m \alpha^{-p_m} \tag{D.21}$$

From Equation D.14 we can obtain an expression for the root axial conductivity at the proximal root as a function of k_{saxm}, α, p_m and $A_{cs,o}$.

$$k_{ax}^o = k_{saxm} \alpha^{-p_m} A_{cs,o} \tag{D.22}$$

Under these assumptions, we can also obtain the axial root conductivity of any particular root in the root system if we also know its order p_r:

$$k_{ax}^{pr} = k_{saxm} \alpha^{-pm/pr} A_{cs,r} \tag{D.23}$$

D.1.5 Effective Axial Root Conductivity

For several applications, we need an estimate of the net effective axial conductivity of a root system. In this document, we define the effective axial conductivity as the capacity of the root system to transport water in the axial direction at a given depth. Several roots of different orders working in parallel transport water from the root system at a given depth. Therefore if we assume the same gradient in water potential for all these roots, the net conductivity is computed as the sum of all these conductivities.

$$K_{e,ax}(z) = \sum_{p}^{N_{p,z}} \sum_{j}^{M_{roots}} k_{ax,j}^{p}(z) = k_{saxm} \sum_{p}^{N_{p,z}} \sum_{j}^{M_{roots}} \alpha^{-pm/pr} A_{cs,j}^{p}(z). \tag{D.24}$$

In addition if we make the assumption that $\alpha = 1$, which is in agreement with several experimental studies [Ozier-Lafontaine et al., 1999], then:

$$K_{e,ax}(z) = k_{saxm} \sum_{p}^{N_{p,z}} \sum_{j}^{M_{roots}} \left(A_{cs,j}^{p}(z) \right) \tag{D.25}$$

Therefore:

$$K_{e,ax} = \underbrace{\underbrace{k_{saxm}}_{\left[\frac{m^4/s/MPa}{m^2_{rootcs}}\right]} \underbrace{[A_{Tcs}(z)]}_{\left[\frac{m^2_{rootcs}}{m^2_{ground}}\right]}}_{\left[\frac{m^4/s/MPa}{m^2_{ground}}\right]} \tag{D.26}$$

Note that $K_{e,ax}$ is an effective conductivity per unit ground area. Also $A_{Tcs}(z)$ is the total cross sectional area working in parallel at a given depth per unit ground area. Computation of A_{Tcs} is challenging, especially for trees with deep root systems. However, it is one of the most relevant variables that impact the axial conductance of the root system. Note that under the assumption of $\alpha = 1$, the cross sectional area can never be higher than the proximal cross sectional area ($A_{Tcs} \leq A_{cs,o}$). In this study the proximal cross sectional area

is the same basal area (A_{BA})obtained in the field. We compute the cross sectional area by assuming an exponential decay function:

$$A_{Tcs}(z) = A_{o,cs}exp^{-z\xi}. \tag{D.27}$$

The axial conductivity K_e is used to compute the total discharge along the root system in the axial direction if the effective gradient of water potential is known. Equation D.28 shows this computation and the respective international system units. Note that using the effective axial conductivity we obtain a discharge per unit ground area $[m^3_{H2O}/s/m^2_{ground}]$. This framework to calculate the effective axial root vertical conductivity is particularly useful in one dimensional models where discharge fluxes per unit of ground area are needed.

$$Q = \left[- \underbrace{\underbrace{K_e}_{\left[\frac{m^4/s/MPa}{m^2 ground}\right]} \underbrace{\frac{\partial H_r}{\partial l_r}}_{\left[\frac{MPa}{m}\right]}}_{\left[\frac{m^3/s}{m^2 ground}\right]} \right]_{\left[\frac{m}{s}\right]} \tag{D.28}$$

D.1.6 Correction for Root Length

As mentioned in the previous section, the effective axial root conductivity is particularly useful in the implementation of vertical ecohydrological models where the gradients in water potential are calculated in the vertical direction only. The discharge along the root axis is given by:

$$Q = \left[-K_e \left(\frac{\partial P_r}{\partial l_r} + \frac{\partial(\rho g z_r)}{\partial l_r} \right) \right] \tag{D.29}$$

It is possible to define a factor f_{lz} defined as the rate of change of the mean root length with respect to z.

$$\mathrm{f_{lz}} = \frac{\partial \overline{\mathrm{l_r}}}{\partial \mathrm{z_r}} \approx \frac{\overline{\mathrm{L_{path}}}}{\Delta \mathrm{z}} \tag{D.30}$$

Multiplying both numerator and denominator in Equation D.29 by f_{lz}, it is possible to express Q in terms of z instead of l, making it possible to solve in the vertical dimension only:

$$\mathrm{Q} = \left[-\mathrm{K_{e,ax}} \left(\frac{\partial \mathrm{P_r}}{\partial \mathrm{l_r}} + \frac{\partial (\rho \mathrm{g z_r})}{\partial \mathrm{l_r}} \right) \right] \frac{\mathrm{f_{lz}}}{\mathrm{f_{lz}}}; \mathrm{f_{lz}} > 0 \tag{D.31}$$

$$\mathrm{Q} = \left[- \left\{ \frac{\mathrm{K_e}}{\mathrm{f_{lz}}} \right\} \left(\frac{\partial \mathrm{P_r}}{\partial \mathrm{z_r}} + \frac{\partial (\rho \mathrm{g z_r})}{\partial \mathrm{z_r}} \right) \right] \tag{D.32}$$

Assuming that the density is constant and multiplying numerator and denominator by $\rho g.$,

$$\mathrm{Q} = \left[- \left\{ \frac{\mathrm{K_e} \rho \mathrm{g}}{\mathrm{f_{lz}}} \right\} \left(\frac{\partial \psi_\mathrm{r}}{\partial \mathrm{z_r}} + 1 \right) \right] \tag{D.33}$$

Table D.1: Ecosystems information used to compute the root hydraulic conductivities.

PFT	**Depth***	z_{50}	z_{95}	A_{BA}	d_{prox}	N_{trees}	$A_{sr,tree}$	$A_{sr,g}$
	[m]*	[m]	[m]	m^2_{root}/m^2_{gr}	[cm]	[Trees/m^2_{gr}]	[$m^2_{sr,root}$/Tree]	[$m^2_{sr,root}/m^2_{gr}$]
Ameriflux Site: Blodgett								
Ponderosa Pine	7	0.37[a]	2.6[a]	6.50	8	0.1293	12.10	1.5647
Shrubs	3	0.19[a]	1.71[a]	3.50	4	0.2785	2.90	0.8283
Bulk	7	0.458	2.39	10.00	-	0.4078	15.07	2.3930
Ameriflux Site: Tapajós								
Upper-Canopy Trees	12	0.65[a]	4.0[a]	12.75	70	0.0033	952	3.1540
Upper-Canopy Lianas	12	0.65[a]	4.0 [a]	3.75	10	0.0477	17.5	0.8451
Mid Canopy	4	0.24[a]	1.5[a]	24.00	35	0.0249	230.8	5.7573
Understory	1	0.07[a]	0.4[a]	4.50	7	0.1169	14.2	1.6651
Bulk	12	0.486	2.265	45.00	-	0.1929	1214.74	11.4215
Ameriflux Site: Harvard								
Deciduous	7	0.6[a]	3.0[a]	12.75	50	0.0125	700	8.734
Evergreen	7	0.6[a]	3.0[a]	11.50	50	0.0058	700	4.099 5
understory	1	0.1[a]	0.4[a]	3.00	7	0.0779	9	0.7015
Bulk	7	0.56[a]	2.82[a]	39.00	-	0.0963	1409	13.5358

A_{BA}**:** Basal Areal

d_{prox} : Average proximal root diameter.

N_{trees} : Number of trees per unit area.

$A_{sr,tree}$: Surface root area per tree.

Continued on Next Page...

Table D.1 – Continued

PFT	**Depth***	z_{50}	z_{95}	A_{BA}	d_{prox}	N_{trees}	$A_{sr,tree}$	$A_{sr,g}$
	[m]*	[m]	[m]	m^2_{root}/m^2_{gr}	[cm]	[Trees/m^2_{gr}]	[$m^2_{sr,roo}$/Tree]	[$m^2_{sr,root}/m^2_{gr}$]

$A_{sr,g}$: Surface root area per ground area

Table D.2: Ecophysiological parameters in Blodgett, Tapajos, and Harvard Forest Ameriflux Sites.

PFT	$V_{c,max}$	J_{max}	m	b	s_f	Ψ_f
Ameriflux Site: Blodgett						
Ponderosa Pine	54	88	13	0.001	1	-2
Shrubs	78	121	13	0.001	1	-2
Bulk	59.4	95	13	0.001	1	-2
Ameriflux Site: Tapajós						
Upper-canopy Trees	59	87	12	0.008	3.2	-2
Upper-canopy Lianas	81	112	12	0.008	3.2	-2
Midcanopy Trees	57	81	12	0.008	3.2	-2
Understory	33	37	12	0.008	3.2	-2
Bulk	60.3	84.4	12	0.008	3.2	-2
Ameriflux Site: Harvard Forest						
Deciduous Trees	50	120	7	0.005	3.2	-1.9
Conifers	50	120	7	0.005	3.2	-1.9
Understory	66	149	7	0.005	3.2	-1.9
Bulk	51.12	122.03	7	0.005	3.2	-1.9

PFT: Plant Funcional Type

$V_{c,max}$: Maximum carboxylation velocity

J_{max} : Maximum rate of electron transport

m : Ball Berry slope

b : Ball Berry intercept

s_f**:** stomatal sensitivity parameter for m. Tuzet model.

Ψ_f**:** parameter for loss of stomatal conductance. Tuzet model.

APPENDIX E

Soil Carbon and Nitrogen Model

E.1 Fine Root Response to Drought

During dry periods, the scarcity of rainfall and the constant demand for moisture from the plants and the atmosphere results in a reduction in soil water potential. This reduction in soil water potential can be severe in locations experiencing Mediterranean climates, where dry seasons are correlated with high temperatures and radiative forcings.

As soil water potential drops it may be advantageous for plants to reduce their hydraulic conductivity. In this study we simulate the response of roots to dry periods by a reduction of the radial conductivity of the root system, Kr. This reduction is calculated using a fine root conductivity loss function (FRCL). FRCL is defined as the fraction of root conductivity that is lost in the fine roots at a given root water potential. This percentage loss is used as a proxy to simulate the loss in radial conductivity of the root system. Equation E.1 shows how Kr is affected by FRCL.

$$\mathrm{Kr} = \mathrm{Kr_{pot}}(1 - \mathrm{FRCL}(\psi_\mathrm{r})). \tag{E.1}$$

In this equation $\mathrm{Kr_{pot}}$ is the potential root radial conductivity occurring if roots are not under water stress. We use the loss conductivity function observed by Domec et al. [2004] for ponderosa pine plants of intermediate age. This function is given by:

$$\mathrm{FRCL} = \frac{100}{1 + \mathrm{e}^{\mathrm{a}(\psi_\mathrm{r} - \mathrm{b})}}. \tag{E.2}$$

In this equation ψ_r is the root water potential in MPa and **a** and **b** are parameters. Parameter **a** regulates the slope of the curve and parameter **b** is the water potential in MPa at which 50% of the conductivity loss occurs. Figure 3d in the manuscript shows the FRCL function used in this study.

The lost of radial conductivity may happen under two different situations.

i. In the No-HR case whenever $\psi_r > \psi_s$ there is a complete hydraulic disconnection between the roots and the soil ($\mathrm{Kr} = 0, \mathrm{FRCL} = 1$) following the definition of No-HR.

ii. In both cases, HR and No-HR, there is a reduction in Kr as a response to low water potential. This response occurs gradually and is regulated by the magnitude of the root water potential ψ_r following Equations E.1 and E.2.

E.2 C-N Model Equations

This section presents the equations for the C-N model implemented in this study. These equations were initially developed by D'Odorico et al. [2003], Manzoni and Porporato [2007], Porporato et al. [2003]. The main advantages of this approach include the simple representation of the dynamics, the consideration of a separate microbial biomass pool, and the capacity to compute analytically the non-linear dynamics that arise between net mineralization and net immobilization of N. In this study we modified the initial framework from a bucket model to a multi-layer approach. We also include the effect of temperature on decomposition and incorporate vertical fluxes of carbon by soil bioturbation processes. In addition, we consider the presence of multiple vegetation species that coexist and impact simultaneously the carbon and nitrogen dynamics in the soil.

The simulation of carbon dynamics is performed by the solution of differential equations that are based on conservation of mass and describe the evolution of carbon concentration in time for each pool. The simulation of nitrogen content in the organic form uses the same differential equations that are used for carbon, but modified by the C:N ratio that is present in the organic pools.

The equations describing the states of carbon and nitrogen in the soil were initially introduced by Porporato et al. [2003], where they considered three pools: litter ($\mathrm{C_l}$), humus ($\mathrm{C_h}$) and microbial biomass ($\mathrm{C_b}$). Later, the same framework was implemented by Manzoni and Porporato [2007], but considering only two pools: soil organic matter ($\mathrm{C_s}$) and microbial biomass ($\mathrm{C_b}$). This simplification facilitates the manipulation of the analytical equations involved in the model. In this study, we follow the approach presented by Manzoni and Porporato [2007], considering only two pools. In addition, we model the transport of organic matter in the soil column by bioturbation using a diffusive approximation.

The rate of change of carbon in the organic matter pool at each layer, including bioturbation, is given by:

$$\frac{\mathrm{dC_s}}{\mathrm{d}t} = \mathrm{ADD_{bio}} + \mathrm{ADD_{root}} - \mathrm{DEC} + \mathrm{BD}. \tag{E.3}$$

In equation E.3, the term $\mathrm{ADD_{bio}}$ is the flux of organic matter due to bioturbation processes in the soil, the term $\mathrm{ADD_{root}}$ is the input of organic matter from root turnover, DEC is an output flux from decomposition and BD is the input from microbial death.

The rate of change of carbon in the microbial biomass pool at each layer is given by:

$$\frac{\mathrm{dC_b}}{\mathrm{d}t} = (1 - r_r)\mathrm{DEC} - \mathrm{BD}. \tag{E.4}$$

In equation E.4 the term $(1 - r_r)$DEC is the fraction of carbon from decomposition that becomes part of the microbial tissues. The remaining, r_rDEC, is the fraction of carbon that is released as CO_2 to the atmosphere.

The rate of decomposition is computed using first order kinetics [Porporato et al., 2003]. In this study it is function of the soil water potential (ψ_s) and soil temperature (T) (equations E.27 and E.28):

$$\mathrm{DEC} = \phi f_{\mathrm{D}}(\psi_{\mathrm{s}}) f_{\mathrm{D}}(\mathrm{T_s}) k_{\mathrm{s}} \mathrm{C_b} \mathrm{C_s}. \tag{E.5}$$

The rate of microbial death is computed by a linear dependence on the microbial biomass concentration $\mathrm{C_b}$ [Porporato et al., 2003]. This approach neglects the influence of environmental factors such as soil water potential and soil temperature.

$$\mathrm{BD} = k_d \mathrm{C_b}. \tag{E.6}$$

The model for the vertical transport of organic matter implemented here is based on approaches presented in previous studies [Braakhekke et al., 2011, Dam et al., 1997, Elzein and Balesdent, 1995, Kaste et al., 2007]. In this study we include only fluxes due to bioturbation and neglect advective fluxes produced by water transport such as fluxes of dissolved organic carbon. Figure E.1 shows a schematic representation of the bioturbation framework. The transport of organic matter by bioturbation is modeled as a diffusion process. Under this framework the rate of change of carbon in the organic matter pool is given by:

$$\frac{\mathrm{dC_s}}{\mathrm{d}t} = \mathrm{D_b(z)} \frac{\mathrm{d}^2 \mathrm{C_s}}{\mathrm{d}z^2}. \tag{E.7}$$

The term $\mathrm{D_b}$ in Equation E.7 is the bioturbation diffusivity. In this study $\mathrm{D_b}$ is assumed to decay exponentially with depth (Equation E.8) following the approach presented in Cousins

et al. [1999].

$$\mathrm{D_b(z) = D_{b,top} exp(-0.1z).} \tag{E.8}$$

In Equation E.8 the term $\mathrm{D_{b,top}}$ represents the bioturbation at the top of the soil where the maximum bioturbation flux occurs. We use $\mathrm{D_{b,top}} = 4\ \mathrm{cm^2/year}$, which is in the range of values reported in previous studies [Dam et al., 1997, Elzein and Balesdent, 1995, Kaste et al., 2007]. We noticed little sensitivity of $\mathrm{D_{b,top}}$ on the results reported in this study. Equation E.8 simulates the transport of carbon in the mineral soil column from horizon O downward. The top boundary condition is given by the flux of organic matter from the litter layer to horizon O ($\mathrm{F_{L-O}}$). The bottom boundary condition is specified as no flux at a maximum depth z_{biot} at which bioturbation fluxes are considered negligible. The rate of change in the organic matter pool in the litter layer is shown in Equation E.9.

$$\frac{\mathrm{dC_{s,litter}}}{\mathrm{d}t} = \mathrm{BM_{Tt}} - \mathrm{F_{L-O}} - \mathrm{DEC_{litter}}. \tag{E.9}$$

In this equation the term $\mathrm{C_{s,litter}}$ is the concentration of organic matter in the litter layer, $\mathrm{BM_{Tt}}$ is the flux of carbon in organic matter from above-ground sources (Equation E.26) and $\mathrm{F_{L-O}}$ is the flux of carbon from the litter to horizon O. $\mathrm{F_{L-O}}$ flux is composed by several processes such as fragmentation of litter and bioturbation. Equation E.10 shows the parameterization of $\mathrm{F_{F-O}}$ implemented in this study.

$$\mathrm{F_{L-O} = C_{s,litter} \Delta z_{litter} k_{litter} f_B(T_{litter})}. \tag{E.10}$$

In Equation E.10 the term Δz_{litter} is the litter layer thickness, $f_B(T)$ is a parameter that accounts for the control of temperature on $\mathrm{F_{L-O}}$ (we use Equation E.28), and k_{litter} is a parameter that regulates the magnitude of $\mathrm{F_{L-O}}$. In this study we calibrate k_{litter} in such a way that the mean annual litter thickness, Δz_{litter}, and the mean annual litter concentration $\mathrm{C_{s,litter}}$ remain constant during all the period of simulation matching the observed values recorded in Blodgett Forest (Table 1 in the manuscript).

The equations that describe the rate of change of nitrogen in the organic matter pool and the microbial biomass pool are based on the equations for carbon (Equations E.3 and E.4). In order to compute the nitrogen dynamics from Equations E.3 and E.4, the C:N ratio in these two pools is needed [Porporato et al., 2003].

$$\frac{\mathrm{dN_s}}{\mathrm{d}t} = \pm \frac{\mathrm{ADD_{bio}}}{(\mathrm{C:N})_{\mathrm{s-bio}}} + \frac{\mathrm{ADD_{root}}}{(\mathrm{C:N})_{\mathrm{ADD}}} - \frac{\mathrm{DEC}}{(\mathrm{C:N})_{\mathrm{s}}} + \frac{\mathrm{BD}}{(\mathrm{C:N})_{\mathrm{b}}} \tag{E.11}$$

$$\frac{\mathrm{dN_b(t)}}{\mathrm{d}t} = \frac{\mathrm{DEC}}{(\mathrm{C:N})_\mathrm{s}} - \frac{\mathrm{BD}}{(\mathrm{C:N})_\mathrm{b}} - \Phi. \tag{E.12}$$

In equation E.11 the term $\mathrm{C{:}N_{s-bio}}$ is the C:N ratio in the soil layer from which the bioturbation flux occurs and the term Φ takes into account the net contribution from mineralization or immobilization. If $\Phi > 0$ there is a net mineralization of N. If $\Phi < 0$ there is a net immobilization of mineral nitrogen by microorganisms. Assuming that the rate of change of the C:N ratio in the microbial biomass remains constant during the simulation period $\left(\frac{\mathrm{d(C:N)_b}}{\mathrm{d}t} = 0\right)$ it is possible to compute an analytical expression for Φ [Porporato et al., 2003]. Considering only two pools of carbon ($\mathrm{C_s}$ and $\mathrm{C_b}$) the expression for Φ is given in Equation E.13 (Equation 14 in Manzoni and Porporato [2007]).

$$\Phi = \mathrm{DEC}\left[\frac{1}{(\mathrm{C:N})_\mathrm{s}} - \frac{1 - r_r}{(\mathrm{C:N})_\mathrm{b}}\right]. \tag{E.13}$$

Under net immobilization there is a net uptake of mineral nitrogen from the soil by microorganisms. In this condition plants and microorganisms access to the same pool of mineral N. This phenomenon generates a competition between plant and microorganisms for available mineral nitrogen in the soil. During mineralization periods microbial activity enhances the accumulation of mineral nitrogen in the soil facilitating plant uptake.

The nitrification flux, NIT, is simulated using Equation E.14 [Porporato et al., 2003]. In this equation f_N is a factor that represents the impact of soil moisture on nitrification. In this study we used the same approach for f_N as the one used for decomposition (Equation E.27). $\mathrm{k_n}$ is the nitrification factor, $\mathrm{C_b}$ is the microbial biomass concentration and $\mathrm{N^+}$ is the concentration of ammonium in the soil.

$$\mathrm{NIT} = f_\mathrm{N}(\psi_\mathrm{s})\mathrm{k_n C_b N^+}. \tag{E.14}$$

The uptake of nitrogen by plants is considered as the addition of two different mechanisms [Porporato et al., 2003]: (i) the mineral nitrogen in the soil moisture that reaches the roots with the transpiration flux (water uptake) $\mathrm{UPN_{wu}}$ and (ii) the mineral nitrogen in water that reaches the roots by diffusion and then is taken by the plants $\mathrm{UPN_{diff}}$. The total mineral nitrogen uptake is then given by $\mathrm{UPN} = \mathrm{UPN_{wu}} + \mathrm{UPN_{diff}}$.

The uptake of mineral nitrogen by the transpiration stream is computed as an advective flux. Nitrogen uptake is computed as the amount of mineral ions transported by the water uptake flux toward the roots assuming a homogeneous ion concentration in soil water. The

total uptake of nitrogen is given by:

$$\mathrm{UPN}^{\pm}_{\mathrm{wu}} = \sum_{\mathrm{j}}^{\mathrm{M_{sps}}} \sum_{\mathrm{i}\in\mathrm{K}}^{\mathrm{N_{layers}}} \left(\frac{\lambda^{\pm} \mathrm{N}^{\pm}_{\mathrm{min}}}{\theta} \mathrm{q_{wu,ij}} \right). \tag{E.15}$$

In Equation E.15, $\mathrm{N}\pm_{\mathrm{min}}$ refers to the concentration of either $\mathrm{NO}_3^-(-)$ or $\mathrm{NH}_4^+(+)$, parameter $\lambda^{\pm}$ represents the fraction of NH_4^+ (+) or NO_3^- (-) that is dissolved in water, $\mathrm{M_{sps}}$ is the number of species and $\mathrm{N_{layers}}$ is the number of soil layers. $\mathrm{q_{wu,ij}}$ is the water uptake by species **j** in layer **i** and **K** represents all those layers where $\psi_s > \psi_r$. Therefore the summation in Equation E.15 only accounts for those layers where the flux of water occurs from the soil to the roots. This assumption neglects the release of mineral nitrogen that may be occurring through water fluxes from the root to the soil by the way of HR.

In this study the uptake of water by diffusion fluxes is computed following the initial approach for a bucket model introduced in Porporato et al. [2003]. In this approach the uptake of nitrogen is proportional to the concentration of mineral nitrogen in the soil (Equation E.16). Following the same principle the total nitrogen uptake from diffusion fluxes is given by:

$$\mathrm{UPN}^{\pm}_{\mathrm{diff}} = \sum_{\mathrm{j}}^{\mathrm{M_{sps}}} \sum_{\mathrm{i}}^{\mathrm{N_{layers}}} \mathrm{N}^{\pm}_{\mathrm{min}} \mathrm{k_{diff,ij}}. \tag{E.16}$$

In Equation E.16, $\mathrm{k_{diff,ij}}$, is a proportionality constant defined for a given layer **i** and species **j**. Following [Porporato et al., 2003] this constant can be calculated as:

$$\mathrm{k_{diff,ij}} = \frac{\lambda^{\pm}}{\theta_{\mathrm{i}} \mathrm{n_i} \Delta \mathrm{z_i}} \left(\frac{\theta_{\mathrm{i}}}{\mathrm{n_i}} \right)^{\mathrm{d}} \mathrm{F_{i,j}}. \tag{E.17}$$

In this equation θ_i is the soil moisture in layer i, $\mathrm{n_i}$ is the porosity in layer i, Δz_i is the thickness of layer **i**, d is a parameter that represents the non-linear behavior of the diffusion process with soil moisture and $\mathrm{F_{i,j}}$ is a scaled diffusion coefficient. F can be conceptualized as the diffusion capacity of ions to move from the soil toward the roots. In this study we assume that F is proportional to the total amount of fine root biomass. For a given species **j** the total magnitude of F in a given layer **i** is given by:

$$\mathrm{F_{i,j}} = \mathrm{BM_{roots,j}} \mathrm{F_{factor}} fr_{\mathrm{i,j}}. \tag{E.18}$$

In Equation E.18, $\mathrm{BM_{roots,j}}$ is the total amount of fine root biomass in species **j**, $fr_{i,j}$ is the fine root fraction in layer **i** for species **j** such that $\sum_i^N fr_{i,j} = 1$ and $\mathrm{F_{factor}}$ is a parameter

that quantifies the efficiency of the roots in capturing ions by diffusion for a given fine root biomass. (Table 1 in the manuscript).

In this study we assume that the total amount of fine root biomass at every time is proportional to the total amount of leaf biomass :

$$\mathrm{BM_{roots}} = \mathrm{km_r BM_{leaves}}. \tag{E.19}$$

Similar to the approach introduced by Porporato et al. [2003] for a bucket model, here $\mathrm{F_{factor}}$ is not related with real diffusion coefficients or measurements. Instead this coefficient is calibrated to regulate the fraction of total mineral uptake that comes from diffusion, $\mathrm{f_{diff}}$. This fraction is given by:

$$\mathrm{f_{diff}} = \frac{\mathrm{UPN_{diff}}}{\mathrm{UPN_{wu}} + \mathrm{UPN_{diff}}} = \frac{\mathrm{UPN_{diff}}}{\mathrm{UPN}} \tag{E.20}$$

In this study the simulations were performed with $\mathrm{F_{factor}} = 1.8\mathrm{mm\ d^{-1}\ kg_{root}^{-1}}$ corresponding to mean annual net values of $\mathrm{f_{diff}}$ between 40 and 60%, and we perform a sensitivity analysis of $\mathrm{F_{factor}}$ on the leaching of nitrogen.

E.3 LAI Dynamics and Litter Production

.

In the model the input of organic matter from the plant to the soil comes mainly from loss of foliage and fine root turnover. We use observations of changes in LAI to compute the turnover of leaves and the input of organic matter into the soil from above-ground sources. In addition, we assume that the input of carbon from below-ground turnover of fine roots is linearly proportional to the above-ground loss of leaves (Equation E.19).

Figure 3 in the manuscript shows the the annual dynamics of LAI. The discrete equation that describes the time evolution of LAI is:

$$\mathrm{LAI_{t+1}} = \mathrm{LAI_t} \pm \mathrm{LAI_{ph}} - \mathrm{LAI_{nt}}. \tag{E.21}$$

In this equation $\mathrm{LAI_{t+1}}$ is the leaf area index at time step $t+1$, $\mathrm{LAI_t}$ is the LAI at timestep t, $\mathrm{LAI_{nt}}$ is the reduction in LAI in a timestep caused by normal turnover of leaves and $\mathrm{LAI_{ph}}$ is the addition or reduction in LAI during that timestep due to either phenological construction or phenological turnover. We assume that in a given tim step either phenological

construction or turnover take place, but not both.

$\mathrm{LAI_{nt}}$, which is the normal turnover produced by the regular deterioration of leaves, is computed using the expected leaf span LS.

$$\mathrm{LAI_{nt}} = \frac{\mathrm{LAI_t}}{\mathrm{LS}}\Delta \mathrm{t}. \tag{E.22}$$

From Equation E.21, the phenological changes in LAI are given by:

$$\mp \mathrm{LAI_{ph}} = \mathrm{LAI_{t+1}} - \mathrm{LAI_t} + \mathrm{LAI_{nt}}. \tag{E.23}$$

$\mathrm{LAI_{ph}}$ could be either positive or negative depending on the dynamics of turnover or construction. Therefore, the total turnover of leaves in a given timestep, expressed in terms of LAI units, is then given by:

$$\mathrm{LAI_{Tt}} = \begin{cases} \mathrm{LAI_{nt}} & \text{if } \mathrm{LAI_{ph}} \geq 0 \\ \\ |\mathrm{LAI_{ph}}| + \mathrm{LAI_{nt}} & \text{if } \mathrm{LAI_{ph}} < 0 \end{cases} \tag{E.24}$$

The flux of carbon from above-ground los of leaves that reaches the soil surface is calculated as:

$$\mathrm{F_{above}} = \frac{\mathrm{LAI_{Tt}}}{\mathrm{SCLA}} \tag{E.25}$$

where SCLA is the specific carbon leaf area index that represents the area per unit mass of carbon in the leaf.

The flux of carbon from below-ground turnover of fine roots that goes to the soil is given by:

$$\mathrm{F_{below}} = \mathrm{F_{above}}\mathrm{km_r}. \tag{E.26}$$

This flux is distributed in the soil for each species independently according to the root distribution $fr_{i,j}$

E.4 Organic Carbon Concentrations and Calibration of k_s and k_b

The soil domain is divided into horizons with similar biogeochemical properties. Each horizon may comprise one or more of the layers implemented in the numerical simulation. Table E.2 shows the different horizons considered, including depth and the numerical simulation layers that are in each horizon. The depth and thickness of horizons displayed in Table E.2 is determined from observations at Blodgett forest [Bird and Torn, 2006, Black and Harden, 1995].

The C-N model requires two main site-specific constants, k_s and k_d (Appendix E.2). These constants control the rate of organic matter decomposition and microbial death respectively. These two processes are microbially regulated. Therefore, k_s and k_d vary with depth according to the type of microbial community that is present in the soil.

The soil column is characterized by strong gradients in soil moisture, soil temperature and carbon and nitrogen concentrations. Shallow layers that are close to the surface are impacted more by the atmosphere. These layers are directly affected by rainfall and incoming solar radiation, and have large fluctuations in temperature and moisture. On the other hand, deeper layers in the soil are less vulnerable to atmospheric conditions. The incoming rainfall and radiative fluxes that reach the surface are filtered throughout the soil column producing more stable conditions of soil moisture and soil temperature at deeper layers. In addition, the input of organic matter and nutrients from plants also follows a distribution with considerably higher fluxes close to the surface .

Strong gradients in environmental variables such as temperature and moisture concentrations throughout the soil column, together with differences in organic carbon input from plants, impact the distribution of microbial communities and their population sizes [Fierer et al., 2003]. In order to capture these processes we calibrate k_s and k_d for each layer independently. The calibration of k_s and k_d was performed by assuming steady state conditions in Equations E.3 and E.4, as suggested in D'Odorico et al. [2003]. In order to use this approach we use mean values of soil moisture and soil temperature reported at Blodgett and the computed profiles of carbon concentration in the organic matter and microbial pool (Table E.2).

Figure 4 shows the carbon concentrations in the organic matter pool and microbial biomass pool at different horizons. These profiles were obtained by applying observed patterns in other locations [Fierer et al., 2003, Jobbágy and Jackson, 2000], and information gathered at Blodgett [Bird and Torn, 2006, Black and Harden, 1995]. The Blodgett data was mostly available for shallow soil layers.

E.5 Soil Moisture and Temperature Dependence

Besides the availability of biochemical energy which is found in remnant products of photosynthetic processes, the activity of microorganisms in soils is controlled primarily by soil moisture and soil temperature conditions. Several experimental studies have monitored the influence of these two variables on microbial activity using direct observations of microbial growth and indirect measurements such as organic matter decomposition and respiration rates [Herron et al., 2009, Iovieno and Bååth, 2008, Qi and Xu, 2001]. The complex interactions involved in microbial processes, the immense microbial diversity and the heterogeneity of the soil domain are factors that challenge our understanding of these dynamics.

Biophysical models developed to simulate the fate of organic matter, decomposition, microbial respiration, or microbial growth use reduction factors to include the influence of soil moisture and temperature in microbial activity. The effect of soil moisture availability has been computed using different mathematical functions. Generally, microbial activity increases with moisture availability. Some models use soil water content as an indicator of available moisture [D.S. Jenkinson, D.E. Adams, 1991, Parton et al., 1987, Porporato et al., 2003, Probert, 1998]. However, experimental studies have shown a strong correlation between soil water potential (ψ_{s}) and microbial activity, [Harris, 1981, Kieft et al., 1987, Sylvia et al., 2005, Wilson and Griffin, 1975]. According to Harris [1981], Sylvia et al. [2005] microbial activity becomes limited when soil matric potential $\psi_{\mathrm{s}} < 4$MPa. Beyond this range the microbial population is composed mainly of fungi which are more tolerant to water stress than bacteria. Some fungi species can sustain growth at lower levels of water potential ($\psi_{\mathrm{s}} = 40$MPa). Although some microorganisms can survive water potential levels below $\psi_{\mathrm{s}} < -10$MPa the rate of several microbial processes decreases considerably. For example it seems the rate of nitrification is negligible below 4 MPa. In this study we include a correction factor for microbial processes such as decomposition and nitrification as a function of water potential instead of soil moisture. We use the correction factor implemented in Andren [1992] (Equation E.27).

$$f_{\mathrm{D}}(\psi_{\mathrm{s}}) = \left(\frac{\mathrm{Log}\frac{|\psi_{\mathrm{min}}|}{|\psi_{\mathrm{s}}|)}}{\mathrm{Log}\frac{|\psi_{\mathrm{min}}|}{|\psi_{\mathrm{top}}|)}} \right). \tag{E.27}$$

In this equation ψ_s is the water potential in the soil, ψ_{min} is the value of ψ_s below which decomposition become negligible, and ψ_{max} is the value of ψ_s above which there is no reduction in decomposition rates. Similarly, several factors have been proposed to consider the

influence of temperature in microbial activity [Andren, 1992, D.S. Jenkinson, D.E. Adams, 1991, Probert, 1998]. In this study we use observations at Blodgett [Qi, 2002, Qi and Xu, 2001] that describe the control on decomposition Equation E.28.

$$f_{\mathrm{D}}(\mathrm{T_s}) = 1.9^{\frac{\mathrm{T_s}-25}{10}}. \tag{E.28}$$

These factors ($f_{\mathrm{D}}(\psi_{\mathrm{s}})\, f_{\mathrm{D}}(\mathrm{T_s})$) are used in Equation E.5 to incorporate the regulation of water potential and soil temperature in the decomposition of soil organic matter.

Table E.1: List of symbols in the carbon and nitrogen model.

Symbol	Description	Symbol	Description
HR	Hydraulic redistribution	ψ_s	Soil water potential [MPa]
NoHR	Hydraulic redistribution is not present	ψ_r	Root water potential [MPa]
HL	Hydraulic lift	T_s	Soil Temperature
HD	Hydraulic descent	ψ_{min}	Min ψ_s below which decomposition rates become negligible
LAI	Leaf area index	ψ_{top}	ψ_s above which there is not reduction on decomposition rates
SCLA	Specific leaf area index of carbon	θ	Soil moisture
LAI_t	Leaf area index at time step t	n	Porosity
LAI_{t+1}	Leaf area index at time step t+1	N_s	Nitrogen content in the soil organic matter pool
LAI_{ph}	Leaf area index change from phenological changes	N_b	Nitrogen content in microbial pool
LAI_{nt}	Leaf area index from normal turn over	Nit	Nitrate pool
LAI_{Tt}	Total leaf area index that drop to the soil	Amm	Ammonium pool
F_{above}	Total flux of carbon biomass from above drop of leaves	N_{min}	Total mineral nitrogen in the soil
F_{below}	Total flux of carbon biomass from below fine roots	M_{sps}	Total number of species
C : N	Carbon to nitrogen ratio	N_{layers}	Total number of layers in the soil
$C : N_b$	Carbon to nitrogen in the microbial pool	$UPN^{\pm}_{wu}$	Plant uptake of water mineral nitrogen from water uptake
$C : N_s$	Carbon to nitrogen ratio in organic matter pool	$UPN^{\pm}_{diff}$	Plant uptake of mineral nitrogen from diffusion in the soil
C_s	Carbon content in the organic matter pool	$q_{wu,ij}$	Water uptake in the ith soil layer from the jth species
$C_{s,litter}$	Carbon content in the organic matte pool in litter	d	Diffusion Parameter θ
C_b	Carbon content in the microbial pool	$F_{i,j}$	Pot. of ions to diffuse towards the roots
$C_{s,litter}$	Carbon content in the microbial pool in the litter	F_{factor}	Diffusion capacity of ions per unit mass of fine roots
ADD	Input flux of biomass in the soil column	fr^j	Distribution of fine roots in the jth species
ADD_{bio}	Input flux of biomass from bioturbation	$f_D(\psi_s)$	Water potential factor on decomposition
ADD_{root}	Input flux of biomass from fine roots turn over	$f_D(T_s)$	Soil temperature factor on decomposition
DEC	Decomposition rate of soil organic matter	f_B	Litter C flux to horizon O Parameter
BD	Death of microbial biomass flux	k_s	Parameter that regulates decomposition
ϕ	parameter that regulates decomposition	k_d	Parameter that regulates microbial death
Φ	Net immobilization/mineralization	k_r	Root hydraulic conductivity

Continued on Next Page...

Table E.1 – Continued

Symbol	Description	Symbol	Description
a	Slope of the FRCL function	$k_{diff,ij}$	Proportionality nitrogen uptake by diff. path.
b	Water Potential at which FRCL is 50%	D_b	Bioturbation diffusion parameter
r_r	Fraction of decomposition that goes to respiration	$D_{b,top}$	Net uptake of CO_2 through photosynthesis
DEC_{litter}	Decomposition flux in the litter layer	T_{litter}	Litter layer temperature
BM_{roots}	Total Root Biomass	BM_{leaves}	Total Leaves Biomass
BM_{Tt}	Total flux of carbon from above-ground	F_{L-O}	Total flux of carbon from litter to horizon O
Δz_i	Thickness of the ith soil layer	Δz_{litter}	Thickness of litter layer
Δk_n	Nitrification rate		

Table E.2: Description of the different horizons included in the simulation.

Depth	**Horizon**	**Layer Simulation**	**Carbon Organic Matter Pool**	**Carbon Microbial Pool**
[cm]	[-]	[-]	[kg m^{-3}]	[g m^{-3}]
0 - 2 cm	O	1	46.0	738
2 - 16 cm	A1	2, 3, 4	36.0	396
16 - 30 cm	A2	5	24.0	129
30 - 50 cm	B1	6	15.0	30
50 - 80 cm	B2	7	7.0	15
80 - 230 cm	C1	8,9	2.0	8
$>$ 230 cm	C2	10,11,12	0.3	3

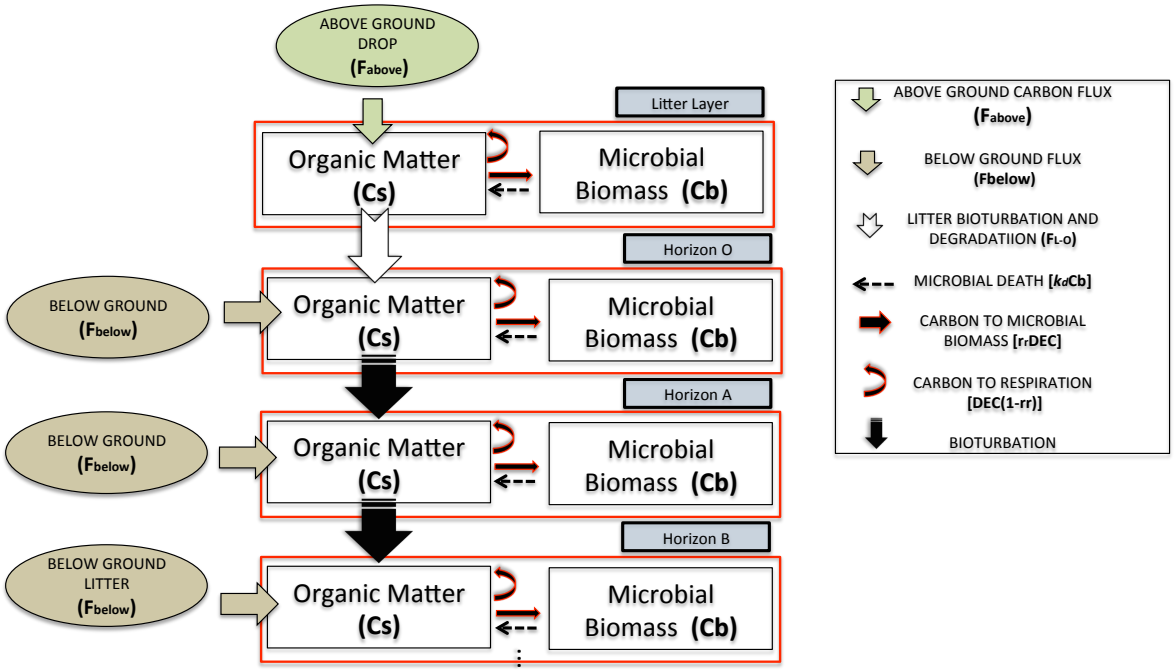

Figure E.1: Schematic representation of the vertical structure and carbon fluxes below the ground. The main inputs of organic matter come from above-ground loss of leaves and below-ground turnover of fine roots. In each soil horizon the pool of organic matter C_s and microbial biomass C_b interact through fluxes such as decomposition and microbial death. The only carbon fluxes that are considered vertically are bioturbation fluxes.

APPENDIX F

Entropy Budget in Open Systems

All ecosystems, either natural or artificially cultivated are thermodynamically open systems that exchange energy and mass with their environment. The rate of change of entropy in an open system is given by the sum of entropy changes due to the interchange of mass and energy with the environment ($\frac{d_e S}{dt}$) plus the rate of entropy production inside the system ($\frac{d_i S}{dt}$) [Kondepudi and Prigogine, 1998].

$$\frac{dS}{dt} = \overbrace{\frac{d_e S}{dt}}^{\substack{\text{External}\\ \text{EnergyandMassFluxes}}} + \overbrace{\frac{d_i S}{dt}}^{\substack{\text{Internal}\\ \text{EntropyProduction}}} \tag{F.1}$$

The total rate of entropy interchanged with the environment comes from energy and mass fluxes.

$$\frac{d_e S}{dt} = \frac{(\overbrace{d_e S_u}^{\text{Energy}} + \overbrace{d_e S_m}^{\text{Mass}})}{dt} \tag{F.2}$$

In this equation $\frac{d_e S_u}{dt}$ is the rate of entropy change in the system originated by energy fluxes between the system and the environment while $\frac{d_e S_m}{dt}$ is the rate of change of entropy produced by mass fluxes between the system and the environment.

There are three main ways of energy transfer between ecosystems and their environment, (i) convective, (ii) conductive and (iii) radiative exchange. The rate of change of internal energy in the system is regulated by the fluxes of energy between the system and it surroundings. Here we group Q_{cc} as those fluxes of energy transferred by convection and conduction while Q_{tr} is the flux of energy by thermal radiation. The total rate of change of internal energy is then given as:

$$\frac{dU_m}{dt} = \left(\frac{dU_{cc} + dU_{tr}}{dt}\right) = Q_{cc} + Q_{tr} \tag{F.3}$$

The rate of change of entropy due to energy fluxes can be computed by integration of the

entropy flux J (entropy per unit surface area per unit time) over the entire surface area that surrounds the control volume. However,the flux of radiation in radiative energy involves fundamental differences compared to the transfer of energy by convection or conduction. Therefore, it is appropriate to separate the entropy fluxes from radiative energy transfer and the entropy fluxes from convection and conduction energy transfer [Wright et al., 2001].

$$\frac{d_e S_u}{dt} = \int_S (J_{cc} + J_{tr}) dA. \tag{F.4}$$

The entropy flux produced by conduction or convection transfer of heat energy can be calculated as the heat flux divided over the temperature following a Clausius formulation. Therefore:

$$\frac{d_e S_u}{dt} = \int_S \Big(\frac{q_{cc}}{T} + J_{tr} \Big) dA \tag{F.5}$$

In this equation q_{cc} is the flux of heat energy transferred by conduction or convection per unit area per unit time. If q_{cc} is integrated over the total boundary surface area that surrounds the system, we obtain Q_{cc} which is the is the net energy transferred by conduction or convection per unit time.

$$Q_{cc} = \int_S (q_{cc} dA) = \frac{dU_{cc}}{dt} \tag{F.6}$$

The rate of change of entropy in the system produced by energy fluxes can then be expressed as:

$$\frac{d_e S_u}{dt} = \frac{Q_{cc}}{T} + \int_S J_{tr} dA = \frac{1}{T} \frac{dU_{cc}}{dt} + \int_S J_{tr} dA \tag{F.7}$$

On the other hand the rate of change of internal energy due to mass fluxes can be expressed as the sum of the rate of change of mole numbers involved in the chemical reactions multiplied by the corresponding chemical potential.

$$\frac{dU_m}{dt} = \sum_i \mu_i \frac{dN_i}{dt}. \tag{F.8}$$

In this Equation the terms N_i and μ_i refer to the mole number and chemical potential respectively of constituent i. Using F.8 it is possible to compute the rate of change of

entropy within the system by mass interchanged between the system and the environment [Kondepudi and Prigogine, 1998].

$$\frac{d_e S_m}{dt} = -\frac{1}{T}\sum_k \mu_k \frac{d_e N_k}{dt} \tag{F.9}$$

Similarly the rate of entropy production within the system by internal chemical reactions of components within the system is given by:

$$\frac{d_i S}{dt} = -\frac{1}{T}\sum_l \mu_l \frac{d_i N_l}{dt} > 0 \tag{F.10}$$

Note that the net entropy production in the system has to be always greater than zero following the second law of thermodynamics. The net rate of change of entropy within the system given in Equation F.1 can be written in more detail as:

$$\frac{dS}{dt} = \overbrace{\frac{Q_{cc}}{T} + \int_S J_{TR} dA - \frac{1}{T}\sum_k \mu_k \frac{d_e N_k}{dt}}^{\frac{d_e S}{dt}} - \overbrace{\frac{1}{T}\sum_l \mu_l \frac{d_e N_l}{dt}}^{\frac{d_i S}{dt}} \tag{F.11}$$

Assuming the system is in steady state condition ($\frac{dS}{dt} = 0$), the net entropy production inside the system will be equal to the net entropy flux (input minus output) across the system boundary. Under this assumption:

$$\overbrace{\frac{Q_{cc}}{T} + \int_S J_{TR} dA - \frac{1}{T}\sum_k \mu_k \frac{d_e N_k}{dt}}^{\frac{d_e S}{dt}} = \overbrace{\frac{1}{T}\sum_m \mu_m \frac{d_e N_m}{dt}}^{\frac{d_i S}{dt}} \tag{F.12}$$

F.1 Approximation for the Calculation of Entropy of Thermal Radiation

The rate of change of internal energy is given in terms of the net amount of heat that is interchanged in the system and the amount of work performed within the control volume.

$$dU = dQ - pdV \tag{F.13}$$

From classical thermodynamics the rate of change of entropy production is expressed in

terms of the net rate of heat in the system.

$$dS = \frac{dQ}{T} \tag{F.14}$$

From equation F.13 the net rate of change of heat can be expressed as a function of the internal energy and the amount of work in the system. This approach allows us to compute the change of entropy of an open system and is the classical approach used in thermodynamics.

$$S = \int dS = \int \frac{dQ}{T} = \int \frac{udV + pdV}{T} \tag{F.15}$$

The rate of entropy flux caused by a heat energy flux is given by:

$$J_{qq} = \frac{E_{qq}}{T} \tag{F.16}$$

In equation F.16 E_{qq} is the energy heat flux. However when the flux of energy is originated by a radiative process instead of heat, Equation F.16 does not hold. It can be shown that for black radiation the pressure p and the internal energy density per unit volume u are given by:

$$p = \frac{u}{3}, u = aT^4 \tag{F.17}$$

Using the expressions for p and u given in F.17 together with Equation F.15 it is possible to show that the total black radiation entropy is given by:

$$S = \frac{4}{3}aT^3V \tag{F.18}$$

From Equation F.18 the flux of entropy for a black radiation can be computed proportional to T^3 and using a constant σ :

$$J_{BR} = \frac{4}{3}\sigma T^3 \tag{F.19}$$

In this Equation the constant σ is the well known Stefan-Boltzmann constant. There is an important empirical evidence of Equation F.19 and also for σ. Furthremore Planck was able to perform a theoretic demonstration of Equation F.19 and obtain a theoretical expression for σ.

$$\sigma = \frac{2\pi\kappa^4}{15c^2h^3} \tag{F.20}$$

In Equation F.20, κ is the Boltzmann constant, h is the Planck constant, and c is the speed of light. Furthremore, the energy flux emmited by a black radiation body is $E_{BR} = \sigma T^4$, therefore from Equation F.19 we can imply that for black radiation Equation F.16 does not hold. Instead there is a constant of $\eta = 4/3$ that multiples $\frac{E_{BR}}{T}$.

$$J_{BR} = \frac{4}{3}\frac{E_{BR}}{T} \neq \frac{E_{BR}}{T} \tag{F.21}$$

Equation F.21 with $\eta = 3/4$ applies only for blackbody radiation. However, the thermal radiation observed in earth systems are far different than a blackbody radiation. Therefore, it is important for earth systems analysis to have an approach for the computation of entropy flux in non-blackbody radiation.

F.1.1 Approximations to Compute Entropy Flux for non-Blackbody Radiation

In this section we present a summary of the different approaches that have been implemented to compute the entropy for non-blackbody radiation fluxes. This summary is based on the review study developed by Wu and Liu [2010]. Here we divided the approaches in two main groups: (1). those that uses a simple approximations where the apply directly E_{BR}/T, and (2) those that attempt to solve the integral entropy flux developed by Planck.

Direct approximations Based on E_{BR}/T

- i. Based on Classic Thermodynamic Clausius Approach

This approach implements directly the Rudolf Clausius entropy definition. Therefore, the entropy flux is computed as the ratio of radiation energy flux and absolute temperature.

$$J = \frac{E_{BR}}{T} \tag{F.22}$$

This approach was initially developed for nonradiative heat transfer and it has been shown to work for this conditions. However, this approach neglects properties embedded in radiative energy such as the pressure term and may underestimate the entropy fluxes.

- ii. Assuming Blackbody Radiation

This approach assumes that all radiation behaves as blackbody. Therefore the flux of entropy

by is given by $J = \frac{4}{3}\frac{E_{BR}}{T}$. Although this approach is appropriate for blackbody radiation it does not hold for non-blackbody. The presence of non-blackbody radiation in earth processes is ubiquitous and this approach may induce significant error in the computation of entropy budgets on earth systems.

-iii Approaches that attempt to solve the integral of entropy spectral radiation flux developed by Planck

Planck was able to show that the spectral radiation energy flux for a blackbody radiation per unit solid angle per unit frequency is given by:

$$I_{v,BR} = \frac{n_o h v^3}{c^2}\left\{\frac{1}{\exp\left(\frac{hv}{\kappa T}\right) - 1}\right\} \tag{F.23}$$

Moreover, Planck was able to show that the spectral radiation entropy flux for a blackbody radiation per unit solid angle per unit frequency is given by:

$$L_{v,BR} = \frac{2hv^3}{c^2}\left\{\left(1 + \frac{c^2 I_v}{n_o h v^3}\right)\ln\left(1 + \frac{c^2 I_v}{n_o h v^3}\right) - \left(\frac{c^2 I_v}{n_o h v^3}\right)\ln\left(\frac{c^2 I_v}{n_o h v^3}\right)\right\} \tag{F.24}$$

The total energy energy flux for a blackbody radiation per unit area (irradiance) with units ($[W/m^2]$) is computed by integration of I_v over all the frequencies and also over the solid angle.

$$E_{BR} = \int_0^\infty dv \int_\Omega I_{v,BR}\cos\theta d\Omega \tag{F.25}$$

Similarly the total entropy flux for a blackbody radiation per unit area with units ($[W/K/m^2]$) is computed if L_v is integrated over all the frequencies and also over the solid angle.

$$J_{BR} = \int_0^\infty dv \int_\Omega L_{v,BR}\cos\theta d\Omega \tag{F.26}$$

Actually it is possible to show that integration of $L_{v,BR}$ over all the frecuencies and solid angle in the entire hemisphere arrives to the same etropy flux introduced in Equation $F.21$, indeed

$$J_{BR} = \int_0^\infty dv \int_\Omega L_{v,BR} \cos\theta d\Omega = \frac{4}{3}\frac{E_{BR}}{T} \tag{F.27}$$

In order to analyze non-blackbody radiation we express the spectral radiation energy flux per unit solid angle per unit frequency as a function of the emissivity.

$$I_v(\varepsilon) = \frac{\varepsilon n_o h v^3}{c^2}\left\{\frac{1}{\exp\left(\frac{hv}{\kappa T}\right)-1}\right\} \tag{F.28}$$

Note that Equation F.28 is the same as Equation F.24, however there is an emmisivity (ε) that defines the capacity of the system to emit energy. When $\varepsilon = 1$ the system behaves as a blackbody. If it is assumed that ε remains constant for all the frequencies. We can then take ε out of the integral and the integration over all the frequencies and solid angle is the same as the one performed for the blackbody radiation:

$$E(\varepsilon) = \int_0^\infty dv \int_\Omega I_v(\varepsilon) \cos\theta d\Omega = \varepsilon\sigma T^4 \tag{F.29}$$

Note that the total energy for a non blackbody radiation differs from that of the blackbody radiation only by the emissivity constant ε. On the other hand, the entropy flux for a non-blackbody radiation can be expressed using Plank's formulation:

$$L_v(\varepsilon) = \frac{\varepsilon n_o h v^3}{c^2}\left\{\left(1+\frac{c^2 I_v(\varepsilon)}{n_o h v^3}\right)\ln\left(1+\frac{c^2 I_v(\varepsilon)}{n_o h v^3}\right) - \left(\frac{c^2 I_v(\varepsilon)}{n_o h v^3}\right)\ln\left(\frac{c^2 I_v(\varepsilon)}{n_o h v^3}\right)\right\} \tag{F.30}$$

Again, as we did before it is possible to compute the total flux of entropy of a non blakbody radiation with emmisivity ε by integration of over all the frecuencies and solid angles.

$$J(\varepsilon) = \int_0^\infty dv \int_\Omega L_v(\varepsilon) \cos\theta d\Omega \tag{F.31}$$

However Equation F.30 is highly non linear and it is challenging to perform this integration. Below we describe some previous approaches that have been formulated to solve the integral in Equation F.31:

- *i. Landsberg and Tonge*

Landsberg and Tonge [1979] propose an approximate expression to compute the integral in Equation F.31 by considering a dilution factor ($\delta < 1$) that adjust to the non-blackbody radiation properties. In this approach, the energy and entropy fluxes from a non blackbody radiation are given by:

$$E = \frac{B\delta\sigma T^4}{\pi} \tag{F.32}$$

$$J = \frac{\frac{4}{3}B\delta X(\delta)\sigma T^3}{\pi} \tag{F.33}$$

Where

$$B = \int cos\theta d\Omega \tag{F.34}$$

$$\delta X(\delta) = \frac{45}{4}\pi^{-4}\int_0^\infty \left\{\left(1+\frac{\delta}{e^\beta-1}\right)\ln\left(1+\frac{\delta}{e^\beta-1}\right) - \left(\frac{\delta}{e^\beta-1}\right)\ln\left(\frac{\delta}{e^\beta-1}\right)\right\}\beta^2 d\beta \tag{F.35}$$

and

$$\beta = h\nu/\kappa T \tag{F.36}$$

Landsberg and Tonge [1979] were able to find an approximate solution for Equation F.35 for low values of ε ($\varepsilon < 0.1$).

$$\delta X(\delta) \approx \delta\left[0.9652 - 0.2777\ln(\delta) + 0.0511\delta\right] \tag{F.37}$$

Mathematically the dilution factor approach and the gray body radiation (used to compute energy fluxes of non-blackbody radiation) are equivalent [Wu and Liu, 2010], and the dilution factor δ used in Landsberg and Tonge [1979] is similar to the emissivity of a gray body.

- ii. Wright et al. [2001]

Although Landsberg and Tonge [1979] were able to obtain a simple expression that computes the entropy for non blackbody radiation still it relays on low dilution factors. Wright et al. [2001] developed an formulation to compute the integral in Equation F.31 that resulted

in better matches over different emissivity ranges.

Starting from the approach exposed in Landsberg and Tonge [1979], the entropy flux for a non blackbody radiation can be computed as the entropy flux for a blakbody radiation (J_{BR}) affected by a function that depends on ε ($f(\varepsilon)$):

$$J = \frac{B\overbrace{\delta X(\delta)}^{f(\varepsilon)}\overbrace{\frac{4}{3}\sigma T^3}^{J_{BR}}}{\pi}. \tag{F.38}$$

The function $f(\varepsilon)$ is the same as $\delta X(\delta)$ (Equation F.35). Note that this function can also be expressed as:

$$f(\varepsilon) = \frac{45}{4\pi^4} I(\varepsilon). \tag{F.39}$$

and therefore the flux of entropy of a non blackbody radiation can be expressed as:

$$J = \frac{45}{4\pi^4} I(\varepsilon) J_{BR}. \tag{F.40}$$

Wright et al. [2001] proposed the next approximation for $I(\varepsilon)$

$$I(\varepsilon) \approx \varepsilon \left(\frac{4\pi^4}{45} - mLn(\varepsilon) \right) \tag{F.41}$$

and two different approaches for m were analyzed (i). m equal a constant c_1 and (ii). m is represented as a linear function of ε with slope c_3 and intercept c_2:

$$m \Rightarrow \left\{ \begin{array}{l} = c_1 \\ = c_2 - c_3\varepsilon \end{array} \right\} \tag{F.42}$$

According to Wright et al. [2001] the second approach ($m = c_2 - c_3\varepsilon$) shows good results with a maximum error lower than 1% for the emissivity range between 0.2 to 1. Therefore, the entropy flux is given by:

$$J = \left\{ 1 + \frac{45Ln(\varepsilon)}{4\pi^4} (\varepsilon c_3 - c_2) \right\} \varepsilon J_{BR} \tag{F.43}$$

F.2 Aoki Approximation to Compute Radiation Entropy Budgets in Earth Systems

Through several publications Ichiro Aoki introduced a simple framework for the calculation of radiation entropy fluxes at the earth surface. In this framework he computes the entropy flux that is present in solar radiation, scattered and diffuse radiation and longwave radiation separately. In this section we briefly describe the approach he used to compute the entropy fluxes in each of these cases.

F.2.1 Entropy of Shortwave Radiation

The shortwave radiation is emitted at high temperatures. In the earth this type of radiation comes from the sun and can be scattered due to interactions with different bodies in the atmosphere or the surface. Therefore, the shortwave energy reaching the surface could be either direct or diffuse. The formulation to compute the entropy flux in these two energy forms are discussed above.

Entropy of Direct Solar Radiation

The flux of radiation energy from the sun that reaches the top of the atmosphere is called solar constant (e_1). Similarly, the flux of radiation entropy at the top of the earth atmosphere is called solar constant of second kind (s_1). The solar constant e_1 has been measured and is equal to 0.1353 $\text{Jcm}^{-2}\text{s}^{-1}$. Aoki [1983] proposed a methodology to compute s_1 assuming that e_1 is known.

The total flux of energy emitted by the sun (in terms of energy per unit area per unit time) is given by Boltzman equation $E_{sun} = \sigma T_o^4$, where σ is the Stefan Boltzman constant and T_o is the sun temperature. Similarly the total entropy flux emitted by the sun (in terms of energy per unit area per unit time per unit temperature) is given by $S_{sun} = \frac{4}{3}\sigma T_o^3$. The energy and entropy emitted by the entire sun area is then given by $\overline{E}_{sun} = 4\pi r_{sun}^2 \sigma T_o^4$ and $\overline{S}_{sun} = 4\pi r_{sun}^2 \frac{4}{3}\sigma T_o^3$ respectively. Note that the entropy can also be expressed as $\overline{S}_{sun} = 4\pi r_{sun}^2 \frac{4}{3}\frac{\overline{E}_{sun}}{T_o}$. By definition the total amount of energy an entropy at $r = R$ is:

$$\begin{aligned} \overline{E}_R &= 4\pi R^2 e_1 \\ \overline{S}_R &= 4\pi R^2 s_1 \end{aligned} \tag{F.44}$$

Assuming there are not losses of energy traveling (mostly in the vacuum) from the sun to

the earth and also there is no net increase in entropy, then the total amount of energy and entropy at $r = r_{sun}$ should be same as the one that is present when the light hit the earth atmosphere at $r = R$ (being R the mean distance from the sun to the earth atmosphere). In other words $\overline{E} = \overline{E_R}$ and $\overline{S} = \overline{S_R}$. It is easily shown that:

$$\begin{aligned} e_1 &= \left(\tfrac{r}{R}\right)^2 \sigma T_o^4 \\ s_1 &= \left(\tfrac{r}{R}\right)^2 \tfrac{4}{3} \sigma T_{sun}^3 = \tfrac{4}{3} \tfrac{e_1}{T_o} \end{aligned} \tag{F.45}$$

Using Equation F.45 and knowing e_1 it is possible to compute s_1. According to Aoki [1983] $s_1 = 3.132\text{x}10^{-5}$ $\text{Jcm}^{-2}\text{s}^{-1}\text{K}^{-1}$. Aoki [1987a] used the expressions in F.45 to calculate the amount of entropy that reaches the surface. The incident solar energy flux over a unit area of a horizontal plane at the top of the atmosphere is given by:

$$Q_e(t) = e_1 \left(\frac{\overline{R}}{R}\right)^2 \cos\left(\theta_o\right) \tag{F.46}$$

where $\overline{R}$ is the mean distance from the sun to the earth and θ_o is the zenith angle. The zenith angle can be expressed in terms of the latitude ϕ, declination of the sun δ and hour and angle h as:

$$\theta_o = sin\phi sin\delta + cos\phi cos\delta cosh. \tag{F.47}$$

The daily solar energy incident at the top of the atmosphere can be calculated by integration of F.46 over a day. The integration is performed from $-H$ to H, where $H = -\tan\phi \tan\delta$ is the hour angle at sunset when $\theta_0 = 90$.

$$\overline{Q}_e(t) = e_1 \left(\frac{\overline{R}}{R}\right)^2 \int_{-H}^{H} \frac{\cos\left(\theta_o\right) dH}{2\pi} = 86400 \frac{e_1}{\pi} \left(\frac{\overline{R}}{R}\right)^2 \left(H \sin\phi \sin\delta + \sin H \cos\phi \cos\delta\right) \tag{F.48}$$

Similarly, following the same approach for the entropy and using s_1, it is possible to obtain the daily solar entropy incident on a unit area of horizontal plane at the top of the atmosphere.

$$\overline{Q}_s(t) = 86400 \frac{s_1}{\pi} \left(\frac{\overline{R}}{R}\right)^2 \left(H \sin\phi \sin\delta + \sin H \cos\phi \cos\delta\right) \tag{F.49}$$

the relationship between $\overline{Q}e$ and $\overline{Q}s$ is given by:

$$\frac{\overline{Q}s}{\overline{Q}e} = \frac{s1}{e1} \tag{F.50}$$

Once the radiation goes inside the atmosphere it experiments several processes that change its entropy due to different interactions with the atmosphere. The energy flux of direct solar radiation over a horizontal plane E_{dr} at the earth surface can be computed as a fraction of the incident energy at the top of the atmosphere, as shown in Equation F.51.

$$E_{dr} = \rho\overline{Q}e \tag{F.51}$$

where, the constant ρ is the transmissivity of solar radiation in the atmosphere. Assuming the same constant value applies for the entropy transmissivity across the atmosphere, it is possible to compute the solar entropy flux at the earth surface:

$$S_{dr} = \rho\overline{Q}s = \rho\overline{Q}e\frac{s1}{e1} = E_{dr}\frac{s1}{e1}. \tag{F.52}$$

Using the results from Equation F.52 it is possible to compute the entropy of direct solar radiation at the earth surface if the energy of the direct solar radiation reaching the surface is known.

Entropy of Diffuse Solar Radiation

Aoki [1982] was able to show that the entropy flux of scattered radiation can be treated as a grey body radiation with emissivity ϵ if the incident radiation is black body and if the reflectivity is independent of the frequency.

Assuming that extraterrestrial solar radiation is black-body then the radiance flux of solar energy radiation in extraterrestrial space k_o is given by:

$$K_o = \frac{1}{\pi}\sigma T_o^4. \tag{F.53}$$

Once the solar radiation reaches the atmosphere it is affected and it is scattered in different directions. Let K_1 be the radiance flux of diffuse solar energy radiation at the earth surface and let us assume that this parameter remains constant among the various directions at which this process occurs. Let us assume there is a parameter ϵ which is frequency independent and links both radiances such that:

$$\epsilon = \frac{K_1}{K_o} \tag{F.54}$$

Note that there is an spectral blackbody intensity flux $I_{v,BRsun} = \frac{n_o h v^3}{c^2}\left\{\frac{1}{\exp\left(\frac{hv}{\kappa T_o}\right)-1}\right\}$ emitted by the sun such that:

$$K_o = \int_0^\infty I_{v,BRsun} dv = \int_0^\infty \left[\frac{2hv^3}{c^2}\left\{\frac{1}{\exp\left(\frac{hv}{\kappa T_o}\right)-1}\right\}\right] dv = \frac{1}{\pi}\sigma T_o^4. \tag{F.55}$$

Using $T_o = 5760$K Aoki [1982] computed $K_o = 0.63\text{x}10^6 \text{GJm}^{-2}\text{yr}^{-1}$. Note that $\int_o^\infty K_o cos\theta d\Omega = E_o$

The spectral intensity of the radiation that is scattered by the atmosphere and reaches the earth surface is given by $I_{v,sc} = \epsilon \frac{n_o h v^3}{c^2}\left\{\frac{1}{\exp\left(\frac{hv}{\kappa T_o}\right)-1}\right\}$ such that:

$$K_1 = \int_0^\infty I_{v,sc}(\epsilon) dv = \int_0^\infty \left[\epsilon\frac{2hv^3}{c^2}\left\{\frac{1}{\exp\left(\frac{hv}{\kappa T_o}\right)-1}\right\}\right] dv = \epsilon\frac{1}{\pi}\sigma T_o^4. \tag{F.56}$$

Similarly, the spectral blackbody intensity entropy flux emitted by the sun is given by:

$$L_{v,BR} = \frac{n_o h v^3}{c^2}\left\{\left(1+\frac{c^2 I_{v,BR}}{2hv^3}\right)\ln\left(1+\frac{c^2 I_{v,BR}}{2hv^3}\right) - \left(\frac{c^2 I_{v,BR}}{2hv^3}\right)\ln\left(\frac{c^2 I_{v,BR}}{2hv^3}\right)\right\} \tag{F.57}$$

Integration of $L_{v,BR}$ results in the total radiance entropy flux per unit of solid angle. Again note that $\int_o^\infty M_o cos\theta d\Omega = J_o$

$$M_o = \int_0^\infty L_{v,BR} = \frac{4}{3\pi}\sigma T_o^4 dv \tag{F.58}$$

The spectral intensity entropy flux of the radiation scattered by the atmosphere and reaching the surface is given by:

$$L_{v,sc} = \frac{2hv^3}{c^2}\left\{\left(1+\frac{c^2 I_{v,sc}(\epsilon)}{2hv^3}\right)\ln\left(1+\frac{c^2 I_{v,sc}(\epsilon)}{2hv^3}\right) - \left(\frac{c^2 I_{v,sc}(\epsilon)}{2hv^3}\right)\ln\left(\frac{c^2 I_{v,sc}(\epsilon)}{2hv^3}\right)\right\} \tag{F.59}$$

Integration of $L_{v,sc}(\epsilon)$ will result in the total entropy flux per unit of soled angle. However,

as mentioned in section F.1.1 this integral is difficult to solve. Note that the computation of entropy flux is similar in scattered radiation reach to the same integral as the computation of the entropy flux in a grey body radiation. In this case the scaterring ratio ϵ resembles the emissivity of the grey body ε.

The energy of diffuse solar radiation incident over a unit area at the earth surface is given by:

$$E_{sc} = \pi K_1 \tag{F.60}$$

The radiance of solar radiation in extraterrestrial space K_o can be computed as in Aoki [1982] using $T_o = 5760K$. Thus, it is possible to compute ϵ as

$$\epsilon = \frac{K_1}{K_o} \tag{F.61}$$

The computation of the entropy flux J_1 (or entropy flux per unit of solid angle M_1) is computed by using one of the methods introduced in section F.1.1. In Aoki [1987a] it is used the approach presented by [Landsberg and Tonge, 1979].

$$J_1 = \frac{4}{3}\epsilon\sigma T_o^3 X(\epsilon) = \frac{4}{3}\frac{K_1\pi}{T_o}X(\epsilon) = \frac{4}{3}\frac{E_{sc}}{T_o}X(\epsilon) \tag{F.62}$$

where $X(\epsilon)$ is a function introduced in [Landsberg and Tonge, 1979]

Longwave

Under the assumption that bodies emitting longwave radiation behave as grey bodies, then the entropy flux can be computed by solving the integral in Equation F.31 if the grey body effective temperature T_e and the grey body emissivity (ε) are known. Following [Landsberg and Tonge, 1979]:

$$S_{lw}(\varepsilon) = \frac{4}{3}\varepsilon\sigma T_e^3 X(\varepsilon) \tag{F.63}$$

The energy emitted by a grey body is given as $E_{lw} = \varepsilon\sigma T_e^4$, thus:

$$S_{lw} = \frac{4}{3}\varepsilon\sigma T_e^3 X(\varepsilon) = \frac{4}{3}\frac{E_b}{T_e}X(\varepsilon) \tag{F.64}$$

F.3 Entropy and Energy Balance

Part of the energy that reaches the surface in the form of radiation is absorbed by the surface while other fraction is reflected. The fraction that is absorbed by the surface is dissipated in different forms or used for photosynthesis (an small fraction).

Equation F.65 shows the balance of radiation energy that reaches the surface of the earth. Energy is a conservative property and therefore energy conservation should be always satisfied. The energy coming to the surface is mostly in the form of shortwave SW_{in} and longwave LW_{in}. Part of the shortwave radiation is reflected back to the atmosphere SW_{out} and a percentage of the energy absorbed by the surface is emitted back as longwave radiation LW_{out}. Thus, the remaining energy Rn results in the net energy that is absorbed by the surface:.

$$Rn = SW_{in} + LW_{in} - SW_{out} - LW_{out} \tag{F.65}$$

At the surface the net energy absorbed can be dissipated in the form of latent LE and sensible H heat to the atmosphere, or can be penetrate down in the soil as ground heat flux (G), or be stored in the surface (ΔE) for different different purposes such asphotosynthesis. In general net radiation is givenn by:

$$Rn = LE + H + G + \Delta E \tag{F.66}$$

The entropy for the different fluxes of Equation F.66 is given by:

$$\begin{cases} S_{LE} = \frac{LE}{T_{surf}} \\ S_H = \frac{H}{T_{surf}} \\ S_G = \frac{G}{T_{surf}} \end{cases} \tag{F.67}$$

REFERENCES

Aanderud, Z. T. and Richards, J. H. (2009). Hydraulic redistribution may stimulate decomposition. *Biogeochemistry*, 95(2-3):323–333.

Abrahams, A. and Parsons, A. . . (1994). *Geomorphology of desert environments*. Chapman & Hall.

Ahn, H. K., Sauer, T. J., Richard, T. L., and Glanville, T. D. (2009). Determination of thermal properties of composting bulking materials. *Bioresource Technology*, 100(17):3974–81.

Albrecht, W. (1940). Land classification in relation to the soil and its development. In *Proceedings of the First National Conference on Landa Classification. Agricultural Experiment Station*. College of Agriculture, University of Missouri, Columbia, Missouri, USA, University of Missouri.

Alder, N. N., Sperry, J. S., and Pockman, W. T. (1996). Root and stem xylem embolism, stomatal conductance, and leaf turgor in Acer grandidentatum populations along a soil moisture gradient. *Oecologia*, 105(3):293–301.

Allton, K., Harris, J., Rickson, R., and Ritz, K. (2007). The effect of microbial communities on soil hydrological processes: A microcosm study utilising simulated rainfall. *Geoderma*, 142(1-2):11–17.

Amenu, G. G. and Kumar, P. (2008). A model for hydraulic redistribution incorporating coupled soil-root moisture transport. *Hydrology And Earth System Sciences*, 12(1):55–74.

Anderson, M. C., Norman, J. M., Meyers, T. P., and Diak, G. R. (2000). An analytical model for estimating canopy transpiration and carbon assimilation fluxes based on canopy light-use efficiency. *AGRICULTURAL AND FOREST METEOROLOGY*, 101(4):265–289.

Andren, O. (1992). Modelling the effects of moisture on barley straw and root decomposition in the field. *Soil Biology and Biochemistry*, 24(8):727–736.

Angers, D. A. and Caron, J. (1998). Plant-induced changes in soil structure : Processes and feedbacks. *Biogeochemistry*, 42(1):55–72.

Aoki, I. (1982). Radiation entropies in diffuse reflection and scattering and application to solar radiation. *Journal of the Physical Society*, 51(12):4003–4010.

Aoki, I. (1983). Entropy productions on the earth and other planets of the solar system. *Journal of the Physical Society of Japan*, 52(3):1075–1078.

Aoki, I. (1987a). Entropy balance in lake biwa. *Ecological Modeling*, 37(3-4):235–248.

Aoki, I. (1987b). Entropy budgets of deciduous plant leaves and theorem of oscillating entropy production. *F Mathematical Biology*, 49(4):449–460.

Aoki, I. (1989). Entropy budget of conifer branches. *Botanical Magazine-Tokio*, 102(1065):133–141.

Armas, C., Kim, J. H., Bleby, T. M., and Jackson, R. B. (2011). The effect of hydraulic lift on organic matter decomposition, soil nitrogen cycling, and nitrogen acquisition by a grass species. *Oecologia*, 168:11–22.

Ayres, E., Steltzer, H., Berg, S., and Wall, D. H. (2009). Soil biota accelerate decomposition in high-elevation forests by specializing in the breakdown of litter produced by the plant species above them. *J Ecol*, 97(5):901–912.

Ball, J., Woodrow, I., and Berry, J. (1987). A model predicting stomatal conductance and its contribution to the control of photosynthesis under different environmental conditions. *Progress in Photosynthesis Research*, 4(U):221 – 224.

Bardgett, R. and Wardle, D. (2010). *Aboveground-Belowground Linkages: Biotic Interactions, Ecosystem Processes, and Global Change*. Oxford Univ Press.

Bassow, S. L. and Bazzaz, F. A. (1997). Intra- and inter-specific variation in canopy photosynthesis in a mixed deciduous forest. *Oecologia*, 109(4):507–515.

Bavel, C. H. M. V. and Hillel, D. I. (1976). Calculating potential and actual Evaporation from a bare soil surface by simulation of concurrent flow water and heat. *Agricultural Meteorology*, 17:453–476.

Berg, B. and McClaugherty, C. . . (2008). *Plant Litter: Decomposition, Humus Formation, Carbon Sequestration*. Springer London, Limited.

Bernacchi, C. J., Morgan, P. B., Ort, D. R., and Long, S. P. (2005). The growth of soybean under free air [CO(2)] enrichment (FACE) stimulates photosynthesis while decreasing in vivo Rubisco capacity. *Planta*, 220(3):434–46.

Bernacchi, C. J., Pimentel, C., and Long, S. P. (2003). In vivo temperature response functions of parameters required to model rubp-limited photosynthesis. *Plant Cell and Environment*, 26(9):1419–1430.

Beven, K. and Germann, P. (1982). Macropores and water flow in soils. *Water Resources Research*, 18(5):1311–1325.

Bird, J. a. and Torn, M. S. (2006). Fine Roots vs. Needles: A Comparison of 13C and 15N Dynamics in a Ponderosa Pine Forest Soil. *Biogeochemistry*, 79(3):361–382.

Black, T. A. and Harden, J. (1995). Effect of timber harvest on soil carbon at blodgett experimental forest, california. *Can. J. For. Res.*, 25:1385–1396.

Bleby, T. M., McElrone, A. J., and Jackson, R. B. (2010). Water uptake and hydraulic redistribution across large woody root systems to 20 m depth. *Plant, cell & environment*, 33(20):2132–2148.

Blizzard, W. E. (1980). Comparative resistance of the soil and the plant to water transport. *Plant Physiology*, 66(5):809–14.

Botkin, D. B., Janak, J. F., and Wallis, J. R. (1972). Some ecological consequences of a computer model of forest growth. *Journal of Ecology*, 60(3):pp. 849–872.

Boucher, D. H. (1985). The idea of mutualism, past and future. In Boucher, D. H., editor, *The biology of mutualism*. Croom Helm, London, UK.

Bouvier-Brown, N. (2008). *Quantifying reactive biogenic volatile organic compounds: Implications for gas- and particle-phase atmospheric chemistry*. University of California, Berkeley.

Braakhekke, M. C., Beer, C., Hoosbeek, M. R., Reichstein, M., Kruijt, B., Schrumpf, M., and Kabat, P. (2011). SOMPROF : A vertically explicit soil organic matter model. *Ecological Modelling*, 222(10):1712–1730.

Bristow, K. L., Campbell, G. S., Papendick, R. I., and Elliott, L. F. (1986). Simulation of heat and moisture transfer through a surface residue-soil system. *Agricultural and Forest Meteorology*, 36:193–214.

Brooks, J. R., Meinzer, F. C., Coulombe, R., and Gregg, J. (2002). Hydraulic redistribution of soil water during summer drought in two contrasting pacific northwest coniferous fores. *Tree Physiology*, 22:1107 – 1117. 100

Brooks, J. R., Meinzer, F. C., Warren, J. M., Domec, J. C., and Coulombe, R. (2006). Hydraulic redistribution in a douglas-fir forest: Lessons from system manipulations. *Plant Cell and Environment*, 29(1):138–150.

Brown, R. W. and Bartos, D. L. (1982). A calibration model for screen-caged Peltier thermocouple psychrometers. *NASA STI/Recon Technical Report N*, 83:16735.

Brutsaert, W. (1975). On a derivable formula for long-wave radiation from clear skies. *Water Resources Research*, 11(5):742–744.

Burgess, S. S. O., Adams, M. A., Turner, N. C., and Ong, C. K. (1998). The redistribution of soil water by tree root systems. *Oecologia*, 115(3):306–311.

Burgess, S. S. O., Adams, M. A., Turner, N. C., White, D. A., and Ong, C. K. (2001). Tree roots: conduits for deep recharge of soil water. *Oecologia*, 126(2):158–165.

Burgess, S. S. O., Pate, J. S., Adams, M. A., and Dawson, T. E. (2000). Seasonal water acquisition and redistribution in the australian woody phreatophyte, banksia prionotes. *Annals of Botany*, 85(2):215–224.

Bussiere, F. and Cellier, P. (1994). Modification of the soil temperature and water content regimes by a crop residue mulch: Experiment and modeling. *Agricultural and Forest Meteorology*, 68(1-2):1–28.

Caldwell, M. M., Dawson, T. E., and Richards, J. H. (1998). Hydraulic lift: Consequences of water efflux from the roots of plants. *Oecologia*, 113(2):151–161. 0

Caldwell, M. M. and Manwaring, J. H. (1994). Hydraulic lift and soil nutrient heterogeneity. *Natural Resources Research*.

Caldwell, M. M. and Richards, J. H. (1989). Hydraulic lift - water efflux from upper roots improves effectiveness of water-uptake by deep roots. *Oecologia*, 79(1):1–5. 0

Campbell, G. and Norman, D. (1998). *An Introduction to Environmental Biophysics*. Springer, New York, 97015706 Gaylon S. Campbell, John M. Norman. ill. ; 24 cm. Includes 362 bibliographical references and index.

Carswell, F. E., Meir, P., Wandelli, E. V., Bonates, L. C. M., Kruijt, B., Barbosa, E. M., Nobre, A. D., Grace, J., and Jarvis, P. G. (2000). Photosynthetic capacity in a central Amazonian rain forest. *Tree Physiology*, pages 179–186.

Celia, M. A., Bouloutas, E. T., and Zarba, R. L. (1990). A general mass-conservative numerical-solution for the unsaturated flow equation. *Water Resources Research*, 26(7):1483–1496.

Chaplin, M. (2006). Do we underestimate the importance of water in cell biology? *Nat Rev Mol Cell Biol*, 7(11):861–866.

Chiarini, L., Bevivino, A., Dalmastri, C., Nacamulli, C., and Tabacchioni, S. (1998). Influence of plant development, cultivar and soil type on microbial colonization of maize roots. *Applied Soil Ecology*, 8(1–3):11–18.

Chorover, J., Kretzschmar, R., Garcia-Pichel, F., and Sparks, D. L. (2007). Soil biogeochemical processes within the critical zone. *Elements*, 3(5):321–326.

Chung, S. O. and Horton, R. (1987). Soil heat and water-flow with a partial surface mulch. *Water Resources Research*, 23(12):2175–2186.

Clark, D. B. (1996). Abolishing virginity. *Journal of Tropical Ecology*, 12:735–739.

Coops, N. C., Hilker, T., Wulder, M. A., St-Onge, B., Newnham, G., Siggins, A., and Trofymow, J. A. (2007). Estimating canopy structure of douglas-fir forest stands from discrete-return lidar. *Trees-Structure and Function*, 21(3):295–310.

Cousins, I. T., Mackay, D., and Jones, K. C. (1999). Measuring and modelling the vertical distribution of semi-volatile organic compounds in soils. ii: model development. *Chemosphere*, 39(14):2519 – 2534.

Dam, D., Veldkamp, E., and Breemen, N. V. (1997). Soil organic carbon dynamics: Variability with depth in forested and deforested soils under pasture in costa rica. *Biogeochemistry*, 39(3):343–375.

Dawson, T. E. (1993). Hydraulic lift and water use by plants. implications for water balance, performance and plant-plant interactions. *Oecologia*, 95(4):565–574.

Dawson, T. E. (1996). Determining water use by trees and forests from isotopic, energy balance and transpiration analyses: The roles of tree size and hydraulic lift. *Tree Physiology*, 16(1-2):263–272.

de Kroon, H., van der Zalm, E., van Rheenen, J. W. a., van Dijk, A., and Kreulen, R. (1998). The interaction between water and nitrogen translocation in a rhizomatous sedge (Carex flacca). *Oecologia*, 116(1-2):38–49.

Deluca, T., Zackrisson, and Sellstedt, A. (2002). Quantifying nitrogen-fixation in feather moss carpets of boreal forests. *Nature*, 419.

D'Odorico, P., Laio, F., Porporato, A., and Rodriguez-Iturbe, I. (2003). Hydrologic controls on soil carbon and nitrogen cycles. ii. a case study. *Advances in Water Resources*, 26(1):59–70.

Dolman, A. J. (1993). A multiple-source land surface energy balance model for use in general circulation models. *Agricultural and Forest Meteorology*, 65(1–2):21–45.

Domec, J.-C., King, J. S., Noormets, A., Treasure, E., Gavazzi, M. J., Sun, G., and McNulty, S. G. (2010). Hydraulic redistribution of soil water by roots affects whole-stand evapotranspiration and net ecosystem carbon exchange. *The New phytologist*, 187(1):171–83.

Domec, J. C., Warren, J. M., Meinzer, F. C., Brooks, J. R., and Coulombe, R. (2004). Native root xylem embolism and stomatal closure in stands of douglas-fir and ponderosa pine: mitigation by hydraulic redistribution. *Oecologia*, 141(1):7–16.

Domingues, T. F., Martinelli, L. A., and Ehleringer, J. R. (2007). Ecophysiological traits of plant functional groups in forest and pasture ecosystems from eastern Amazo nia , Brazil. *Plant Ecology*, pages 101–112.

Drewry, D. T., Kumar, P., Long, S., Bernacchi, C., Liang, X.-Z., and Sivapalan, M. (2010a). Ecohydrological responses of dense canopies to environmental variability: 1. Interplay between vertical structure and photosynthetic pathway. *Journal of Geophysical Research*, 115(G4):1–25.

Drewry, D. T., Kumar, P., Long, S., Bernacchi, C., Liang, X.-Z., and Sivapalan, M. (2010b). Ecohydrological responses of dense canopies to environmental variability: 2. Role of acclimation under elevated CO 2. *Journal of Geophysical Research*, 115(G4):1–22.

D.S. Jenkinson, D.E. Adams, A. W. (1991). Model Estimates of CO2 emmisions from soil in response to global warming. *Nature*.

Eagleson, P. S. (1978a). Climate, soil, and vegetation .1. introduction to water-balance dynamics. *WATER RESOURCES RESEARCH*, 14(5):705–712.

Eagleson, P. S. (1978b). Climate, soil, and vegetation .2. distribution of annual precipitation derived from observed storm sequences. *Water Resources Research*, 14(5):713–721.

Eagleson, P. S. (1978c). Climate, soil, and vegetation. 3. simplified model of soil moisture movement in liquid-phase. *Water Resources Research*, 14(5):722–730.

Eagleson, P. S. (1978d). Climate, soil, and vegetation. 4. expected value of annual evapotranspiration. *Water Resources Research*, 14(5):731–739.

Eagleson, P. S. (1978e). Climate, soil, and vegetation. 5. derived distribution of storm surface runoff. *Water Resources Research*, 14(5):741–748.

Eagleson, P. S. (1978f). Climate, soil, and vegetation. 6. dynamics of annual water-balance. *Water Resources Research*, 14(5):749–764.

Eagleson, P. S. (1978g). Climate, soil, and vegetation. 7. derived distribution of annual water yield. *Water Resources Research*, 14(5):765–776.

Eagleson, P. S. (1982). Ecological optimality in water-limited natural soil-vegetation systems: 1. theory and hypothesis. *Water Resources Research*, 18(2):325–340.

Egerton-Warburton, L. M., Querejeta, J. I., and Allen, M. F. (2008). Efflux of hydraulically lifted water from mycorrhizal fungal hyphae during imposed drought. *Plant signaling & behavior*, 3(1):68–71.

Elzein, A. and Balesdent, J. (1995). Mechanistic simulation of vertical distribution of carbon concentrations and residence times in soils. *Soil Science Society of America Journal*, 59(5):1328.

Emerman, S. H. and Dawson, T. E. (1996). Hydraulic lift and its influence on the water content of the rhizosphere: An example from sugar maple, acer saccharum. *Oecologia*, 108(2):273–278.

Eom, A. H., Hartnett, D. C., and Wilson, G. W. T. (2000). Host plant species effects on arbuscular mycorrhizal fungal communities in tallgrass prairie. *Oecologia*, 122(3):435–444.

Espeleta, J. F., West, J. B., and Donovan, L. A. (2004). Species-specific patterns of hydraulic lift in co-occurring adult trees and grasses in a sandhill community. *OECOLOGIA*, 138(3):341–349.

Farquhar, G. D., Caemmerer, S. V., and Berry, J. A. (1980). A biochemical-model of photosynthetic co2 assimilation in leaves of c-3 species. *Planta*, 149(1):78–90. p.

Fath, B. D., PATTEN, B. C., and CHOI, J. S. (2001). Complementarity of ecological goal functions. *Journal of Theoretical Biology*, 208(4):493–506.

Fay, P. A. (2009). Precipitation variability and primary productivity in water-limited ecosystems: how plants 'leverage'precipitation to 'finance'growth. *New Phytologist*, 181(1):5–8.

Fierer, N., Schimel, J. P., and Holden, P. A. (2003). Variations in microbial community composition through two soil depth profiles. *Microbiology*, 35:167–176.

Fisher, J. B., Baldocchi, D. D., Misson, L., Dawson, T. E., and Goldstein, A. H. (2007). What the towers don't see at night: nocturnal sap flow in trees and shrubs at two ameriflux sites in california. *Tree Physiology*, 27(4):597–610.

Fisher, J. B., DeBiase, T. A., Qi, Y., Xu, M., and Goldstein, A. H. (2005). Evapotranspiration models compared on a sierra nevada forest ecosystem. *Environmental Modelling & Software*, 20(6):783–796.

Foley, J. A., Prentice, I. C., Ramankutty, N., Levis, S., Pollard, D., Sitch, S., and Haxeltine, A. (1996). An integrated biosphere model of land surface processes, terrestrial carbon balance, and vegetation dynamics. *Global Biogeochemical Cycles*, 10(4):603–628.

Frensch, J. and Steudle, E. (1989). Axial and radial hydraulic resistance to roots of maize (zea-mays-l). *Plant Physiology*, 91(2):719–726. , axial conductivity, radial conductivity,.

Galantowicz, J. F., Entekhabi, D., and Njoku, E. G. (1999). Tests of sequential data assimilation for retrieving profile soil moisture and temperature from observed l-band radiobrightness. *IEEE TRansactions on Geoscience and Remote Sensing*, 37(4):1860–1870.

Gascoin, S., Ducharne, A., Ribstein, P., Perroy, E., and Wagnon, P. (2009). Sensitivity of bare soil albedo to surface soil moisture on the moraine of the zongo glacier (bolivia). *Geophysical Research Letters*, 36(2):n/a–n/a.

Golchin, A., Oades, J., Skjemstad, J., and Clarke, P. (1994). Soil structure and carbon cycling. *Soil Research*, 32(5):1043–1068.

Goldstein, A. H., Hultman, N. E., Fracheboud, J. M., Bauer, M. R., Panek, J. A., Xu, M., Qi, Y., Guenther, A. B., and Baugh, W. (2000). Effects of climate variability on the carbon dioxide, water, and sensible heat fluxes above a ponderosa pine plantation in the sierra nevada (ca). *Agricultural and Forest Meteorology*, 101(2-3):113–129.

Grime, J. P., Mackey, J. M. L., Hillier, S. H., and Read, D. J. (1987). Floristic diversity in a model system using experimental microcosm. *Nature*, 328(6129):420–422.

Hansen, R. A. (1999). Red oak litter promotes a microarthropod functional group that accelerates its decomposition. *Plant and Soil*, 209(1):37–45.

Harris, R. (1981). *Effect of water potential on microbial growth and activity. Water Potential Relations in Soil Microbiology*. Soil Science Society of America Inc.

Haverd, V. and Cuntz, M. (2010). Soil-litter-iso: A one-dimensional model for coupled transport of heat, water and stable isotopes in soil with a litter layer and root extraction. *Journal of Hydrology*, 388(3-4):438–455.

Hawkins, H.-J., Hettasch, H., West, A. G., and Cramer, M. D. (2009). Hydraulic redistribution by protea "sylvia" (proteaceae) facilitates soil water replenishment and water acquisition by an understorey grass and shrub. *Functional Plant Biology*, 36(8):752.

Herron, P. M., Stark, J. M., Holt, C., Hooker, T., and Cardon, Z. G. (2009). Microbial growth efficiencies across a soil moisture gradient assessed using 13C-acetic acid vapor and 15N-ammonia gas. *Soil Biology and Biochemistry*, 41(6):1262–1269.

Hobbie, S. E. (1992). Effects of plant species on nutrient cycling. *Trends in Ecology & Evolution*, 7(10):336–9.

Holdaway, R. J., Sparrow, A. D., and Coomes, D. a. (2010). Trends in entropy production during ecosystem development in the Amazon Basin. *Philosophical transactions of the Royal Society of London. Series B, Biological sciences*, 365(1545):1437–47.

Holling, C. S. (1964). The analysis of complex population processes. *The Canadian Entomologist*, 96(1-2):335–347.

Hoosbeek, M. R. and Bryant, R. B. (1992). Towards the quantitative modeling of pedogenesis —a review. *Geoderma*, 55(3–4):183–210.

Horton, J. L. and Hart, S. C. (1998). Hydraulic lift: A potentially important ecosystem process. *Trends In Ecology & Evolution*, 13(6):232–235.

Huang, B. G. and Nobel, P. S. (1994). Root hydraulic conductivity and its components, with emphasis on desert succulents. *Agronomy Journal*, 86(5):767–774.

Hultine, K. R., Cable, W. L., Burgess, S. S. O., and Williams, D. G. (2003). Hydraulic redistribution by deep roots of a chihuahuan desert phreatophyte. *Tree Physiology*, 23(5):353–360.

Hultine, K. R., Scott, R. L., Cable, W. L., Goodrich, D. C., and Williams, D. G. (2004). Hydraulic redistribution by a dominant, warm-desert phreatophyte: seasonal patterns and response to precipitation pulses. *Functional Ecology*, 18(4):530–538.

Humes, K. S., Kustas, W. P., Moran, M. S., Nichols, W. D., and Weltz, M. A. (1994). Variability of emissivity and surface temperature over a sparsely vegetated surface. *Water Resources Research*, 30(5):1299–1310.

Huston, M. A. (2012). Precipitation, soils, npp, and biodiversity: resurrection of albrecht's curve. *Ecological Monographs*, 82(3):277–296.

Hutyra, L. R., Munger, J. W., Saleska, S. R., Gottlieb, E., Daube, B. C., Dunn, A. L., Amaral, D. F., de Camargo, P. B., and Wofsy, S. C. (2007). Seasonal controls on the exchange of carbon and water in an Amazonian rain forest. *Journal of Geophysical Research - Biogeosciences*, 112(G3).

Huxman, T. E., Snyder, K. a., Tissue, D., Leffler, a. J., Ogle, K., Pockman, W. T., Sandquist, D. R., Potts, D. L., and Schwinning, S. (2004). Precipitation pulses and carbon fluxes in semiarid and arid ecosystems. *Oecologia*, 141(2):254–68.

Iovieno, P. and Båå th, E. (2008). Effect of drying and rewetting on bacterial growth rates in soil. *FEMS microbiology ecology*, 65(3):400–7.

Ishikawa, C. M. and Bledsoe, C. S. (2000). Seasonal and diurnal patterns of soil water potential in the rhizosphere of blue oaks: Evidence for hydraulic lift. *Oecologia*, 125:459 – 465.

Ivanov, V. Y., Bras, R. L., and Curtis, D. C. (2007). A weather generator for hydrological , ecological , and agricultural applications. *Water Resources*, 43(August 2006).

Ivanov, V. Y., Vivoni, E. R., Bras, R. L., and Entekhabi, D. (2004). Catchment hydrologic response with a fully distributed triangulated irregular network model. *Water Resources Research*, 40(11):n/a–n/a.

Jackson, R. B., Mooney, H. A., and Schulze, E. D. (1997). A global budget for fine root biomass, surface area, and nutrient contents. *Proceedings Of The National Academy Of Sciences Of The United States Of America*, 94(14):7362–7366.

Jackson, R. B., Sperry, J. S., and Dawson, T. E. (2000). Root water uptake and transport: using physiological processes in global predictions. *Trends In Plant Science*, 5(11):482–488. P10

Jin, M. and Liang, S. (2006). An improved land surface emissivity parameter for land surface models using global remote sensing observations. *Journal of Climate*, 19(12):2867–2881.

Jobbágy, E. G. and Jackson, R. B. (2000). the Vertical Distribution of Soil Organic Carbon and Its Relation To Climate and Vegetation. *Ecological Applications*, 10(2):423–436.

Kaste, J. M., Heimsath, A. M., and Bostick, B. C. (2007). Short-term soil mixing quantified with fallout radionuclides. *Geology*, 35(3):243.

Kätterer, T., Reichstein, M., Andrén, O., and Lomander, A. (1998). Temperature dependence of organic matter decomposition: a critical review using literature data analyzed with different models. *Biology and Fertility of Soils*, 27(3):258–262.

Katul, G. G., Mahrt, L., Poggi, D., and Sanz, C. (2004). One- and two-equation models for canopy turbulence. *Boundary-Layer Meteorology*, 113(1):81–109.

Kieft, T., Soroker, E., and Firestone, M. (1987). Microbial biomass response to a rapid increase in water potential when dry soil is wetted. *Soil Biology and Biochemistry*, 19(2):119–126.

Kieft, T. L., Amy, P. S., Brockman, F. J., Fredrickson, J. K., Bjornstad, B. N., and Rosacker, L. L. (1993). Microbial abundance and activities in relation to water potential in the vadose zones of arid and semiarid sites. *Microbial Ecology*, 26(1):pp. 59–78.

Koivusalo, H., Heikinheimo, M., and Karvonen, T. (2001). Test of a simple two-layer parameterisation to simulate the energy balance and temperature of a snow pack. *Water*, 79:65–79.

Kondepudi, D. and Prigogine, I. . . (1998). *Modern thermodynamics: from heat engines to dissipative structures*. John Wiley.

Kramer, P. (1933). The intake of water through dead root systems and its relation to the problem of absorption by transpiring plants. *Americal Journal of Botany*, 20(7):481–492.

Kumar, P. (2010). Modeling water and nutrient transport through the soil-root-canopy continuum: Explicitly the below- and above-ground processes. In *American Geophysical Union, Fall Meeting*.

Kumar, P. (2011). Typology of hydrologic predictability. *Water Resources Research*, 47(July 2010):1–9.

Kurpius, M. R., Panek, J. A., Nikolov, N. T., McKay, M., and Goldstein, A. H. (2003). Partitioning of water flux in a sierra nevada ponderosa pine plantation. *Agricultural and Forest Meteorology*, 117(3-4):173–192.

Laio, F., Porporato, A., Fernandez-Illescas, C. P., and Rodriguez-Iturbe, I. (2001a). Plants in water-controlled ecosystems: active role in hydrologic processes and response to water stress - iv. discussion of real cases. *Advances In Water Resources*, 24(7):745–762.

Laio, F., Porporato, A., Ridolfi, L., and Rodriguez-Iturbe, I. (2001b). Plants in water-controlled ecosystems: active role in hydrologic processes and response to water stress - ii. probabilistic soil moisture dynamics. *Advances in Water Resources*, 24(7):707–723.

Landsberg, P. T. and Tonge, G. (1979). Thermodynamics of the conversion of diluted radiation. *J. Phys. A Math. Gen.*, 12(4):551–562.

Le, P. V. V., Kumar, P., and Drewry, D. T. (2011). Implications for the hydrologic cycle under climate change due to the expansion of bioenergy crops in the Midwestern United States. *PNAS*, 108(37).

Lee, J. E., Oliveira, R. S., Dawson, T. E., and Fung, I. (2005). Root functioning modifies seasonal climate. *Proceedings of the National Academy of Sciences of the United States of America*, 102(49):17576–17581.

Liste, H.-H. and White, J. C. (2008). Plant hydraulic lift of soil water – implications for crop production and land restoration. *Plant and Soil*, 313(1-2):1–17.

Lotka, A. J. (1922). Contribution to the energetics of evolution. natural selection as a physical principle. *Proceedings of the National Academy of Sciences of the United States of America*, 8:147–154.

Lotka, A. J. (1925). Elements of physical biology.

Ludwig, F., Dawson, T. E., Kroon, H., Berendse, F., and Prins, H. H. T. (2003). Hydraulic lift in acacia tortilis trees on an east african savanna. *Oecologia*, 134(3):293–300.

Ludwig, F., Dawson, T. E., Prins, H. H. T., Berendse, F., and Kroon, H. (2004). Below-ground competition between trees and grasses may overwhelm the facilitative effects of hydraulic lift. *Ecology Letters*, 7(8):623–631.

Lundquist, E. J., Scow, K. M., Jackson, L. E., Uesugi, S. L., and Johnson, C. R. (1999). Rapid response of soil microbial communities from conventional, low input, and organic farming systems to a wet/dry cycle. *Soil Biology and Biochemistry*, 31(12):1661–1675.

Luvall, J. C., Lieberman, D., Lieberman, M., Hartshorn, G. S., and Peralta, R. (1990). Estimation of tropical forest canopy temperatures, thermal response numbers and evapotranspiration using an aircraft-based thermal sensor. *Photogrammetric Engineering and Remote Sensing*, v. 56, no. 10, p. 1393-1401.

Lvovich, M. (2004). *On estimating the hydraulic properties of unsaturated soils*. Ame. Geophys. Union.

Manzoni, S. and Porporato, a. (2007). A theoretical analysis of nonlinearities and feedbacks in soil carbon and nitrogen cycles. *Soil Biology and Biochemistry*, 39(7):1542–1556.

Manzoni, S. and Porporato, A. (2009). Soil carbon and nitrogen mineralization: Theory and models across scales. *Soil Biology and Biochemistry*, 41(7):1355 – 1379.

Martyushev, L. and Seleznev, V. (2006). Maximum entropy production principle in physics, chemistry and biology. *Physics Reports*, 426(1):1–45.

Marulanda, A., Azcón, R., and Ruiz-Lozano, J. M. (2003). Contribution of six arbuscular mycorrhizal fungal isolates to water uptake by lactuca sativa plants under drought stress. *Physiologia Plantarum*, 119(4):526–533.

Matzner, S. L. and Richards, J. H. (1996). Sagebrush (Artemisia tridentata Nutt.) roots maintain nutrient uptake capacity under water stress. *Journal of Experimental Botany*, 47(8):1045–1056.

McClain, M. E., Boyer, E. W., Dent, C. L., Gergel, S. E., Grimm, N. B., Groffman, P. M., Hart, S. C., Harvey, J. W., Johnston, C. A., Mayorga, E., McDowell, W. H., and Pinay, G. (2003). Biogeochemical hot spots and hot moments at the interface of terrestrial and aquatic ecosystems. *Ecosystems*, 6(4):301–312.

McCulley, R. L., Jobbágy, E. G., Pockman, W. T., and Jackson, R. B. (2004). Nutrient uptake as a contributing explanation for deep rooting in arid and semi-arid ecosystems. *Oecologia*, 141(4):620–8.

Meinzer, F. C., Brooks, J. R., Bucci, S., Goldstein, G., Scholz, F. G., and Warren, J. M. (2004). Converging patterns of uptake and hydraulic redistribution of soil water in contrasting woody vegetation types. *Tree Physiology*, 24(8):919–28.

Melchior, W. and Steudle, E. (1993). Water transport in onion (allium - cepa l) roots - changes of axial and radial hydraulic conductivities during root development. *Plant Physiology*, 101(4):1305–1315.

Mendel, M., Hergarten, S., and Neugebauer, H. J. (2002). On a better understanding of hydraulic lift: a numerical study. *Water Resources Research*, 38(10):1/1–1/10. P-RAC 0

Misson, L., Panek, J. A., and Goldstein, A. H. (2004). A comparison of three approaches to modeling leaf gas exchange in annually drought-stressed ponderosa pine forests. *Tree Physiology*, 24(5):529–541.

Misson, L., Tang, J. W., Xu, M., McKay, M., and Goldstein, A. (2005). Influences of recovery from clear-cut, climate variability, and thinning on the carbon balance of a young ponderosa pine plantation. *Agricultural and Forest Meteorology*, 130(3-4):207–222.

Misson, L., Tu, K. P., Boniello, R. A., and Goldstein, A. H. (2006). Seasonality of photosynthetic parameters in a multi-specific and vertically complex forest ecosystem in the sierra nevada of california. *TREE PHYSIOLOGY*, 26(6):729–741.

Molina, R. and Trappe, J. M. (1982). Patterns of ectomycorrhizal host specificity and potential among pacific northwest conifers and fungi. *Forest Science*, 28(3):423–458.

Mooney, H. A., Gulmon, S. L., Rundel, P. W., and Ehleringer, J. (1980). Further observations on the water relations of prosopis tamarugo of the northern atacama desert. *Oecologia*, 44(2):pp. 177–180.

Moorcroft, P. R., Hurtt, G. C., and Pacala, S. W. (2001). A method for scaling vegetation dynamics: The ecosystem demography model (ed). *Ecological Monographs*, 71(4):557–585. 50

Moreira, M. Z., Scholz, F. G., Bucci, S. J., Sternberg, L. S., Goldstein, G., Meinzer, F. C., and Franco, A. C. (2003). Hydraulic lift in a neotropical savanna. *Functional Ecology*, 17(5):573–581.

Muñoz, M., Squeo, F., León, M., Tracol, Y., and Gutiérrez, J. (2008). Hydraulic lift in three shrub species from the Chilean coastal desert. *Journal of Arid Environments*, 72(5):624–632.

Nadezhdina, N., David, T. S., David, J. S., Ferreira, M. I., Dohnal, M., Tesa, M., Gartner, K., Leitgeb, E., and Nadezhdin, V. (2010). Trees never rest : The multiple facets of hydraulic redistribution. *Library*, 444(July):431–444.

Negrete-Yankelevich, S., Fragoso, C., Newton, A., Russell, G., and Heal, O. W. (2008). Species-specific characteristics of trees can determine the litter macroinvertebrate community and decomposition process below their canopies. *Plant and Soil*, 307(1-2):83–97.

Neumann, R. and Cardon, Z. (2012). The magnitude of hydraulic redistribution by plant roots: a review and synthesis of empirical and modeling studies. *New Phytol*, 194(2):337–352.

Nikolov, N. (1995). Coupling biochemical and biophysical processes at the leaf level: An equilibrium photosynthesis model for leaves of C3 plants. *Ecological Modelling*, 80(2-3):205–235.

Nikolov, N. and Zeller, K. F. (2003). Modeling coupled interactions of carbon, water, and ozone exchange between terrestrial ecosystems and the atmosphere. i: Model description. *ENVIRONMENTAL POLLUTION*, 124(2):231–246.

Njoku, E. G. and Entekhabi, D. (1996). Passive microwave remote sensing of soil moisture. *Journal of Hydrology*, 184(1–2):101–129.

Noordwijk, M., Spek, L., and Willigen, P. (1994). Proximal root diameter as predictor of total root size for fractal branching models. *Plant and Soil*, 164(1):107–117.

NRC (2001). *Basic Research Opportunities in Earth Science*. National Research Council. The National Academies Press.

Nye, P. and Tinker, P. (1977). *Solute Movement in the Soil-Root System*. University of California Press, Blackwell Scientific Publications.

Oades, J. M. (1993). The role of biology in the formation, stabilization and degradation of soil structure. *Geoderma*, 56(1–4):377–400.

Oakley, B. B., North, M. P., and Franklin, J. F. (2003). The effects of fire on soil nitrogen associated with patches of the actinorhizal shrub *ceanothus cordulatus*. *Plant and Soil*, 254(1):35–46.

Ogee, J. and Brunet, Y. (2002). A forest floor model for heat and moisture including a litter layer. *Journal of Hydrology*, 255(1-4):212–233.

Oleson, K. W., Lawrence, D. M., Gordon, B., Flanner, M. G., Kluzek, E., Peter, J., Levis, S., Swenson, S. C., Thornton, E., Dai, A., Decker, M., Dickinson, R., Feddema, J., Heald, C. L., Lamarque, J.-f., Niu, G.-y., Qian, T., Running, S., Sakaguchi, K., Slater, A., Stöckli, R., Wang, A., Yang, L., Zeng, X., and Zeng, X. (2010). Technical Description of version 4 . 0 of the Community Land Model (CLM). Technical report, National Center for Atmospheric Research.

Ozawa, H., Ohmura, A., Lorenz, R. D., and Pujol, T. (2003). The second law of thermodynamics and the global climate system: A rewview of the maximum entropy production principle. *Reviews of Geophysics*, 41(4).

Ozier-Lafontaine, H., Lecompte, F., and Sillon, J. (1999). Fractal analysis of the root architecture of gliricidia sepium for the spatial prediction of root branching, size and mass: model development and evaluation in agroforestry. *Plant and Soil*, 209(2):167–179.

Pacala, S. W. (1986a). Neighborhood models of plant population dynamics. 2. multi-species models of annuals. *Theoretical Population Biology*, 29(2):262 – 292.

Pacala, S. W. (1986b). Neighborhood models of plant population dynamics. 4. single-species and multispecies models of annuals with dormant seeds. *The American Naturalist*, 128(6):pp. 859–878.

Pacala, S. W. and Silander, J. A., J. (1990). Field tests of neighborhood population dynamic models of two annual weed species. *Ecological Monographs*, 60(1):pp. 113–134.

Panek, J. A. (2004). Ozone uptake, water loss and carbon exchange dynamics in annually drought-stressed pinus ponderosa forests: Measured trends and parameters for uptake modeling. *Tree Physiology*, 24(3):277–290.

Park, H.-T., Hattori, S., and Tanaka, T. (1998). Development of a numerical model for evaluating the effect of litter layer on evaporation. *Journal of Forest Research*, 3(1):25–33.

Parton, W. J., Schimel, D., Cole, C. V., and Ojima, D. (1987). *Analysis of factors controlling soil orgnic matter levels in Great Plains Grasslands*. Springer.

Passioura, J. B. (1988). Water transport in and to roots. *Annual Review Of Plant Physiology And Plant Molecular Biology*, 39:245–265.

Pearl, R. and Reed, L. . J. (1920). On the rate of growth of the population of the united states since 1790 and its mathematical representation. *Proceedings of the National Academy of Sciences of the United States of America*, 6(6).

Peterson, P. (1975). *Native Trees of the Sierra Nevada*. California natural history guides. University of California.

Plamboeck, A. G. H. P. (2008). Conifer seedling survival under closed-canopy and manzanita patches in the sierra nevada. *Madroño*, 55(3):193–203.

Porada, P., Kleidon, A., and Schymanski, S. J. (2011). Entropy production of soil hydrological processes and its maximisation. *Earth Syst. Dynam.*, 2(2):179–190.

Porporato, A., D'Odorico, P., Laio, F., and Rodriguez-Iturbe, I. (2003). Hydrologic controls on soil carbon and nitrogen cycles. i. modeling scheme. *Advances in Water Resources Research*, 26(1):45–58.

Porporato, A., Laio, F., Ridolfi, L., and Rodriguez-Iturbe, I. (2001). Plants in water-controlled ecosystems: active role in hydrologic processes and response to water stress - iii. vegetation water stress. *Advances In Water Resources*, 24(7):725–744.

Pregitzer, K. S., Hendrick, R. L., Fogel, R., and Hendrick, L. (1993). The demography of fine roots in response to patches of water and nitrogen. *New Phytol*, 125:575–580.

Prieto, I., Armas, C., and Pugnaire, F. I. (2012). Tansley review Water release through plant roots : new insights into its consequences at the plant and ecosystem level. *New Phytologist*.

Prieto, I., Martínez-Tillería, K., Martínez-Manchego, L., Montecinos, S., Pugnaire, F. I., and Squeo, F. a. (2010). Hydraulic lift through transpiration suppression in shrubs from two arid ecosystems: patterns and control mechanisms. *Oecologia*, 163(4):855–65.

Prigogine, I. and Wiame, J. M. (1946). Biologie et thermodynamique des phenomenes irreversibles. *Experientia*, 2(11):451–453.

Probert, M. (1998). APSIM's water and nitrogen modules and simulation of the dynamics of water and nitrogen in fallow systems. *Agricultural Systems*, 56(1):1–28.

Qi, Y. (2002). Temperature sensitivity of soil respiration and its effects on ecosystem carbon budget: Nonlinearity begets surprises. *Ecological Modelling*, 153(1-2):131–142.

Qi, Y. and Xu, M. (2001). Separating the effects of moisture and temperature on soil CO 2 efflux in a coniferous forest in the Sierra Nevada mountains. *Plant and Soil*, pages 15–23.

Querejeta, J., Egerton-Warburton, L., and Allen, M. (2007). Hydraulic lift may buffer rhizosphere hyphae against the negative effects of severe soil drying in a California Oak savanna. *Soil Biology and Biochemistry*, 39(2):409–417.

Querejeta, J. I., Egerton-Warburton, L. M., and Allen, M. F. (2003). Direct nocturnal water transfer from oaks to their mycorrhizal symbionts during severe soil drying. *Oecologia*, 134(1):55–64.

Quijano, J., Kumar, P., and Drewry, D. T. D. (2013). Passive regulation of soil biogeochemical cycling by root water transport. *Submitted Water Resources Research*.

Quijano, J. C., Kumar, P., Drewry, D. T., Goldstein, A., and Misson, L. (2012). Competitive and mutualistic dependencies in multispecies vegetation dynamics enabled by hydraulic redistribution. *Water Resour. Res.*, 48(5).

Rasmussen, C., Troch, P. A., Chorover, J., Brooks, P., Pelletier, J., and Huxman, T. E. (2011). An open system framework for integrating critical zone structure and function. *BIOGEOCHEMISTRY*, 102(1-3):15–29.

Rathfelder, K. and Abiola, L. M. (1994). Mass conservative numerical-solutions of the head-based richards equation. *Water Resources Research*, 30(9):2579–2586.

Richardson, A. D., Hollinger, D. Y., Dail, D. B., Lee, J. T., Munger, J. W., and Keefe, J. O. (2009). Influence of spring phenology on seasonal and annual carbon balance in two contrasting New England forests. *Tree Physiology*, pages 321–331.

Richrads, J. H. and Caldwell, M. M. (1987). Hydraulic lift - substantial nocturnal water transport between soil layers by artemisia-tridentata roots. *Oecologia*, 73(4):486–489. 0

Richter, D. D., Markewitz, D., Trumbore, S. E., and Wells, C. G. (1999). Rapid accumulation and turnover of soil carbon in a re-establishing forest. *Ecosystems*, 400(July):14–16.

Rillig, M. C. and Mummey, D. L. (2006). Mycorrhizas and soil structure. *New Phytologist*, 171(1):41–53.

Rodriguez-Iturbe, I., Porporato, A., Laio, F., and Ridolfi, L. (2001). Plants in water-controlled ecosystems: active role in hydrologic processes and response to water stress - i. scope and general outline. *Advances in Water Resources*, 24(7):695–705.

Rose, K. L., Graham, R. C., and Parker, D. R. (2003). Water source utilization by *Pinus jeffreyi* and *Arctostaphylos patula* on thin soils over bedrock. *Oecologia*, 134(1):46–54.

Rossiter, D. G. and Riha, S. J. (1999). Modeling plant competition with gaps object-oriented dynamic simulation model. *Agron. J*, 91:773–783.

Ruiz-Lozano, J. (2003). Arbuscular mycorrhizal symbiosis and alleviation of osmotic stress. new perspectives for molecular studies. *Mycorrhiza*, 13(6):309–317.

Ryel, R. J., Caldwell, M. M., Yoder, C. K., Or, D., and Leffler, A. J. (2002). Hydraulic redistribution in a stand of artemisia tridentata: evaluation of benefits to transpiration assessed with a simulation model. *Oecologia*, 130(2):173–184.

Saleska, S., Miller, S., Matross, D., Goulden, M., Wofsy, S., da Rocha, H., de Camargo, P., Crill, P., Daube, B., de Freitas, H., Hutyra, L., Keller, M., Kirchhoff, V., Menton, M., Munger, J., Pyle, E., Rice, A., and Silva, H. (2003). Carbon in amazon forests: Unexpected seasonal fluxes and disturbance-induced losses. *SCIENCE*, 302(5650):1554–1557.

Saxton, K. E. and Rawls, W. J. (2006). Soil water characteristic estimates by texture and organic matter for hydrologic solutions. *SOIL SCIENCE SOCIETY OF AMERICA JOURNAL*, 70(5):1569–1578.

Schaap, M. G., Bouten, W., and Verstraten, J. M. (1997). Forest floor water content dynamics in a douglas fir stand. *Journal of Hydrology*, 201(1-4):367–383.

Schade, G. W. (2002). Plant physiological influences on the fluxes of oxygenated volatile organic compounds from ponderosa pine trees. *Journal of Geophysical Research*, 107:3111–3123.

Schenk, H. J. and Jackson, R. B. (2002). The global biogeography of roots. *Ecological Monographs*, 72(3):311–328. P40

Schimel, D. S., Braswell, B. H., and Parton, W. J. (1997). Equilibration of the terrestrial water, nitrogen, and carbon cycles. *Proceedings of the National Academy of Sciences*, 94(16):8280–8283.

Schneider, E. and Kay, J. (1994). Life as a manifestation of the second law of thermodynamics. *Mathematical and Computer Modelling*, 19(6–8):25 – 48.

Scholz, F. G., Bucci, S. J., Goldstein, G., Meinzer, F. C., and Franco, A. C. (2002). Hydraulic redistribution of soil water by neotropical savanna trees. *Tree Physiology*, 22(9):603–612.

Schrodinger, E. (1944). *What is life ? The physical aspect of the living cell.* Cambridge : University Press.

Schulze, E. D., Caldwell, M. M., Canadell, J., Mooney, H. A., Jackson, R. B., Parson, D., Scholes, R., Sala, O. E., and Trimborn, P. (1998). Downward flux of water through roots (ie inverse hydraulic lift) in dry kalahari sands. *Oecologia*, 115(4):460–462.

Schymanski, S. J., Kleidon, A., Stieglitz, M., and Narula, J. (2010). Maximum entropy production allows a simple representation of heterogeneity in semiarid ecosystems. *Philosophical transactions of the Royal Society of London. Series B, Biological sciences*, 365(1545):1449–55.

Scott, R. . . L. ., Cable, W. . . L. ., and Hultine, K. . . R. . (2008). The ecohydrologic significance of hydraulic redistribution in a semiarid savanna. *Water Resources Research*, 44(2).

Shinozake, K., Yoda, K., Hozumi, K., and Kira, T. (1964). A quantitative analysis of plant form - the pipe model theory: Ii. further evidence of the theory and its application in forest ecology. *Japanese Journal of Ecology*, 14(4):133–139.

Shugart, H. H., J. and West, D. C. (1980). Forest succession models. *BioScience*, 30(5):pp. 308–313.

Silver, W. L., Neff, J., McGroddy, M., Veldkamp, E., Keller, M., and Cosme, R. (2000). Effects of soil texture on belowground carbon and nutrient storage in a lowland amazonian forest ecosystem. *Ecosystems*, 3(2):193–209.

Singh, B. K., Munro, S., Potts, J. M., and Millard, P. (2007). Influence of grass species and soil type on rhizosphere microbial community structure in grassland soils. *Applied Soil Ecology*, 36(2–3):147–155.

Siqueira, M., Katul, G., and Porporato, A. (2008). Onset of water stress, hysteresis in plant conductance, and hydraulic lift: Scaling soil water dynamics from millimeters to meters. *Water Resources Research*, 44(1):W01432. P0

Smart, D. R., Carlisle, E., Goebel, M., and Núñez, B. A. (2005). Transverse hydraulic redistribution by a grapevine. *Plant, Cell and Environment*, pages 157–166.

Smith, D. M., Jackson, N. A., Roberts, J. M., and Ong, C. K. (1999). Reverse flow of sap in tree roots and downward siphoning of water by grevillea robusta. *Functional Ecology*, 13(2):256–264.

Smith, S. G. (2005). Effects of moisture on combustion characteristics of live California chaparral and Utah foliage. Master's thesis, Brigham Young University.

Stephens, S. L. and Moghaddas, J. J. (2005). Fuel treatment effects on snags and coarse woody debris in a sierra nevada mixed conifer forest. *Forest Ecology and Management*, 214(1–3):53 – 64.

Sylvia, D. M., Fuhrmann, J. J., Hartel, P. G., and Zuberer, D. A. (2005). *Principles and Applications of Soil Microbiology*. Pearson, Prentice Hall.

Tang, J. W., Misson, L., Gershenson, A., Cheng, W. X., and Goldstein, A. H. (2005). Continuous measurements of soil respiration with and without roots in a ponderosa pine plantation in the sierra nevada mountains. *Agricultural and Forest Meteorology*, 132(3-4):212–227.

Tyree, M. and Zimmermann, M. (2002). *Xylem Structure and the Ascent of Sap*. Springer Series in Wood Science. Springer.

Tyree, M. T. and Sperry, J. S. (1988). Do woody plants operate near the point of catastrophic xylem dysfunction caused by dynamic water stress?: Answers from a model. *Plant physiology*, 88(3):574–80.

Urbanski, S., Barford, C., Wofsy, S., Kucharik, C., Pyle, E., Budney, J., McKain, K., Fitzjarrald, D., Czikowsky, M., and Munger, J. W. (2007). Factors controlling co2 exchange on timescales from hourly to decadal at harvard forest. *Journal of Geophysical Research*, 112(G2):G02020.

Valizadeh, G. R., Rengel, Z., and Rate, A. W. (2003). Response of wheat genotypes efficient in p utilisation and genotypes responsive to p fertilisation to different p banding depths and watering regimes. *Australian Journal of Agricultural Research*, 54(1):59–65.

van Genuchten, M. and Leij, F. (1992). *Indirect methods for estimating the hydraulic properties of unsaturated soils*, chapter On estimating the hydraulic properties of unsaturated soils, pages p. 1 –14. Univ. of California.

Vetterlein, D. and Marschner, H. (1993). Use of a microtensiometer technique to study hydraulic lift in a sandy soil planted with pearl millet (pennisetum americanum [l.] leeke). *Plant and Soil*, 149(2):275–282.

Vitousek, P. M. and Matson, P. a. (1984). Mechanisms of nitrogen retention in forest ecosystems: a field experiment. *Science (New York, N.Y.)*, 225(4657):51–2.

Vitousek, P. M. and Walker, L. R. (1989). Biological invasion by myrica-faya in hawaii - plant demography, nitrogen fixation, ecosystem effects. *Ecological Monographs*, 59(3):247–265.

Volterra, V. I. T. O. (1926). Variations and fluctuations in the number of individuals among animals living together. *J. Cons. Perm. Int. Ent. Mer.*, 2((3)):31–112.

Walker, A. R. F., Cheng, W., and Johnson, D. W. (2010). Mycorrhization of Ponderosa Pine in a Second-Growth Sierra Nevada Forest. *Western North American Naturalist*, 70(1):1–8.

Wang, G. (2011). Assessing the potential hydrological impacts of hydraulic redistribution in Amazonia using a numerical modeling approach. *Water Resources Research*, 47(2).

Wang, G., Alo, C., Mei, R., and Sun, S. (2010). Droughts, hydraulic redistribution, and their impact on vegetation composition in the Amazon forest. *Plant Ecology*, 212(4):663–673.

Wang, J. and Bras, R. L. (2011). A model of evapotranspiration based on the theory of maximum entropy production. *Water Resources Research*, 47(3):W03521.

Wardle, D. A., Bardgett, R. D., Klironomos, J. N., Setälä, H., van der Putten, W. H., and Wall, D. H. (2004). Ecological linkages between aboveground and belowground biota. *Science*, 304(5677):1629–1633.

Warren, J. M., Brooks, J. R., Dragila, M. I., and Meinzer, F. C. (2011). In situ separation of root hydraulic redistribution of soil water from liquid and vapor transport. *Oecologia*, 166(4):899–911.

Warren, J. M., Brooks, J. R., Meinzer, F. C., and Eberhart, J. L. (2008). Hydraulic redistribution of water from pinus ponderosa trees to seedlings: evidence for an ectomycorrhizal pathway. *New Phytologist*, 178(2):382–394.

Warren, J. M., Meinzer, F. C., Brooks, J. R., Domec, J. C., and Coulombe, R. (2007). Hydraulic redistribution of soil water in two old-growth coniferous forests: Quantifying patterns and controls. *New Phytologist*, 173(4):753–765.

Wilson, J. and Griffin, D. (1975). Water potential and the respiration of microorganisms in the soil. *Soil Biology and Biochemistry*, 7(3):199–204.

Wilson, K. (2000). Factors controlling evaporation and energy partitioning beneath a deciduous forest over an annual cycle. *Agricultural and Forest Meteorology*, 102(2-3):83–103.

Wright, H. and Bailey, A. (1982). *Fire ecology, United States and southern Canada*. Wiley Classics in Ecology and Environmental Science. Wiley.

Wright, S., Scott, D., Haddow, J., and Rosen, M. (2001). On the entropy of radiative heat transfer in engineering thermodynamics. *International Journal of Engineering Science*, 39(15):1691 – 1706.

Wu, W. and Liu, Y. (2010). Radiation entropy flux and entropy production of the earth systems. *Reviews of Geophysics*, 48(2008RG000275):1–27.

Wullschleger, S. D., Jackson, R. B., Currie, W. S., Friend, A. D., Luo, Y., Mouillot, F., Pan, Y., and Shao, G. (2001). Below-ground processing in gap models for simulating forest response to global change. *Climatic Change*, 51.

Xu, M. and Qi, Y. (2001). Soil-surface co2 efflux and its spatial and temporal variations in a young ponderosa pine plantation in northern california. *Global Change Biology*, 7(6):667–677.

Yoder, C. K. and Nowak, R. S. (1999). Hydraulic lift among native plant species in the mojave desert. *Plant and Soil*, 215(1):93–102.

Zogg, G. P., Zak, D. R., Ringelberg, D. B., Macdonald, N. W., Pregitzer, K. S., and White, D. C. (1997). Compositional and functional shifts in microbial communities due to soil warming. *Soil Science Society of America Journal*, 61(2):475–481.

Zou, C. B., Barnes, P. W., Archer, S., and McMurtry, C. R. (2005). Soil moisture redistribution as a mechanism of facilitation in savanna tree-shrub clusters. *Oecologia*, 145(1):32–40.